# Synthesis and characterization of nano- and microcrystalline ternary *MAX*-Materials (*M* = Ni, Co; *A* = Li, In, Sn, Pb, Tl; *X* = S, Se, $PO_4$)

## Diffusion/Intercalation of metals into binaries as mechanism of formation and application as electrode materials


**Dissertation**

zur Erlangung des Doktorgrades der Naturwissenschaften (Dr. rer. nat.)

der Fakultät für Chemie und Pharmazie

der Universität Regensburg

vorgelegt von

**Stefan Rommel**

aus Augsburg

im Jahr 2016

The experimental part of this work was carried out between November 2012 and July 2015 at the Institute of Inorganic Chemistry at the University of Regensburg under the supervision of Prof. Dr. Richard Weihrich.

**Submission of thesis:** March 2016
**Date of colloquium:** 03.05.2016

**Board of examiners:**

| | |
|---|---|
| Chairman: | Prof. Dr. Alkwin Slenczka |
| 1st Referee | Prof. Dr. Richard Weihrich |
| 2nd Referee | Prof. Dr. Arno Pfitzner |
| 3rd Referee | Prof. Dr. Frank-Michael Matysik |

**Statutory declaration**

I, Stefan Rommel, hereby confirm that my thesis entitled “Synthesis and characterization of nano- and microcrystalline ternary *MAX*-Materials (*M* = Ni, Co; A = Li, In, Sn, Pb, Tl; *X* = S, Se, $PO_4$), Diffusion/Intercalation of metals into binaries as mechanism of formation and application as electrode materials” is the result of my own work. I did not receive any aid or help of any kind not mentioned in this thesis. All sources and/or materials applied are listed and specified in the thesis.

Furthermore, I confirm that this thesis has not yet been submitted as part of another examination process neither in identical nor in similar form.

_____ _____

Place, Date Signature

Parts of this thesis were already published:

1. **S. Rommel**, N. Schall, C. Brünig, R. Weihrich
   Challenges in the synthesis of high voltage electrode materials for lithium-ion batteries: a review on $LiNiPO_4$
   *Monatsh. Chem.,* **2014**, *145*, 385-404.

2. **S. Rommel**, N. Schall, C. Brünig, J. Rothballer, R. Weihrich
   Characterization of the carbon-coated $LiNi_{1-y}Co_yPO_4$ solid solution synthesized by a non-aqueous sol-gel route
   *Ionics,* **2015**, *21*, 325-333.

3. **S. M. Rommel**, R. Weihrich
   Selective reaction of $Ni^{2+}$ and SnS as a way to Ni@SnS and $Sn_2Ni_3S_2$ nanocrystals - control of product formation and shape
   *Chem. Eur. J.,* **2015**, 21, 9863-9867.

4. **S. M. Rommel**, A. Krach, P. Peter, R. Weihrich
   Conversion reactions of solids: from a surprising 3-step mechanism towards directed product formation
   *Chem. Eur. J.,* **2016**, 22, 6333-6339.

Furthermore, following contributions were published during the thesis:

1. J. Rothballer, F. Bachhuber, **S. M. Rommel**, T. Söhnel, R. Weihrich
   Origin and effect of In-Sn ordering in $InSnCo_3S_2$: a neutron diffraction and DFT study
   *RSC Adv.*, **2014**, *4*, 42183-42189.

2. N. Kunkel, D. Rudolph, A. Meijerink, **S. M. Rommel**, R. Weihrich, H. Kohlmann, T. Schleid
   Green Luminescence of Divalent Europium in the Hydride Chloride EuHCl
   *Z. Anorg. Allg. Chem.*, **2015**, 641, 1220-1224.

3. R. Weihrich, W. Yan, J. Rothballer, P. Peter, **S. M. Rommel,** S. Haumann, F. Winter, C. Schwickert, R. Pöttgen
   Tuneable anisotropy and magnetism in $Sn_2Co_3S_{2-x}Se_x$ – probed by $^{119}$Sn Mößbauer spectroscopy and DFT studies
   *Dalton Trans.*, **2015**, 44, 15855-15864.

## Conference Paper/Poster

1. **S. M. Rommel**, R. Weihrich, N. Schall, C. Brünig
   Detailed analysis of different synthesis methods and electrochemical performance of $LiNiPO_4$ and its derivatives
   14th European Conference on Solid State Chemistry
   France, Bordeaux, 07.10.-10.07.2013

2. J. Rothballer, W. Yan, A. Furtner, S. Tragl, **S. Rommel**, R. Weihrich
   Electric Field Gradients in NiIn and $In_2Ni_3S_2$
   International School on Ab initio Modelling of Solids 2014
   Germany, Regensburg, 20.07.-25.07.2014

3. **S. M. Rommel**, S. Haumann, P. Peter, R. Weihrich
   Zur Reindarstellung des $LiNiPO_4$
   17. Vortragstagung Fachgruppe Festkörperchemie und Materialforschung
   Germany, Dresden, 15.09.-17.09.2014
   *Z. Anorg. Allg. Chem.* **2014**, 640, 2372

4. **S. Rommel**, R. Weihrich
   Conversion chemistry of SnS as a way to Ni@SnS and $Sn_2Ni_3S_2$ nanocrystals – control of product formation and shape
   GDCh-Wissenschaftsforum Chemie 2015
   Germany, Dresden, 30.08.-02.09.2015

# Talks

1. R. Weihrich, **S. M. Rommel**
   On Synthesis Routes and purity of $LiNiPO_4$
   Power our future 2014, The 2nd International Forum on Progress and Trends in Battery and Capacitor Technologies
   Spain, Vitoria-Gasteiz, 01.04.-04.04.14

2. R. Weihrich, **S. M. Rommel**, W. Yan, A. Furtner, A. Krach
   Neue Synthesewege zu $M_zA_yX_x$-Phasen
   17. Vortragstagung Fachgruppe Festkörperchemie und Materialforschung
   Germany, Dresden, 15.09.-17.09.2014
   *Z. Anorg. Allg. Chem.* **2014**, 640, 2325

# TABLE OF CONTENTS

# ACKNOWLEDGEMENT

Some persons, institutions and companies have made important contributions to this thesis. Without them, the last years would not have been so enjoyable and my PhD would even not have been possible. For this reason, they deserve to be acknowledged accordingly.

I would like to first of all thank my supervisor Prof. Dr. Richard Weihrich for awaking my interest in inorganic chemistry and for taking me with him to Regensburg and later on to Augsburg. I am very thankful that he gave me the opportunity and freedom to conduct independent research in the field of materials science. His assistance, support and many helpful discussions granted a continuous improvement of this thesis.

My colleagues of our working group Jan Rothballer, Frederik Bachhuber, Philipp Peter, Wenjie Yan, Andrea Furthner, Sebastian Haumann, Alexander Krach and Amadeus-Samuel Tragl for the good working atmosphere and pastimes.

Prof. Dr. Arno Pfitzner, his working group and the technical staff for providing the space, technical equipment and support.

Marianne Köpf and Prof. Dr. Tom Nilges of the TU München and Dr. Thomas Lunkenbein and Gisela Weinberg of the Fritz Haber Institute of the Max Planck Society (Berlin) for SEM and EDX measurements.

PD Dr. Rainer Müller for the evaluation of the specific surface area of selected samples.

Dr. Norbert Schall, Dr. Christian Brünig, Holger Kunz and Jasmin Dollinger from Süd Chemie/Clariant for galvanostatic cycling tests and useful discussions, concerning the electrochemical interpretation.

Professor Dr. Matysik, Jonas Mark and Christian Iffelsberger for guidance and the possibility to measure CV in their institute.

Professor Dr. Armin Reller and his work group for the assistance at the University of Augsburg.

I want to especially thank my parents and my brother, as well as my girlfriend for supporting me during my studies and all other life situations.

Last but not least I would also like to express my gratitude to the Deutsche Forschungsgemeinschaft (DFG) for financial support.

# I. Introduction

## 1. Motivation and structure of the thesis

The present thesis can be divided into two thematical units. Both units are connected to each other as they deal with nano- and microcrystalline multinary solid-state compounds where the single phase synthesis, especially in the nano scale, is very hard to accomplish or even not yet known. This work contributes to this problem by generating a better understanding of the mechanisms of formation of these compounds which are taking place in polyol, pure solid-state and sol-gel reactions. The knowledge is used afterwards to selectively design the compounds according to the special requirements.

The creation and development of innovative technologies is often based on the availability of **solid-state materials** with appropriate physical and chemical properties[1-4]. The impact of functional bulk materials in daily life is best exemplified by the semiconductor industry[5-8]. Any targeted synthesis of the demanded materials requires intelligent combinations of chemical compositions, structures and functions.

Today, **ternary or multinary materials** for high-temperature ceramic superconductors, superionic or spintronic materials, topological insulators, high-voltage electrode materials, magnetic alloys, and catalytic materials are deemed as promising candidates to initiate ground speaking changes in relevant technologies, including communications, **energy-storage**, transportation, and chemical manufacturing. Their synthesis is increasingly assisted by computational chemistry[9-11]. However, in any case the bottleneck for the availability still is the **chemical synthesis** of any desired material that should be smart, low cost, and sustainable with respect to resource and environmental aspects. Unfortunately, little is known in **reaction mechanisms** for bulk inorganic materials or in ways to direct paths of synthesis that is daily work in organic synthesis. For applications, knowledge on ways for modifications, reactions and stability, became highly desired. Rational synthesis strategies have to be developed to control formation, growth mechanisms and shape.

In recent years, a range of new methods in chemical synthesis appeared with the rise of **nanoscale chemistry**. New solution based low-temperature methods, like the polyol route[12-18] or the synthesis in ionic liquids[19-23] have been identified and developed as an effective alternative to produce phase-pure micro- or nanoscale inorganic compounds.

Regarding transition metal, binary oxide and chalcogenide nanoparticles synthetic concepts are meanwhile well developed[18, 24-26]. Therein, conversion or addition of function was successfully shown for a range of oxide or nitride nanomaterials under retention of particle size and shape[27, 28]. However, the established methods are hardly transferable to synthesize multi-metal or intermetallic compounds for enhanced novel functions. Often, these compounds can still only be prepared by solid-state reactions, which are expensive, time consuming and no control of the shape is possible. Furthermore, the problem of directing reactions occurs when multiple products are possible in a phase diagram and the mechanisms taking place are still not understood.

One of the rare reports comprises the fascinating concept of **conversion reactions of binary to ternary nanoparticles**. Important examples are intermetallic $Bi_2Pd$ and BiPt nanoparticles that serve as ‘‘single source’’ reagent for the oxidation into the mixed metal oxide $Bi_2PdO_4$ and $Bi_2Pt_2O_7$[26] under retaining its shape. The morphology controlled conversions of the binary chalcogenides, $PbS_{dendrite}$ to ***shandite*-type** $Ni_3Pb_2S_{2,dendrite}$ and $Bi_2S_{3,rod}$ to ***parkerite*-type** $Ni_3Bi_2S_{2,rod}$ also join this rank[29, 30]. They serve as a kind of starting point of **the first thematical unity of this thesis**.

Chapter III and IV combine the concept of conversion chemistry of binaries with the DFG supported project “Halfantiperovskites (HAP)” of our working group. The $M_3A_2X_2$ (HAP) compounds were classified as multi metal ordered half antiperovskites with layered partial [$M_3S_2$] structures[31-34]. They attracted attention, as magnetic and electronic properties can be tuned by substitution of *M*=Ni, Co, Rh, Pd and *A*=In, Tl, Pb, Sn. The properties and supposed applications are related to intermetallic *A*-*M* and chalcogenide like behavior and range from small band gap semiconductors and thermoelectrics[35-37] to half metal ferromagnets[37, 38] and catalysts[30, 39-41]. The aim was to develop new solution based soft-chemical methods for the reactive templated and (if possible) morphology templated synthesis of selected ternary $Ni_3A_2X_2$ or bifunctional hybrid/core-shell particles with the same stoichiometry. Here, the second main subject of studies of our work group turns into focus, too, i.e. studies of competing and metastable solid phases (SPP1415, “crystalline non equilibrium phases”). In this respect, the conversion reactions can be seen as ways to direct reactions and control product formation, as binary chalcogenides and intermetallics were applied as templates. The environmental friendly polyol process was used to discuss the influence of different parameters like starting materials, temperature, time and pressure on the resulting products.

Chapter III exclusively deals with the element combinations of possible nickel *shandite*-type compounds ($M$ = Ni; $A$ = In, Tl, Sn, Pb; $X$ = S, Se). Binary chalcogenides acted as the templates. By carefully adjusting the redox and equilibrium conditions it was tried to learn to selectively direct the reaction towards conversion reactions (binary chalcogenide→different binaries or ternary *shandite*-type compounds) or deposition reactions (binary chalcogenide→core-shell/hybrid particles). By a deposition reaction, important functional combinations of a semiconductor and a metal in the same particle are formed. Such combinations are of particular interest as the metal can provide an anchor point for electrical and chemical connections to the functional semiconductor part. These bifunctional particles can furthermore be transformed into ternary solid-solutions afterwards. The experimental findings were summarized in a general applicable synthesis protocol. A major focus lay on the design of special morphology of the samples. Further attention was given to the elucidation of possible mechanisms of formation which proved to be different for the *shandite* and *parkerite* phases (Chapter IV). After the successful synthesis, selected samples were characterized in terms of specific surface area and thermomechanical properties and compared to their bulk counterparts. In addition, the mechanism of formation in solution were compared to that in pure solid-state reactions, which was evaluated by in situ HT-XRD of different binary sulfides with nickel.

Chapter IV solely deals with the stoichiometry of the nickel *parkerite*- or *pyrite*-type compounds $Ni_3Bi_2X_2$ ($X$ = S, Se). Here, the binary chalcogenide $Bi_2X_3$ and the intermetallic compound NiBi were applied as reactive templates. The impacts of both precursors on the resulting products were evaluated and a possible mechanism of formation with the intermediates Bi-NiBi-$Ni_3Bi_2S_2$ is proposed. In a second step, the selenium containing counterparts were prepared, starting from NiBi. A possible pathway for the selective synthesis of the *parkerite* (3:2:2 composition) or the competing *pyrite* phase (1:1:1 composition) is shown and discussed in terms of energetic classifications by DFT calculations. This chapter shows one of the first reports, where intermetallics are used to access multinary systems by conversion reactions.

**The second thematical unity** of this thesis deals with the electrochemical characterization of multinary electrode materials. The electrochemical reaction of lithium with binaries or other compounds can in principle undergo conversion or so called **intercalation reactions**. Conversion reactions are known when lithium is reacted with different binaries, like $FeF_2$,

$FeF_3$, $CuF_2$[42, 43], NiO[44] or ternaries like $MnFe_2O_4$[45] or $CuCr_2Se_4$[46]. A prerequisite for electrochemical reversibility is the formation of a bicontinuous network of metal atoms, which provides a pathway for local electron transport through the respective insulating phase. In contrast to that, during intercalation reactions lithium is inserted into a host matrix with essential retention of the crystal structure[47]. Lithium titanium disulfide has become the prototypical ideal intercalation cathode[48], showing essentially complete reversibility in lithium reactions at very high rate. However, the potential of only approx. 2 volts in a lithium titanium disulfide cell is insufficient for many applications. Inspired by the success of $LiCoO_2$'s[49] commercial development, with its inherent higher voltage, researchers have extended their interests to ***olivine*-structured orthophosphates Li*M*$PO_4$** (*M* = Fe, Mn, Co, and Ni). These are seen as alternative electrode materials for the next generation of rechargeable lithium ion batteries[50]. Today, most of the secrets of $LiFePO_4$ and $LiMnPO_4$ have been solved. Lithium iron phosphate has shown various advantages in terms of high theoretical capacity, high-rate capability, long-term cycle performance, stability, safety, environmental benignity, and low-cost raw material[50-54]. As the voltage of Fe- and Mn-based olivine intercalants are low-energy producers compared to Ni and Co compounds, research now tries to solve the problems of these electrode materials. But still, fundamental aspects are not understood and often, even the redox step of $Ni^{3+}/Ni^{2+}$ can hardly be activated because of various (most often speculative) reasons[55]. Especially $LiNiPO_4$ seldom shows electrochemical activity and more than ever very bad cyclability. The likely reasons for that behaviour were recently summarized[55] by our workgroup and some possible strategic approaches to circumvent the inherent problems were identified.

Further studies in Chapter V are consequently devoted to the *olivine* compounds $LiNiPO_4$ and $LiCoPO_4$ and its solid-solution $LiNi_{1-y}Co_yPO_4$. The samples are prepared by a sol-gel synthesis, which combines numeral positive effects, like an in-situ carbon coating, small particles and single phase materials. Structural and electrochemical properties of the samples are studied and the formation of the conducting side phase $Ni_3P$ is also evaluated. New insights into the activation of the nickel redox couple and other structure property relations of these samples are gained.

Simultaneously, a home-made cyclovoltammetric cell was built for the electrochemical testing of electrode materials. The financial and special conditions required that just inexpensive components were used. Furthermore, the cell had to be constructed in a manner that it could

also operate outside a glove box. All steps, from the electrolyte, over the cathode, to the lithium anode and the cell were optimized by the use of a known standard material. The operational functionality was shown for $LiCoO_2$. First characterizations of materials with unknown electrochemical behaviour were also conducted.

Some results which are subsequently shown in this thesis were already published in relevant journals[55-58] or are in preparation.

## 2. Inorganic nanomaterials

Nanoscience deals with materials where at least one of the dimensions is in the 1–100 nm range. An important aim in the development of nanoparticles is the improvement of certain materials properties, which are already inherent with the bulk material. Thereby, same material properties can be reached with solely a fraction of the otherwise required amount of raw materials. Nanoparticles are therefore seen to contribute to the materials and resource efficiency goals, stated by the politics[59, 60].

Nevertheless, the big interest on nanoparticles is not only based on the resource-saving material usage, but for the most part on the development of new, in comparison to the bulk different properties and applications. Those features of such materials strongly depend on their size and shape of the particles[61]. Very small nanoparticles with diameters of a few nanometres are comparable to molecules. Hence, the electronic and atomic structures of such small nanoparticles exhibit unusual features, markedly different from those of the bulk materials (e.g., lower melting points, higher specific surface areas, specific optical properties, mechanical strengths, and specific magnetizations). Those properties might prove attractive in various industrial applications. Especially for the battery technology, nanoparticles of known bulk materials proved to improve the electrochemical performance drastically[55].

Nanoparticles have already a long tradition and can be traced back to the Roman period. For example, colloidal metals were used to dye glass articles and fabrics and as a therapeutic aid in the treatment of arthritis[62]. The Purple of Cassius, formed on reacting stannic acid with chloroauric acid, was a popular purple dye in the antiquity. The gold particles don’t show the typical golden colour, but are purple because of their small particle size and the thus

appearing plasmonic resonance. But even today the research on nanoparticles enjoys great popularity. Thereby, mainly catalytic[63, 64], optical[65, 66] and magnetical properties[67], are paramount.

Two different approaches are known for the preparation of nanoparticles. The first is the breakdown (top-down) method by which an external force is applied to a solid that leads to its break-up into smaller particles. For instance ball mill methods or laser ablation[68]. Although these methods have been employed on a large scale to synthesize inorganic nanomaterials, they are limited in their ability to fine-tune the resulting properties, which are dependent on parameters such as particle size, uniformity, and morphology[69]. In order to gain better control over the physical parameters of the desired inorganic nanomaterials, build-up (bottom-up) chemical routes have been developed and are commonly used. The bottom-up method that produces nanoparticles using self-organizing processes – i.e. single atoms and molecules are assembled into larger nanostructures. Often, the so-called "hot-injection' method is applied, where a precipitating agent is fed to a heated solution[70, 71]. Other approaches directly precipitate particles from solution using the different solubility of compounds in acid or alkaline solutions[72]. The bottom-up method makes is possible to synthesize nanomaterials with different sizes and specific shapes, e.g. zero-dimensional nanocrystals, one-dimensional nanowires and nanotubes and two-dimensional nanofilms and nanowalls. This is mainly due to the fact that bottom-up approaches lead to an intimate mixing of the precursors and also surface stabilizers like polyvinylpyrrolidone (PVP) and Cetyltrimethylammonium bromide (CTAB) can be used[73, 74]. Those stabilizers modify the surface and thereby influence the resulting size and morphology of the resulting nanoparticles. The sol-gel and polyol techniques and also the concepts of conversion chemistry and templating which have been applied in this thesis can also be ascribed to the bottom-up approaches. These syntheses employ lower temperatures and shorter reaction times and allow for greater kinetic control over the final products.

## 3. Conversion Chemistry

Chemical conversion is a very vaguely defined term in chemical reaction engineering, often related with the terms yield and selectively[75]. Hereby, the conversion describes the ratio of

how much of a reactant has reacted. For selectively and yield there are contradictory definitions in the literature. Most often yield describes how much of a desired product was formed, whereas selectively describes how much of the desired product was formed in ratio to the undesired product.

In nowadays literature the term “conversion reaction” or “conversion chemistry” is widely used and is especially promoted by the group of Schaak[25]. The general synthesis protocol involves the conversion of preformed metal (nano-)particles into the desired compound. The use of the (nano-)crystalline templates helps to define the composition, crystal structure, and morphology of the products. By this approach numerous different nanostructures, such as rods, dendrites, cubes and so forth can be obtained. Even hollow particles, which are not typically accessible using thermal decomposition reactions can be easily made using a Kirkendall-type mechanism[76]. The term conversion chemistry can be categorized into 3 possible processes[77]: Diffusion based processes, deposition processes and transmetalation processes.

### a) Diffusion based process

Often, simple diffusion based processes are taking place during conversion reactions. They occur in many pure solid-state reactions but also in many of the solution-based methods. Hence, the diffusion of metals and chalcogenides into different materials has been extensively investigated in bulk[78-80] and nanomaterials[81-83].

For example, simple diffusion-mediated oxidation reactions of metal nanoparticles can be used to synthesize high-quality metal oxide nanoparticles such as CoO[81], $Fe_2O_3$ [82], and $Fe_3O_4$[83]. Often elevated temperatures under air or mild oxidants are sufficient for such conversions. Furthermore, diffusion-based methods can be used to convert metal nanoparticles to metal sulfides and other chalcogenides. For example Alivisatos and co-workers showed the conversion of Co nanocrystals into $Co_3S_4$ and $Co_9S_8$ nanocrystals in the presence of sulfur in solution[83, 84]. These strategies can also produce hollow nanocrystals via the Kirkendall effect[84-86]. Regarding binaries as reactants many different reactions are possible. Yang and co-workers studied the thermal behaviour of $Cu_2S$ in the presence of $N_2$ and $O_2$. The nanowires are stable in $N_2$, but they are oxidized by $O_2$ to $Cu_2O$ and to CuO at

higher temperatures by a diffusion based process[87]. The combination of a metal and a semiconductor in the same particle is also greatly dependent on the diffusional behaviour of the respective metal in the semiconductor. Such combinations are of particular interest as the metal can provide an anchor point for electrical and chemical connections to the functional semiconductor part. As such a combination is also of technological importance for applications in doped materials, catalysts, and functional spintronic/energy devices[88-90] those systems are very often studied. Most often the metal is a noble metal, like for example Au or Ag, e.g. Au-PbSe[91], Au-PbTe[89] or Ag-PbS[92]. When no reaction to ternaries or other binaries is apparent, very different diffusion phenomenons can be obtained, depending on the applied reactants. The diffusion of Au in $Ag_2S$ from the core to the surface is reported by Ying et al. In the first stage, Au atoms diffuse uniformly in $Ag_2S$ from the core to the surface of $Ag_2S$. Au nanocrystals then evolve on the surface of $Ag_2S$ due to Ostwald ripening[93]. In contrast, Banin reports on the room-temperature reaction of Au with InAs nanoparticles[94]. In this case, Au diffuses into the InAs particles to form an Au core coated by an amorphous shell.

In reaction pairs where solid-solutions are possible, it becomes increasingly challenging to selectively direct the reaction towards solid-solutions or other products, like core-shell or hybrid/janus particles[95]. When core-shell or hybrid particles are the desired product, deposition or transmetalation processes have to be applied.

**b) Transmetalation process**

The second widely applied conversion reaction belongs to the group of transmetalation. Such reactions involve the reaction of a metal nanoparticle ($M_1$) with an organometallic complex ($RM_2$) and result in the formation of core–shell or hybrid (nano-)particles[96, 97]. Highly effective synthetic methods based on the overall transmetalation process have been suggested for the synthesis of $M_I@M_{II}$ ($M_I$ = Co and $M_{II}$ = Pt, Cu, Au and Pd), where a shell element ($M_{II}$) can cover core metals ($M_I$) uniformly using partial redox-transmetalation reaction[98]. Girolami et al. performed mechanistic studies of the reactions of $Rh(hfac)(C_2H_4)_2$ and $Pt(hfac)_2$ on copper surfaces under ultrahigh vacuum conditions in order to elucidate the factors responsible for the differences among the surface-selective metallization processes[98]. When a metal-ligand complex in a positive metal oxidation state ($M_{II}^{x+}L_i^{x-}$) approaches another metal surface ($M_I$), $M_{II}L_i$ molecules can be reduced through the sacrificial oxidation of

the $M_I$ surface atoms to produce $M_{II}$ deposition on the $M_I$ metal surface via a redox transmetalation process. This knowledge has been used to establish the redox metalation process for the synthesis of alloys for specific applications. For example Cho and co-workers obtained 10 nm-sized core-shell Sn-Cu nanoalloys by reacting $Cu(acac)_2$ with tin nanoparticles[99]. The core-shell Sn@Cu anode material further demonstrated significantly improved rate capability at higher C rates than Sn@C nanoparticles.

### c) Deposition process

An easy deposition reaction is apparent, when the seed compound is not oxidized during the reaction. For example $Au^{3+}$ can be reduced effectively by dodecylamine (DDA) in toluene in the presence of PbSe nanocrystals[91]. The evolution from nanocomposites with multiple Au deposition on the particle surface to those with a single Au domain, and further to pineapple-like morphologies has been illustrated by increasing the molar ratio of Au/PbSe during the synthesis. A challenging problem is the formation and control of symmetric/asymmetric semiconductor–metal heterogeneous nanostructures. The final morphology of the nanocomposites is depending on whether the surface of the substrate particles allow for only a single nucleation site or multiple ones. As demonstrated in earlier reports, $Ag_2S$ nanocrystals were shown to have only a single site[100], whereas CdS[101], PbS[102, 103] nanocrystals could provide multiple sites on their surfaces for the nucleation of gold. Interestingly, Cheon et al. showed that it is possible to selectively grow Co on top of metallic Pt nanoparticles or alloys depending on the applied redox pair[95]. The core-shell particles could be transformed to the "solid-solution" at elevated temperatures.

## 4. Reactive templating/Morphological templating

The term "template" outside the chemical context corresponds to a mould which can be filled with content. Templates applied in chemistry almost have the same meaning. They can be used in conversion reactions where they behave as a model or pattern to help to generate a desired product. The reactions can be divided into methods which involve "non-reactive" templates and some which involve "reactive" templates.

When considering “non-reactive” templating techniques, the template acts as an external scaffold and can be removed once the reaction is complete. Many of the first trials which used a non-reactive template involved a porous silica or silica carbide template which helped to constrain the nanoparticles in the desired morphology[104-106]. By and by, also other templates, like anodic aluminum oxide (AAO)[107] or biological templates like urea-formaldehyde (UF) resin[108] were established. A major drawback of this method involves the need to remove the external template by heat or leaching and the instability of the final product to stand alone without the template. As a consequence reactive templating is becoming increasingly popular, where preformed particles are used in the chemical conversion and the product reflects the characteristics of the reactant. Dawood[109] categorized the template-based syntheses into compositional , morphological, and structural templating.

### a) Morphological templating

As the properties of nanoparticles with different shapes and sizes differ significantly, morphological templating becomes increasingly important. Templating is one of the most accurate techniques for the controlled synthesis of nanostructured materials. Therefore, precursors with distinct morphology are used as reactive template for the formation of products with the desired shape which are otherwise difficult to obtain[110]. The concept of this method was originally demonstrated by Lieber and co-workers, who found out that highly crystalline nanorods of metal carbides could be formed by reacting carbon nanotubes with the vapours of metal oxides or halides at elevated temperatures[111]. Another example was reported by Xia and co-workers where uniform nanowires of t-Se were employed as chemical templates to generate Se@CdSe nanocables and then CdSe nanotubes[112]. The key process is the disproportionation of elemental Se into $Se^{2-}$ and $SeO_3^{2-}$ species at the surfaces of individual Se nanowires, which led to the formation of a thin (5-10 nm), uniform, conformal sheath around each template. Uniform nanotubes of CdSe were left behind as the final product when the unreacted, t-Se cores were sublimated by heating the samples at 230 °C[112]. The group around Alivisatos is also very active in this field and reported the oxidation of Co nanocrystals to form hollow CoO nanocrystals where the spherical shape of the primary particles remains unchanged. A small increase in the size of the nanoparticles is consistent with the volume expansion that would be expected for the conversion from Co to CoO[84]. The list of examples could well become an endless one, as it is used so often. Similar to single

metal nanoparticles, intermetallic nanoparticles can also be used as reactive templates and add another dimension of complexity to the final product. For example, the Schaak group was successful in oxidizing intermetallic $Bi_2Pd$ and BiPt nanoparticles that serve as ‘‘single source’’ reagent for the reaction into the mixed metal oxide $Bi_2PdO_4$ and $Bi_2Pt_2O_7$[26] under retaining its shape. The reaction proceeds over a two-step oxidation process. Once thermally oxidized, $Bi_2Pd$ nanoparticles form a $Bi_2O_3$/Pd nanocomposite which transforms into textured $Bi_2PdO_4$ upon further heating.

### b) Compositional templating

Compositional templating gives insight and predictability into the resulting material’s composition. When we consider a balanced chemical equation, this type of conversion is clearly evident already from the name, alone. For example, Alivisatos and co-workers showed the transformation of Co nanocrystals into $Co_3S_4$ and $Co_9S_8$ nanocrystals in the presence of sulfur in solution[84]. In both instances, the resulting nanocrystals incorporated the size and morphology and most importantly the composition of the reactant particles. This concept can also be transferred to binary chalcogenide particles as reactant, as shown by Wang[29]. Dendritic PbS serves as template for the formation of $Ni_3Pb_2S_2$ in the presence of $Ni^{2+}$ in an alkaline polyol solution. For binary intermetallic templates only one example can be found in the literature so far. Brady and co-workers reported the conversion of intermetallic $Cr_3Pt$ nanoparticles into $Cr_3PtN$ under a $N_2$ atmosphere[113]. Nanoscale $Cr_3Pt$ dispersions were readily converted to near single-phase $Cr_3PtN$, whereas nitridation of coarse $Cr_3Pt$ particles resulted in a discontinuous-type reaction to form a lath mixture of $Cr_3PtN$ and a more Cr-rich $Cr_3Pt$ or β-Cr.

### c) Crystal structure templating

The templating of the crystal structure does not play a role in this thesis and is therefore only briefly discussed here.

Sometimes, certain metastable species are one of multiple polymorphs of the same material and therefore it is difficult to selectively direct the reaction towards the formation of one

polymorph over the other. Crystal structure templating addresses that point. One of the pioneers in this field of research again, is the Alivisatos group who chemically transformed CdSe and CdS into $Ag_2Se$ and $Ag_2S$ via cation exchange[114]. The connectivity of the $Se^{2-}/S^{2-}$ sublattice of CdSe and CdS remains mainly unchained during that process. Furthermore Schaak and co-workers used ZnO as structural template as it crystallizes in the same structure as the high temperature polymorphs of ZnS and ZnSe[115]. By this, the high temperature polymorphs could be prepared at temperatures as low as 160 °C. Control experiments showed that without the application of ZnO as starting template the low temperature polymorphs (zinc-blende) of ZnS and ZnSe are formed.

The use of pre-formed nanoparticles as templates has emerged as a powerful tool for the design and the synthesis of complex nanocrystalline solids. It is used for programming morphological complexity into multinary nanocrystal systems that require simultaneous control over composition, crystal structure, and nanocrystal shape and size.

## 5. The polyol process

The use of polyols for the synthesis of small particles was first reported by Fievet, Lagier and Figlarz[12, 13] in 1989. They also introduced the term “polyol process” or “polyol synthesis” within their work. At the beginning the polyol synthesis started with single metals like Co, Ni, Cu, and Pt particles and was extended to further metals, intermetallics[18] and alloys such as $Co_{20}Ni_{80}$, FeNi, $Co_xCu_{1-x}$, or FeCoNi[116] step by step. The general feature of the polyol process is the reduction of metallic compounds like oxides, hydroxides or other salts in a liquid alcohol medium. The organic liquid (e.g., ethylene glycol, glycerol, diethylene glycol) acts as a reducing and dissolving medium at moderate temperatures.

The polyol method is advantageous as

- it enables an accurate control of the size distribution and shape of the particles from the micrometric to the colloidal scale.
- the high boiling points of the polyols allow synthesis temperatures of 200 – 320 °C without the necessity of high pressure and autoclaves[117].

- polyols show solubilities of compounds similar to water, which allows the use of low-cost metal salts (e.g., halides, nitrates, sulfates) as starting materials[116].
- the chelating effect of the polyols is highly beneficial for controlling particle nucleation, particle growth and agglomeration of nanoparticles. This is obtained as the polyols adhere on the particle surface (especially on oxides) and serve as colloidal stabilisers.
- crystalline nanomaterials can be obtained right from the liquid phase. Thus, a powder post-sintering can be avoided that may otherwise result in uncontrolled particle growth and agglomeration.

The general mechanism of the reduction of metals in ethylene glycol (eg), which is used in this thesis, is still under discussion and poorly understood. In the original publication of Fievet, Lagier and Figlarz a duplicative oxidation of acetaldehyde, previously produced by dehydration of ethylene glycol is identified as the reducing agent present in the reaction[118] (eq. (1)-(2)).

$$HOCH_2CH_2OH \rightarrow CH_3CHO + H_2O \quad \textbf{(1)}$$

$$2\,M^{2+} + 2\,CH_3CHO + 2\,OH^- \rightarrow 2\,M + CH_3COCOCH_3 + 2\,H_2O \quad \textbf{(2)}$$

Instead, Xia et al[119] ascribe the acetaldehyde production to the hydroxide anions from the metal precursors applied by Fievet, Lagier and Figlarz. In their opinion acetaldehyde cannot account for the general reductive power of ethylene glycol (eg) under most reaction conditions. The reductive behaviour of ethylene glycol is believed to stem from glycolaldehyd which is formed by oxidation at higher temperatures in air (eq. (3)). At lower temperatures ethylene glycol as a reductant itself becomes more significant.

$$2\,HOCH_2CH_2OH + O_2 \rightarrow HOCH_2CHO + 2\,H_2O \quad \textbf{(3)}$$

## 6. The sol-gel process

Sol-gel methods only slightly differ from solvothermal methods – often a fluent transition takes place. The main difference is that the starting materials form a solid gel after some time of aging. Subsequently, this gel can be transferred to the calcination process, the actual reaction process. After this step, the product almost always occurs in carbonized form[120, 121]. For the gelation process, three different approaches are used: a) gelation of a solution of colloidal powders; b), hydrolysis and polycondensation of alkoxide or nitrate precursors followed by hypercritical drying of gels; c) hydrolysis and polycondensation of alkoxide precursors followed by aging and drying under ambient atmospheres[122]. Sol-gel preparations start from solution of the appropriate precursors and salts, which leads to a thorough mixing, a great advantage in the preparation of different compounds as compared with the traditional solid-state method. The formation of a gel with a high degree of homogeneity reduces the need of atomic diffusion during the calcination process, allowing therefore the reaction to the desired phases at much lower temperatures and shorter calcination times than in solid-state reactions. By the correct selection of the parameters, like choice of the precursors and preparation conditions, the sol-gel method allows tailoring of the properties of the resulting compounds.

A good example, where the sol-gel process is often applied can be found in the research for optimized cathode materials. For the gel often starting materials like ethylene glycol, citric acid or acrylamide are applied as they combine multiple positive effects: an in-situ carbon coating, small particles and single phase materials. By such a sol-gel synthesis it was possible to activate the $Ni^{3+}/Ni^{2+}$ step in $LiNiPO_4$ for the first time[123-125].

## 7. Lithium-ion/intercalation battery

### 7.1. Why Li-ion batteries

One of the major challenges of today is to ensure a continuous supply of energy in response to the ever-growing demand. As society becomes more and more mobile and increasing proportions of energy are acquired by regenerative energy sources, which produce energy in a

discontinuous manner, the demand for a reliable secondary (rechargeable) battery of high energy and power density has increased noticeably. Therefore new increasingly powerful mobile as well as stationary storage materials need to be explored. At the moment lithium-ion technology is one of the most promising to fulfil the upcoming needs of energy storage materials[126, 127]. The high potential in energy density compared to other techniques like lead acid, Ni–Cd, and Ni–MH batteries are the main drivers for this technology. For example the energy density of lithium-ion batteries is typically twice that of the standard nickel– cadmium batteries[128].

## 7.2. Operation principle

A standard lithium-ion battery consists of an anode, cathode, separator, current collectors (mostly Al and Cu), and electrolyte, as shown in Figure 1. In such a battery during the discharge process electrons leave the anode through an external circuit where they perform beneficial work just before entering the cathode. To maintain neutrality of charge, cations are simultaneously released out of the anode into the electrolyte and transport the positive charge to the cathode.

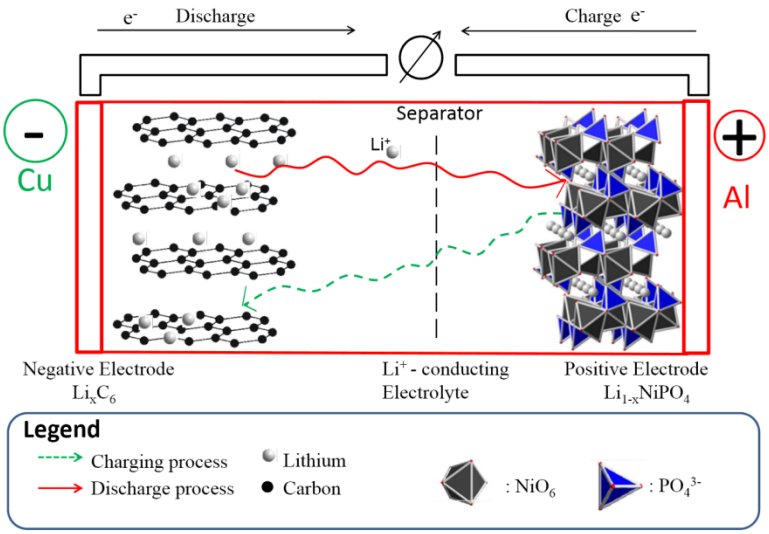


**Figure 1:** Typical setup and functional principle of a lithium-ion battery.

With a lithium-ion battery it is thus possible to enable the conversion of chemical energy and also storage of electrochemical energy. The performance of rechargeable lithium-ion batteries strongly depends on the active materials employed in both, anodes and cathodes. The cathode

serves as a host component in which the working ion $Li^+$ can reversibly be intercalated/deintercalated[129, 130]. For this a transition metal with a redox pair e.g., $Fe^{2+/}Fe^{3+}$, $Mn^{2+/}Mn^{3+}$, $Co^{2+}/Co^{3+}$ or $Ni^{2+}/Ni^{3+}$, which accepts or donates electrons is needed. The main aspect of research is therefore to identify framework structures with suitable interstitials in the structure and simultaneously appropriate working redox energy of an environmentally friendly and reasonable transition metal cation.

# II. Experimental techniques

In this chapter the used chemicals and the applied analytical methods are summarized. Detailed information about the different synthesis methods (solid-state, polyol and sol-gel) can be found in the corresponding sub-chapters.

## 1. Applied chemicals

**Table 1:** Applied chemicals and purity (Part 1).

| Substance | Formula | Manufacturer | Purity [%] |
|---|---|---|---|
| Sn powder | Sn | ChemPur | >99 |
| Ethylene glycol | $C_2H_6O_2$ | Fluka | >99,5 |
| Hydrazinium hydroxide | $N_2H_5OH$ | Merck | ≈100 |
| Ethylenediamine | $C_2H_8N_2$ | Sigma-Aldrich | >99 |
| Thioacetamide | $C_2H_5NS$ | Sigma-Aldrich | >99 |
| Selenourea | $CH_4N_2Se$ | Sigma-Aldrich | 98 |
| Nickel(II) chloride hexahydrate | $NiCl_2*6H_2O$ | Alfa Aesar | 98 |
| Palladium powder | Pd | ChemPur | >99,9 |
| D(+)-Glucose monohydrate | $C_6H_{12}O_6*H_2O$ | Merck | / |
| Bismuth pieces | Bi | ChemPur | 99.999 |
| Cobalt(II) acetylacetonate | $C_{10}H_{14}CoO_4$ | Merck | 98 |
| Indium shot | In | ChemPur | 99,99 |
| Lithium acetate dihydrate | $C_2H_3O_2Li*2H_2O$ | Jansen Chimica | 98 |
| Nickel acetate tetrahydrate | $Ni(OOCCH_3)_2*4H_2O$ | ChemPur | 99 |

**Table 2**: Applied chemicals and purity (Part 2).

| Substance | Formula | Manufacturer | Purity [%] |
|---|---|---|---|
| Nickel powder | Ni | Chempur | 99.99 |
| Lead granules | Pb | Chempur | 99.999 |
| Lead(II) nitrate | $Pb(NO_3)_2$ | Merck | >99 |
| Sulfur | S | Sigma-Aldrich | 99.998 |
| Lead oxalate | $PbC_2O_4$ | Puratronic | 99.999 |
| Selenium black | Se | Merck | 99.5 |
| Tin(II) chloride | $SnCl_2*2H_2O$ | Merck | 98 |
| Tellurium pieces | Te | Chempur | 99.999 |
| Sodium hydroxide pellets | NaOH | Merck | 99 |
| Polyvinylpyrrolidone MS40.000 | $(C_6H_9NO)_n$ | Alfa-Aesar | / |
| Poly(vinylidene fluoride) powder | $(-CH_2CF_2-)_n$ | Alfa Aesar | / |
| Carbon black, acetylene | C | Alfa Aesar | >99.9 |
| Thallium granules | Tl | Chempur | 99.999 |
| Cobalt powder | Co | Chempur | 99.9 |

## 2. Characterization Methods

### 2.1. Powder X-ray diffraction (XRD)

For the roentgenographic phase and structure analysis the products were characterized by X-ray powder diffraction, using a Huber G670 diffractometer, equipped with an imaging plate with monochromatic $Cu_{Ka1}$ radiation ($\lambda$=1.54060 Å, Ge-monochromator, increment $\Delta\theta$=0.005°, Bragg angular range (asym. transmission 4° ≤ 100°)).

The measurements under ambient conditions were carried out on flatbed sample holders. Therefore the crushed and ground sample was fixed with silicon paste (Baysilone-Paste, Bayer) on a MYLAR® polyester film (see Figure 2 a). For in situ high-temperature measurements, the sample was finely crushed and ground and placed in an evacuated mark tube. After adjustment of the mark tube and the heating mantle (see Figure 2 b) a temperature range from RT to 900 °C was accessible. In situ low-temperature XRD measurements could also be performed with a special attachment, shown in Figure 2 c. Therefore, the sample was

fixed with silicon paste on an alumina foil and enclosed by it. Temperatures up to 8 K were reached in the high-vacuum low-temperature chamber.

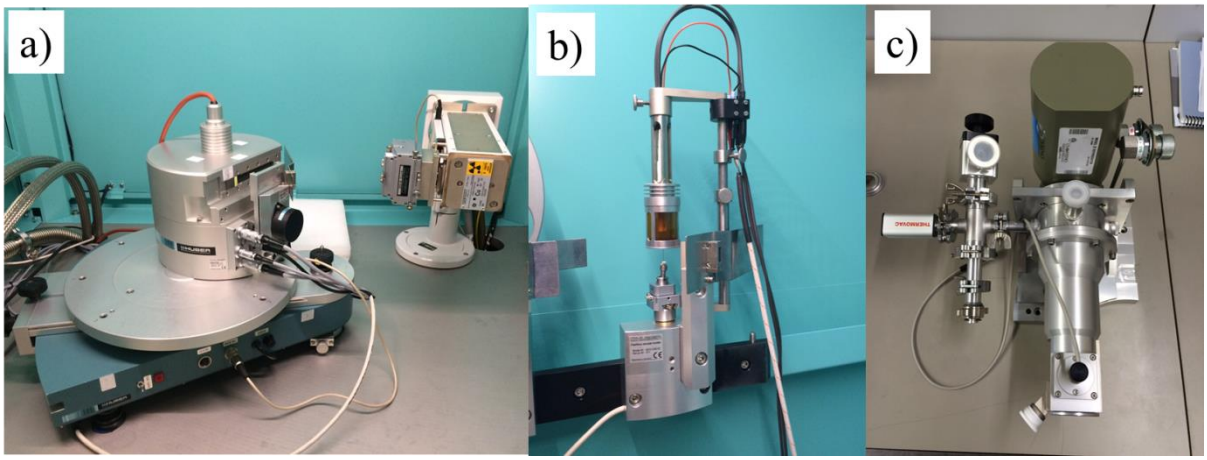


**Figure 2:** Huber G670 diffractometer with a) flatbed sample holder b) high-temperature attachment and c) low-temperature attachment.

Indexing and refining of the obtained diffractogram was done with the software WinXPOW[131] from STOE. Rietveld refinements were performed with JANA2006[132] and Fullprof[133].

## 2.2. Scanning electron microscopy (SEM)

Morphologies of the as-prepared samples were investigated with scanning electron microscopy using a Zeiss Digital Scanning Microscope DSM 950, equipped with a secondary electron detector and a tungsten source. Therefore, the samples were mainly left in their original state, without grinding to preserve the morphology. For better contrast, the samples were sputter coated with gold. Some of the measurements were performed by Dr. Thomas Lunkenbein at the Electron Microscopy Group of the Fritz-Haber-Institute (Max-Planck-Gesellschaft). In this technology, the electron microscope produces an image of the sample by scanning it with a focused beam of electrons. The electrons interact with atoms in the sample and produce signals that can be used to draw an enlarged picture about the sample's surface topography and composition with a high depth of field.

## 2.3. UV-VIS spectroscopy

UV-Vis measurements were operated on a NIR-UV/VIS Spectrometer (Omega 20, Bruins Instruments) with an integrating sphere. The reflection behaviour of the samples was evaluated in the range of 380 nm < λ< 800 nm with pure $BaSO_4$ as a reference. One spatula of the dry sample was homogenized with $BaSO_4$ and pressed into the sample holder for the measurement. The reflection spectra were transferred into the absorption spectra using the Kubelka-Munk-Transformation.

## 2.4. Raman spectroscopy

Raman spectra were recorded with an Oriel MS260i Spectrometer with a He-Ne laser (λ=632.78 nm), equipped with a CCD camera (Andor DB401-UV). The setup was a self-construction of the group of Professor Alkwin Slenczka from the chair of physical chemistry of the University of Regensburg.

## 2.5. FIR/MIR spectroscopy

IR measurements were performed on a FT-IR Spectrometer (Varian 670 FTIR). The spectra were recorded with a GladiATR® probehead (Pike Technologies). Measurements in the medium IR-range (MIR, 4000–400 $cm^{-1}$, ν=2,5-25 μm) and in the far-range (FIR, 400–10 $cm^{-1}$, ν=25 μm–1 mm) were performed. Therefore the dry and carefully crushed and ground powders were directly attached on the ATR crystal.

## 2.6. Nitrogen sorption (BET)

The Nitrogen sorption measurements were performed by PD Dr. Rainer Müller in the laboratories of the Institute of Physical and Theoretical Chemistry of the University of Regensburg. Therefore, the samples were put into long ampoules and dried at high-vacuum. An adsorption-desorption-isotherm of $N_2$ was determined at -196 °C from which the specific surface area could be calculated afterwards by the BET-theory. This method takes advantage of the fact that the amount of adsorbed or desorbed gas is proportional to the specific surface area of the sample.

## 2.7. Cyclovoltammetric measurements (CV)

In this work a self-constructed three-electrode configuration was used for cyclovoltammetric measurements. The electrochemical potential of the reference/auxiliary electrode was fixed by the application of lithium, so that the cell potential could be interpreted in terms of an equilibrium half-cell reaction between the counter (lithium) and the working electrode (contained the active material at which the cell reaction took place). That cell design allowed events at the working electrode to be monitored during the experiment. For the experimental details of the applied setup and the preparation of the electrodes see chapter V.3.1. During the cyclovoltammetric experiments, the potential scan was started at an initial potential where no electrolysis occurred. The scan continued at the desired linear scan rate to the switching potential, then reversed the direction and returned to the initial potential (Figure 3 a). The magnitude of the resulting current and its dependence on the applied potential then provided the analytical information[134, 135]. A typical voltammogram is characteristic, with rather unsymmetrical shapes but equal heights of anodic and cathodic peaks (Figure 3 b).

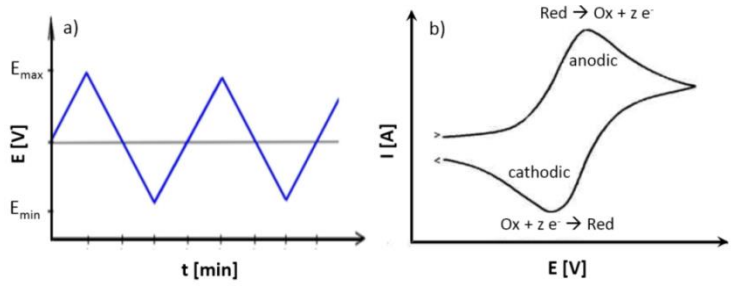


**Figure 3:** a) Potential scan of a cyclovoltammetric measurement b) Representation of a typical reversible cyclic voltammogram.

## 2.8. Galvanostatic battery cycling

Batteries of the $LiNi_yCo_{1-y}PO_4$ solid solution were electrochemically tested at the laboratories of Süd Chemie/Clariant Produkte (Deutschland) GmbH in Moosburg. The cycling was carried out by a galvanostatic-potentiostatic process (Constant Current Constant Voltage, CCCV). Initially, the electrode was galvanostatically charged to a defined charging potential (Constant current) and afterwards recharged potentiostatically (Constant Voltage), i.e. the potential was held until the charging current dropped below a specific current limit. The decharging was performed galvanostatically again up to a defined potential limit. Charging, recharging and decharging formed one cycle.

## 2.9. Calculation of the size and strain with WinXPOW

To determine the crystallite size with WinXPOW, first of all a full profile pattern fitting, including a base line of the diffraction patterns was performed, assuming a pseudo voigt line shape. This accounts for the asymmetry for each peak, from which the Bragg angle, peak intensity, and the angular width at half maximum intensity (β) were determined. To determine the instrumental broadening which does not arise from crystallite size, a $LaB_6$ standard or crystalline sample of the examined compound was taken as reference in the calculations. Based on these results, the particle size and strain of the respective particles could be estimated from XRD line broadening using the Scherrer or Wilson[136] method implemented in WinXPOW. The contribution of both shares was furthermore evaluated by the Williamson-hall plot[137].

# III. Conversion chemistry of binary sulfides and selenides $A_yX_x$ ($A$ = In, Tl, Pb, Sn; $X$ = S, Se) with $Ni^{2+}$ to 'solid-solution' ternaries or hybrid particles – Mechanisms of formation, morphological templating and structural characterization

## 1. Introduction and objective

Mixed metal chalcogenides have been extensively studied in the last decades due to their unusual chemical and physical properties, which are often directly related to the combination of infinite heterometallic and chalcogenide-like bonds within the crystal structure[138]. The heterometallic frameworks range from 1D chains in $M_4ETe_4$ ($M$ = Ta; $E$ = Si, Fe)[139] to 2D slabs in $Sc_6MTe_2$ ($M$ = Cu, Ag, Cd)[140], and 3D frameworks in $Ta_9M_2S_6$ ($M$ = Fe, Co, Ni)[141] and $Er_7Ni_2Te_2$[142].

Mixed metal chalcogenides with the general formula $M_3A_2X_2 \triangleq AM_{3/2}X \triangleq A_2[M_3X_2]$ and $M$ = Ni, Co, Rh, Pd; $A$ = In, Tl, Pb, Sn and $X$ = S, Se attracted attention since the magnetic and electronic properties can be tuned by substitution. The properties and supposed applications are related to the mentioned intermetallic $A$–$M$ and chalcogenide-like behaviour and range from small bandgap semiconductors and thermoelectrics[35-37] to half-metal ferromagnets[37, 38], catalysts[30, 39, 41] and superconductivity[143-145]. All structures of this class have one feature in common - They can be derived from the structure of the perovskite. Weihrich and co-workers introduced the description of the so-called "half-antiperovskites"[31-33, 38], to which belong the *Shandite,* $Ni_3Pb_2S_2$, *Parkerite*, $Ni_3Bi_2S_2$, *Laflammeite*, $Pd_3Pb_2S_2$ and other related compounds. All of them are dominated by layered partial $[M_3X_2]$ structures, with short $M$-$M$ distances which can form zigzag chains that result in their remarkable physical properties. Figure 4 shows a summary of all known HAP compounds until now. The *shandite*-type compounds are marked with yellow, whereas the *parkerite*-type ones are marked with blue color. The primary concern of this thesis is being put on all nickel containing phases with the $M_3A_2X_2$ stoichiometry. The actual chapter, chapter III especially deals with the stoichiometry of the nickel containing *shandite*-type compounds. To date, most of them were prepared by solid-state reactions only and their mechanisms of formation was not yet understood.

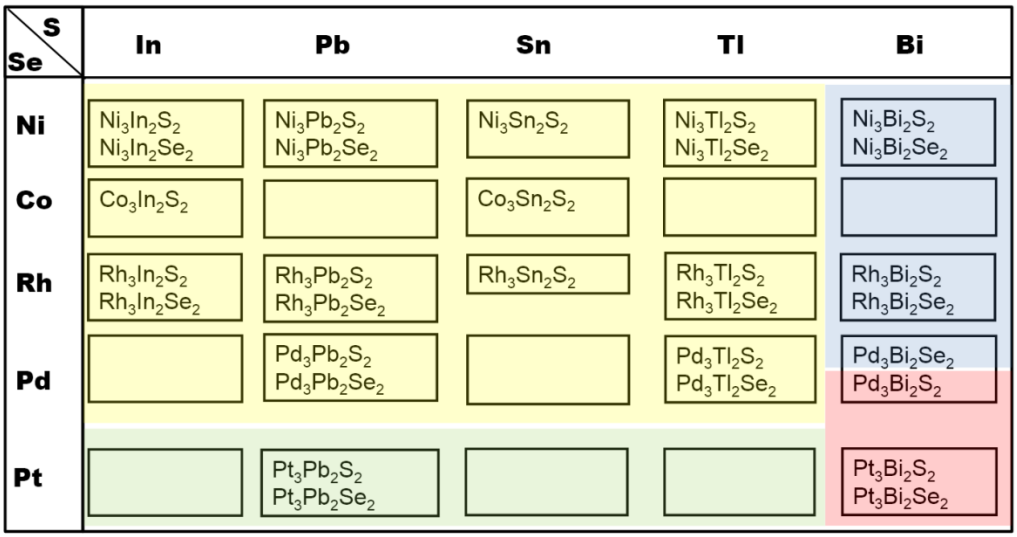


**Figure 4:** Overview sketch of all known HAP compounds until now. (yellow background: trigonal *shandite* type compounds, green: orthorhombic $M_3Pb_2X_2$ compounds, blue: monoclinic *parkerite* type compounds, red: cubic $Pd_3Bi_2S_2$ and $Pt_3Bi_2X_2$ type).

## 1.1. Preliminary remark and objective of this section

*Method of synthesis*

The polyol synthesis was chosen as it combines many advantageous features, as already mentioned in the introduction. The method is reproducible, resource-saving and also in principle suitable for the processing of large batches. For this thesis it was especially beneficial that crystalline nanomaterials can be obtained right from the liquid phase and very many parameters can easily be changed in the synthesis protocol. By this it was possible to generate new insights into the mechanisms which are taking part during the reactions.

*Synthesized materials*

For the present thesis only element combinations of different chalcogenide binaries with nickel were evaluated. These systems seemed to be very promising as

a) $Ni^{2+}$ salts are cheap and have a good solubility in ethylene glycol. The low costs for one approach allow for repetitions, which is important to clarify the mechanisms of formation and the parameters which influence the resulting products.
b) two publications have already been published which deal with the synthesis of ternary nickel *shandite*- ($Ni_3Pb_2S_2$)[29] and *parkerite*-type ($Ni_3Bi_2S_2$)[30, 109] compounds, starting from binaries (in that case PbS and $Bi_2S_3$, respectively). However, therein mechanisms, reaction paths and ways to direct reactions to different products (control of product formation) remained unclear or unknown before the present work.
c) together with the Rh system, nickel shows the largest number of known and characterized *shandite*- and *parkerite*-type compounds. This speaks for a certain stability of the samples and might simplify the synthesis.
d) most of the nickel binaries and intermetallics are well known.

*Objective*

The aim of this chapter is the evaluation of solution-based conversion routes of binaries with $Ni^{2+}$. In this chapter following results will be shown:

a) The influence of reaction time, reaction temperature, reductant, alkalinity and different reactants (stoichiometry, morphology, etc.) on the corresponding products is evaluated.
b) The factors which lead to "solid-solution"-type $Ni_3A_2X_2$ compounds or hybride/core-shell Ni@$A_yX_x$ (y=1-2; x=1-3) compounds are shown.
c) The different redox-reactions and mechanisms of formation are evaluated and discussed. Based on this a general reaction protocol for the targeted control of the different products is developed.
d) The transformation of hybride/core-shell Ni@$A_yX_x$ to ternaries by elevated temperatures is exemplified.
e) The possibilities of morphology templating from binaries to ternaries are shown. Morphologies from dendrites, to cubes, octahedron or stars are attempted.

For selected samples with special morphology further characterizations and methods are applied.

a) The temperature dependent structural and mechanical properties are evaluated.
    a. Annealing effects on crystallinity, particle size and strain
    b. Structural properties at low-temperature conditions by in situ powder diffraction
b) The specific surface area of nanoparticles with different morphologies vs. bulk compounds is compared.
c) The mechanisms of formation of the *shandite*-type compounds during the polyol reaction are compared to that during a pure solid-state reaction for selected samples.

## 1.2. The *shandite* structure

The *shandite*-type $M_3A_2X_2$ compounds crystallize in the space group $R\bar{3}m$ (No 166) which results in 4 atomic sites (*M*, *A*1, *A2*, *X*). Two different settings are possible, the hexagonal and the primitive trigonal. In the hexagonal setting the *M*-atoms are located on 9d Wyckoff positions (1/2, 0, 1/2) with two-fold symmetry and built kagome nets of corner-sharing *M*3 triangles. These layers are stacked in an ABC sequence. Each of the *M*3 triangles is capped above or below the kagome sheets by an *X* atom. There are two different *A*-positions, *A*1 and *A*2 in the structure. *A*1 on Wyckoff position 3a (0,0,0) is found between the *M* layers in a trigonal antiprismatic environment of *M* atoms. *A*2 on 3b (0,0,1/2) lies in the middle of each hexagon, configuring the centre of a hexagonal bipyramid along with two *X* atoms. *X* is located on a 6c site (0,0,z) with three-fold symmetry and is centred by a slightly distorted substructure of *A*1 and *A*2. The *M*-atoms are in distorted tetragonal-dipyramidal $X_2A_4$ coordination. All the atoms are fixed by symmetry except the *z* coordinate of *X* which varies between different compounds.

The *shandite* structure can also be regarded as build from face-sharing octahedra formed by the coordination of each *M* atom by two *A*1, two *A*2 and two sulphur atoms forming layers of distorted face-sharing bipyramides $MA_1A_2X_2$. This view of the structure was developed in our group by the concept of ordered half antiperovskites $M_3A_2X_2 = M_{3/2}AX$. It is based on the structural relation of *shandites* to *antiperovskites* like $Ni_3MgC$ ($Pm\bar{3}m$) as described in a series of publications of our work group[31-33, 146-149]. It is indicated by the HAP unit in

Figure 5 and explained here briefly by three steps. First, the structural type-antitype relation of $Ni_3MgC$ and cubic *perovskite* ($CaTiO_3$) is given as Ni in the *antiperovskites* is found on the O sites of the *perovskites*, Mg on the Ca sites, and C on the Ti sites. Second, in *shandite* and *parkerite* type $Ni_{3/2}AX$ = $Ni_3A_2X_2$ compounds, only half of the *M* = Ni sites of the *antiperovskite* (i.e. *perovskite* O sites) are occupied, half remain unoccupied. Third, *M* site ordering is observed, that causes the low dimensional structures and reduces symmetry to $R\bar{3}m$ (*shandites*), *C2/m* (*parkerites*), *I213* ($Hg_3S_2Cl_2$ type). By the structural relation the unusual coordination of the atoms in *shandite* and *parkerite* type compounds is understood: similar to $Ni_3MgC$ the Ni atoms are found in tetragonal bipyramides [$NiA_4X_2$] that indicate Ni(0), $d^{10}$ states. As a consequence for subsequent reactions $Ni^{2+}$ from the educts must be reduced to form the $M_3A_2X_2$ compounds. Structural anisotropy is related to the reduced coordination from $CNi_6A_8$ to $SNi_3A_8$ (cube in Figure 5) and from $MgNi_{12}$ to $ANi_6$, Details on the HAP concept are shown in the mentioned papers[31-33, 146-149].

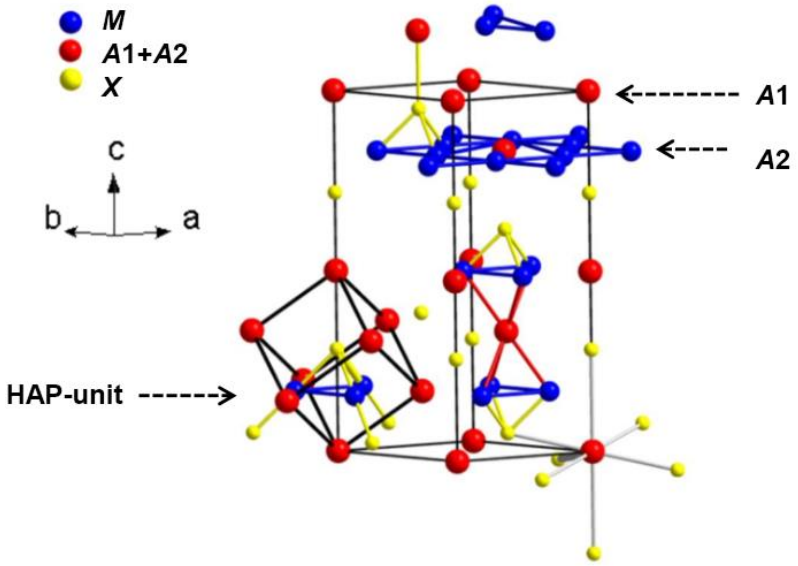


**Figure 5:** Crystal structure of the *shandite*-type compounds.

## 2. Experimental

### 2.1. Reduction of $Ni^{2+}$

As the reduction of $Ni^{2+}$ during most of the syntheses plays a key role, this step is devoted an extra subchapter here. In both, in the ternary *shandite* and the hybrid/core-shell compounds, nickel exhibits the oxidation state zero[40]. Consequently, $Ni^{2+}$ has to be reduced during the synthesis.

The applied polyol acts as both, solvent and reducing agent for $Ni^{2+}$. Noble metals such as Pd, Au, and Ag can be obtained via polyol process under neutral or even acidic conditions as the reduction potential of ethylene glycol itself is already high enough. However, for the $Ni^{2+}$ reduction a certain level of alkalinity is necessary due to its lower oxidation potential. Tang et al.[150] underline the great role of the alkalinity during the polyol process. According to them, pure metallic Ni cannot be obtained when the concentration of NaOH is below 0.3 M. As already seen in eq. (1)-(2) the hydroxonium ions are mandatory to produce enough decomposition products of ethylene glycol with its inherent higher reducing force. Our own results confirm these findings. $NiCl_2*6H_2O$ could not be reduced in pure ethylene glycol, even when it was refluxed for 18 h at 197 °C. In contrast, when basic ethylene glycol was used (concentration > 0.4 M), elemental Ni was obtained.

The reduction process is often supported by additional reductants and chelating agents which are given to the reaction mixture. Well known representatives that are also used in this work are hydrazine (hyd) and ethylenediamine (en). With hyd already 60 °C is suitable for an entire reduction of $Ni^{2+}$ under basic conditions[151, 152]. Hyd is generally accepted as strong reducing and also chelating agent $[Ni(N_2H_4)^{2+}]$[153]. The net mechanism can be written as follows:

$$2\ Ni^{2+} + 4\ OH^- + N_2H_4 \rightarrow 2\ Ni + N_2 + 4\ H_2O \qquad \textbf{(4)}$$

Ethylenediamine is attributed to have strong polarity, strong chelating ability and a certain reducing ability, which is important for many reactions. It is hardly surprising, that ethylenediamine is often used as dissolving medium and chelating agent[154, 155]. The reducing ability is discussed controversially. Under solvothermal conditions it is reported, that ethylenediamine is able to reduce Ag(+I) to Ag, Sb(+II) to Sb, and Cu(+II) to Cu at temperatures around 130-140 °C[156, 157]. Nickel is less noble and has a stronger reduction

potential. Here, no reports are available where ethylenediamine is used as reductant for the reaction of Ni(+II) to Ni(0). Furthermore no decomposition products of the same are known.

To explore this question more thoroughly, a few own experiments were conducted. When ethylenediamine is given into a solution of $Ni^{2+}$, immediately a change of colour from green to violet can be observed, as the $Ni(en)_x^{2+}$ complex is formed[155, 158]. It became apparent that refluxing $NiCl_2*6H_2O$ in ethylene glycol (eg) and ethylenediamine at 197 °C is not able to produce elemental Ni. In contrast, when NaOH was given to the reaction medium (>0.4 M), elemental Ni was obtained. But still, the reaction needed higher temperatures than the experiments with hydrazine hydrate as reducing agent. It is concluded that ethylene glycol or rather its decomposition products are responsible for the reduction and not ethylenediamine.

## 2.2. General synthesis strategy for the chemical conversion of binaries to ternaries or to hybrid particles - Flow chart of the applied synthesis protocol

The starting point of our examinations is a report of Shao and co-workers in 2008[29]. The group describes the synthesis of $Ni_3Pb_2S_2$, starting from dendritic PbS and $NiCl_2*6H_2O$ in basic ethylene glycol and hydrazine hydrate as reducing agent. In the present work, this low temperature polyol route was modified and converted into a general applicable synthesis strategy with two fundamental different pathways. Pathway a) describes the conversion of binaries to ternary *shandite*-type compounds and pathway b) the conversion of binaries to hybrid/core-shell particles $Ni@A_yX_x$.

The synthesis route followed in general the flow chart depicted in Figure 6. First of all, the stoichiometric ratio of the starting materials, mostly the corresponding $A_yX_x$ ($y$ = 1-2, $x$ = 1-3) (0.71 mmol) and $NiCl_2*6H_2O$ (0.47 mmol) were added to a 250 mL round-bottom flask and magnetically stirred in the polyol medium (70-100 mL). Treatment with ultrasonic sound ensured sufficient redispergation of the starting materials. For temperatures below 200 °C ethylene glycol was applied as dissolving and reaction medium, whereas for temperatures >200 °C, high boiling tetraethylene glycol (TEG) was used. Subsequently, the alkalinity was set by adding a certain amount of NaOH under continuous stirring. To enable the higher reduction potential of the polyol medium, at least a concentration of 0.3 M NaOH is needed.

At this point the reaction scheme can be divided into the two mentioned pathways. The key difference between pathway a) and b) is the velocity of nickel reduction which takes place. It can be mainly influenced by the application of either ethylenediamine or hydrazine as chelating and reducing agent. Thereby, completely different products can be obtained. The results of pathway a) with ethylenediamine mainly aimed at the conversion to a ternary $Ni_3A_2X_2$ compound, but also the different side phases and other reaction products were of interest. These results are presented in chapter III.3. Pathway b) with hydrazine hydrate aimed to produce bifunctional, hybrid magnetic and semiconducting particles. The results are summarized in chapter III.4.

In pathway a), the temperature of the reaction mixture was gradually increased to high temperatures with different heating ramps and refluxed for 0.5–10.5 h (eg: 166–197 °C, TEG: >200 °C). After cooling to room temperature, the products were filtered and washed several times with distilled water and alcohol and dried at 80 °C overnight.

In contrast, pathway b) can be named "reductive deposition method". In this pathway the reaction mixture is not refluxed, but kept at temperatures as low as 60-70 °C for several hours. This temperature seems to be not enough to form the ternary *shandite* compounds. But in strong alkaline medium, using hydrazine as strong reducing agent, $Ni^{2+}$ is reduced to its elemental state and coated onto the corresponding $A_yX_x$ starting material. It has to be mentioned that this is explicitly no reductive transmetalation[25, 95, 159] as nothing is oxidized in the binary template. The products were filtered and washed several times with distilled water and alcohol and dried at 80 °C overnight. In a further step, the hybrid particles were subjected to a typical solid-state reaction (quartz ampoule at 500–700 °C) to proof the possibility to generate the corresponding "solid-solution" ternary phase under morphology retention.

The big advantage of the applied synthesis protocol lies in the great variety of parameters that can be changed individually. By applying different starting materials, reaction milieus, chelating/reducing agents, reaction temperatures and times it was possible to get a deeper understanding of the mechanisms of conversion of binaries to ternaries, templating effects and the redox behaviour of the metals taking part. By slight modifications the synthesis protocol is valid for all known $Ni_3A_2S_2$ compounds and could even be extended to its selenium homologues, which will be shown accordingly.

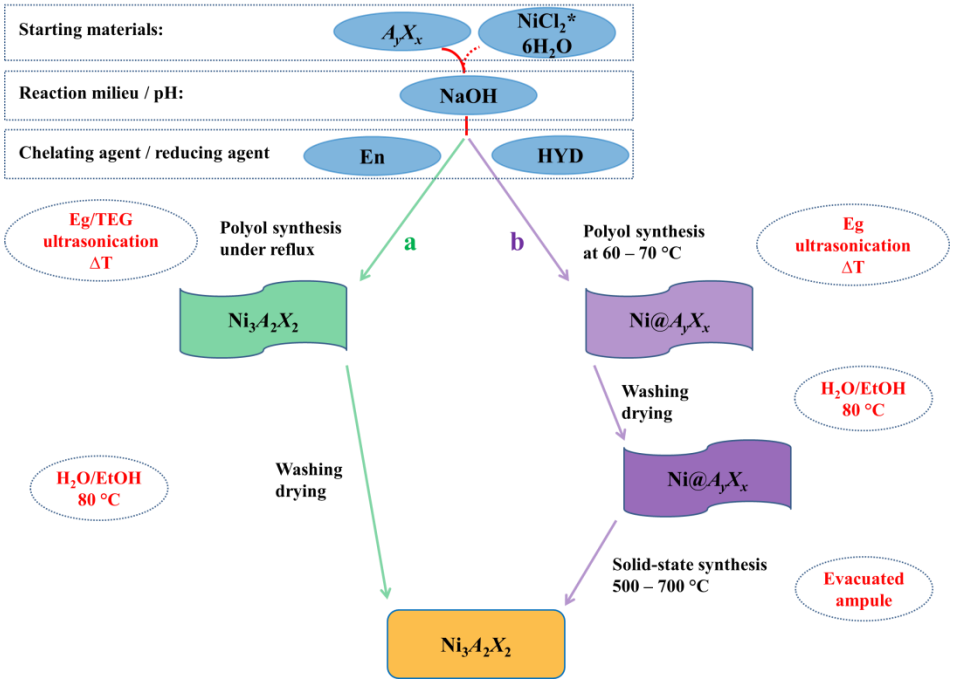


**Figure 6:** Flow chart of the applied reaction protocol.

## 2.3. Synthesis of the starting materials/templates

*High-temperature solid-state syntheses for the preparation of the bulk templates*

For the synthesis of the bulk samples the corresponding stoichiometry of the respective elements was ground in an agate mortar and placed in a quartz ampoule. The ampoule was purged with argon for three times and melt off under vacuum ($p < 2*10^{-2}$ mbar). The ampoule was then placed in a tilted tube furnace, annealed for different times and quenched or slowly cooled to room temperature. The applied temperature profiles were optimized with respect to the corresponding melting points of the compounds. Table 3 summarizes all synthesized bulk samples and gives comments on their corresponding heating ramp (hr), holding time and cooling rate (cr). In a standard reaction a slow heating ramp of 1 °C/min was used, or the temperature was held at 300 °C overnight, so that the liquid sulphur or selenium was able to react with the corresponding metal, without blowing up the ampoule. All samples containing thallium were weighed in, in an argon filled glove box. The adhered paraffinic oil and the oxide/passivation layer were scratched off before weighing. Before using the products, they were ground in air and the phase purity was monitored by powder X-ray diffraction

.

**Table 3:** Temperature profiles for the preparation of the bulk samples, which served as precursor for the conversion reactions.

| Compound | Temperature [°C] | Comment |
|---|---|---|
| PbS | 830 | hr 5 °C/min, 14 days, quenched |
| PbSe | 900 | hr 1 °C/min, 27 days, quenched |
| SnS | 400 - 830 | hr 1 °C/min, 1 day at 300 °C, hr 1 °C/min, 11 days at 830 °C, cr 0.5 °C/min |
| InS | a) 500 – 750 | hr 1 °C/min, 1 day at 500 °C, hr 1 °C/min, 3 days at 750 °C, cr 3 °C/min |
| | b) 600 | hr 1 °C/min, 8 days at 600 °C, cr 3 °C/min |
| $In_2S_3$ | 850 | hr 1 °C/min, 11 days, cr 0.5 °C/min |
| InSe | 610 | hr 1 °C/min, 8 days, cr 0.5 °C/min |
| $In_2Se_3$ | 840 | hr 1 °C/min, 8 days, cr 0.5 °C/min |
| $Tl_2S_2$ | 500 - 180 | hr 1 °C/min, 5 days at 500 °C, cr 0.5 °C/min, 9 days at 180 °C, quenched |
| $Tl_2S$ | 450 | hr 1 °C/min, 10 days, cr 0.5 °C/min |
| $Tl_2Se_2$ | 500 - 180 | hr 1 °C/min, 5 days at 500 °C, cr 0.5 °C/min, 9 days at 180 °C, quenched |
| $Ni_3S_2$ | 500 - 900 | hr 1 °C/min 500 °C 1 day, hr 1 °C/min, 5 days at 900 °C, quenched |

*Solution-based syntheses for the preparation of the nanoscopic templates*

**$SnS_{spherical}$:** The SnS starting material was prepared by a modified solvothermal route described in reference [160]. Sn powder and excess thiourea were added to a glass ampoule that had been filled with the solvent mixture (water/ethylenediamine = 1:1) up to 80% of the total volume. The ampoule was sealed and maintained at 180 °C for 12 h. After cooling down to room temperature the products were washed thoroughly with distilled water and ethanol and dried at 75 °C.

**$PbS_{dendrites}$:** $PbS_{Dendrites}$ were synthesized according to literature [161]. In a typical synthesis procedure, 0.002 mole of $PbCl_2$ and 0.003 mole of thiourea were dispersed in ethylene glycol (EG) under stirring. The mixture was transferred into a Teflon lined stainless steel container of 45 mL capacity and filled with TEG up to 90%. The sealed container was maintained at 120 °C for 22 h in a drying cabinet, and then naturally cooled to room temperature. The black products were collected and washed with de-ionized water and ethanol in a Büchner funnel.

**$PbS_{octahedron}$:** $PbS_{Octahedron}$ were synthesized according to literature [162]. In a typical experiment, 0.002 mol $Pb(CH_3COO)_2*3H_2O$, 0.006 mol sulfur powder, and 25 mL DEG were

mixed in a three-necked vessel equipped with a condenser. The mixture was rapidly heated to 180 °C under nitrogen atmosphere and held for 1 h under continuous stirring. After the sample was naturally cooled to room temperature, carbon disulfide was added to the reaction vessel to dissolve the unreacted sulfur powder. The black product was collected by centrifugation and repeatedly washed with ethanol afterwards.

**$PbS_{cube}$:** $PbS_{cubes}$ were synthesised in the same manner as described for $PbS_{octahedron}$, except that $Na_2S$ was used instead of S and that the mixture was reacted at 240 °C.

**$In_2S_3$ nanoflowers**[163]: 10 mmol of $In(NO_3)_3$ and 60 mmol of thioacetamide (TAA) were dissolved in 100 mL deionized water and continuously stirred for 30 min to form a clear solution. The solution was then transferred into a round bottom flask and refluxed at 105 °C for 30 min which yielded an orange colour precipitate. The orange colour precipitate was harvested by centrifugation and washed several times using deionized water and ethanol to remove, and then dried in an air oven at 70 °C overnight.

**$PbSe_{dendrite}$:** For dendritic PbSe particles[164], $Pb(NO_3)_2$ (0.00116 mol) and selenourea (0.00297 mol) were dissolved in water (33 mL) and filled in a autoclave with 40 mL capacity. After 120 °C for 24 h, the autoclave was allowed to naturally cool down. The product was cleaned with water and EtOH and dried in a drying cabinet at 70 °C.

**$PbSe_{square}$:** According to Yu[165], PbSe square particles were prepared by refluxing 0.035 mol $PbC_2O_4$ and 0.0035 mol Se in 35 mL ethylene glycol at 150 °C in an autoclave with 40 mL capacity. The product was cleaned with water and EtOH and dried in a drying cabinet at 70 °C.

**$PbSe_{nanosphere}$:** PbSe nanospheres were synthesized by a modified synthesis route of Gao et al.[166]. 0.005 mol $PbAc_2*3H_2O$ and 0.005 mol Se powder were dispersed in 50 mL ethylene glycol, supported by ultrasonic treatment. The mixture was stirred at 197 °C for 10 h after the addition of 25 ml ethylenediamine and 0.5 g NaOH. The product could be washed and separated by centrifugation with water and EtOH. Afterwards the powder was dried at 70 °C in a drying cabinet. $PbSeO_3$ was obtained as side phase and could not be eliminated by washing with hot water.

## 3. Conversion chemistry of binary sulfides and selenides with $Ni^{2+}$ to 'solid-solution' $Ni_3A_2X_2$ with *shandite* structure and other side reactions

The first subsections, of chapter III.3 deal with the sulfur compounds as they proved to be much more promising, with respect to a complete transformation to its solid-solution and clarification of the mechanism of formation. A more complete picture is driven for those compounds. The second part of the subsections is about the selenium compounds – here no complete reaction to the ternary shandite phase could be achieved. Furthermore, often some phases could not be identified. These chapters are therefore skimped.

### 3.1. Ni-SnS system[1]

In the Ni-SnS system meanwhile three ternary compounds with varying stoichiometry and fascinating structure motifs are known, namely $Ni_9Sn_2S_2$, $Ni_6SnS_2$ and $Ni_3Sn_2S_2$. The first two candidates could be prepared by a chemical vapour transport with $I_2$ at 540 °C. Their crystal structures can be considered as assembled from bimetallic nickel−tin and nickel−sulfide slabs alternating along the crystallographic *c*-axis[167]. $Ni_3Sn_2S_2$ belongs to the above mentioned *shandite*-type compounds, whose structure was already described by Clauss[168] and Zabel[169].

In the solid state $Ni_3Sn_2S_2$ can be obtained from the elements (Ni, Sn, S), from heazlewoodite ($Ni_3S_2$) and elemental Sn, or from SnS and Ni at 900 °C[39, 170, 171]. Mechanisms of formation are not yet known, pure samples are hardly obtained, and it is barely possible to influence the size, as well as to selectively control the morphology of particles under these conditions. However, this becomes possible on the nano-scale, which will be shown accordingly. Subsequently, not only a solution based route for the morphology controlled reaction of SnS to nano sized $Ni_3Sn_2S_2$ at a temperature below 200 °C is shown for the first time but also an elucidation of the reaction mechanism. By varying reaction parameters the formation of hybrid/core-shell particles, $Ni_3Sn_2S_2$, $Ni_3S_2$, and $Ni_{1.523}Sn$ can be controlled from a modified polyol synthesis for isotypic $Ni_3Pb_2S_2$[29].

[1] Some of the results of the Ni-SnS system were already published in:
S. M. Rommel, R. Weihrich, Selective reaction of $Ni^{2+}$ and SnS as a way to Ni@SnS and $Sn_2Ni_3S_2$ nanocrystals - control of product formation and shape, *Chem. Eur. J.,* **2015**, 21, 9863-9867

### 3.1.1. Optimized one-pot synthesis for the conversion of SnS to $Ni_3Sn_2S_2$

According to pathway a) in Figure 6, for the optimized synthesis of $Ni_3Sn_2S_2$, $SnS_{spherical}$ was reacted with $NiCl_2 \cdot 6H_2O$ in basic ethylene glycol (0.512g NaOH in 70 mL eg) at 197 °C for 10.5 h. Ethylenediamine (5 mL) served as the chelating agent. Essentially phase-pure spherical SnS was used as reactive template in the synthesis. Some small reflections of the SnS sample can be attributed to elemental Sn (Figure 7 a, marked with an asterisk). During the heating process, the temperature was kept constant for half an hour at 50, 100, and 150 °C, before raising the temperature with a slow heating ramp (about 3 °C/min). XRD data for $Ni_3Sn_2S_2$ (Figure 7 b) confirms the trigonal *shandite* phase (space group $R\bar{3}m$, No 166). No characteristic peaks are observed for impurities, such as SnS, NiS, $Ni_6SnS_2$, or $Ni_9Sn_2S_2$[167], which are apparent in the phase diagram. Further evidence for the quality and the composition of the $Ni_3Sn_2S_2$ sample was obtained by energy dispersive X-ray spectroscopy (Figure 63 in the appendix). The typical composition of 3:2:2 at.% for Ni, Sn, and S is observed at good agreement (3.17:2.10:2.00 at. %).

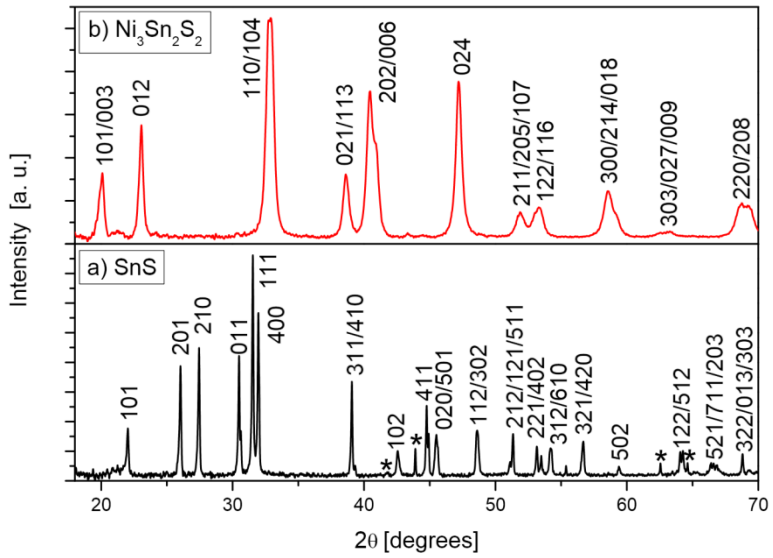


**Figure 7:** XRD pattern of a) SnS. Almost phase pure SnS was obtained according to reference [160] and used as reactive template. Elemental Sn as side phase is marked with an asterisk, b) $Ni_3Sn_2S_2$, which was synthesized at 197 °C for 10.5 h, with a slow heating ramp and stops for half an hour at 50, 100, 150 °C during the heating process.

The refined lattice constants for the measured sample are $a$ = 5.455(3) Å and $c$ = 13.188(3) Å, which is in accordance with the previously reported data ($a$ = 5.4606(2) Å and

$c$ = 13.188(1) Å)[39]. An average crystallite size of 21.8 nm was estimated by the Scherrer equation[172], based on XRD line widths (calculated at the peak with hkl 024).

Figure 8 a-d shows SEM images of SnS nanospheres and $Ni_3Sn_2S_2$ as-prepared at different magnifications. It is obvious that the products adopt the same spherical shape as the precursor SnS.

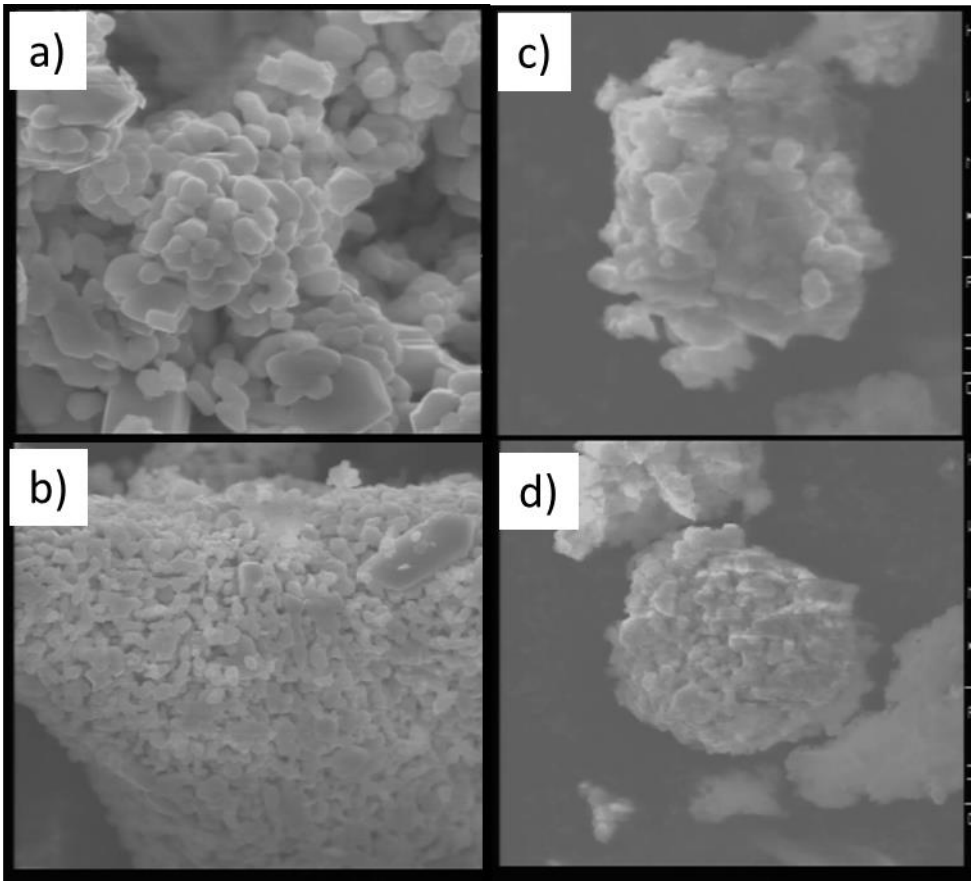


**Figure 8:** SEM images of a, b) SnS and c, d) $Ni_3Sn_2S_2$ at a magnification of 2 and 5 µm, respectively.

These results suggest a template-dependent growth mechanism. We suppose that SnS acts as both precursor and reactive template, which is converted into the ternary $Ni_3Sn_2S_2$.

### 3.1.2. Clarification of the reaction mechanism

A plausible formation mechanism of the ternary nanostructure involves at least three steps (eq. (5)-(7)). When en is added to the reaction mixture, the stable nickel complex $Ni(en)_x^{2+}$ is

formed immediately[155, 158], which is indicated by a change in colour of the solution to purple. The formation of this complex is essential for the whole reaction, as free $Ni^{2+}$ tends to form nickel sulfides, which is accompanied by the decomposition of SnS (see below). At higher temperatures of around 140–160 °C, the solution turns to black, as $Ni(en)_x^{2+}$ decomposes slowly and $Ni^{2+}$ is reduced to the elemental state. This is associated with the moderate intensity reductive characteristic of en[30, 157, 173], and also ethylene glycol itself in strong alkaline solution[118, 119]. The in situ produced Ni is, in theory highly active, and it can be incorporated immediately in the present SnS under retention of its shape[174].

$$Ni^{2+} + x\ en \rightleftharpoons [Ni(en)_x]^{2+} \quad \textbf{(5)}$$

$$HOCH_2CH_2OH \rightarrow CH_3CHO + H_2O \quad \textbf{(6a)}$$

$$2\ Ni^{2+} + 2\ CH_3CHO \rightarrow 2\ Ni_{\ in\ situ} + CH_3COCOCH_3 + 2H^+ \quad \textbf{(6b)}$$

$$3\ Ni + 2\ SnS \rightarrow\ Ni_3Sn_2S_2 \quad \textbf{(7)}$$

The structure transformation from orthorhombic SnS to trigonal $Ni_3Sn_2S_2$ by Ni interdiffusion is depicted in Figure 9. Although a complete reorganisation of the structure has to take place during the reaction, the structural motif of shrunk squares is maintained. Due to the reorganisation it is all the more surprising that this reaction proceeds at low temperatures in a solution-based route.

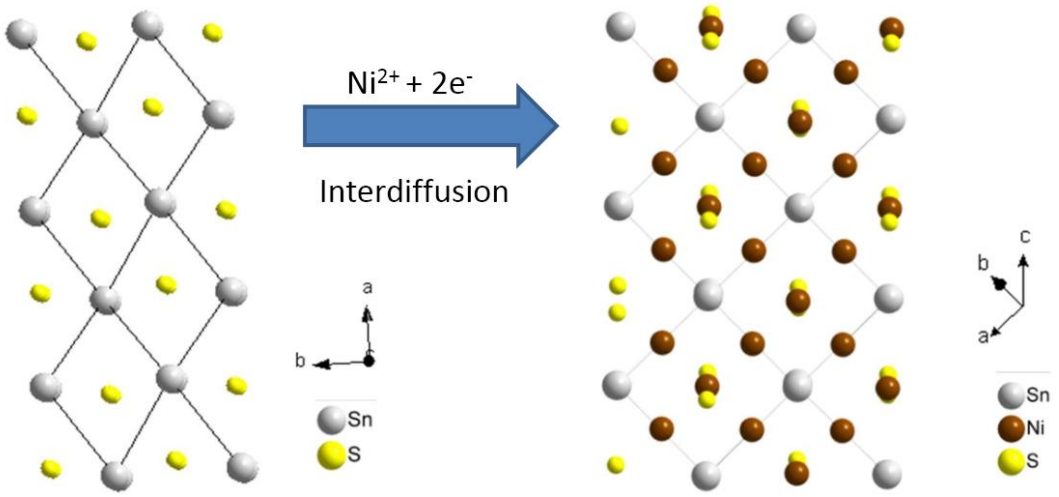


**Figure 9:** Reaction from orthorhombic SnS to trigonal $Ni_3Sn_2S_2$. The structure motif of shrunk squares is prevailed. Nevertheless, a complete reorganization of the structure takes place.

With 2.19 Å the Ni-S-distance is much shorter than expected for the ionic radii (2.28 Å). This is in accordance with the presumption of covalent Ni-S networks and $Ni^0$ ($d^{10}$) which might be one of the driving forces for the formation of $Ni_3Sn_2S_2$.

Interesting results were obtained when the proposed mechanism was studied using different temperatures, morphology of the SnS template, and reducing agents. Therefore, a series of related experiments was designed.

### 3.1.3. Influence of different parameters on products

**Role of ethylene glycol and ethylenediamine**

The solvent medium and reducing agent ethylene glycol has often been used for reduction of metal ions and also as inhibitor for coagulation[118, 119]. The present studies confirm that $NiCl_2$*6 $H_2O$ can be reduced to the elemental state by just refluxing in ethylene glycol and NaOH, with or without the addition of ethylenediamine (eq. 8). Nevertheless, without ethylenediamine, larger and agglomerated Ni particles are obtained, which is in accordance with the literature[118, 175, 176]. Further, the formation of a certain amount of nickel sulfides is observed when en is not added to the solution. In the present case, NiS[177] and $Ni_3S_2$[178] are then formed, with $S^{2-}$ released from SnS. Intermetallic $Ni_{1.523}Sn$[179] is also found, which is assumed to result from a co-reduction of $Sn^{2+}$ and $Ni^{2+}$ (eq. 9a - 11b).

| | | |
|---|---|---|
| Red: | $Ni^{2+} + 2\ e^- \rightarrow Ni$; | (8) |
| Sol.-eq.: | $SnS \rightleftharpoons Sn^{2+} + S^{2-}$; | (9 a) |
| Sol.-eq.: | $Ni^{2+} + S^{2-} \rightleftharpoons NiS$; | (9 b) |
| Red: | $3\ Ni^{2+} + 2\ S^{2-} + 2\ e^- \rightarrow Ni_3S_2$; | (10 a) |
| Red: | $3\ NiS \rightarrow Ni_3S_2 + S^{2-}$; | (10 b) |
| Red: | $3\ Ni + 2\ Sn^{2+} + 4\ e^- \rightarrow Ni_3Sn_2$; | (11 a) |
| Co-Red: | $2\ Sn^{2+} + 3\ Ni^{2+} + 10\ e^- + \rightarrow Ni_3Sn_2$; | (11 b) |

Red=reduction, Sol. eq.=solution equilibrium, and Co-Red= co-reduction.

**Effect of heating ramp, temperature, and reaction time on products**

The temperature dependent stability of the $[Ni(en)_x]^{2+}$ complex explains the challenging reproducibility and sensitivity of the reaction using different heating ramps and temperatures. With the initially described slow heating ramp, the formation of $Ni_3Sn_2S_2$ from SnS and $Ni^{2+}$ in eg with en starts at a temperature below 166 °C. In this temperature region the $Ni(en)_x^{2+}$ complex starts to decompose and $Ni^{2+}$ is slowly released to the reaction solution and rapidly reduced, mainly by the decomposition products of ethylene glycol. The Ni formed in situ should then be incorporated immediately into SnS to form $Ni_3Sn_2S_2$. At a low $Ni^{2+}$ concentration, reduction is thus preferred. By using a rapid heating ramp, NiS, $Ni_3S_2$, and unreacted SnS, are found as products in the XRD patterns (see Figure 10). Clearly, $Ni(en)_x^{2+}$ and SnS decompose too quickly under these conditions. The formation of NiS is then related to high concentration of uncomplexed $Ni^{2+}$.This clearly demonstrates the role of the solubility product of NiS, which is reached when $Ni^{2+}$ is not hidden in the en-complex. Furthermore, the concentration of $S^{2-}$ in solution is due to the dissolution equilibrium of SnS and increases at high temperature. When $S^{2-}$ is consumed by the formation of NiS, it is recovered by dissolving SnS in accordance with the concept of Le Chatelier (eq. (9a, b)). By extending the reaction time and keeping the rapid heating ramp constant, SnS disappears, but the amount of $Ni_3Sn_2S_2$ does not increase. Instead, the quantity of $Ni_3S_2$ rises, which is an indicator of progressive reduction of $Ni^{2+}$, which is present in NiS (eq. (10 a, b)). At long reaction times $Ni_{1.523}Sn$ appears, as either the product of a co-reduction of $Ni^{2+}$ and $Sn^{2+}$ or a further reductive interdiffusion process of $Sn^{2+}$ on Ni particles (eq. (11 a, b)).

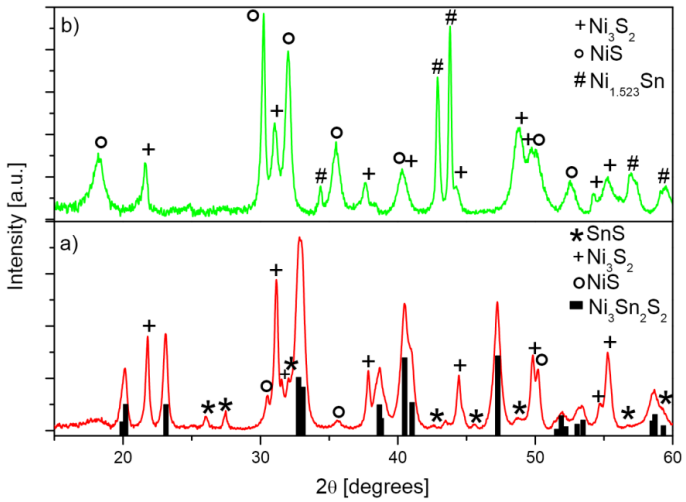


**Figure 10:** a) Reaction products of a synthesis with a rapid heating ramp. b) Reaction products of a synthesis where all starting materials were injected into the refluxing solution.

**Role of the SnS source**

In addition to the importance of the reaction temperature and heating ramp we found that the tin sulfide source plays an important role in this modified polyol process. Two kinds of SnS sources ($SnS_{spherical}$, $SnS_{bulk}$) were tested for the preparation of $Ni_3Sn_2S_2$. As shown before, it is possible to synthesize the phase-pure *shandite* phase, when using spherical SnS under optimized conditions. Whereas, when $SnS_{bulk}$ (prepared by a solid-state method) is used, only small amounts of the target *shandite* phase are observed. Prominent side phases $Ni_3S_2$, and $Ni_{1.523}Sn$, plus a small unknown phase, are also apparent. Different heating ramps and reaction times did not increase the amount of $Ni_3Sn_2S_2$. One can conclude that the small particle size and the morphology of the applied SnS precursor plays a key role in the synthesis of $Ni_3Sn_2S_2$. Because of the increased surface to volume ratio diffusion in nanoparticles is much faster than in the bulk materials[88]. This can possibly lead to facilitated chemical transformation of the particles.

**Hydrazine as reducing agent (Ni-SnS hybrid/core-shell particles)**

The reactions with hydrazine hydrate as reducing agent are a short preview to chapter III. 4 and are just mentioned here to discuss the different redox reactions, occurring in the Ni-SnS system. When ethylenediamine is replaced by hydrazine as the additional reducing agent and the temperature is lowered to 60 – 70 °C, only a small amount of $Ni_3Sn_2S_2$ is formed, and the main products were Ni and SnS according to the X-ray diffraction data (Figure 69). No consecutive reactions are observed in solution, especially for SnS, which does not dissolve. The washed and dried product reacts to $Ni_3Sn_2S_2$ in a solid state reaction at T = 500–700 °C. It is concluded on hybrid or even core-shell particles.

The whole system presented is determined by equilibrium and redox reactions (eq. 8-11b), which have been summarized in Scheme 1. As shown above, the concentration of free $Ni^{2+}$ is particularly crucial for the competing reduction to $Ni^0$ or the formation of NiS.

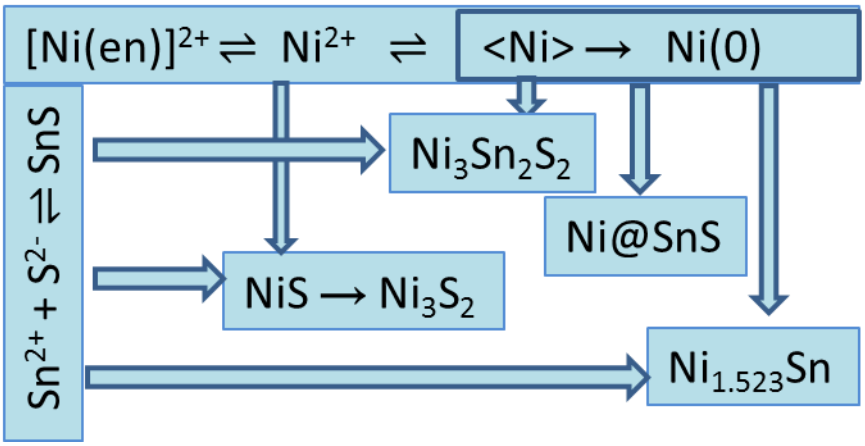


**Scheme 1:** Equilibrium and redox reactions in the SnS, $[Ni(en)_x]^{2+}$ system.

To exclude any other mechanisms of formation for the $Ni_3Sn_2S_2$ phase, like a dissolution–precipitation process, which proceeds over chemical intermediates like $Ni_3S_2$ or NiS, the following tests were conducted. In one approach all starting materials were injected into refluxing ethylene glycol, which resulted in NiS, $Ni_3S_2$, and $Ni_{1.523}Sn$ (Figure 10 b). Further experiments were all conducted at the optimized slow heating ramp for $Ni_3Sn_2S_2$, described before, and refluxed at 197 °C for 10.5 h; by using $Ni_3S_{2,bulk}$ and $SnCl_2{\cdot}2H_2O$ as starting materials, the reaction stopped at $Ni_3S_2$, with a small NiS side phase. $NiCl_2{\cdot}6H_2O$, $SnCl_2{\cdot}2H_2O$, and $Na_2S$/S also resulted in $Ni_3S_2$ and NiS, with the addition of $Ni_{1.523}Sn$, when $Na_2S$ was applied. These results altogether underline that one challenging point of the synthesis is the integrity of SnS. After dissolution of SnS it is not possible to get to the $Ni_3Sn_2S_2$ phase. With careful adjustments, the method is applicable to other M+AX systems too, which is shown in the following chapters. Based on these experiences compounds with varying *M* content like PtSnS[180] or $Pd_5InSe$[181] should also be possible to synthesise.

### 3.2. Ni-PbS System

In the Ni-PbS systems only two ternary compounds are known so far, $Ni_3Pb_2S_2$[33, 182] and $Ni_{151.5}Pb_{24}S_{92}$[183]. The latter one with its inherent high nickel content has been described by Popovkin and co-workers and shows well-defined clusters, formed by nickel atoms. It exhibits an infinite three-dimensional network of heterometallic Ni-Pb bonds. The absence of nickel clusters in the $Ni_3Pb_2S_2$ *shandite*-type compound is attributed to the low nickel content as compared to that in $Ni_{151.5}Pb_{24}S_{92}$. Both compounds can be prepared from the elements by

solid-state methods. Whereas $Ni_3Pb_2S_2$ is stable over a broad temperature range, $Ni_{151.5}Pb_{24}S_{92}$ is only stable between 490–578 °C.

As already mentioned, the group around Shao et al. already described a low-temperature polyol route to dendritic $Ni_3Pb_2S_2$[29]. A unidirectional diffusion of the in situ produced Ni, into the template PbS was proposed. But still, re-evaluating this compound and its solution-based synthesis appeared to be necessary, as no properties of the nanoparticles were studied and the synthesis could not be reproduced properly by us in previous investigations. As PbS is known to be even more stable than SnS an understanding of the complex interplay of different parameters on reaction products seemed to be worthwhile. During this thesis a further emphasis was placed on the templating of different morphologies and the low-temperature structural behaviour of the different morphologies (see chapter III.5.3).

### 3.2.1. Optimized One-pot synthesis for the conversion of PbS to $Ni_3Pb_2S_2$

In the optimized synthesis, dendritic PbS (octahedral PbS can also be used – this will be shown in the following chapters) and $NiCl_2*6H_2O$ (molar ratio $NiCl_2*6H_2O$:PbS = 3:2) were reacted in basic ethylene glycol (0.54 g NaOH in 80 mL eg) with ethylenediamine (5 mL) as chelating agent according to Figure 6, pathway a. In order to investigate the crystallization process of $Ni_3Pb_2S_2$ the temperature- and time-dependent XRD patterns of the reaction were monitored (Figure 11). At the beginning of the reaction (Figure 11 a) all peaks belong to the starting material PbS. Already at a temperature of around 166 °C, or even earlier, the first peaks of the *shandite* phase appear and the amount of PbS diminishes. This process can be carried forward by increasing the temperature and reaction time (Figure 11 b-d). After 2.5 h at 197 °C the entire PbS is consumed and single-phase $Ni_3Pb_2S_2$ is obtained. No other impurities occur during the whole synthesis. The broad reflexions of the X-ray powder diffraction patterns indicate the nanoparticular shape of the product.

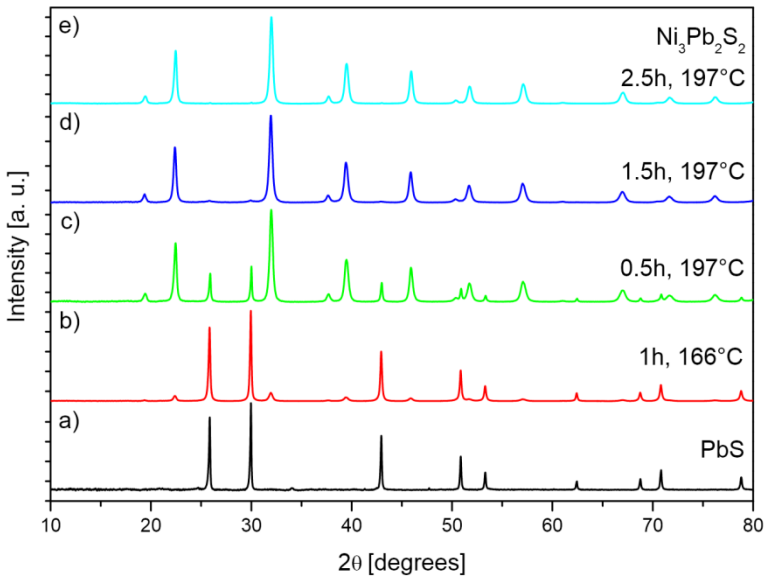


**Figure 11:** Temperature- and time-dependent conversion reaction of PbS with $NiCl_2*6H_2O$ to ternary $Ni_3Pb_2S_2$.

### 3.2.2. Clarification of the reaction mechanism

Keeping in mind the general considerations about the temperature dependent reductive characteristic of ethylene glycol and the chelating ability of ethylenediamine (see also the introduction and chapter III.2.1) the reaction mechanism can be proposed as follows.

PbS is known as a very stable and unreactive mineral; it cannot be dissolved, but dispersed in the basic reaction medium, consisting of eg and en. $Ni^{2+}$ in contrast is readily soluble and can be complexed by en in a first step. In a second step $Ni^{2+}$ can be progressively reduced to the elemental state, as soon as $[Ni(en)_x]^{2+}$ becomes unstable at higher temperatures. This process is accompanied by a change of colour from purple to black. Most likely the reductant is not en, but the decomposition product of eg at higher temperatures (eq. (12)-(14)). The in situ produced Ni is supposed to be highly active and can be immediately incorporated in the template PbS (eq. (15)). The net reaction can therefore be formulated as a unidirectional diffusion of Ni into PbS as already proposed by Shao et al. [29].

$$Ni^{2+} + x\ en \rightleftharpoons [Ni(en)_x]^{2+} \quad \textbf{(12)}$$

$$HOCH_2CH_2OH \rightarrow CH_3CHO + H_2O \quad \textbf{(13)}$$

$$2\ Ni^{2+} + 2\ CH_3CHO \rightarrow 2\ Ni_{in\ situ} + CH_3COCOCH_3 + 2\ H^+ \quad \textbf{(14)}$$

$3\ Ni + 2\ PbS \rightarrow Ni_3Pb_2S_2$ **(15)**

### 3.2.3. Influence of different parameters on products

**Starting materials:**

A) *Effect of different morphologies of the PbS templates on phase purity and shape of the products (morphological templating)*

Four different PbS precursors were used to study the effect of different PbS templates on phase purity and shape of the reaction products. $PbS_{bulk}$, which was prepared by a standard solid-state reaction and nanoparticular $PbS_{dendrite}$, $PbS_{octahedron}$ and $PbS_{cube}$ from solution based syntheses. This is in particular interesting here as diffusion into bulk and different shaped nanoparticles is known to behave very different and the mechanism of formation of $Ni_3Pb_2S_2$ is found to be a unidirectional diffusion of Ni into PbS (see 3.2.2 and Shao et al.[29]).

$PbS_{dendrite}$ and $PbS_{octahedron}$ can be thoroughly converted to $Ni_3Pb_2S_2$ by the optimized synthesis conditions, shown above. In contrast to that, attempts to react $PbS_{bulk\ or}$ $PbS_{cube}$ with $NiCl_2*6H_2O$ showed that only a small proportion of ternary shandite can be formed. Even working with fourfold Ni excess and the application of longer reaction times of up to 15 h did only slightly increase the amount of the shandite phase, instead additional elemental Ni appears.

This phenomenon can be explained by taking into consideration the prerequisites that facilitate diffusion in crystalline materials. The material should contain:

(i) interfaces which provide short diffusion paths

(ii) a high density of defects, such as grain boundaries and vacancies

(iii) defects originating from the curvature of surfaces[184]

(iv) other driving forces, for example, stress fields and dislocations in the crystal that may introduce fast diffusion paths

Nanoparticles therefore exhibit a higher reactivity than their bulk counterparts as they fulfill most of the mentioned prerequisites[88, 185]. The higher surface area leads to an increased surface to bulk atom ratio and to an increased amount of reaction sites. As the heterogeneous reaction occurs on the surface of the applied PbS particles, the PbS nanostructures should encourage a much faster Ni diffusion and enable a fast chemical conversion of the particles as a whole. For the big bulk PbS particles it is proposed that the chemical reorganization during the conversion process is kinetically inhibited and slower compared to the nanoparticles. It is even possible that a $Ni_3Pb_2S_2$ shell is built up which serves as kind of a blocking layer, where Ni cannot pass through. The reaction of $PbS_{dendrite}$, $PbS_{octahedron}$ and $PbS_{bulk}$ can be explained by these considerations. Unfortunately, the incomplete reaction of the small $PbS_{cube}$ particles cannot be understood by that. To address this question, a closer look at the morphologies of the PbS samples (Figure 12-Figure 14) is beneficial.

The left side of Figure 12 shows the dendritic PbS which served as template for the conversion reaction with $Ni^{2+}$. The crystallites exhibit a dendritic or fishbone like morphology with branches of around 190 nm in thickness and varying lengths. Furthermore the surface of the branches looks very rough and all faces are curved. These characteristics indicate that there should be inherent defects, vacancies and a big surface area, which promote diffusion. An entire conversion of the dendritic PbS to $Ni_3Pb_2S_2$ is therefore more probable.

A comparison of the morphology of the utilized dendritic PbS (Figure 12, left side) with the end products (Figure 12, right side) reveals that the shape is perfectly preserved. The dendritic PbS is therefore suitable as a morphological and reactive template in the synthesis of $Ni_3Pb_2S_2$, as already shown by the workgroup of Shao[29]. Figure 12 g) and h) show a higher magnification of the blue marked sections of Figure 12 e) and f). As expected, the thickness of every single branch is enlarged. The radius of the marked branches shows an increase from 190.7 to 268.6 nm. If one treats the shape of a branch as a cylinder with the length of 1 nm, the volume would increase from 114248.70 $nm^3$ to 226653.23 $nm^3$ (198.39%). That roughly matches with the volume increase from a single PbS to a $Ni_3Pb_2S_2$ crystallite (176.58%). It is assumed that the dendritic shape is prevailed because Ni can diffuse into the template from almost every direction, promoted not only by the shape, but also by the curvature and roughness of the templates. No special growth direction is preferred and even more important, the dendrites do not break.

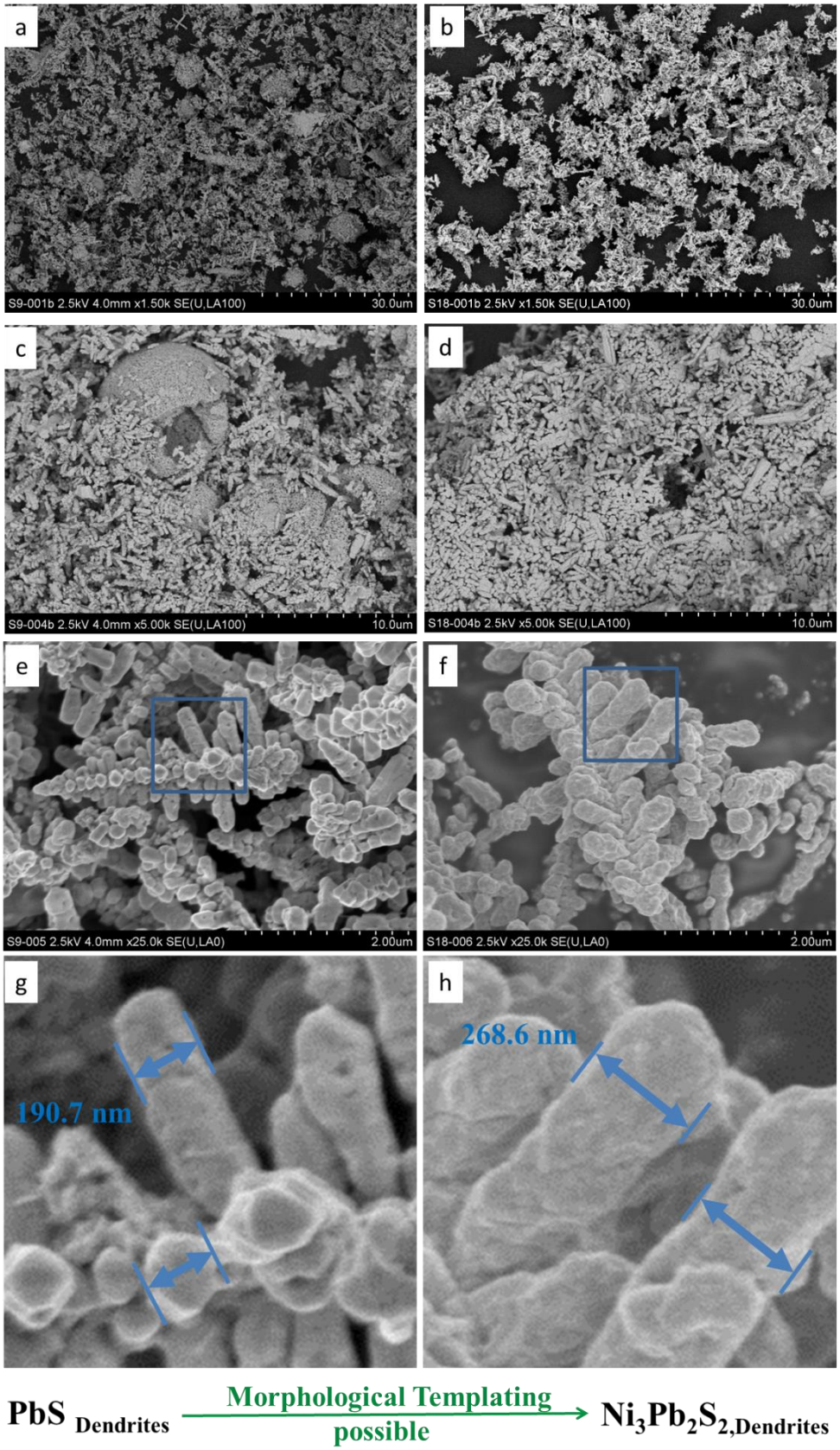


**Figure 12:** SEM pictures of starting material $PbS_{dendrite}$ (left side) and product $Ni_3Pb_2S_2$ (right side). g) and h) show the insets of e) and f) at bigger magnification.

This is in contrast to the reaction of octahedral PbS, where a complete conversion to $Ni_3Pb_2S_2$ is possible but the morphology cannot be templated, as will be shown accordingly. The octahedral shaped PbS particles can be seen on the left side of Figure 13. It is obvious that the size and edge length of the particles differs, but in general the shape takes that of a capped octahedron for every particle. After the conversion to $Ni_3Pb_2S_2$, no uniform morphology can be observed anymore (Figure 13, right side). A lot of very small particles with different shapes and sizes are obtained. This information suggests that the octahedra are split during the conversion reaction – the possible driving force for ongoing conversion into $Ni_3Pb_2S_2$. A cracking of the particles is not very surprising since the whole structure of PbS has to be transformed into $Ni_3Pb_2S_2$, which is accompanied by a rearrangement of all involved atoms. Furthermore, the stress of the octahedral shaped particles is supposed to be very high. A complex interplay between crystallinity and stress of the former PbS particles might be the key point for a successful conversion to $Ni_3Pb_2S_2$, here.

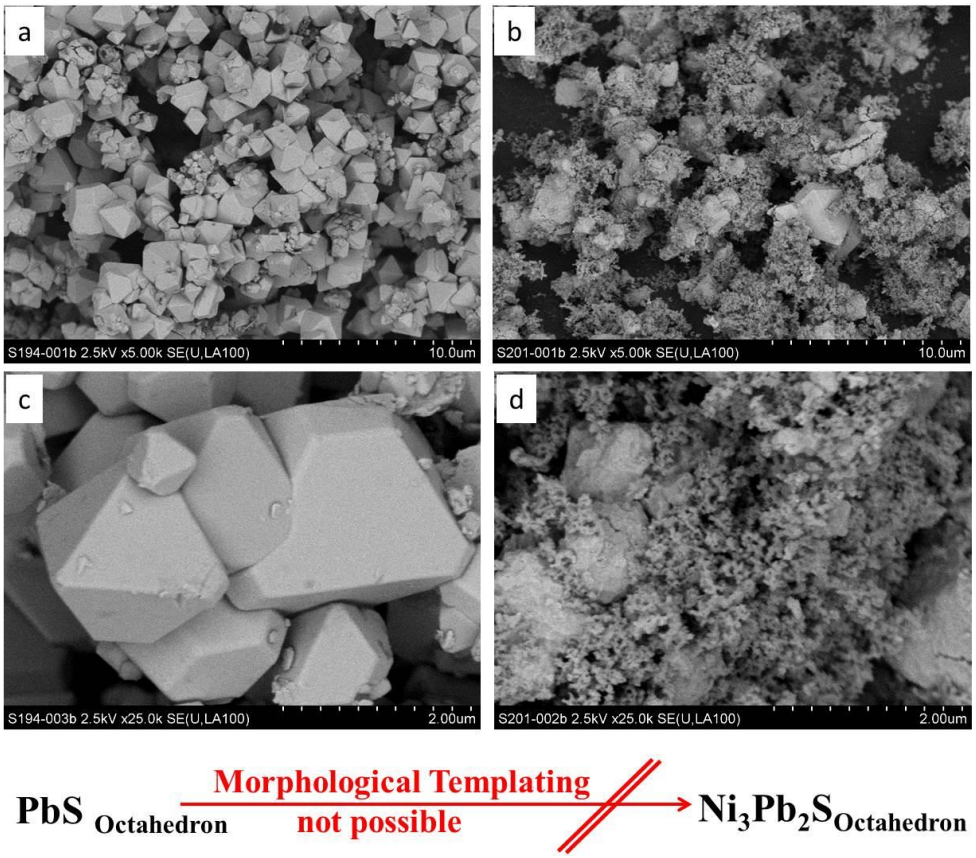


**Figure 13:** SEM pictures of starting material $PbS_{octahedron}$ (left side) and the resulting product, $Ni_3Pb_2S_2$ (right side).

Cubic shaped PbS as reactant cannot be entirely converted into $Ni_3Pb_2S_2$ under the same conditions, applied for dendrites and octahedra. An astonishing result, as the particles should be very small with an edge length of <100 nm, according to literature [162] (Figure 14 a). This shape leads to a big surface area, stress fields and also the diffusion paths should be approximately short enough. The quality of our own SEM measurement is very low, but still it can be seen that very small particles are obtained (Figure 14 b). The main part of these particles seems to be strongly agglomerated. After the conversion to $Ni_3Pb_2S_2$, this agglomeration is still the same. One can conclude that this agglomeration is responsible for the sluggish kinetics of the conversion reaction as for $PbS_{dendrite}$ and $PbS_{octahedron}$ clearly separated particles with defined morphology dominate the picture.

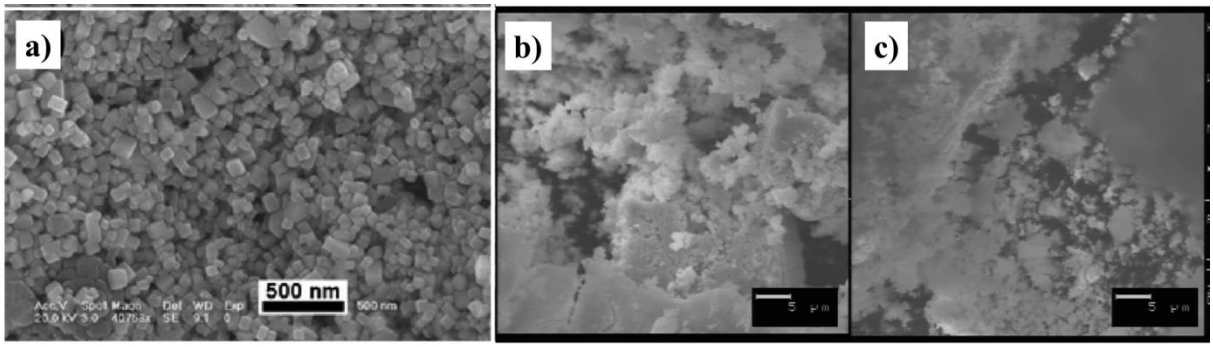


**Figure 14:** a) SEM picture of starting material PbScube. Reprinted with permission from reference [162]. Copyright 2008 American Chemical Society. b) SEM picture of $PbS_{cube}$ from own synthesis c) SEM picture of the result of a partial transformation of PbS to $Ni_3Pb_2S_2$.

Another approach to explain the differences between the four PbS templates can be made on a pure theoretical basis. Assuming that the cubes cannot be cleaved into smaller particles during the reaction, it is possible that the diffusion process itself leads to a kind of passivation area, consisting of $Ni_3Pb_2S_2$, especially at the corners of the cubes, where Ni atoms from both sides cross their ways (Figure 15).

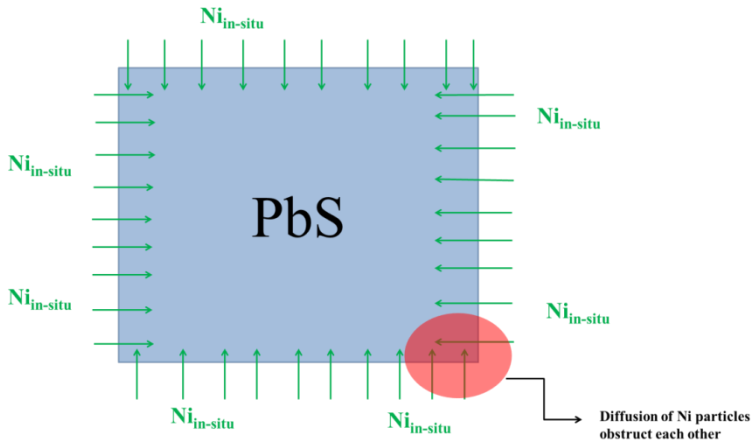


**Figure 15:** Diffusion of Ni into cubic shaped PbS templates. The Ni atoms hinder one another at the corners. It is assumed that Ni diffusion through an already created $Ni_3Pb_2S_2$ layer is hampered and Ni is blocked at these positions.

*B) Effect of Nickel excess*

It should be made clear, that the reduction of $Ni^{2+}$ was complete after 2.5 h at 197 °C, at the latest. This could be verified by two observations. First, by a complete conversion of PbS to $Ni_3Pb_2S_2$ in the optimized synthesis with $PbS_{dendrite}$ or $PbS_{cube}$. Second, by annealing a sample which was not entirely converted to $Ni_3Pb_2S_2$ after 2.5 h at 500-700 °C. This led to a complete conversion to the ternary and proved that Ni was already linked to PbS after that time.

When dendritic PbS was used, a fourfold nickel excess under otherwise optimized conditions (see III.3.2.1), led to a big Ni side phase and a product of a co-reduction, NiPb[186]. With bulk PbS, a big nickel excess increased the amount of the ternary shandite phase, but still some PbS was left over, besides elemental Ni. Nevertheless, the equilibrium seems to be shifted to the $Ni_3Pb_2S_2$ compound under Ni excess, according to Le Chatelier. Interestingly, no NiPb could be observed. Dendritic PbS might be more prone to such reactions as its specific surface area is significantly higher than its bulk counterpart.

*C) Role of the pH as well as the reductant and chelating agent*

Based on the optimized synthesis for $PbS_{dendrite}$, the effect of the pH (NaOH), as well as of the chelating agent (en) and/or reductant (hyd) was studied by additional experiments (Table 4). Dendritic PbS was used for all experiments.

**Table 4:** Role of the pH as well as of the chelating agent and reductant. The usage of NaOH , reductant or chelating agent is marked with a "x". All experiments were conducted with dendritic PbS. The applied volume for hyd or en was 5 mL.

| NaOH | Ethylenediamine (en) | Hydrazine hydrate (hyd) | Product |
|---|---|---|---|
| / | / | / | NiS, $Ni_3S_4$, $Ni_7S_6$ |
| high (0.54 g) | / | / | PbS, Ni, $Ni_3S_2$, $Ni_3Pb_2S_2$ |
| high (0.54 g) or low (0.16 g) | x | / | $Ni_3Pb_2S_2$ |
| low (0.16 g) | / | x | PbS, Ni, $Ni_3Pb_2S_2$ |
| high (0.54 g) | / | x | PbS, Ni, $Ni_3Pb_2S_2$, Pb |

All three "parameters", namely the pH, the reductant and the chelating agent play a key role in the synthesis procedure, as will be shown accordingly. A reaction control with neither NaOH nor en or hyd leads to just different Nickel sulfides and no shandite phase is formed. Despite that, in basic eg the reductive power is enough to reduce $Ni^{2+}$, so that at least some $Ni_3Pb_2S_2$ is formed. Unfortunately, PbS, Ni and $Ni_3S_2$ occur as side phases. This is in accordance with the results presented in chapter III.2.1 and III.3.1.

Hyd and en are able to form strong complexes with $Ni^{2+}$ and therefore $Ni^{2+}$ is only gradually released during the reaction. Without the application of any complexing agent even the solubility products of nickel sulfides can be exceeded and different nickel sulfides are formed. In contrast, when ethylenediamine is used in weak or strong alkaline eg, complete conversion of the template PbS to $Ni_3Pb_2S_2$ is reached, and especially no nickel sulfides are observed. Trials to reproduce the attempt of Shao et al. with hydrazine hydrate in only weak basic ethylene glycol (0.16 g NaOH in 80 mL eg) resulted in big side phases of unreacted PbS and elemental Ni. By conducting the reaction under stronger alkaline conditions (5.4 g NaOH in 80 mL eg), even elemental Pb along with the aforementioned phases could be observed. These result altogether lead to the same conclusions which were also drawn for the Ni-Sn-S system. For hydrazine as reductant it can be concluded that the reduction of $Ni^{2+}$ is very fast, and proceeds at already low temperatures. The conversion of PbS and especially the diffusion of

nickel into the template is too slow, so that a Ni layer is formed around PbS. This is why a magnetic powder was obtained in these approaches. The combination of basic ethylene glycol and ethylenediamine seems to produce optimal conditions for the exclusive conversion reaction to $Ni_3Pb_2S_2$ as the in situ produced nickel is gradually released and is able to diffuse into the template PbS.

## 3.3. Ni-InS system

$Ni_3In_2S_2$ was detected by Range and Zabel[187] in 1968 when they performed high-pressure experiments on $In_2S_3$, which reacted with the nickel mount of their press at temperatures above 400 °C. Its single crystal structure was refined by Weihrich and co-workers in 2005[32]. $Ni_3In_2S_2$ exhibits paramagnetic and metallic behaviour up to very low temperature with a conductivity, comparable to that of lead ($3x10^{-5}\Omega^{-1}cm$)[188, 189]. In the ternary Ni-In-S system another compound is known, namely the *spinell*-type $NiIn_2S_4$. It was discovered by Hahn et al. by reacting *spinell*-type $In_2S_3$[190] with different bivalent metal sulfides.

Two indium sulfides with different compositions are known and were used in this thesis: Indium(III) sulfide is the inorganic compound with the formula $In_2S_3$. Three different polymorphs exist at normal pressure: The red β-$In_2S_3$ modification with a defect spinel, tetragonal structure (7.62 Å)[190] transforms into the yellow α-$In_2S_3$ above 420 °C with a defect cubic face-centred structure (5.36 Å)[191-192]. γ-$In_2S_3$ in turn has a layered structure and is only stable above 754 °C, unless adding As or Sb[193]. The red, β, form is considered to be the most stable form at room temperature. In contrast to that In(II)S, forms the orthorhombic InS which is homotypic to SnS and HgCl[194].

### 3.3.1. Optimized one-pot synthesis for the conversion of InS and $In_2S_3$ to $Ni_3In_2S_2$

In the optimized synthesis, bulk $In_2S_3$ or InS and $NiCl_2*6H_2O$ were reacted in basic ethylene glycol (0.54 g NaOH in 80 mL eg) with ethylenediamine (5 mL) as chelating agent (molar ratio Ni:In = 3:2), according to Figure 6 pathway a). In order to investigate the crystallization process of $Ni_3In_2S_2$ the temperature- and time-dependent XRD patterns of the reaction were monitored in Figure 16. Figure 16 a) shows the starting material $In_2S_{3,bulk}$ which was used for

the conversion reaction. At temperatures below 170 °C, no reaction is observed (not shown here) and still only $In_2S_3$ can be seen. When the temperature is increased to 197 °C, the first peaks of the *shandite* phase appear and the amount of $In_2S_3$ diminishes. Unfortunately, the reaction is even not complete after 10.5 h (Figure 16 c). However, under a fourfold Ni excess $In_2S_3$ can be completely transformed to $Ni_3In_2S_2$. Then of course, metallic Ni is observed as side phase (Figure 16 d).

The same reaction control is also possible, when bulk InS is applied (Figure 66 in the appendix). As with $In_2S_3$, after 10.5 h at 197 °C and fourfold Ni excess (Ni:$In_2S_3$ = 12:1), almost the entire $InS_{bulk}$ is converted to the ternary shandite phase. It is noteworthy to mention, that no other impurities, apart from elemental Ni, occur during the syntheses, regardless of the applied precursor.

If one compares the results of the syntheses with $In_2S_3$ and InS as starting materials, big differences in size and crystallinity of the resulting $Ni_3In_2S_2$ become apparent. The broad peaks of the X-ray powder diffraction patterns of the product which was synthesized with $In_2S_{3,bulk}$ (Figure 16), indicate the nanoparticular shape and perhaps also poor crystallinity of the product. In contrast, when $InS_{bulk}$ was used, the end product shows very narrow peaks, which hints on big particle size and good crystallinity (Figure 66 in the appendix). These results can be explained by taking the different possible mechanisms of formation into account.

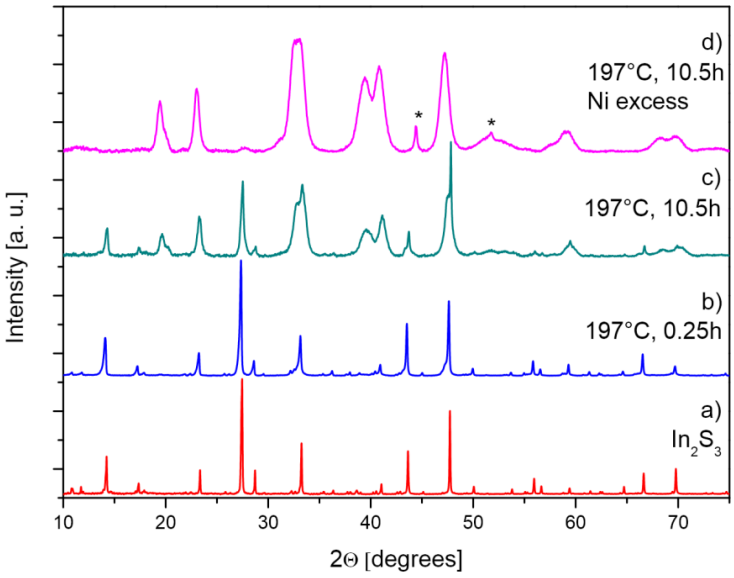


**Figure 16:** a) Starting material $In_2S_{3,bulk}$, b) Result after reacting at 197 °C for 0.25 h c) Result after reacting at 197 °C for 10.5 h d) Result after reacting at 197 °C for 10.5 h with fourfold nickel excess.

### 3.3.2. Clarification of the reaction mechanism

A plausible mechanism of formation of the ternary *shandite*-type compound, starting from $InS_{bulk}$ and $In_2S_{3,bulk}$, can be postulated as follows. As the reaction is driven according to the general synthesis protocol (Figure 6, pathway a)), equation (5)-(6b) are also valid here. $Ni^{2+}$ will be gradually reduced at rising temperatures and times and the in situ produced nickel is assumed to be very reactive.

For the conversion of InS to $Ni_3In_2S_2$ one has to conclude that the mechanism is a unidirectional diffusion of Ni into the binary precursor (see eq. (16)), which was already observed for all other Ni *shandite*-compounds described in previous chapters. This can be underlined by two observations. First, almost no side phases appear during the reaction. Especially no nickel sulfides are formed, which is one of the main problems in the Ni-SnS system. The second and probably weightier fact is the mentioned narrow shape of the XRD peaks, which does not change during the reaction. This hints on a direct transformation of the InS precursor, as for a decomposition-formation process smaller particles would be excepted.

$$2\ InS + 3\ Ni \rightarrow Ni_3In_2S_2 \qquad \textbf{(16)}$$

The conversion of $In_2S_3$ obviously has to occur along a different reaction mechanism, as considered already from the stoichiometry. Still, no side products appear during the reaction but the peak shape changes drastically, towards more broad peaks. A bigger structural transformation suggests itself here. The author assumes that Ni diffuses into $In_2S_3$ and $Ni_3In_2S_2$ is formed under a simultaneous expulsion of $S^{2-}$. This reaction might be encouraged as incompletely coordinated sulfur atoms are present in $In_2S_3$[163, 195], which can be separated easily. The excess on sulfur atoms can be washed out during the cleaning process, as most probably water soluble $Na_2S$ is formed. Furthermore, the solubility degree of $In_2S_3$ should be much higher than that of $Ni_3In_2S_2$ which prefers the formation of the less soluble $Ni_3In_2S_2$ compound.

Interesting results were obtained when the proposed mechanism was studied using different temperatures, morphology of the $In_2S_{3,bulk}$ template and reducing agents. Therefore, a series of related experiments was designed.

### 3.3.3. Influence of different parameters on products

**Influence of the starting materials**

*A) Bulk InS/$In_2S_3$ vs. nanoparticular $In_2S_3$*

As already mentioned, when bulk InS or bulk $In_2S_3$ is applied all of the corresponding binary precursor can be transformed to the ternary *shandite* under a fourfold nickel excess. By contrast, nanoparticular and less crystalline $In_2S_3$ ($In_2S_3$ nanoflowers) is not suited for the synthesis of ternaries, as it decomposes and reacts to NiS, $Ni_3S_2$ and some other sulfur compounds. The bulk precursors seem to be more stable under these conditions.

B) $NiCl_2*6H_2O$ vs. $Ni_{nano}$

In contrast to $NiCl_2*6H_2O$ which is able to react in a conversion reaction, elemental $Ni_{nano}$ does not react with $InS_{bulk}$, at all. Even not at temperatures around 280 °C for 10.5 h. As the collected in situ reduced nickel has been stored in air, a possible agglomeration of the particles or the formation of a small NiO layer has to be taken under consideration. The in situ formed nickel during the one-pot reaction seems to be much more reactive and one of the key points of the reaction.

*C) Working under $In_2S_3$ or Ni excess*

When twice as much $In_2S_{3,bulk}$ is applied under otherwise optimized conditions, only $Ni_3In_2S_2$ and a big amount of $In_2S_3$ are observed as end products. This underlines the stability of $In_2S_{3,bulk}$ and clarifies that a transformation of $In_2S_3$ to $Ni_3In_2S_2$ is the only reaction which is taking place during the synthesis.

A big Ni excess is a prerequisite for the successful conversion of the entire $In_2S_3$. It is assumed that according to Le Chatelier the equilibrium state can be shifted to the ternary product. The intrinsic driving force for the transformation of InS or $In_2S_3$ to $Ni_3In_2S_2$ seems not to be that strong, as compared to the Ni-PbS system. This is in an absolute contrast to the solid-state synthesis of the *shandite* phases, where $Ni_3In_2S_2$ belongs to the most stable and

easy to synthesize compounds. One reason might be found in the applied morphology of the $In_2S_3$ precursor which possibly does not promote or facilitate the conversion reaction to $Ni_3In_2S_2$. Or simply $In_2S_3$ is more stable than $Ni_3In_2S_2$.

D) *Effect of heating ramp, temperature, and reaction time on products*

The reaction is quite independent of the applied heating ramp. In contrast, the reaction temperature has a much bigger effect on the obtained end products. It is found that a temperature of 166 °C is not high enough to form any $Ni_3In_2S_2$. The reaction starts at temperatures higher than 166 °C. A reaction time of 10.5 h was sufficient to complete the conversion reaction under Ni excess. Nevertheless, one has to assume that shorter reaction times are also valuable. Significant longer reaction times (>24 h) did not increase the amount of $Ni_3In_2S_2$, when the stoichiometric ratio of the starting materials was 3:2 (for Ni:InS). The same is for higher temperatures (up to 300 °C in TEG).

### 3.4. Ni-TlS system

In the thallium–sulfur system, many types of sulfides have been reported: $Tl_2S$[196], $Tl_4S_3$[197], TlS[198, 199], $Tl_2S_5$[200] , $Tl_2S_9$[201] and $TlS_2$. Thallium chalcogenides possess unique physical properties, important for different practical applications[202, 203]. Recently, binary and ternary thallium chalcogenides, for example TlS, $Tl_2S$, $Tl_4S_3$ or $TlInS_2$ received a great deal of attention due to their optical and electrical properties in view of possible optoelectronic device applications[204-209]. The great number of these compounds and thus the large variety of their physical properties are determined by different oxidation states of thallium atoms (+1, +3 and also mixed valent) in the compounds[210, 211]. The applied TlS of this work is a binary or also called double sulfide[198] and can also be written as follows:

$TlS = Tl_2S_2 = Tl^{I}[Tl^{III}S_2] = Tl^{I}{}_2S{*}Tl^{III}{}_2S_3$

For TlS, an earlier work of our group could clearly identify Tl(I) and Tl(III) within the DOS, orbital, and AIM analysis[211]. Assuming Ni(0) and S(-II) in $Ni_3Tl_2S_2$ a similar situation with Tl(I) and Tl(III) on the different A = Tl sites could be estimated as well as the rare Tl(+II)

situation that is found in the high pressure form of TlS. However, the two different thallium atoms in $Ni_3Tl_2S_2$ do not differ in orbital contributions; they show a weak positive charge for both methods. This gives evidence against a mixed valence of Tl in $Ni_3Tl_2S_2$. The studies indicated an intermediate state with characteristics between Tl(I) and Tl(III)[211]. Recent studies provided a closer insight in terms of anisodesmic bonding in *shandites*. The A = In, Tl, Sn, and Pb sites show different bonding types to different neighbours that is also known e.g. for oxygen in silicates (covalent to Si, ionic to $M^{x+}$ neighbours). The *A* (here: Tl) sites in *shandites* behave as metal to Ni neighbours and form multicenter bonds (see recent papers on bonding in $Co_3InSnS_2$[34, 35, 147]). On the other hand, they behave like cations towards sulfur neighbours. This view is underlined by $^{119}$Sn Mößbauer spectroscopy, studies on the electric field gradients and the electron localisation function (ELF). Consequently, the *shandites* were described by charge balancing between $A^{n+}$ cations and a negatively charged covalent $[Ni_3S_2]^{n-}$ network.

In the Ni-Tl-S system only one other ternary compound is known, $Ni_2TlS_2$. This phase belongs to the first chalcogenides found to crystallize in the $ThCr_2Si_2$-structure type[212]. Unlike the already known representatives of this structure type they show a pronounced partial ionic character.

### 3.4.1. Optimized one-pot synthesis for the conversion of TlS to $Ni_3Tl_2S_2$

In the optimized synthesis, $TlS_{bulk}$ and $NiCl_2*6H_2O$ were reacted in basic ethylene glycol (0.54 g NaOH in 80 mL eg) with ethylenediamine (5 mL) as chelating agent (molar ratio Ni:Tl = 3:2), according to Figure 6 pathway a). In order to investigate the crystallization process of $Ni_3Tl_2S_2$ the temperature- and time-dependent XRD patterns of the reaction were monitored (Figure 17, from bottom to top). One can see that already a reaction temperature of 166 °C for 1 h is enough to form a small amount of the ternary *shandite* phase. This is directly linked to the decomposition of the binary sulfide, TlS, which cannot be detected anymore. By XRD only $Ni_3Tl_2S_2$ as minor phase and $Tl_2S$ as the main phase can be found. When the temperature is increased to 197 °C, already after 0.5 h, $Ni_3Tl_2S_2$ makes up the main part and the amount of $Tl_2S$ shrinks. After a very long reaction time of 15.5 h, the entire TlS (and thus

the $Tl_2S$ intermediate) is transformed to $Ni_3Tl_2S_2$. The broad reflexions of the X-ray powder diffraction patterns indicate the nanoparticular shape of the product.

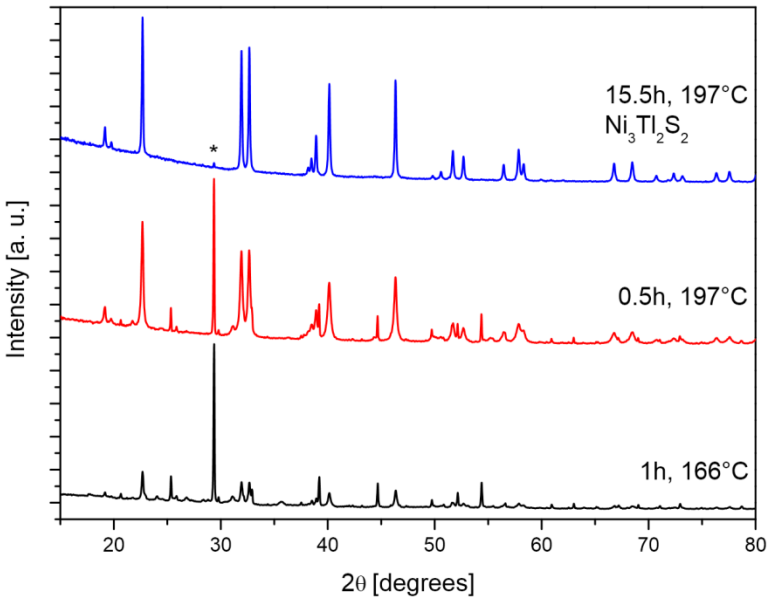


**Figure 17:** Conversion reaction of TlS and $NiCl_2*6H_2O$ to $Ni_3Tl_2S_2$ in basic ethylene glycol after different reaction times and temperatures. A small amount of unreacted $Tl_2S$ is signed with an asterisk.

The SEM pictures, presented in Figure 18, reveal another interesting feature of the particles which were obtained by the modified polyol process. First of all, the particles are much smaller and less agglomerated than their bulk counterpart, $Ni_3Tl_2S_{2,bulk}$ (Figure 18 c and d), as already suggested by XRD. Second the particles seem to coarsely take the shape of stars or flakes. A more precisely determination of the length and width is not possible with the help of these SEM pictures. Nevertheless, this is the first report of a one-dimensional nanostructure of a ternary *shandite*-type phase. The almost single phase sample, shown in Figure 17 (blue colour) showed an increased specific surface area of 4.26 $m^2g^{-1}$ (see also chapter 5.2).

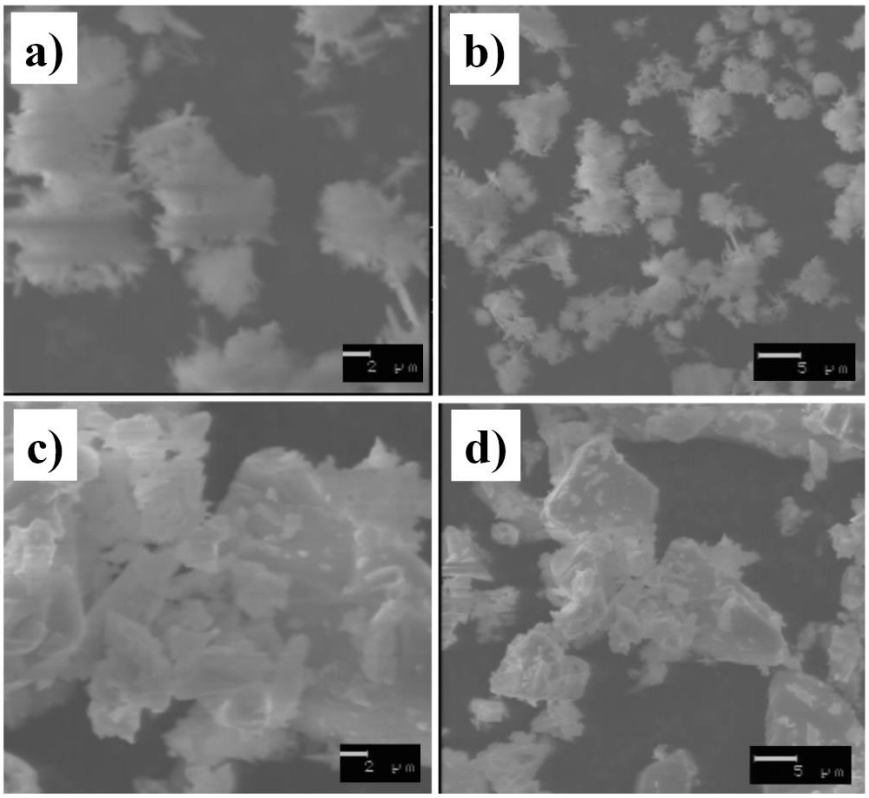


**Figure 18:** SEM pictures of $Ni_3Tl_2S_2$ synthesised by the modified polyol process (a and b) vs. $Ni_3Tl_2S_2$ synthesised by a high-temperature solid-state reaction at a magnification of 2 and 5 µm, respectively.

### 3.4.2. Clarification of the reaction mechanism

Reactions that start with the bulk precursor TlS, lead to smaller particles than expected (see Figure 18 a and b). This speaks for a "decomposition" of the applied $TlS_{bulk}$, which can consequently not act as a morphological template. TlS can be classified as a binary or so called double sulfide, $TlS = Tl_2S_2 = Tl^I[Tl^{III}S_2] = Tl^I{}_2S{*}Tl^{III}{}_2S_3$, as already mentioned. The fact that no TlS is left over as product after short reaction time, suggests that TlS decomposes completely and reacts to $Ni_3Tl_2S_2$ and $Tl_2S$ in a second step. Stoichiometric considerations afford that some $Ni^{2+}$ and $S^{2-}$ is released (eq. (17)). Ethylenediamine is strictly required in that step, as uncomplexed $Ni^{2+}$ would immediately form different nickel sulfides (NiS and $Ni_3S_2$).

$$\frac{1}{2}TI_2S \cdot TI_2S_3 + 3\,[Ni(en)_x]^{2+} \rightarrow \frac{1}{2}Ni_3TI_2S_2 + \frac{1}{2}TI_2S + \frac{1}{2}S^{2-} + \frac{3}{2}[Ni(en)_x]^{2+} \quad \textbf{(17)}$$

It is assumed that the Tl(III) part of $Tl^{III}[Tl^{I}S_2]$ is successively reduced and reacts to the ternary $Ni_3Tl_2S_2$. The Tl(I) part is not able to react directly to $Ni_3Tl_2S_2$, but forms $Tl_2S$. $Tl_2S$ is more sluggish in its reaction. This is a not very surprising result, as it is known that Tl(I) compounds are more stable than Tl(III) compounds and in general very stable in neutral solutions[213, 214]. However, in alkaline solutions Tl(I) ions undertake oxidation into Tl(III). It therefore seems obvious that formally first the binary sulfide TlS is formed again. After dissolution its Tl(III) part again is able to react to $Ni_3Tl_2S_2$ more quick than the Tl(I) part, which forms $Tl_2S$ instead (eq. (18) and (19)).

$$\downarrow \frac{1}{2}TI_2S + \frac{1}{2}S^{2-} \rightarrow \frac{1}{2}TI_2S_2 = \frac{1}{4}\,TI_2S \cdot TI_2S_3 \quad \textbf{(18)}$$

$$\downarrow \frac{1}{4}\,TI_2S \cdot TI_2S_3 + \frac{3}{2}[Ni(en)_x]^{2+} \rightarrow \cdots \quad \textbf{(19)}$$

This reaction pathway could be confirmed by reacting $Tl_2S_{bulk}$ with $NiCl_2$*$6H_2O$ and $Na_2S$ under otherwise optimized conditions, which resulted also in $Ni_3Tl_2S_2$, even if with some unreacted $Tl_2S$. The unreacted $Tl_2S$ which was left over can be ascribed to the decreased reactivity of the applied bulk material. Furthermore, the reaction of $Tl_2S_{bulk}$ with $Na_2S$ under the same conditions reacts to an unidentifiable compound.

### 3.5. Ni-PbSe System

So far, very little is known in the Ni-Pb-Se system. Only one ternary compound, $Ni_3Pb_2Se_2$[215], which is isostructural to $Ni_3Pb_2S_2$ has been reported to date. Hiller[216], and later Clauss and co-workers[217] could show complete miscibility in the $Ni_3Pb_2S_2$–$Ni_3Pb_2Se_2$ solid-solution. Furthermore PbS and PbSe crystallize in the same cubic face-centred space group with $a$ = 5.934 Å and $a$ = 6.128 Å, respectively. This, and the fact that $Ni_3Pb_2Se_2$ can be prepared by PbSe and Ni and also $Ni_3Se_2$ and Pb in solid-state syntheses gave cause for hope

that the conversion reaction of PbSe to $Ni_3Pb_2Se_2$ with $Ni^{2+}$ or other interesting reactions are also possible by the modified polyol process of this work. By taking into consideration the previous knowledge which was gained in the Ni-PbS system, it was expected that the same trends could be also valid for Ni-PbSe.

### 3.5.1. Clarification of the reaction mechanism

In a first approach, the same reaction conditions that led to a complete conversion reaction in the Ni-PbS system were also applied for the Ni-PbSe system. Figure 19 a) and b) shows the applied PbSe before and after the reaction with $Ni^{2+}$ in basic ethylene glycol (NaOH 0.54 g in 70 mL eg) and ethylenediamine (3.6 mL) at 197 °C for 2.5 h (molar ratio Ni:PbSe = 3:2). Unfortunately, just a small amount of the PbSe is converted to the ternary $Ni_3Pb_2Se_2$. Nevertheless, the reactions in the Ni-PbSe system are clearly comparable to that of the Ni-SnS and Ni-PbS system. As only PbSe and $Ni_3Pb_2Se_2$ are apparent in the XRD pattern, the in situ produced nickel (eq. (5)-(6b)) is supposed to incorporate into the PbSe structure under conversion to the ternary $Ni_3Pb_2Se_2$ (eq. (20)).

$$3\ Ni + 2\ PbSe \rightarrow Ni_3Pb_2Se_2 \quad \textbf{(20)}$$

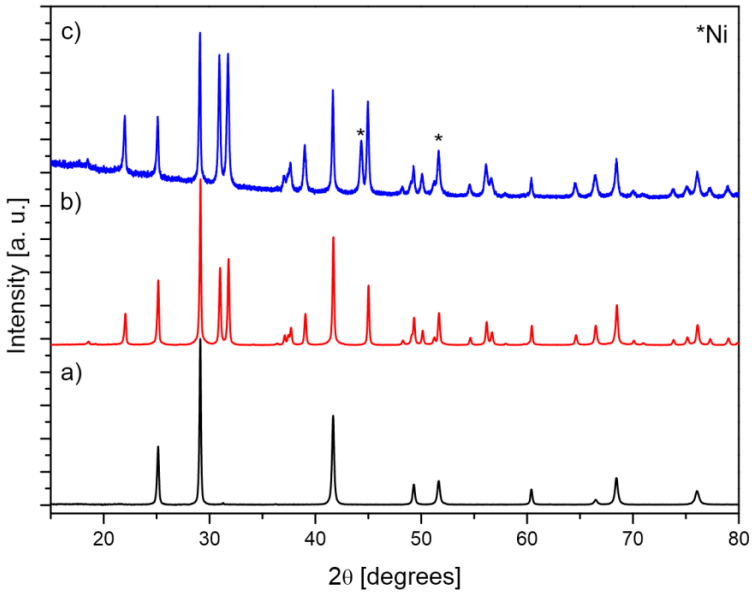


**Figure 19:** a) $PbSe_{bulk}$, which was used during the synthesis b) After reaction with $NiCl_2*6H_2O$ in basic ethylene glycol and en as chelating agent in a stoichiometric ratio of Ni:PbSe = 3:2 c) Stoichiometric ratio of Ni: PbSe = 12:2 under the same conditions.

Different parameters were changed to explore the opportunity to initiate a complete conversion reaction of PbSe to $Ni_3Pb_2Se_2$. Nevertheless, after some unsuccessful trials it turned out that the results could hardly be improved. The quantity of investigated parameters was therefore kept low, and only very general conclusions are driven.

### 3.5.2. Influence of different parameters

*A) Effect of Ni excess*

Nickel excess led to the expected big Ni side phase under all conditions. In contrast to the Ni-PbS system, no other products of a possible co-reduction, or the like appeared. This underlines the great stability of PbSe. Another attempt of explanation makes use of the HSAB ("Hard and Soft Acids and Bases") concept[218], where $Se^{2-}$ is classified as a soft base and $Ni^{2+}$ as a hard acid. This hints on a weak stability of the Ni-Se compounds. In Figure 19 the reaction of $PbSe_{bulk}$ (a) with $NiCl_2*6H_2O$ is shown. Once with equimolar Ni (b) and once with fourfold Ni excess under otherwise same conditions (c). The amount of $Ni_3Pb_2Se_2$ was remarkably increased, when a large Ni excess was used.

*B) Effect of different morphologies of the PbSe template on completeness of the conversion to $Ni_3Pb_2Se_2$*

Four different morphologies of the PbSe samples were used in the synthesis, namely $PbSe_{dendrite}$, $PbSe_{square}$, $PbSe_{nanosphere}$ and $PbSe_{bulk}$. Effectively, no big difference between the different morphologies was noted. Only a slight preference of the dendritic PbSe over the other binary precursors became apparent.

*C) Effect of longer reaction times, higher reaction temperature and higher heating ramp*

The effect of longer reaction time was studied at PbSe square particles with the same amount of ethylenediamine (3.6 mL) and NaOH (0.54 g). An increase of the reaction time from 2.5 h to 16 h slightly raised the amount of the $Ni_3Pb_2Se_2$ phase. The kinetics of this reaction seems to be slower than that of the Ni-PbS system. Even refluxing a Ni+PbSe+$Ni_3Pb_2Se_2$ mixture in dioctyl ether at 350 °C for 12 h could not further increase the amount of $Ni_3Pb_2Se_2$.

The impact of the heating ramp in combination with a high reaction temperature was studied by heating PbSe and $NiCl_2*6H_2O$ (in 70 mL TEG, 3.6 mL en and 0.33 g NaOH), with a very high heating ramp, to a temperature of 260 °C for 2.5 h. The amount of $Ni_3Pb_2Se_2$ decreases dramatically and a bigger Ni side phase can be seen. This supports the theory that a too fast reduction of $Ni^{2+}$ leads to the deposition of nickel on the surface of PbSe and a further conversion is prevented. Longer reaction times might offer the best chance to further increase the yield of the ternary *shandite* phase, as observed for the Co-SnS system[219].

*D) The effect of omitting binary PbSe as starting material*

Subsequently carried out reactions have shown, that the reaction of $NiCl_2*6H_2O$, $Pb(NO_3)_2$ and Se in eg with en (3.6 mL) and NaOH (5.4 g), at 197 °C for 11 h, also ends up in $Ni_3Pb_2Se_2$ and PbSe. Nevertheless, the amount of $Ni_3Pb_2Se_2$ is much less, compared to when PbSe is taken as the starting material. It is assumed that PbSe is first formed in the reaction medium, and then, a certain amount of Ni is able to diffuse into the structure to form the

ternary shandite. The driving force for the formation of PbSe seems to be that strong, that no other binary nickel selenides are formed.

*E) Role of the pH as well as the chelating agent and reductant*

When PbSe is just reacted with $NiCl_2*6H_2O$ in ethylene glycol, without the addition of a reductant and/or reducing agent, no reaction does proceed (see Table 5). Only PbSe can be detected in the XRD pattern. This highlights again the stability of PbSe in eg against the free $Ni^{2+}$ that is not reduced under these conditions (see also chapter III.2.1). When ethylenediamine is used in weak alkaline solution, a certain conversion of PbSe to $Ni_3Pb_2Se_2$ is possible. A stronger basic reaction milieu does not improve the results. The additional reducing agent hydrazine and a fast heating ramp leads to a very fast reduction of $Ni^{2+}$ and no ternary shandite is formed. Again it can be concluded that hybrid particle or even core-shell particles are formed (Ni@PbSe).

**Table 5:** Results of a synthesis at 197 °C, for 11 h with dendritic PbSe and $NiCl_2*6H_2O$ as starting materials. The different parameters pH, chelating agent and reductant were varied.

| NaOH | Ethylenediamine (en) | Hydrazine hydrate (HYD) | Product |
|---|---|---|---|
| / | / | / | PbSe |
| Low (0.1599 g) or high (0.54 g) | X | / | PbSe, $Ni_3Pb_2Se_2$ |
| 0.1599 g | / | 10 mL | PbSe, Ni |

The general trend of less stability of the selenium *shandite*-type compounds appears to end up in a more tough challenge to transform binary PbSe in a conversion reaction. Nevertheless, a considerable big amount of PbSe could be converted into $Ni_3Pb_2Se_2$.

## 3.6. Ni-InSe system

No ternary compounds, other than $Ni_3In_2Se_2$ are known to date in the Ni-In-Se system. Its structure was estimated by Zabel in analogy to isotypic compounds[220] and later on refined from single crystal data by Weihrich and Anusca[221].

In analogy to $Ni_3In_2S_2$ and also the general increased instability of the selenium *shandite*-type compounds, it was already expected that an entire conversion reaction of InSe to $Ni_3In_2Se_2$ could end up in problems. This was confirmed as the preparation of single phase $Ni_3In_2Se_2$ was not possible by the applied polyol method. Other binary phases, other than the *shandite*-type phase seem to be more stable here.

### 3.6.1. Clarification of the reaction mechanism

After reacting $InSe_{bulk}$ with $NiCl_2*6H_2O$ (molar ratio Ni:InSe = 3:2) in basic ethylene glycol (NaOH 0.54 g) and ethylenediamine (5 mL), according to the synthesis protocol, presented in Figure 6 pathway a), $Ni_3In_2Se_2$ is clearly visible (blue line in Figure 20). Nevertheless a big amount of unreacted $InSe_{bulk}$ (green line) and a further unknown compound can be observed. Under Ni excess, almost everything of the starting material InSe is consumed, but still an unknown side phase is present. It is assumed that also here, the mechanism of formation is a unidirectional diffusion of Ni into the binary precursor InSe (eq. (21)). As some side phases are formed, InSe seems to react under these conditions.

$$3\ Ni + 2\ InSe \rightarrow Ni_3In_2Se_2 \qquad \textbf{(21)}$$

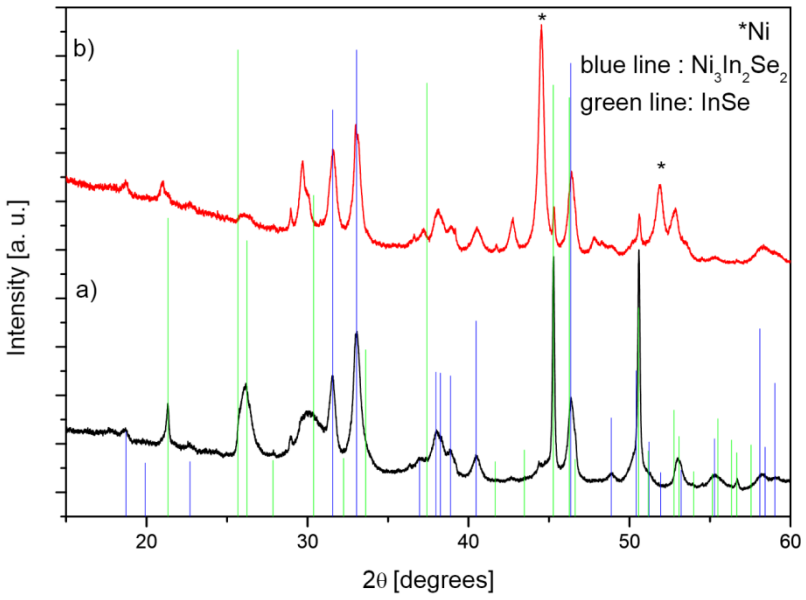


**Figure 20:** a) Reaction of $InSe_{bulk}$ at 197 °C for 10.5 h b) Reaction of $InSe_{bulk}$ at 197 °C for 10.5 h with Ni excess.

### 3.6.2. Influence of different parameters

When $InSe_{bulk}$ was reacted with elemental Ni, only a very small amount of $Ni_3In_2Se_2$ was formed, even at 350 °C. Nevertheless, this approach shows another possible pathway for the formation of the ternary *shandite* phase. Especially the application of nanoparticular Ni seems to be promising.

Bulk $In_2Se_{3,bulk}$ proved not to work as precursor for the transformation to $Ni_3In_2Se_2$. Different nickel selenides and indefinable amounts were observed under all circumstances. The general problem of less stability of the selenium *shandites*, compared to the sulfur counterparts becomes obvious here. This is underlined by the fact that a reaction at 300 °C does not lead to any ternary shandite, but only to an unidentifiable less crystalline mixture of compounds ($InSe_{bulk}$, NaOH 0.54 g, en 5 mL).

## 3.7. Ni-TlSe system

TlSe, just like TlS can be classified as a double selenide, $TlSe = Tl_2Se_2 = Tl^I[Tl^{III}Se_2] = Tl^I_2Se*Tl^{III}_2Se_3$[198]. In principle one would expect that the reaction is quite similar to that of TlS. Surprisingly, the Ni-TlSe system belongs to the ones in which no ternary *shandite* phase is known yet, which is also the case for the Ni-SnSe system. Instead, only the tetragonal $Ni_2TlSe_2$ appears in the phase diagram, so far[222].

### 3.7.1. Conversion reaction of TlSe with $Ni^{2+}$

For a possible diffusion of nickel into TlSe only one polyol reaction was performed. Therefore, TlSe and $NiCl_2*6H_2O$ were reacted according to the general reaction scheme (Figure 6, pathway a; NaOH 0.54 g; en: 5 mL, eg: 80 mL) for a long reaction time of 17 h at 197 °C (molar ratio Ni:TlSe = 3:2).

As for the Ni-TlS system, $Tl_2Se_2$ decomposes completely during the reaction and cannot be observed as side product after the reaction. Additionally, there is no indication for any formed $Ni_2TlSe_2$. The main product most probably consists of the yet unknown $Ni_3Tl_2Se_2$. But clearly $Ni_3Se_2$, $Tl_5Se_3$ and an unknown phase (most likely a nickel or thallium selenide) are seen as side phases. $Ni_3Tl_2Se_2$ can be indexed and refined in the $R\bar{3}m$ space group with

a = 5.5124(2) Å, c = 14.5123(7) Å and V = 381.90(3) Å$^3$. Unfortunately, the results of the Rietveld refinement are less tangible as the corresponding quality factors are very low. Mainly because of the different side phases which cannot be excluded because of overlap (see Figure 67 in the appendix). Therefore, the analogy considerations have to be sufficient.

### 3.7.2. $Ni_3Tl_2Se_2$ and bistability with $Ni_2TlSe_2$

To gain more information about this system, a pure solid-state reaction was also applied. Therefore, TlSe and Ni (molar ratio 2:3) were reacted at different times and temperatures in an evacuated ampoule and quenched to RT. Oddly enough Klepp and Boller[222] were able to synthesise roentgenographic single-phase $Ni_2TlSe_2$ by applying the same starting materials by annealing at 400 or 800 °C. No $Ni_3Tl_2Se_2$ is mentioned in their manuscript. Nevertheless, in our experiments the concurrence between the two ternaries $Ni_3Tl_2Se_2$ and $Ni_2TlSe_2$ can be seen. All samples (reacted at 600 – 900 °C) consisted of $Ni_3Tl_2Se_2$, $Ni_2TlSe_2$, $Tl_5Se_3$ and unreacted Ni. By an increase of the temperature, the amount of the ternary $Ni_3Tl_2Se_2$ rises. Unfortunately, during this work no single phase *shandite* was obtained. If the reaction is kinetically prohibited, a very long reaction time at 900 °C, or higher might be needed. However, in case of thermodynamic instability, i.e. if $Ni_3Tl_2Se_2$ is metastable with respect to decomposition, a different reaction path has to be found to synthesize the product. These questions can be investigated by preliminary ab initio calculations on relative stabilities as developed and applied recently by Bachhuber in our group on pyrite type compounds[9, 223, 224].

## 4. Conversion chemistry of binary sulfides and selenides with $Ni^{2+}$ to hybrid/core-shell particles and transformation to a 'solid-solution' *shandite*-type phase

Diffusion of metals or chalcogenides in semiconductors has been extensively investigated in bulk[78-80] and nanomaterials[78, 225], due to its technological importance for applications in semiconductor integrated circuits, doped materials, catalysts and functional spintronic devices. Nowadays, multifunctional hybrid (nano-)particles, core-shell structures of alloys

and metal-semiconductor devices that combine different properties with tuneable size and morphology generate much interest. The combination of a metal and a semiconductor in the same particle is of particular interest as the metal can provide an anchor point for electrical and chemical connections to the functional semiconductor part[88-90]. Many systems of a noble metal and a semiconductor have been investigated, e.g. Au-PbSe[91], Au-PbTe[89], Ag-PbS[92], Ag-SnS[226] and Au-PbS[102]. These are all systems, where no reaction to ternaries is known and 'just' different diffusion phenomena are taking place. In reaction pairs where solid solutions are possible, it becomes increasingly challenging to selectively direct the reaction towards solid-solutions or other products, like core-shell or hybrid/janus particles. Such a questioning is apparent in the Co-Pt system[95], where it is possible to form "solid solution" type alloys such as $CoPt_3$ nanoparticles, or on the other hand "$Co_{core}$-$Pt_{shell}$" type nanoalloys.

This raised the question to explore the possibility to grow metallic nickel domains on top of selected semiconductors (PbS, PbSe, SnS), which are in principle able to form the ternary *shandite* phase under certain conditions. Moreover, the driving forces for the formation of the *shandite* phase or for the formation of the competing hybrid phases (Ni@PbS, Ni@PbSe, Ni@SnS) should be evaluated.

Pathway a) of the applied synthesis protocol (see chapter III. 3.), aimed at the formation of the ternary *shandite*-type solid solutions. Depending on the applied binary precursor, this led to either a complete conversion to the ternary *shandite* phase, or just a part of the binary reacted in a conversion reaction, and unreacted binary with elemental Ni was left over. In contrast in pathway b), where ethylenediamine was replaced by hydrazine hydrate as additional strong reducing agent, the results changed dramatically. A summary of the realized experiments is presented in Table 6.

**Table 6:** Results of a synthesis with Hydrazine (10 mL), NaOH (0.54 g), $NiCl_2*6H_2O$ in 70 mL ethylene glycol at different temperatures and times. The ratio of $Ni^{2+}$ to *M-X* was 3:2.

| Precursor | Result of polyol-synthesis | Result after annealing |
|---|---|---|
| $PbS_{dendrite}$ | 197 °C, 2.5 h:<br>PbS, $Ni_3Pb_2S_2$, Pb, Ni | / |
| $PbS_{dendrite}$ | 70 °C, 10 h:<br>PbS, Ni, $Ni_3Pb_2S_2$ (main product) | 500 °C, 7 d:<br>$Ni_3Pb_2S_2$ (100%) |
| $PbS_{octahedron}$ | 70 °C, 10 h:<br>PbS, Ni, $Ni_3Pb_2S_2$ (very low) | 1st approach: 500 °C, 7 d<br>$Ni_3Pb_2S_2$ (100%)<br>2nd approach: 300 °C, 7 d<br>$Ni_3Pb_2S_2$ (83.4%), PbS(10%), Ni (6.5%)<br>2nd annealing does not change anything (w/o grinding)<br>After grinding: $Ni_3Pb_2S_2$ (100%) |
| $PbS_{bulk}$ | 70 °C, 10 h:<br>PbS, Ni, $Ni_3Pb_2S_2$ (very low) | 1st approach: 500 °C, 7 d:<br>$Ni_3Pb_2S_2$ (100%)<br>2nd approach: 300 °C, 7 d<br>$Ni_3Pb_2S_2$ (84%), PbS(5%), Ni (11%)<br>2nd annealing does not change anything (w/o grinding)<br>After grinding: $Ni_3Pb_2S_2$ (100%) |
| $PbSe_{cube}$ | 70 °C or 197 °C, 10 h:<br>PbSe, Ni | 500 °C, 7 d:<br>$Ni_3Pb_2Se_2$ (100%) |
| -"- | -"- | 300 °C, 7 d:<br>$Ni_3Pb_2Se_2$ (47%), PbSe (30%), Ni (23%)<br>2nd annealing does not change anything (w/o grinding)<br>After grinding: $Ni_3Pb_2Se_2$ (100%) |
| $SnS_{spherical}/SnS_{bulk}$ | 70 °C, 12 h:<br>Ni, SnS, $Ni_3Sn_2S_2$ (very low) | 500-700 °C, 7 d:<br>$Ni_3Sn_2S_2$<br>Small side phase of $Ni_3S_2$ and $Ni_{1.523}Sn$ |
| $SnS_{spherical}$ | 197 °C, 5.5 h<br>$Ni_3Sn_2S_2$ (67%), $Ni_3S_2$ (28%), Ni (5%) | / |

## Ni-PbS

Starting with the results of the Ni-PbS system, it becomes obvious that in contrast to the report of Wang et al.[29], in our approaches no phase pure synthesis of $Ni_3Pb_2S_2$ was possible when hydrazine was applied as reducing agent. The reductive potential of hydrazine is that stong, that even PbS can be reduced to elemental Pb at high temperatures (Table 6). Additionally, crystalline Ni is always apparent in the XRD. Longer reaction times do not increase the amount of $Ni_3Pb_2S_2$, which hints on very slow diffusion of nickel into the lattice of PbS.

A reaction temperatur of 60 °C was not enough to reduce $Ni^{2+}$ and only PbS could be verified by powder diffraction. A further increase in reaction temperature to 70 °C led to completely

different results, depending on the morphology of the applied PbS. For $PbS_{bulk}$ and $PbS_{octahedron}$ the reaction ends up with elemental Ni and PbS and only a very small amout of $Ni_3Pb_2S_2$ is detected. This is in contrast to dendritic $PbS_{dendrite}$ where the main phase is already the ternary *shandite* phase. This is the lowest temperature for the formation of a shandite phase, which has ever been reported. These results suggest that the dendritic morphology catalyses the conversion of PbS to $Ni_3Pb_2S_2$ to a certain kind. Thus, it is in principle possible to selectively direct the reaction towars the ternary solid-solution or the hybrid particles by an adequate choice of the morphology, reducing agent and temperature.

The washed and dried hybrid particles (PbS + Ni mixtures) can be converted to $Ni_3Pb_2S_2$ by annealing at 500 °C. Interestingly, when the annealing temperature was lowered to 300 °C, after one week, there was still unreacted PbS and Ni left over. A second annealing at the same temperature, without grinding in advance, did not improve the results. After the sample had been crushed, the reaction to the *shandite* phase was possible (Figure 21). Differences in the diffusion rate of PbS and Ni across the interface between the two materials possibly led to the formation of voids by the so-called Kirkendall effect[184]. The diffusion of Ni into PbS might be prevented by these voids. Theoretically possible is also that the formed $Ni_3Pb_2S_2$ acts like a kind of blocking layer, through which no further diffusion of PbS or Ni is possible.

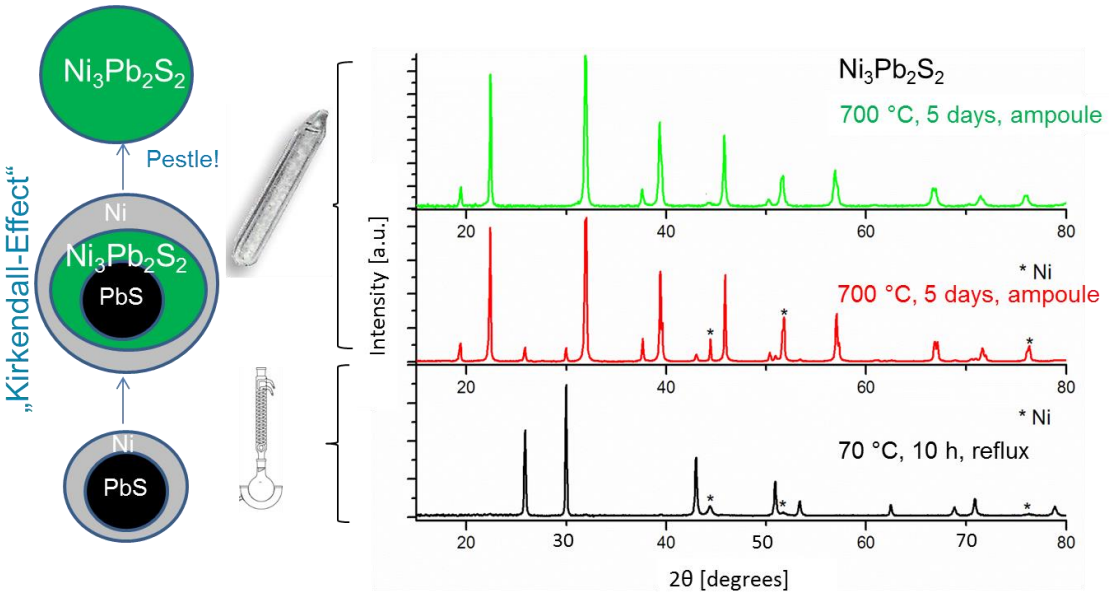


**Figure 21:** Bottom: Result of $PbS_{bulk}$ and $Ni^{2+}$ at 70 °C with hydrazine as reducing agent. Hybrid particles, consisting of PbS and Ni are formed Middle: After annealing at 300 ° for 7 d. Most of the hybrid particles are converted to the ternary *shandite*-type phase. Top: After grinding and annealing at 300 °C. Everything is converted to the ternary *shandite*-type phase.

The characteristic of the obtained Ni@PbS particles was further characterized by SEM measurements and magnetic separation. The magnetic separation experiments revealed that at least hybrid particles (or even core-shell particles) were obtained, as the entire powder reacts magnetic. Moreover, the nickel distribution seems to be quite homogeneous as 500 °C are already enough to entirely convert the Ni@PbS particles to $Ni_3Pb_2S_2$. As at this temperature neither PbS, nor Ni are molten, the diffusion length seems to be short enough to be overcome by solid state diffusion. The corresponding SEM pictures of the obtained particles are presented in Figure 22 (and Figure 68 in the appendix).

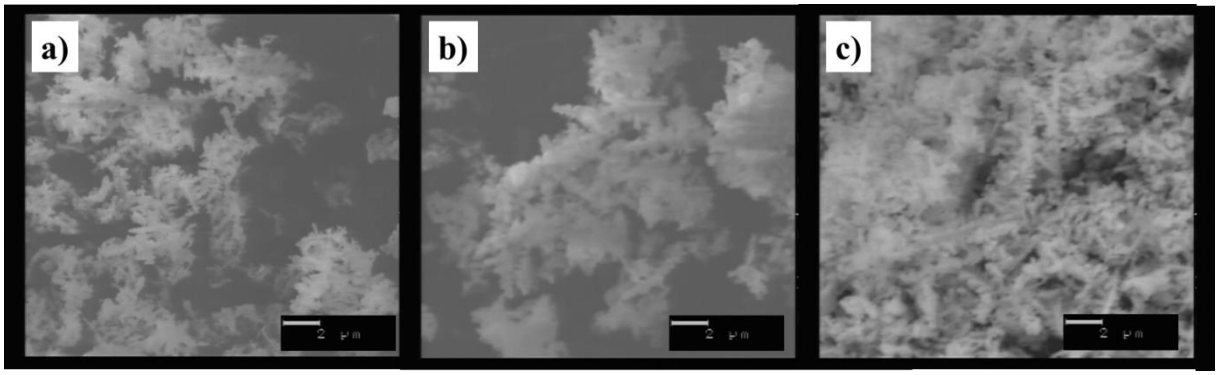


**Figure 22:** a) $PbS_{dendrite}$ b) $Ni@PbS_{dendrite}$ c) $Ni_3Pb_2S_2$ after annealing of $Ni@PbS_{dendrite}$ at 500 °C for 7 d. Resolution 2µm.

If we compare the starting dendritic $PbS_{dendrite}$ with the nickel coated Ni@PbS particles a significant loss of morphology is observed. The surface of the Ni@PbS particles becomes very uneven; dendrites can hardly be observed anymore at this stage. After annealing, the shape seems to be recovered to a certain kind and despite the high calcination temperature of 500 °C the agglomeration is still low. These results hint on a second way for the fabrication of morphology controlled *shandite*-type particles. The main adjusting screws which have to be improved hereby are the homogeneous nucleation of Ni on the PbS particles and the calcination temperature.

**Ni-PbSe and Ni-SnS**

In the Ni-PbSe and Ni-SnS system, basically the same results as for Ni-PbS were obtained. Whereas in the Ni-SnS system, $SnS_{spherical}$ and $SnS_{bulk}$ were applied, in the Ni-PbSe system only cubic $PbSe_{cube}$ was used. The outstanding effect of the dendritic $PbS_{dendrite}$ is underlined, as none of the binary PbSe or SnS precursors catalyses the low-temperature reaction to the ternary *shandite*. Only traces of the corresponding *shandite* phase are observed after the reaction at 70 °C in the polyol medium. The reduction of $Ni^{2+}$ seems to be too fast to form $Ni_3Pb_2Se_2$ or $Ni_3Sn_2S_2$ under these conditions, so that elemental Ni is formed on PbSe and SnS (appendix, Figure 69, marked with an asterisk). No consecutive reactions are observed in solution, especially SnS does not dissolve. The washed and dried products react to $Ni_3Pb_2Se_2$ or $Ni_3Sn_2S_2$ by either annealing at 500 °C or by annealing two times at 300 °C with an intermediate grinding for $Ni_3Pb_2Se_2$. For $Ni_3Sn_2S_2$ always some minor side phases of $Ni_3S_2$ and $Ni_{1.523}Sn$ appear after annealing at 500–700 °C.

The characteristic of the Ni@PbSe and Ni@SnS was also examined by magnetic separation and revealed an all-magnetic powder. But SEM pictures for the reaction $PbSe_{cube} \rightarrow Ni@PbSe \rightarrow Ni_3Pb_2Se_2$, presented in Figure 23, suggest that Ni is not really homogeneously covering the PbSe particles. Instead, the cubes seem to be unregularly plated by Ni ‘drops’. These findings are supported by a great variety in the intensity of the EDX spectra and the backscattered electrons picture. In this case the cubic shape of the particles seems to get completely lost after annealing at 500 °C.

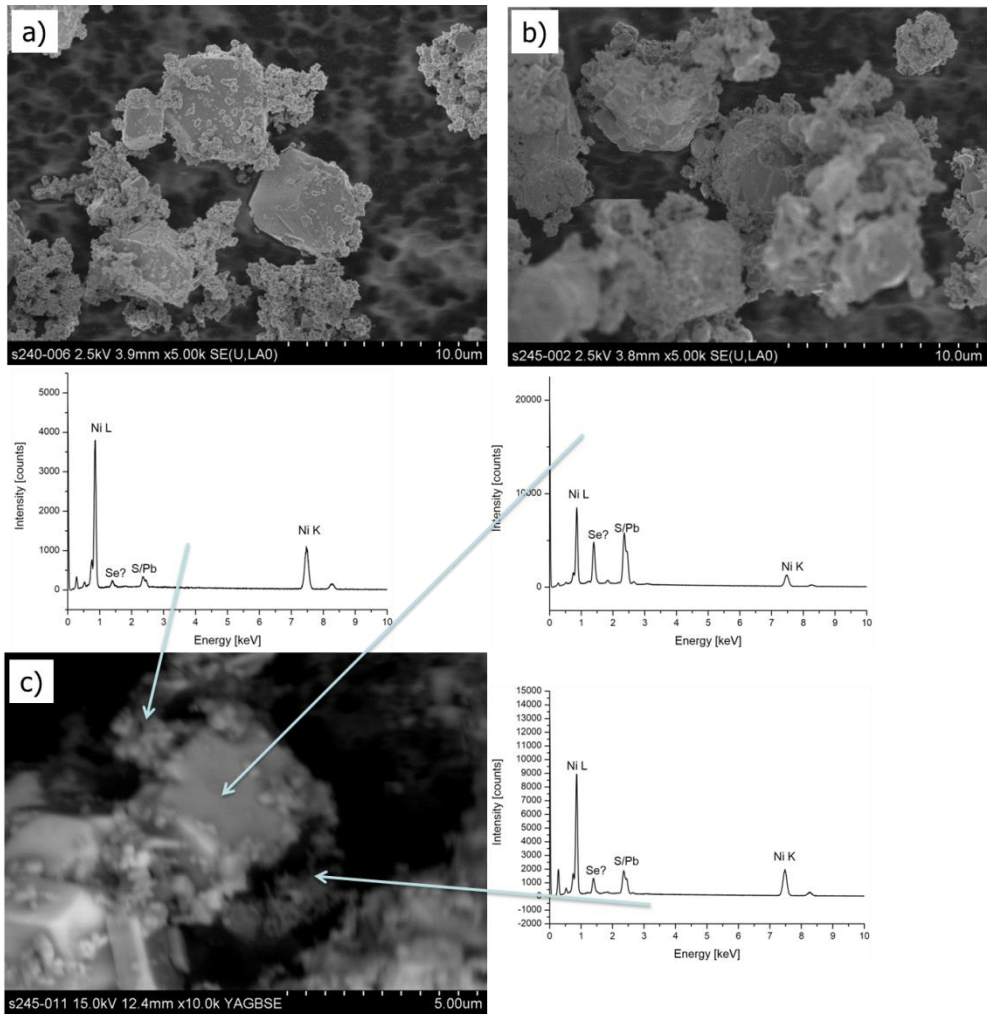


**Figure 23:** a) Ni@$PbSe_{cube}$ b) $Ni_3Pb_2Se_2$ after annealing of Ni@$PbSe_{cube}$ at 500 °C for 7 d. c) Picture with a backscattered electrons detector and corresponding EDX spectra.

In sum, it can be said that after rapid reduction of $Ni^{2+}$ with hydrazine at 70 °C, Ni is not able to diffuse into the binary precursors, but core-shell or hybrid particles are formed. However, they can be converted to the corresponding ternary by solid-state reactions at $T \geq 300$ °C. The discussed method leads to ways to obtain related compounds and functionalized materials.

## 5. Further characterizations on selected samples and reaction systems

### 5.1. Purity of the samples after washing and effect of particle size on IR spectra

The efficiency of the cleaning process could be proven by investigating selected samples in the middle IR range (Figure 24). The series of the $Ni_3Pb_2S_2$ samples, shown in Figure 11 were evaluated and compared to a typical bulk sample of $Ni_3Pb_2S_2$ (Figure 24 a). No characteristic bands for solid-state vibrations or a possible organic molecule appear in any sample. This shows that washing with $H_2O$ and EtOH is suitable for a complete removal of absorbed organic species from the synthesized particles. The applied EtOH evaporates completely afterwards by drying at 80 °C in a drying cabinet. If we compare the bulk vs. the nanoparticular samples, a rising trend of higher absorbance can be seen. This can be attributed to the higher specific surface area of the smaller particles. Starting from the smallest dendritic PbS, particle size is rising towards higher reaction times and temperatures, as more Ni is inserted into the template. This trend is clearly reflected by the infrared measurements.

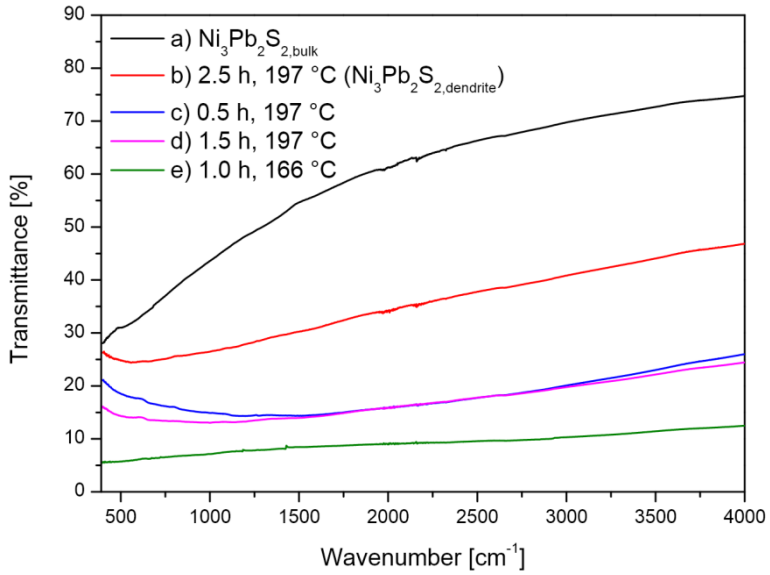


**Figure 24:** Exemplary FTIR spectra of some samples after washing with $H_2O$ and EtOH. a) Reference bulk sample of $Ni_3Pb_2S_2$ b) dendritic $Ni_3Pb_2S_2$ c-e) mixtures of $PbS_{dendrite}$ and $Ni_3Pb_2S_2$ of not completed conversion reactions.

## 5.2. Specific surface area and optical properties of bulk vs. nanoparticles

The colouring and specific surface area of selected samples of $Ni_3Pb_2S_2$ and $Ni_3Tl_2S_2$ were determined visually and by nitrogen sorption, respectively (Figure 25, left side). A comparison between the reference, $Ni_3Pb_2S_{2,bulk}$, and dendritic $Ni_3Pb_2S_{2,dendrite}$ leads to a more than 20 times larger specific surface area, accompanied by a change of colour from pale grey to black. The $Ni_3Tl_2S_2$ sample exhibits a more than 13 times higher specific surface area than the bulk reference. This trend is supported by the corresponding XRD patterns (Figure 25, right side) showing a significantly broader peak shape for the nanoparticles, compared to the bulk samples.

The effects of an increased specific surface area and a colour change can be explained by taking the much smaller particle size of the dendritic $Ni_3Pb_2S_{2,dendrite}$ and the small $Ni_3Tl_2S_2$ particles into consideration. In general, the specific surface area is increased as the particle size becomes small or the material is porous[227]. In our case as the particles are not porous the increased specific surface area is due to the increased surface to volume ratio of the nanoparticles. This higher surface area is very favourable for possible applications of ternary *shandites* in catalytic processes like hydrodesulfurization (HDS)[228] as the available reaction sites of the materials are increased. As $Ni_3Pb_2S_2$ and $Ni_3Tl_2S_2$ exhibit metallic character, the colour change of grey to black can only be attributed to the smaller particle sizes. The known effect of an increased band gap between the valence and the conduction bands with decreasing particle size[229] is only valid for semiconductors where a blue shift of the absorption spectrum can be observed.

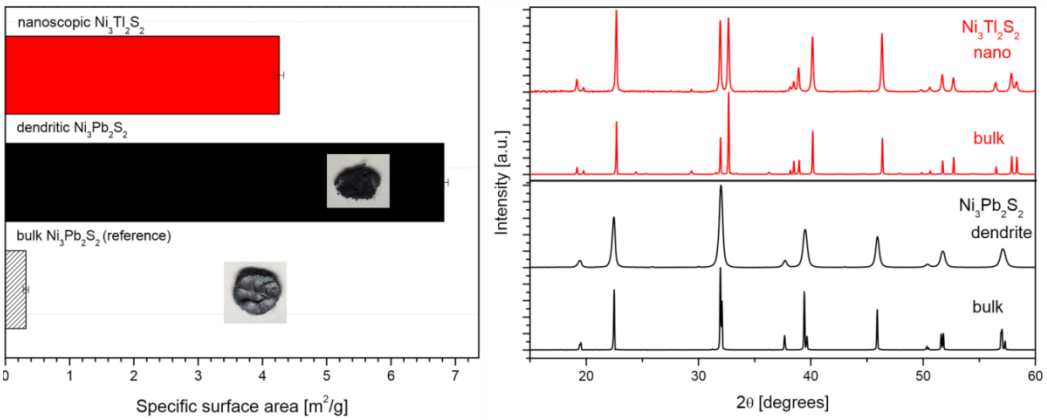


**Figure 25:** Left side: Specific surface area and colouring of bulk $Ni_3Pb_2S_{2,bulk}$ as reference vs. dendritic $Ni_3Pb_2S_{2,dendrite}$ and the small $Ni_3Tl_2S_2$ particles. Right side: XRD powder patterns of dendritic $Ni_3Pb_2S_2$ and nanoscopic $Ni_3Tl_2S_2$ vs. their bulk counter parts.

## 5.3. Temperature-dependent structural and mechanical properties of *shandite*-type compounds with different morphology

### 5.3.1. Effect of sintering on cell parameters and size and strain of dendritic $Ni_3Pb_2S_{2,dendrite}$

To study the changes in microstructure during the early stage of sintering of dendritic $Ni_3Pb_2S_2$ nanoparticles, the powder was annealed at temperatures between 200 – 700 °C in an evacuated ampoule. The temperature was hold for 3 h with a heating and cooling rate of 5 C°/min. The rhombohedral unit cell with space group $R\bar{3}m$ of the *shandite*-type compounds[220] can be verified to every time (Figure 26). Figure 26 b) shows an enlarged section of the XRD powder diffraction patterns between 55 and 60 °C. Higher temperatures cause a systematic sharpening of the Bragg reflections due to an increase of the crystallite size and to an increased degree of crystallization. Furthermore, the peak positions are gradually shifted towards lower 2θ values because of deviations in the crystal lattice after the annealing procedure.

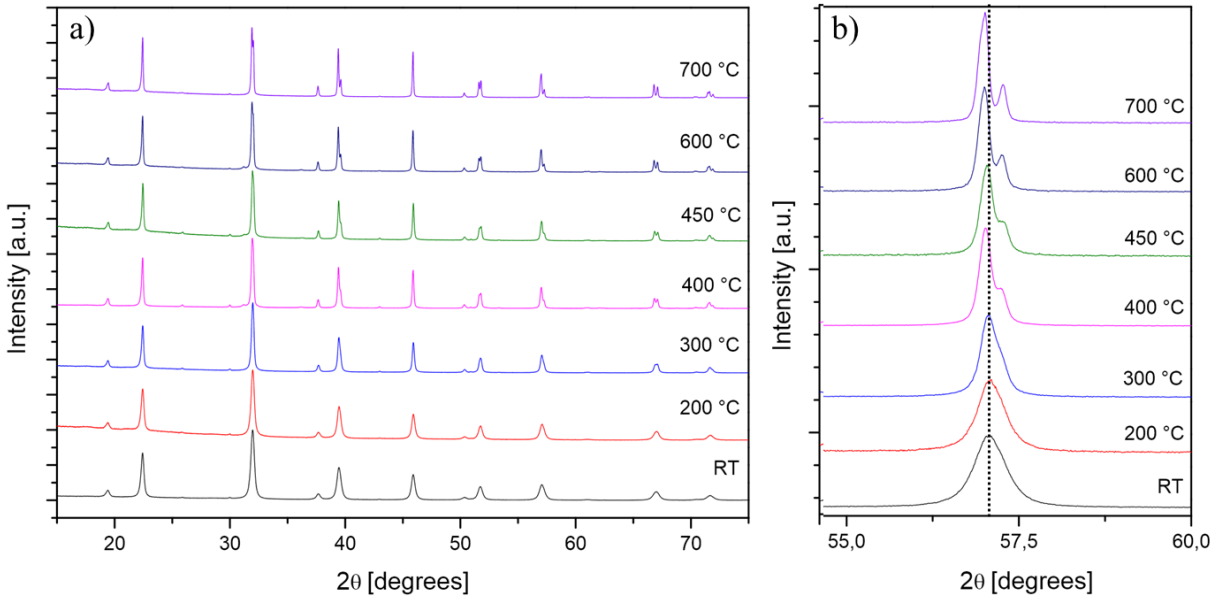


**Figure 26:** a) XRD of $Ni_3Pb_2S_{2,dendrite}$ after annealing at 200 – 700 °C for 3 h b) Enlarged section of the XRD patterns between 55 and 60 °. The dotted line serves as a guide for the eye.

The cell parameters of the $Ni_3Pb_2S_2$ sample were evaluated by Rietveld refinement with the program Fullprof[133] (Figure 27 a). Between 25 – 300 °C, the *a*-axis and the volume slightly decrease, whereas an increase of the *c*-axis from 13.6061(3) to 13.6141(3) Å is indicated. This

seems to be the best way to decrease the strain in a first step (Figure 27 b). It is known for many materials, that strain release is in advance and then grain growth follows[230]. In the temperature range between 300 – 700 °C, the *a*-axis and volume slightly increase from 5.5802(7) to 5.5897(5) Å and 367.126(9) to 368.295(7) $Å^3$, respectively. The *c*-axis almost stays constant. If one compares the cell parameters at RT with the reference of Zabel[220] (red dotted line in Figure 27 a), one can see that the cell parameters of the dendritic nanoparticle are clearly smaller. A rising convergence is obtained after annealing at high temperatures. This means that the cell parameters are growing with a higher degree of crystallinity and larger particle size. These results are in concert with the literature[231, 232]. It has often been reported that the unit cell parameters of nanoparticles are usually lower than that of the bulk and that the particle shape can have a big effect on total lattice variation.

An estimation of the crystallite sizes was done with the algorithm of Scherrer[172] and Wilson[136] and with the Williamson-Hall plot[137], implemented in the software package WinXPOW[131]. The calculated size and strain parameters of the different methods are depicted in Figure 27 b. As expected, the crystallite size was found to increase with sintering temperature, according to both methods. For the strain, the opposite effect can be observed. This contrary trend of size and strain parameters is well known for nanoparticles and has also been reported for related *perovskite*-type powders[233]. Sintering processes generally decrease lattice defects and strain, but usually also cause the coalescence of smaller grains, resulting in an increased average grain size for the nanoparticles[234]. The significant differing results in particle size between the Scherrer and Williamson-Hall method are due to the presence of strain, which also contributes to the broadening of the peaks[235]. This is not considered in the Scherrer method. Therefore, the Scherrer equation leads to an underestimation of the size of the crystallite.

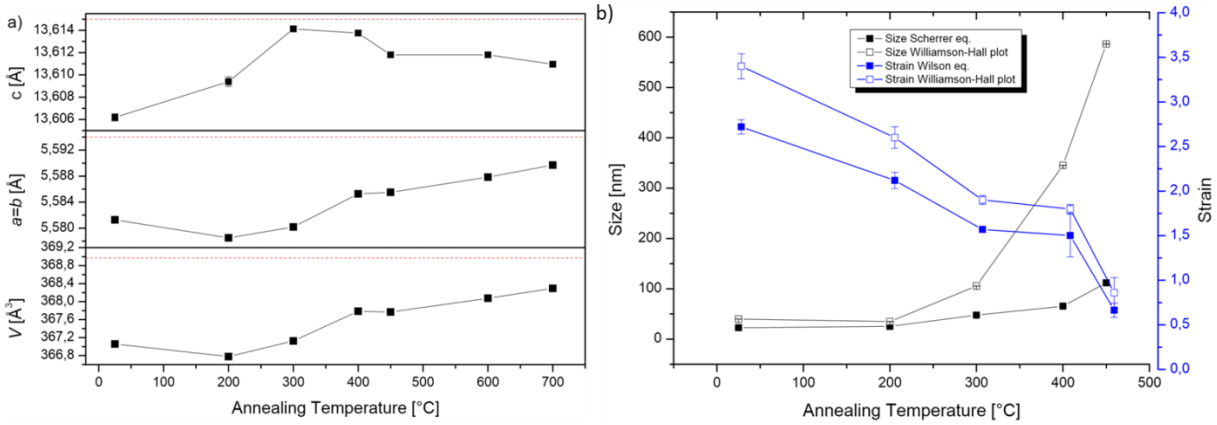


**Figure 27:** a) Cell parameter vs. annealing temperature of dendritic $Ni_3Pb_2S_2$ at 25 – 700 °C. The red dotted line marks the reference cell parameter (Zabel[220]). b) Size and strain vs. annealing temperature of dendritic $Ni_3Pb_2S_2$, calculated with the Scherrer and Wilson equation or Williamson-Hall plot at 25 – 450 °C. At temperatures above 450 °C the calculated values for size and strain did exceed the validity range of the Scherrer equation and are therefore not included. All peaks were used for the calculations.

The broadening of the peaks due to strain increases at higher 2θ values. If the strain is not considered, the calculated crystallite size therefore decreases. At high angles, the calculated crystallite size can be over 62% smaller (see Table 7).

**Table 7:** Calculated particle size for dendritic $Ni_3Pb_2S$ (not sintered), for different 2θ values.

| (h,k,l) | 2θ | L=(Kλ)/βcos(θ) |
|---|---|---|
| (003) | 19.393 | 40.23 |
| (012) | 22.411 | 50.55 |
| (110) | 31.967 | 37.57 |
| (021) | 37.670 | 36.72 |
| (202) | 39.468 | 30.38 |
| (024) | 45.904 | 33.96 |
| (205) | 50.358 | 21.18 |
| (116) | 51.723 | 25.52 |
| (214) | 57.078 | 22.35 |
| (027) | 61.008 | 19.21 |
| (220) | 66.980 | 19.73 |
| (131) | 70.554 | 19.26 |
| (036) | 71.671 | 18.90 |
| (134) | 76.204 | 20.68 |
| (226) | 80.677 | 17.61 |
| (404) | 85.045 | 15.35 |

### 5.3.2. Low-temperature structural properties of *shandite*-type compounds with different morphology evaluated by in situ XRD

To determine the stability and temperature-dependent structural properties of selected $Ni_3Pb_2S_2$ and $Ni_3Tl_2S_2$ samples with different morphologies, LT-XRD spectra were recorded from RT to 12 K under high vacuum. Therefore, the ground samples were enclosed in an alumina foil and transferred to the vacuum chamber of the XRD device. The samples were allowed to get into the steady-state for 30 min before each measurement was started.

The corresponding XRD patterns for $Ni_3Pb_2S_2$ (octahedra: Figure 71, dendrite: Figure 72, bulk: Figure 73) and $Ni_3Tl_2S_2$ (bulk: Figure 74, nano: Figure 75) are attached in the appendix. It can be seen that, although it is commonly expected that the structure and stability of finite-size particles may differ from those of the bulk system[236, 237], the crystalline structure of all nanoparticles remains in $R\bar{3}m$ symmetry and all samples are stable over the whole evaluated temperature range.

Figure 28 and Figure 29 show the temperature dependence of the cell parameters, the unit cell volume as well as the $c/a$ ratio for the $Ni_3Pb_2S_2$ and $Ni_3Tl_2S_2$ samples with different morphologies. The depicted values are based on a model in which peak shape asymmetry was not refined; this gives the most accurate cell dimensions possible in the absence of an internal standard.

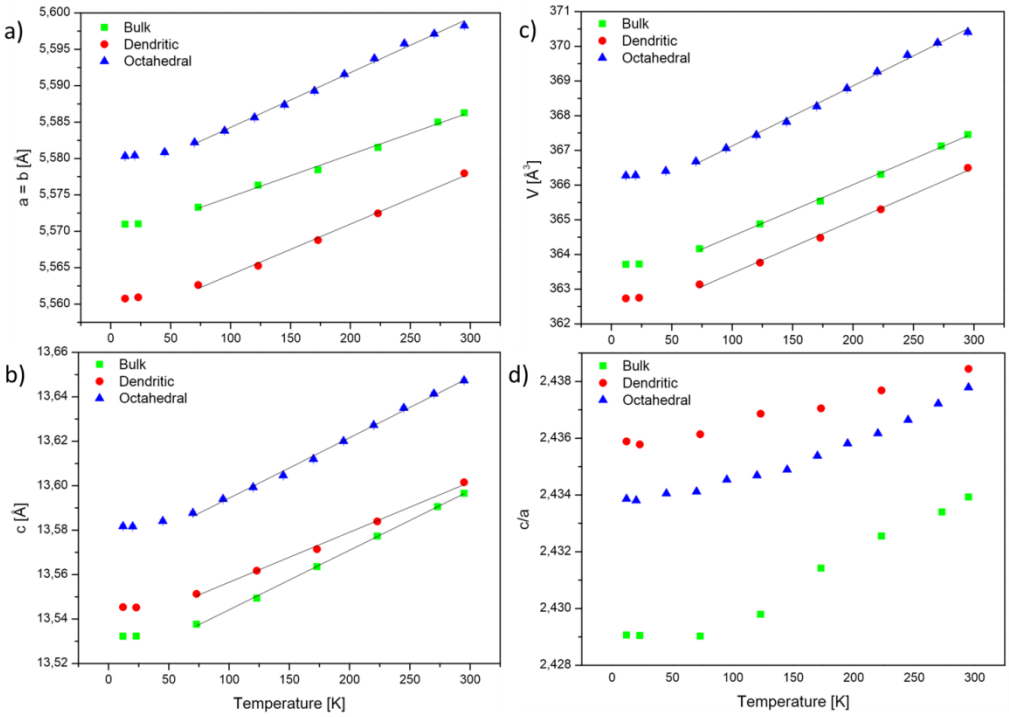


**Figure 28:** Temperature-dependence of a) the *a*-axis b) the *c*-axis c) the unit cell volume, and d) the *c*/*a* ratio of the different $Ni_3Pb_2S_2$ morphologies.

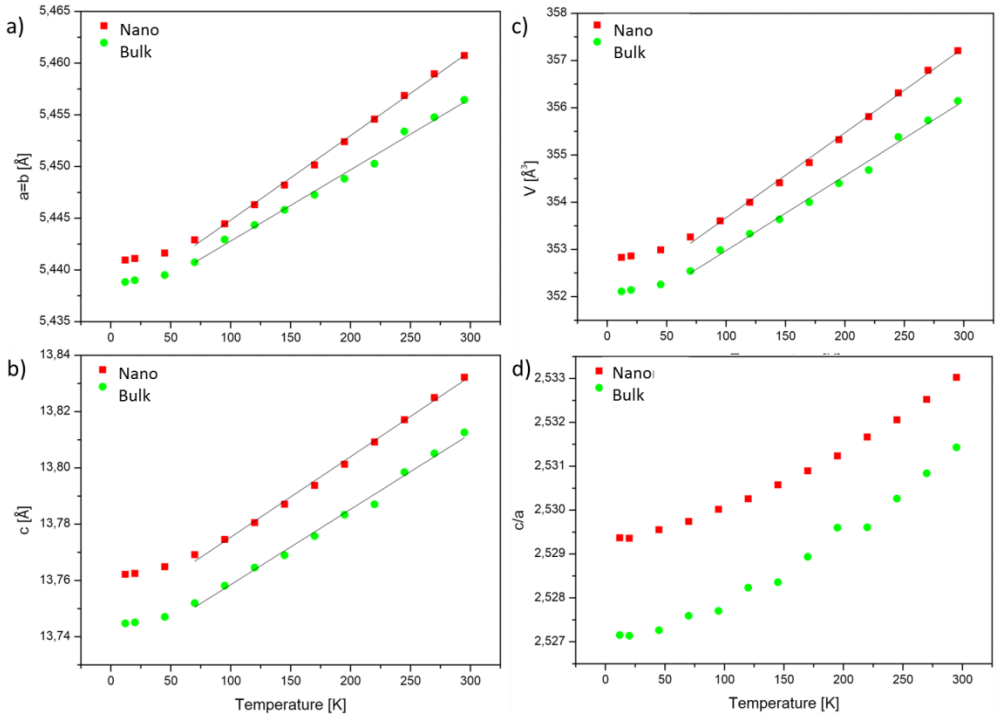


**Figure 29:** Temperature-dependence of a) the *a*-axis b) the *c*-axis c) the unit cell volume d) the *c*/*a* ratio of the different $Ni_3Tl_2S_2$ morphologies.

Following conclusions can be drawn:

- An essential linear expansion of all evaluated parameters with the temperature is observed. This is common to most of the materials as the average amplitude of the atoms' vibrating within the material increases. This, in turn, increases the separation between the atoms causing the material to expand. As the material does not go through a phase change, the expansion can be easily related to the temperature change.
- A small levelling of the curves is seen between 12 – 50 K. This might hint on a maximum contraction which can be reached by "freezing" the atomic motion. A further contraction is not possible without a phase transformation.
- The *c*/*a* ratio increases linearly with temperature
- Besides the linear contraction, which is present in all samples, there are two main differences:
    - The slope of the linear fit of the cell parameters
    - The starting values for the cell parameters of the samples at room temperature

Beginning with the latter one, one can see that at room temperature all cell axes of the octahedral $Ni_3Pb_2S_2$ are bigger than that of the dendritic and the bulk sample (Figure 28 and Table 8). The bulk sample takes a middle position for the *a*-parameter and the volume, but exhibits the lowest *c*-axis. However, the *a*-axis of the dendritic sample is so small, that the lowest volume is obtained. Therefore the observed sequence of the *c*/*a* ratio is dendritic > octahedral > bulk.

For $Ni_3Tl_2S_2$ the cell parameters of the nanoparticles are considerable larger than that of the bulk phase (Figure 29 and Table 8). This leads to an increased volume and *c*/*a* ratio of the nanoparticles. The *c*/*a* ratio concerns interlayer spacing (1/3 $c_{hex}$) of the Ni Kagomé nets[147]. This means in practical terms, that the spacing becomes bigger with smaller particle size for $Ni_3Pb_2S_2$ and $Ni_3Tl_2S_2$.

The thermal expansion, observed, is one of the most basic properties of a material and occurs in almost every system[238, 239]. It is connected not only with basic properties, like for example the temperature-dependent variation of the energy band gap, but also influences the thermal properties (thermal conductivity, specific heat). This behaviour can be understood by accounting for the effects of the anharmonic lattice potential on the equilibrium lattice separations and can be given a numerical value by the ***thermal coefficient of expansion***

***(TCE)***. For crystals with a noncubic symmetry, as seen for the *shandite*- and *parkerite*-type phases, the thermal expansion is generally anisotropic, due to the anisotropic nature of the crystal bonding. Hence it is of interest from a physical point of view to investigate anisotropic thermal expansion of these compounds[240, 241]. The TCE describes the change of the length or volume (volume expansivity) in percent per kelvin. The knowledge of such values may be useful for material design purpose to determine if failure by thermal stress may occur[230, 242].

As already mentioned, the cell constants and the volume of all evaluated samples change linearly with the temperature between 70 – 295 K. A small levelling of the curves is seen between 10 – 50 K. Expansion coefficients are therefore quoted from linear regression of the 70 (=$T_2$) to 295 K (=$T_1$) data points (see Table 8). The mean or average thermal expansion coefficient (TEC)[242, 243] is defined by:

$$\alpha_{\perp,\parallel} = \frac{1}{L_0}\frac{\Delta L}{\Delta T} = \frac{1}{L_0}\frac{L(T_2)-L(T_1)}{T_2-T_1} \quad \textbf{(22)}$$

*L* hereby corresponds to the respective *a*- or *c*-axis, or to the volume, when the volume expansivity is calculated. Suffixes ⊥ and ∥ denote the directions perpendicular and parallel to the *c*-axis. In a perfect linear dependence of the cell parameters, $\frac{\Delta L}{\Delta T}$ is similar to the slope *m* of the connecting line between L($T_2$) and L($T_1$). To proof the accuracy of the linearity, the slope *m* derived from the origin fit was inserted into the equation.

$$\alpha' = \frac{1}{L_0}\,\mathrm{m} \quad \textbf{(23)}$$

For the temperature-dependent volume expansion (volume expansivity), basically the same equations are valid.

$$\beta = \frac{1}{V_0}\frac{\Delta V}{\Delta T} \quad \textbf{(24)}$$

$$\text{and } \beta' = \frac{1}{V_0}m \quad \textbf{(25)}$$

**Table 8:** The lattice parameters and their ratios at 295 K for bulk, dendritic and octahedral $Ni_3Pb_2S_2$ and bulk and nano $Ni_3Tl_2S_2$. The mean thermal expansion values $\alpha_\perp$ and $\alpha_\parallel$ between 290 – 73 K, calculated with dL/dT. $\alpha'_\perp$ and $\alpha'_\parallel$, calculated with the slope *m* of the origin-fits. The mean volume expansivity $\beta$ was calculated by dV/dT and for $\beta'$ the slope *m* of the origin-fits was applied.

| | $Ni_3Pb_2S_{2,bulk}$ | $Ni_3Pb_2S_{2,dendrite}$ | $Ni_3Pb_2S_{2,octahedron}$ | $Ni_3Tl_2S_{2,bulk}$ | $Ni_3Tl_2S_{2,nano}$ |
|---|---|---|---|---|---|
| $a_{\_295\,K}$ (Å) | 5.5852(2) | 5.5779(2) | 5.5982(2) | 5.4564(2) | 5.4607(2) |
| $c_{\_295\,K}$ (Å) | 13.5941(3) | 13.6015(7) | 13.6473(7) | 13.8126(3) | 13.8321(5) |
| $c/a_{\_295\,K}$ | 2.4339 | 2.4384 | 2.4378 | 2.5314 | 2.5330 |
| $\alpha_\perp$ ($K^{-1}$) | $9.8260*10^{-6}$ | $1.2381*10^{-5}$ | $1.2749*10^{-5}$ | $1.2794*10^{-5}$ | $1.4510*10^{-5}$ |
| $\alpha_\parallel$ ($K^{-1}$) | $1.9061*10^{-5}$ | $1.6629*10^{-5}$ | $1.9419*10^{-5}$ | $1.9514*10^{-5}$ | $2.0250*10^{-5}$ |
| $\alpha'_\perp$ ($K^{-1}$) | $1.0396*10^{-5}$ | $1.2486*10^{-5}$ | $1.3431*10^{-5}$ | $1.2623*10^{-5}$ | $1.4960*10^{-5}$ |
| $\alpha'_\parallel$ ($K^{-1}$) | $1.9718*10^{-5}$ | $1.6564*10^{-5}$ | $1.9940*10^{-5}$ | $1.9374*10^{-5}$ | $2.0677*10^{-5}$ |
| $\beta$ ($K^{-1}$) | $3.8608*10^{-5}$ | $4.1272*10^{-5}$ | $4.4767*10^{-5}$ | $4.4951*10^{-5}$ | $4.9084*10^{-5}$ |
| $\beta'$ ($K^{-1}$) | $4.0386*10^{-5}$ | $4.1447*10^{-5}$ | $4.6705*10^{-5}$ | $4.4505*10^{-5}$ | $5.0419*10^{-5}$ |

From Figure 28, Figure 29 and Table 8 it can be seen that the cell axes and the total cell volume are getting bigger with the temperature - thus a positive thermal expansion is obtained for all samples. A comparison of the $\alpha$ and $\alpha'$ values reveals that an adequate linearity is given as the results just differ on the second decimal place. Furthermore it becomes obvious that the volume expansivity $\beta$ of the nanoparticular samples is significant larger than that of the bulk particles for $Ni_3Pb_2S_2$ and $Ni_3Tl_2S_2$. The enhanced TEC of nanocrystalline materials is usually attributed to the increased grain-boundary component in the nanostructures. Lu and Sui[244] for example noticed that the linear TEC increases markedly with a reduction of the average grain size in porosity-free nanocrystalline Ni–P samples. Lu and co-workers[245] furthermore observed an enhancement of the volume TEC of nanocrystalline hexagonal selenium with a reduction of the grain size. Their results suggest larger displacements of the atoms from their ideal lattice locations and more defects in the nc-Se samples with its smaller grains which effects the TEC.

This in accordance for nanocrystalline $Ni_3Tl_2S_2$, where both, $\alpha_\perp$ and $\alpha_\parallel$ are considerably larger than for its bulk counterpart. The anisotropy of the *shandite* phases can be seen in the different behaviour of the TECs. The ratio of $\frac{\alpha_\parallel}{\alpha_\perp}$ is 152.52% for the bulk and 139.56% for the nanoscopic sample, respectively. This leads to a bigger shrinkage of the *c*/*a* ratio at lower temperatures for the bulk phase.

The results are more complicated to interpret within the $Ni_3Pb_2S_2$ system. As expected, $\alpha_\perp$ of the bulk phase takes up the lowest rank. But for $\alpha_\parallel$ the very low value of the dendritic sample is striking. A possible explanation is that the dendrites mainly grow along the *a*- and *b*-axis, so that the enlargement of the *c*-axis has a lower effect on the whole crystal, compared to the bulk and octahedral samples, where the orientation is more randomly. These effects are also expressed in the ratio of $\alpha_\parallel / \alpha_\perp$ where the order is bulk (189.6%) > octahedron (148.47%) > dendrite(132.66%). The high values of $\alpha_\perp$ and $\alpha_\parallel$ for $Ni_3Pb_2S_{2,octahedron}$ in comparison to $Ni_3Pb_2S_{2,dendrite}$ can most likely also be attributed to the intrinsic properties of the well-defined dendrites vs. an unregular morphology in $Ni_3Pb_2S_{2,octahedron}$.

### 5.3.3. Hysteresis effect of the lattice parameters during in situ XRD

A possible hysteresis effect of the lattice parameters during the in situ XRD measurements was examined for bulk and dendritic $Ni_3Pb_2S_2$ samples. The point symbols are kept small, so that the error bars are visible in the pictures. From the cell parameters, depicted in Figure 30, one can see that there is a very small hysteresis, the most pronounced in the *a*-axis. At room temperature the structure relaxes again to its original state. This makes clear that the deviation is right in detection range. Similar results were observed for all ternary *shandite* and *parkerite* samples. Such low hysteresis effects are not uncommon in many materials, as the structure needs time to rearrange and to relax. Possibly, a longer stabilization period at the respective temperature would already cure this phenomenon.

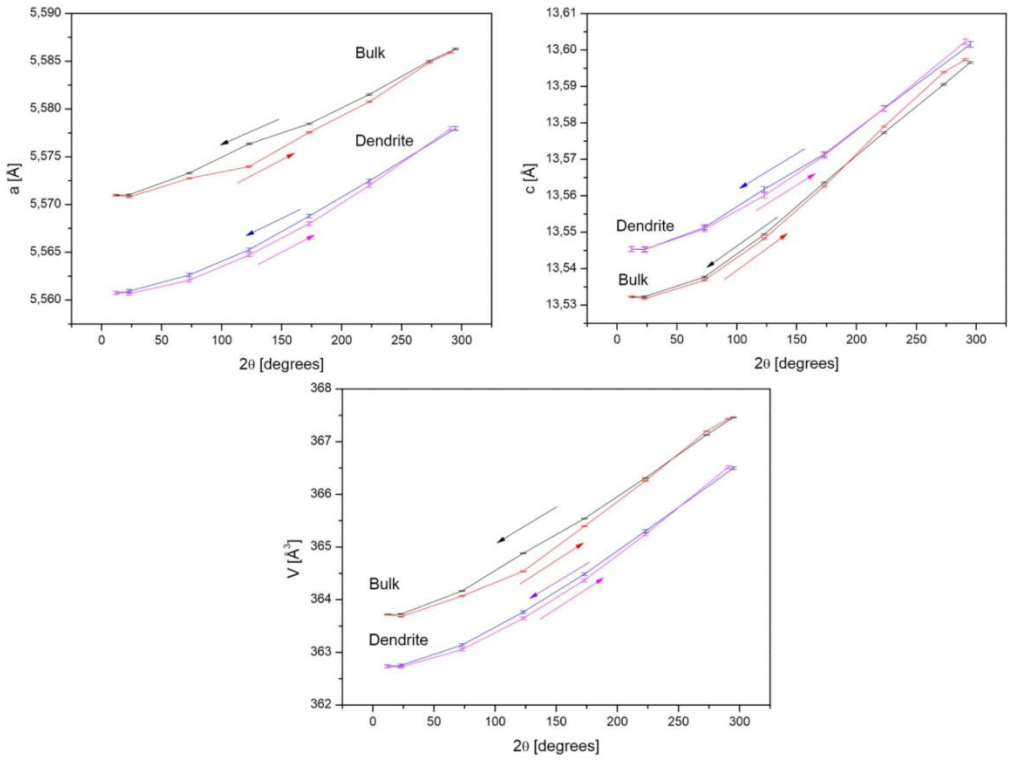


**Figure 30:** Cooling and defrosting curves of the lattice parameter of dendritic and bulk $Ni_3Pb_2S_2$. Directions are included by arrows.

## 5.4. Evaluation of the solid-state reaction paths of different binaries with Ni by in situ HT-XRD

Knowledge about the reactions which take place in pure diffusion controlled syntheses, thus in syntheses which proceed at high temperatures and mainly in closed, evacuated reaction vessels, are still very rare. Often, only empirical data is available about reaction paths and the corresponding end products. Regarding the *shandite* family, it is known that different element combinations are possible as starting materials in the solid-state synthesis[32, 170, 216, 220, 246]. For example $Ni_3Pb_2S_2$ can be synthesized from the elements, but also from binary PbS and $Ni_3S_2$.

a) 3 Ni + 2 Pb +2 S → $Ni_3Pb_2S_2$

b) 3 Ni + 2 PbS → $Ni_3Pb_2S_2$

c) $Ni_3S_2$ + 2 Pb → $Ni_3Pb_2S_2$

In this part of this work, the selected systems Ni-PbS, Ni-PbSe and Ni-SnS are more precisely investigated in terms of solid-state reaction paths. The task of this chapter is to show the "pure" diffusion controlled solid-state reactions between the selected binaries and the metal Ni under elevated temperatures. The mechanisms of the reaction between PbS/PbSe/SnS and $NiCl_2*6H_2O$ in ethylene glycol already proved to be a simple diffusion of the in situ produced Ni into the lattices of PbS/PbSe/SnS. As this behaviour is strongly suggestive of a typical solid-state diffusion process, although it proceeds in solution, these systems were believed to serve as good starting points to show the selective formation of the desired products by a diffusion based process. Furthermore PbS/PbSe/SnS are known as very stable materials which are not supposed to decompose under the applied temperatures. Pathway a) is avoided as it is assumed that the reaction of elemental sulphur in piths may cause problems and also will take much time to proceed. Furthermore pathway c) is avoided as elemental Pb and Sn are known to behave as X-ray absorber and fluorescent element, respectively.

**Ni-PbS system**

Reacting Ni, Pb and S at 500 °C for 1 week resulted in mainly the desired $Ni_3Pb_2S_2$ phase after quenching, besides elemental Ni and Pb, as well as PbS and $Ni_3S_2$ as side phases. In contrast to that, starting from the elements and using 700 °C for one week produced single-phase $Ni_3Pb_2S_2$ after quenching. Therefore, it is concluded that this reaction is a complex interplay between different reactions. Probably in a first step the different sulfides are formed and these react further in a second step.

If the reaction is started with the pairs PbS/Ni or $Ni_3S_2$/Pb it should in principle be possible to follow one defined diffusion process in specific temperature ranges. In some pre-experiments it was shown, that PbS and Ni can already be entirely converted to the *shandite* phase by annealing at 500 °C for 1 week and quenching. At 300 °C unreacted PbS and Ni is left over. A temperature range between 300 – 500 °C was therefore considered appropriate. In the study Ni and PbS (molar ratio 3:2) were placed in a fuzed capillary and subjected to in situ HT-XRD measurements. At the bottom of Figure 31, the starting materials Ni and PbS are shown at RT. By increasing the reaction time and temperature, $Ni_3Pb_2S_2$ is gradually formed (marked with yellow). During the whole reaction no other phases emerge. This proofs that the net reaction is a diffusion of Ni into PbS in this temperature range. It is assumed that the starting

materials can be totally converted into the ternary phase at this temperature with a respective prolonged reaction time.

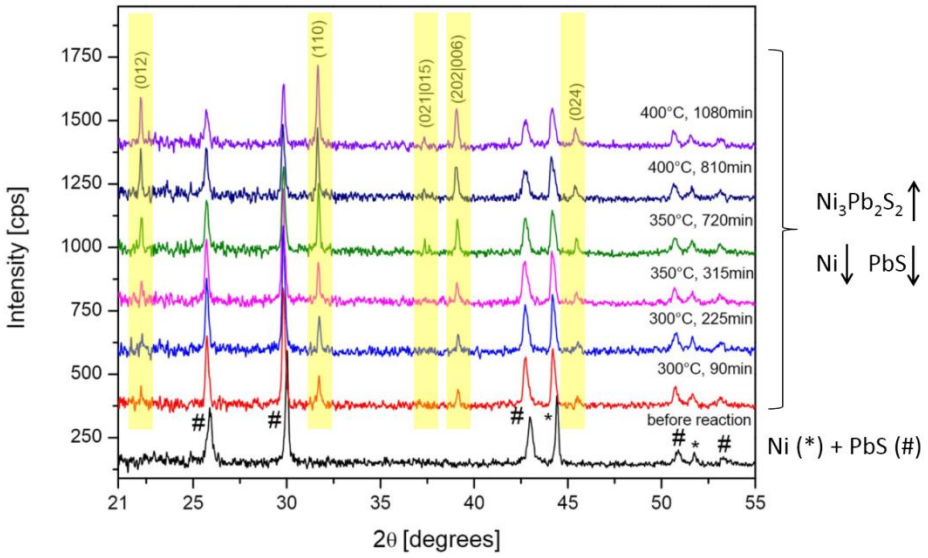


**Figure 31:** In-situ XRD of 3 Ni + 2 PbS in an evacuated pith. At the bottom the starting materials Ni and PbS before the reaction are depicted. After increasing the temperature and the reaction time, the $Ni_3Pb_2S_2$ phase becomes present and starts to rise (marked with yellow) under consumption of Ni and PbS.

To quantitatively monitor the crystallization process of the reaction, the integrated intensities of the present phases were evaluated. The integrated peak areas confirm the proposed mechanism of formation, as Ni and PbS are decreasing with a simultaneous increase of $Ni_3Pb_2S_2$ (Figure 32). It is noteworthy to mention that the same trends are also visible in the unintegrated intensities. In general, a linear trend is observed for all isothermal sections (300 °C, 350 °C, 400 °C), owing to a constant diffusion at similar temperature. The slope rises at higher temperatures but seems to be nearly the same for 350 - 400 °C. This accounts for higher diffusion at higher temperatures, which is a typical effect, observed in diffusion controlled processes. Unfortunately, the nature of the performed experiment fails to show the complete conversion reaction as the reaction time was too short.

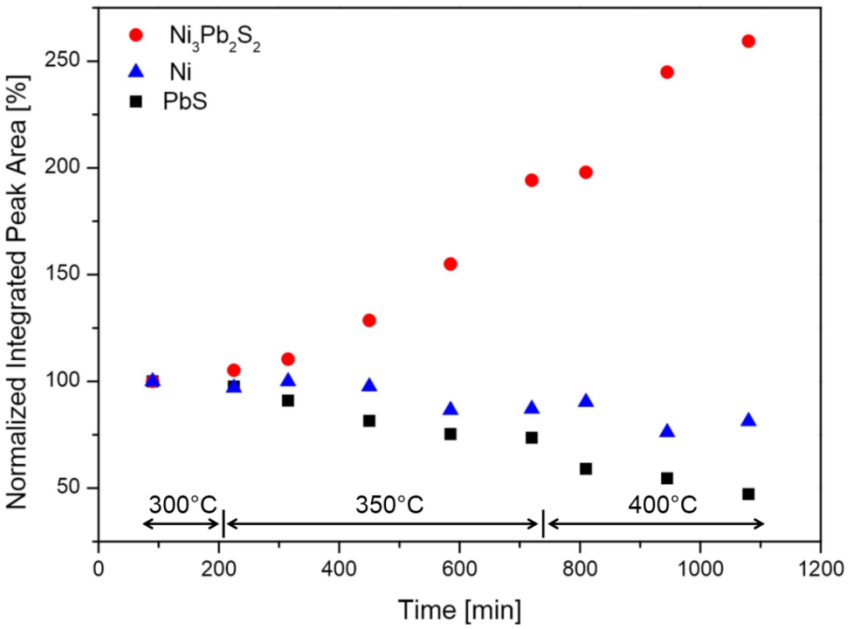


**Figure 32:** Normalized integrated intensities of the Ni, PbS and $Ni_3Pb_2S_2$ phases vs. time and temperature. For Ni, PbS and $Ni_3Pb_2Se_2$ the miller indices (111), (200) and (110) were used, respectively.

To clarify the stability range of $Ni_3Pb_2S_2$ and to detect possible other reaction products, which take place in the Ni + PbS system, additional non-isothermal in situ XRD measurements at higher temperatures (50 – 850 °C) were taken into consideration. The XRD data, presented in Figure 33, suggests that at temperatures between 300 and 400 °C only the formation of $Ni_3Pb_2S_2$ (marked with yellow) under consumption of PbS (blue) and Ni (green) occurs, as already shown before. At temperatures above 400 °C the appearance of $Ni_3S_2$ (red) can be observed, accompanied by a further shrinkage of PbS and Ni. These results may be a hint on the formation of $Ni_3Pb_2S_2$ by diffusion of Ni in PbS, which competes with the emergence of $Ni_3S_2$ and liquid Pb (not visible in the XRD above the melting point of lead). At very high temperature (>800 °C) all formed phases are melted with the exception of PbS (mp.: 1114 °C) and Ni (mp.: 1445 °C[247]). Additional peaks which are not colour-coded originate from the applied quartz glass ampoule that seems to crystallize or even gets porous at this high temperature. When the reaction is stopped at 850 °C and cooled to RT elemental Pb, besides PbS, Ni and $Ni_3Pb_2S_2$ crystallizes out again.

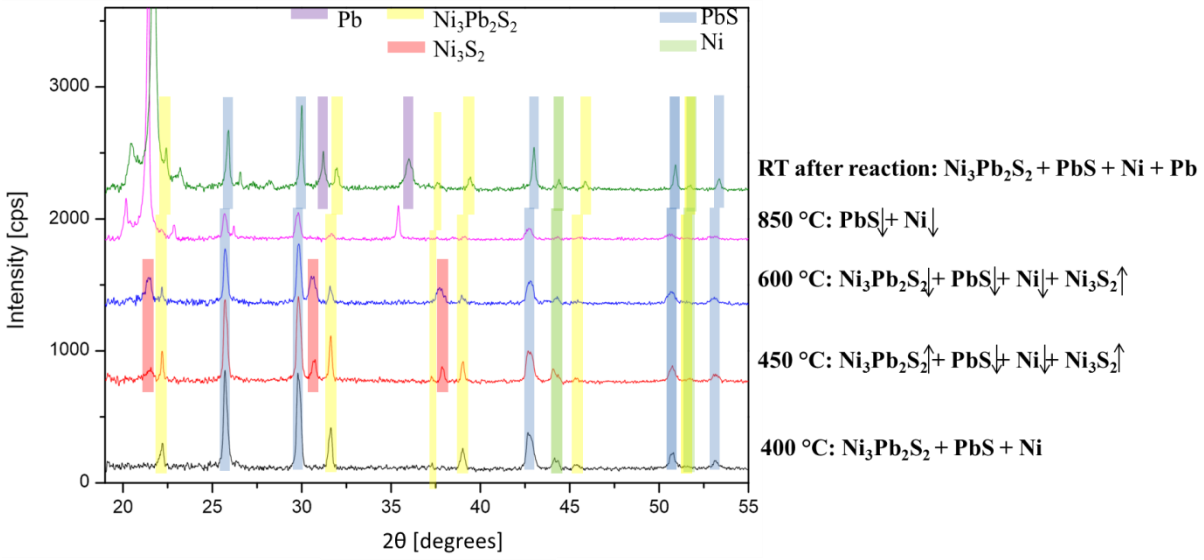


**Figure 33:** In situ XRD of a 3 Ni + 2 PbS mixture at different temperatures. Unmarked phases are due to the experimental setup. At temperatures above 800 °C it is assumed that the quartz glass crystallizes or gets porous.

The results can be better interpreted by taking the DTA measurement of a $Ni_3Pb_2S_2$ bulk sample into account (Figure 34). A weak endothermic peak is indicated at 411 °C. This can possibly be attributed to the decomposition of $Ni_3Pb_2S_2$ into $Ni_3S_2$ and Pb, as suggested by the in situ XRD. As the measurement stops at 400 °C a possible recrystallization peak cannot be detected in Figure 34. In the further course two bigger endothermic peaks at 757.33 and 785.15 °C can be observed. The latter one is very close to the given melting points of $Ni_3S_2$ (790 °C[248, 249]) and $Ni_3Pb_2S_2$ (≈750 °C[216], 792 °C[250]). If we assume that the melting point of $Ni_3S_2$ could be determined in adequate manner (as $Ni_3S_2$ can be used as a single compound), the peak around 757.33 °C should most likely correspond to the melting point of $Ni_3Pb_2S_2$. The big exothermic peak can be ascribed to the formation/recrystallization of $Ni_3Pb_2S_2$. The results of the in situ powder diffraction and the DTA measurement are in accordance with the results of Zabel[171] who reported elemental lead as side phase, after quenching the reacted samples at 900 °C. In contrast, when he slowly cooled down the sample from 900 °C to 600 °C and then quenched, no lead was detectable. Our results confirm these findings with the exception that temperatures up to 700 °C are valuable. This speaks for a competitive situation between $Ni_3Pb_2S_2$ and $Ni_3S_2$+Pb at temperatures below the melting points of $Ni_3Pb_2S_2$ and $Ni_3S_2$. Nevertheless, a certain kind of pre-orientation between $Ni_3S_2$ and Pb hast to be already apparent, as quenching leads to the demanded $Ni_3Pb_2S_2$. Quenching from temperatures above the melting points of $Ni_3Pb_2S_2$ and $Ni_3S_2$, mainly leads to the stable PbS and Ni and only little $Ni_3Pb_2S_2$ is formed. Some Pb probably is left over as it often forms

small lead rolls which are not able to react fast enough when the sample is quenched to room temperature.

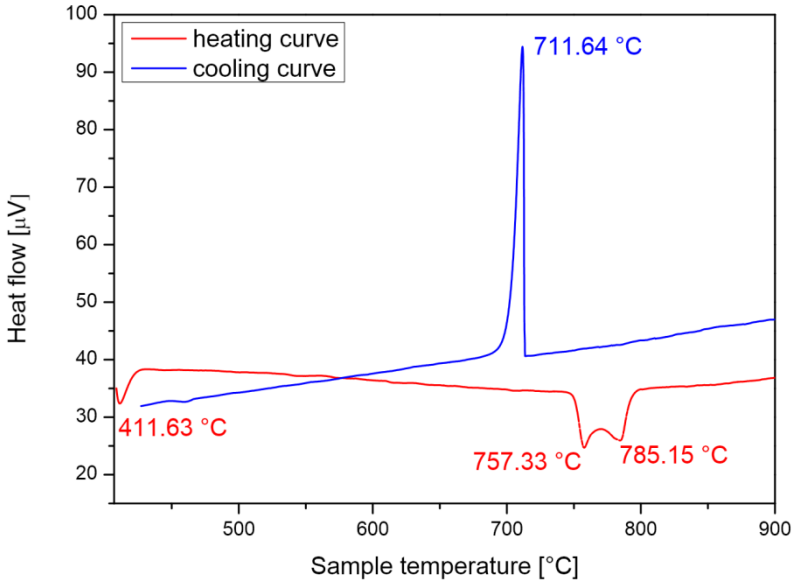


**Figure 34:** DTA curves of a $Ni_3Pb_2S_2$ bulk sample.

These findings are furthermore in accordance with Zargarova et al. who report on a complex chemical interaction of PbS and Ni with the formation of $Ni_3Pb_2S_2$ according to a peritectic reaction[251]. Mariolacos and co-workers observed a new ternary phase, named SHN ($Pb_9Ni_{60}S_{31}$) - an intermediate between *shandite*, *heazlewoodite*, and Ni at ≥554°; the SHN decomposes at 605-615 °C[252]. This phase was later on re-described as $Ni_{151.5}$ $Pb_{24}S_{92}$ by Baranov[183]. Such (intermediate-)compounds, reported by Mariolacos and Baranov could not be detected during the reactions.

**Ni-PbSe system**

For the Ni-PbSe pair basically the same results as for Ni-PbS were expected, because of the great similarity between PbS and PbSe with regard to their stability and reactivity. Reacting Ni and PbSe and also elemental Ni, Pb and Se at 500 - 700 °C for one week, followed by quenching, resulted in single phase $Ni_3Pb_2Se_2$. Nevertheless, it has to be mentioned that very short ampoules/piths had to be applied, as otherwise PbSe was transported and precipitated at the colder end.

Selected patterns of the in situ HT-XRD measurement of the reaction between PbSe and Ni at 400 – 500 °C can be seen in Figure 35. As expected, 400 °C are readily enough to form $Ni_3Pb_2Se_2$ which is highlighted in yellow. No other intermediate phases can be observed. The normalized integrated peak area proves that $Ni_3Pb_2Se_2$ is progressively formed under the consumption of PbSe. The shrinkage of the Ni part could not be evaluated because of an overlap of the peaks. During the long isothermal measurement at 400 °C, a constant diffusion reaction is observed, indicated by the same slope of the curves. Obviously, raising the temperature to 500 °C increases the velocity of the reaction. Nevertheless, a complete conversion to $Ni_3Pb_2Se_2$ is still not reached after 2301 min.

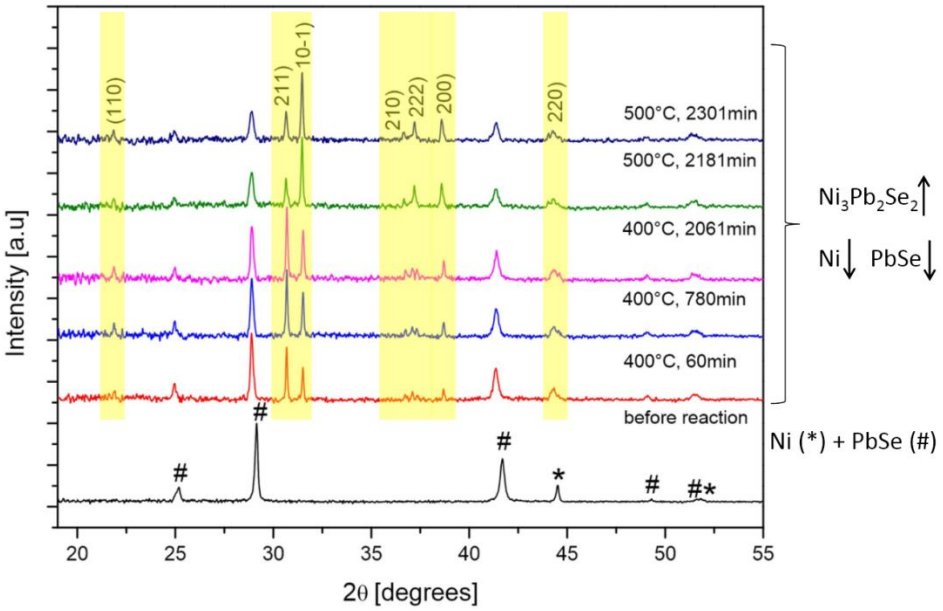


**Figure 35:** In situ XRD of 3 Ni + 2 PbSe in an evacuated pith. At the bottom the starting materials Ni and PbSe are visible. After increasing the temperature and reaction time the $Ni_3Pb_2Se_2$ phase becomes present and starts to rise (marked with yellow), accompanied by the decrease of the Ni and PbSe fraction.

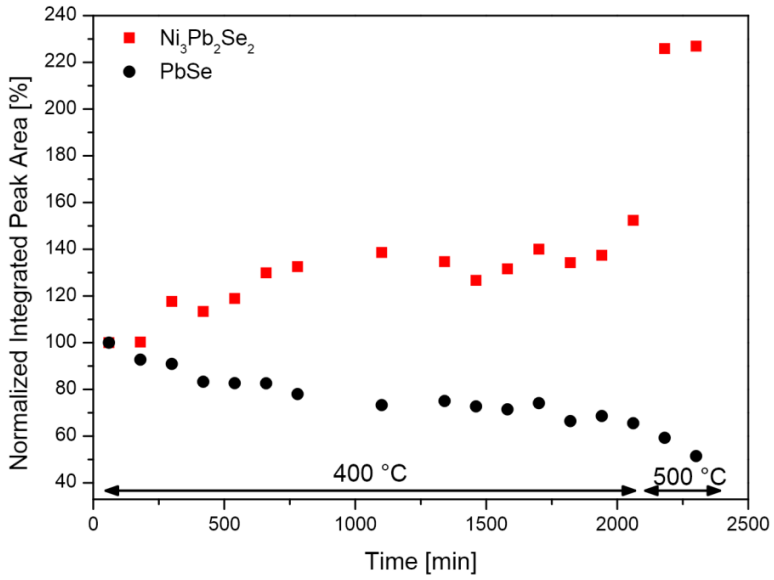


**Figure 36:** Normalized integrated intensities of the PbSe and $Ni_3Pb_2Se_2$ phases vs. time and temperature. For PbSe and $Ni_3Pb_2Se_2$ the miller indices (200) and (211) were used, respectively. Ni could not be evaluated because of overlap.

### Ni-SnS system

The reactions in the Ni-SnS system seem to be more complex than in the Ni-PbS and Ni-PbSe system. Often $Ni_3Sn_2S_2$ samples were poisoned with $Ni_{1.523}Sn$[179], NiSn[253] or $Ni_3S_2$[254]. Interestingly, the same side phases appear during the solution based synthesis and the pure solid-state synthesis. During this work the synthesis of $Ni_3Sn_2S_2$ was attained from the elements (500 °C for 1 week and quenching to RT). Different approaches with SnS and Ni as starting material led to side phases each time. Therefore the in situ HT-XRD proved to be very difficult, as no section could be found, where only one specified reaction takes place. This is why always some concurrence reactions are seen, which is hard to interpret. Figure 37 shows the reaction of 3 Ni + 2 SnS at temperatures between 300 – 350 °C. Despite the poor quality of the measurement it becomes obvious that $Ni_3Sn_2S_2$ and $Ni_{1.523}Sn$ are formed simultaneously. Between 400 – 450 °C, $Ni_{1.523}Sn$ disappears and an up to now unknown phase is formed (not shown). These concurrence reactions during that temperature range already demonstrate why it is so difficult to obtain single phase $Ni_3Sn_2S_2$ powders. PbS and PbSe favour the formation of the *shandite* formation over any other products.

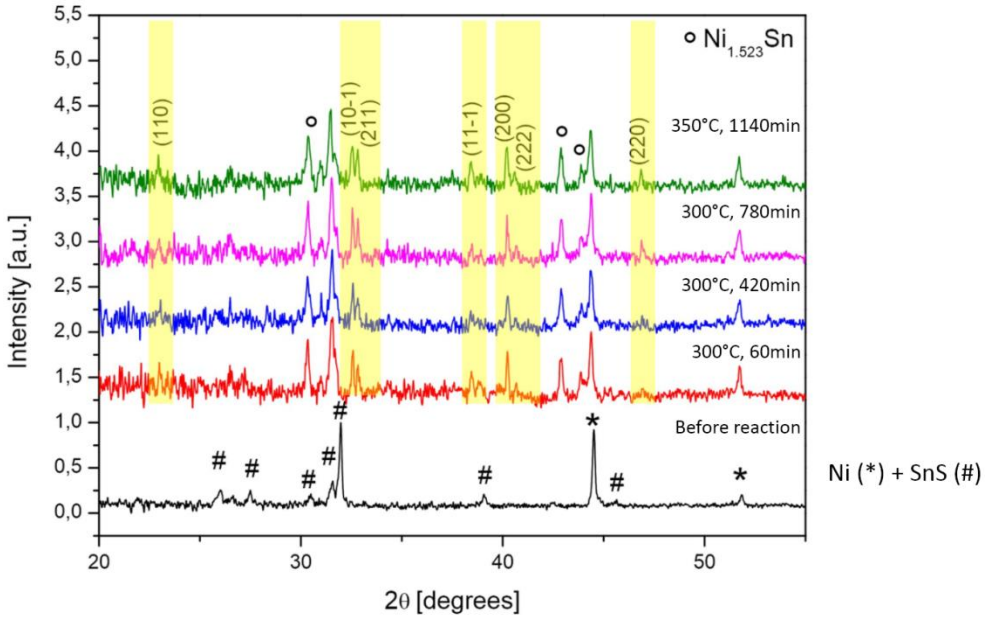


**Figure 37:** In situ XRD of 3 Ni + 2 SnS in an evacuated pith. At the bottom the starting materials Ni and SnS are visible. After increasing the temperature and reaction time $Ni_3Sn_2S_2$ (marked with yellow) but also $Ni_{1.523}Sn$ is seen.

In sum, these in situ XRD experiments are able to clarify that PbS, PbSe and SnS can already be converted to the corresponding ternary *shandite*-type compounds at relatively low temperatures in pure solid-state reactions. The mechanism is a simple diffusion of Ni into the respective binary precursor. An imitation of the mechanisms which are present at the solution-based method is therefore also possible in a solid-state reaction for selected reaction pairs.

## 6. Summary and discussion

This chapter describes the conversion reactions of binary chalcogenide precursors with $Ni^{2+}$ in polyol media under different conditions. A general applicable synthesis protocol is developed by means of which selected binaries can be either converted into ternary compounds with *shandite*-type structure or to hybrid particles. The ternary *shandite* compounds are formed by a simple unidirectional diffusion of the in situ produced nickel into the precursor. For selected samples even the morphology can be templated by this process. The hybrid or core-shell particles result from a deposition of nickel onto the respective precursor. This process can be controlled by the velocity of the nickel reduction. As the hybrid particles can be transformed

to the corresponding ternary phase by an affiliated solid-state reaction, a second way for the morphology controlled synthesis of ternary compounds is also demonstrated.

Selected *shandite*-type particles with different morphology were furthermore characterized and compared to each other.

The following general conclusions can be drawn for all "Ni-binary chalcogenide precursor" systems during the synthesis:

- For all sulfur containing compounds a complete conversion to the corresponding ternary *shandite*-type is possible by the modified polyol reaction, even if some modifications are needed. This is not the case for all examined selenium containing "Ni-binary chalcogenide precursor systems" where conversion is supressed to a certain kind and/or different side phases appear.
- The morphology of the binaries plays a key role during the conversion reactions. Some morphologies accelerate or even catalyse the transformation. In some cases the precursor can even act as a morphological template. This is especially the case for the synthesis of spherical $Ni_3Sn_2S_2$ and dendritic $Ni_3Pb_2S_2$. When dendritic PbS is used as reactive and morphological template, already temperatures of 70 ° are enough to form the *shandite* phase – This is the lowest temperature, ever reported for a *shandite* compound.
- Diffusion of Ni into the applied precursor determines the mechanism of formation. Thereby the velocity of the reduction plays a big role. A very fast reduction with the help of hydrazine in basic ethylene glycol as reductant leads to hybrid particles.
- For an entire conversion of the binary reactant to the ternary *shandite*, ethylenediamine and basic ethylene glycol are mandatory. In these optimised conditions $Ni^{2+}$ is chelated and slowly released when en decomposes at higher temperatures. Only then, it is reduced to elemental nickel in small proportions. The combination of this slow release and higher temperature seems to accelerate the diffusion of Ni, so that a complete conversion of the template is reached and especially no nickel sulfides are observed.
- Bulk precursors are much less reactive, than their nanoscale counterparts. The only bulk precursor, which can entirely react to the ternary *shandite*-phase is $Tl_2S_2$. The binary sulfide decomposes in the reaction milieu and therefore is able to react further in a second step.

- In general, Ni excess accelerates the conversion reaction – most likely due to Le Chatelie's principle of the least compulsion.
- The mechanism of nickel diffusion into binary precursors, taking place in solution, can be imitated and observed during in situ HT-XRD measurements at selected temperatures and element combinations.
- Fascinating results could be gained when selected nanoparticles were sintered or evaluated by in situ LT-XRD. The comparison of the structural behaviour of nanoparticles vs. bulk particles showed some clear deviations.

In the **Ni-SnS system** reductive diffusion of $Ni^{2+}$ into SnS particles was shown to selectively form $Ni_3Sn_2S_2$, hybrid, or even core-shell Ni@SnS, $Ni_{1.523}Sn$, and $Ni_3S_2$, by tuning the reaction conditions at low temperatures. The main challenge of this system is the instability of SnS in the basic reaction medium. Fine adjustment of reaction temperature and duration, morphology of the template SnS, and the application of ethylenediamine as supporting chelating agent, influence the formation of the final products. Their formation was controlled by carefully adjusting redox and equilibrium reactions. With this approach spherical $Ni_3Sn_2S_2$ could be formed by morphological templating starting from spherical SnS and helpful insights were gained, which were transferred to other "Ni-binary chalcogenide precursor systems". Based on these results the reaction protocol could be developed, which was used for all following systems. In-situ HT-XRD of the Ni-SnS system between 200 – 350 °C, revealed competing phases, which underlines why $Ni_3Sn_2S_2$ is hardly obtainable by pure solid-state reactions.

The results of the **Ni-PbS system** can be summarized as follows. $Ni_3Pb_2S_2$ is formed by a simple diffusion of Ni into the template PbS in the basic ethylene glycol reaction medium. During all reactions PbS proved to be very stable and almost no side phases occurred. PbS dendrites and octahedra could be entirely converted into the ternary $Ni_3Pb_2S_2$, whereas this was not possible for PbS cubes or bulk. Morphological templating, starting from dendritic PbS was successful. Templating of the octahedral shape was not possible, as the octahedra are split into smaller particles with different shape during the conversion reaction. Interestingly, templating was also possible by heating up $Ni@PbS_{dendrite}$ at temperatures between 300 - 500 °C. This hints on a second entirely underdeveloped possibility for the morphological templating of ternary compounds. The dendritic $Ni_3Pb_2S_2$ particles exhibit a specific surface area of 6.82 $m^2g^{-1}$, which is more than 21 times higher than its bulk counterpart. After

annealing of the dendritic samples, the crystallite size was found to increase with sintering temperature according to the Scherrer and Wilson equation and Williamson-Hall plot. For the strain the opposite effect was observed. The low-temperature structural properties of different $Ni_3Pb_2S_2$ samples (bulk, dendritic, octahedral) were also examined by in situ LT-XRD. An essential linear expansion of all evaluated parameters between 70 – 295 K was observed – this results in a positive thermal expansion. The main difference can be seen in the volume expansivity of the nanoparticles, which is significantly larger than that of the bulk particles. The big anisotropy of the *shandite*-type phase is expressed in the different behaviour of the TEC's $\frac{\alpha_{\parallel}}{\alpha_{\perp}}$. A very low $\alpha_{\parallel}$ of the dendritic sample is probably the most striking observation. Possibly the dendrites mainly grow along the *a*- and *b*-axis, so that the enlargement of the *c*-axis has a lower effect on the whole crystal, compared to the bulk and octahedral samples, where the orientation is more randomly. Furthermore, hysteresis effects were evaluated on a dendritic $Ni_3Pb_2S_2$ sample and showed only a very small deviation of the cell parameters. In situ HT-XRD of a Ni + PbS sample in the temperature range between 300 – 400 °C revealed the selective formation of $Ni_3Pb_2S_2$ by diffusion of Ni into PbS. The reactions taking place in the polyol medium and in a solid-state reaction are therefore quite comparable or can be imitated.

In the **Ni-In-S system** two different binary bulk precursors could be converted into the ternary *shandite* phase – even if only under nickel excess: $In^{(II)}S$ and $In^{(III)}{}_2S_3$. The big nickel excess seems to be necessary to direct the equilibrium towards the ternary phase (Le Chatelier). When $In_2S_3$ was applied less crystalline and smaller particles were observed, as compared to the results of InS. This can be explained by the need to cleave sulfur from $In_2S_3$ during the diffusion of nickel into the structure. The excess $S^{2-}$ can be washed out afterwards by the cleaning process. An adequate crystallinity of the $In_2S_3$ precursor seems to be very important, as $In_2S_3$ which was synthesised in solution at low temperatures, decomposed completely and did not react to any ternary.

**Ni-TlS system:** $Ni_3Tl_2S_2$ is the only compound of the *shandite* family which could be synthesised in a phase pure manner by starting with a binary bulk precursor ($Tl_2S_2$). This is dedicated to the unique proposed reaction mechanism, which most possibly proceeds over the formal "$Tl_2S_3$" of the double salt, $Tl_2S_2$. $Tl_2S$ is left over and reacts more sluggish to $Ni_3Tl_2S_2$ over the possible intermediates $Tl_2S_2$ or "$Tl_2S_3$". Due to the special mechanism of formation, the reaction is also possible starting from $Tl_2S$ and sulfur. The $Ni_3Tl_2S_2$ powder exhibited a

specific surface area of 4.26 $m^2g^{-1}$, which is more than 13 times higher than its bulk counterpart. The low-temperature structural properties of bulk and nano $Ni_3Tl_2S_2$ were furthermore characterised by in situ LT-XRD. Here also a broad range of linearity with a positive thermal expansion could be observed between 70 – 295 K. The volume expansivity of the nanorods is significantly larger than that of the bulk particles. Furthermore, for nanocrystalline $Ni_3Tl_2S_2$ both, $\alpha_\perp$ and $\alpha_\parallel$ are considerably larger than their bulk counterpart. The anisotropy of the shandite phases is expressed by the ratio of $\frac{\alpha_\parallel}{\alpha_\perp}$ is 152.52% for the bulk and 139.56% for the nanorods, respectively.

The general trend of less stability of the selenium containing *shandite*-type compounds appears to end up in a more tough challenge to transform the binaries in a conversion reaction - specific statements and general trends were hard to obtain. Unknown side phases and less reactivity were one of the main problems. Therefore in the selenium "nickel-binary precursor" system lesser experiments were conducted:

**Ni-PbSe system:** PbSe proved to be a very stable and unreactive compound, which barely undergoes conversion reactions. Nevertheless, a considerable part of the PbSe precursor could be converted to $Ni_3Pb_2Se_2$ by the applied modified polyol process. Working with a big nickel excess could increase the yield of formed $Ni_3Pb_2Se_2$. Surprisingly, the different morphologies of the PbSe samples did not show bigger changes – If at all, PbSe dendrites were slightly more reactive to such a conversion. Ni@PbSe hybrid particles could be easily converted to $Ni_3Pb_2Se_2$ in a solid-state reaction. Unfortunately, morphological templating was not possible during the conversion. In situ HT-XRD of Ni + PbSe between 400 – 500 °C showed a selective formation of the $Ni_3Pb_2Se_2$ phase by diffusion of Ni into PbSe. An imitation of the mechanisms of formation of the $Ni_3Pb_2Se_2$ phase, which are taking place in the polyol medium is therefore also possible during a solid-state reaction, when the correct temperature is chosen.

In the **Ni-InSe system**, $InSe_{bulk}$ could be converted to $Ni_3In_2Se_2$ to a certain kind. Instead, $In_2Se_3$ decomposed under these conditions and different other products were formed. As already observed for $Ni_3In_2S_2$, working under big nickel excess improved the yield of formed $Ni_3In_2Se_2$. Furthermore, it was also possible to start up a conversion reaction between elemental $Ni_{nano}$ and InSe. Nevertheless, the reactions were far away from an entire turnover and were poisoned by side phases.

**Ni-TlSe:** The reaction of $Tl_2Se_2$ with nickel in the modified polyol synthesis and also during a solid-state reaction led to the, to date, unknown $Ni_3Tl_2Se_2$ phase. The *shandite* phase hereby stands in concurrence to the $Ni_2TlSe_2$ phase. Different other known and unknown side phases made it almost impossible to draw any conclusions on the mechanism of formation. Due to analogy to the other evaluated examples it is concluded that also here Ni diffuses into a part of the double salt under the formation of the $Ni_3Tl_2Se_2$ phase. The left over ions seem to react to different other products.

# IV. Functional conversion of Bi, $Bi_2S_3$ and $Bi_2Se_3$ to ternary nanoparticles: a surprising 3-step mechanism towards directed product formation - The concept of applying intermetallics for the synthesis of ternaries[2].

## 1. Introduction and objective

### 1.1. Preliminary remark and objective

The mixed metal chalcogenides with the general structure $M_3Bi_2X_2$ (with $M$ = Ni, Co, Pt, Pd and $X$ = S, Se) belong to the group of the *parkerite*[255]. The structure determination of the original mineral *parkerite* ($Ni_3Bi_2S_2$), discovered by Scholtz[256], remained a challenging task over decades[255-259]. The main difference between the *shandite*- and *parkerite*-type structure is that the latter one contains Bi atoms in its crystal lattice. In addition to the compositional discrepancies, the crystal structures of the two phases also have some other differences: In the *parkerite* *M*-occupied bipyramides $X_2Bi_4$ are edge-sharing and allow for a relation to the monoclinic axes. In contrast, in the *shandite* phases, *M*-occupied bipyramides $X_2A_4$ ($A$ = In, Tl, Pb, Sn) are corner-sharing. These differences suggest that the mechanism of formation of the two phases might also be different.

Just a few years after Scholtz' discovery, an attempt to synthesize ullmannite (NiSbS)-analogous NiBiS resulted in the composition $Ni_3Bi_2S_2$[260]. Up to now NiBiS could still not be prepared. Regarding the selenium system, both, the 1:1:1 *pyrite*-type[261] and 3:2:2 *parkerite*-type[262] phases are well-known. This competition between a 1:1:1 and a 3:2:2 stoichiometry is a major aspect of this part of the thesis. In the last years increased research activities could be found on these compounds triggered by the discovery of superconductivity in $Ni_3Bi_2X_2$ ($X$ = S, Se)[143] and $Pd_3Bi_2Se_2$[263], a charge-density wave in $Rh_3Bi_2Se_2$[264] and the application of *pyrite*-type compounds in photovoltaic and electrochemical cells[265, 266].

The design of their compositions and structures is increasingly assisted by computational chemistry and modeling[9, 223, 224]. Again, the bottleneck for their availability is the chemical

[2] Parts of this work were already published in: S.M. Rommel, A. Krach, P. Peter, R. Weihrich, Conversion reactions of solids: from a surprising 3-step mechanism towards directed product formation, *Chem. Eur. J.* **2016**, accepted

synthesis of the desired material that should be low size, smart, low cost, and sustainable with respect to resource and environmental aspects. Unfortunately, little is known in reaction mechanisms for bulk inorganic materials or in ways to direct paths of synthesis that is daily work in organic synthesis. Conventional syntheses of these compounds from melt require temperatures above 800 °C and annealing for several days[146, 259]. Such a setup exclusively produces bulk materials. Nanometer-scale dimensions in order to probe possible size effects on the properties are not possible with this approach. Currently there are only two reports of a low-temperature solution-based approach for the synthesis of a ternary compound of the Ni/Bi/*X* system[30, 109]. No selenium containing *parkerite* compounds have ever been synthesized from solution and the mechanisms of formation are still not fully understood.

*Objectives*

In 2005 Shao and co-workers[30] reported on a low-temperature self-template route to rod-shaped $Ni_3Bi_2S_2$ particles. Contrary to the formation of $Ni_3Sn_2S_2$ from SnS (see chapter III) this mechanism is not very obvious simply from stoichiometric considerations. The reported low-temperature route to $Ni_3Bi_2S_2$ starts with $Bi_2S_3$, $NiCl_2*6H_2O$ (molar ratio 1:3) and ethylenediamine in basic ethylene glycol. An estimated diffusion driven formation from $Bi_2S_3$ and $Ni^{2+}$ seems surprising because of the change in the Bi:*X* ratio. The claimed Ni diffusion into the template $Bi_2S_3$ must involve not only interdiffusion of an additional element (here Ni) but also a loss (expected: S). Furthermore, in the route of Shao et al., solid Bi is found as side product which cannot be explained by such a mechanism.

1. Based on this ambiguity our first aim was to clarify a more probable mechanism of the reaction.

   The detailed study led to the discovery that $Bi_2S_3$ reacts in a surprising multi-step mechanism with Bi and NiBi as intermediate reactive templates.
2. Based on this, the concept of using intermetallics for the synthesis of ternaries is introduced and further developed.
3. In a following step, the study is extended to the selenium containing compounds. Strategies are developed to suppress binary selenides and also to control the formation of the competing products $Ni_3Bi_2Se_2$ and NiBiSe.

4. The feasibility of morphological templating is evaluated starting from $Bi_2S_3$, Bi and NiBi
5. Selected samples are investigated in terms of thermal stability and low-temperature structural behavior.
    a. $Ni_3Bi_2S_2$ nanorods are sintered at different temperatures to study the effect on cell parameters, size and strain
    b. $Ni_3Bi_2S_2$ bulk and nanorods are investigated by in situ LT-XRD to clarify and compare the structural stability and sample specific TEC values.

The reported results are a first example of directed reactions to adjust the *M* content along the *AX* + *M* path. These reactions are fascinating because (1) they are done in solution at low temperatures compared to the solid state; (2) they introduce significant changes in structure and properties. They open soft routes to fascinating novel highly anisotropic $M_3A_2X_2$ compounds that contain the weak metal $Ni_3Sn_2S_2$ with Ni(0)[40], half metal $Co_3Sn_2S_2$[149], or thermoelectric $InSnCo_3S_2$[36]. Finally, (3) they allow to study reaction mechanisms and product control.

## 1.2. The *parkerite* and *pyrite* structure

The investigated ternary compounds can be classified according to their metal content either as *pyrite* related NiSbS-type, NiBi*X*[9, 180, 223, 267] or as *half antiperovskites* (HAP), $Ni_3Bi_2X_2$[31-33, 146-149]. The first structural family can be derived from the mineral *pyrite* ($FeS_2$) and the characteristic structural feature is a Ni framework that is surrounded by heteroatomic Bi*X* entities in a fcc like arrangement (Figure 38 a). Ni atoms are therefore found in octahedrons $NiBi_3Se_3$. Different ordering variants emerge from different dumbbell orientations[223]. The latter *parkerite* group embraces structurally related compounds with a $M_3Bi_2X_2$ stoichiometry (*M*: late transition metals, *X*: S, Se, Te) that can be described by means of a common *perovskite*-type superstructure with *X*-centered Bi cubes and a half occupation of *M* sites on the available tetragonal bipyramides $X_2Bi_4$ which leads to a layered structure motif (Figure 38 b). Two chains of edge-sharing Ni occupied $X_2Bi_4$ polyhedra are aligned parallel along the *b*-axis within 2 perpendicular layers of the bismuth substructure. The third chain runs perpendicular to *b* within the mirror plane[33, 148].

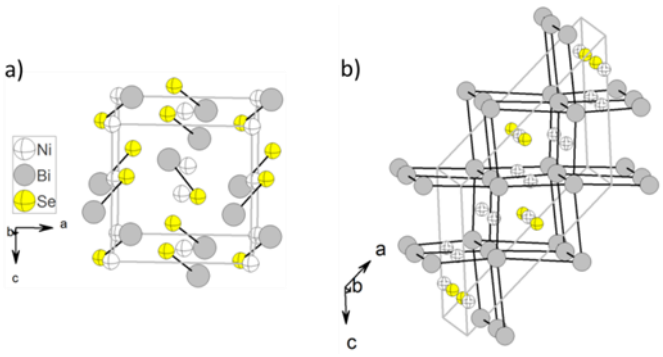


**Figure 38:** Examples of the investigated structures. a) Cubic NiBiSe[261] and b) Monoclinic cell of $Ni_3Bi_2Se_2$[262].

## 2. Experimental

*Synthesis of $Bi_2S_3$ nanorods:* The $Bi_2S_3$ nanorods were synthesized according to reference [268].

*Synthesis of $Bi_2Se_3$:* Elemental Bismuth powder (0.522 g) and Se black powder (0.296 g) was stirred in ethylenediamine (6 mL) overnight. The resulting precipitate was washed with water and ethanol and dried at 80 °C in a drying cabinet. To increase crystallinity, the obtained powder was annealed at 250 °C for 3 h under flowing argon according to Li[269].

*Reproduction of the one-pot synthesis of $Ni_3Bi_2S_2$:* The One-Pot synthesis of the ternary $Ni_3Bi_2S_2$ was performed according to a slightly modified report of Shao[30]. A mixture of $Bi_2S_3$ (0.129 g) and $NiCl_2$ *$6H_2O$ (0.178 g, molar ratio 1:3) in 70 ml ethylene glycol was added to a 100 ml round-bottom flask, magnetically stirred and treated with ultrasound. Then NaOH (0.545 g) and ethylenediamine (5.05 mL) were added. After the NaOH dissolved completely the flask was heated and the mixture was refluxed at 197 °C for 0.5 – 10.5 h in air. After cooling to room temperature, the products were centrifuged and washed several times with water and ethanol and dried at 60 °C.

*All other modifications of the syntheses conditions can be found in the appendix. They are referenced with $AR_n$ (n corresponds to the number of the respective reaction).*

*Quantum Chemical Calculations:* The first-principles calculations were carried out within the framework of density functional theory (DFT) with exchange-correlation functionals in the generalized gradient approximation (GGA)[270, 271] according to Perdew-Burke-Ernzerhof (PBE). Full geometry optimizations were executed with the Vienna Ab initio Simulation Package (VASP)[272-275], atomic site parameters and cell constants were therefore allowed to fully relax with the conjugant gradient algorithm. The interactions between the ions and the electrons are described by the projector-augmented-wave (PAW) method[276, 277] with scalar-relativistic potentials and a cutoff energy of 500 eV. All structure optimizations were performed in three subsequent steps with an initial *k*-grid mesh of 4 x 4 x 4 rising to 8 x 8 x 8 and 12 x 12 x 12 to reach sufficient accuracy. Particularly for large unit cells, this offers an additional verification of the performed calculations. A structure optimization was considered to be converged with a difference in total energy of less than 1 x $10^{-6}$ eV and a maximum Hellmann-Feynmann force of 1 x $10^{-4}$ eV/Å. The final values of the total energies of the investigated systems were obtained with energy differences (between last and second to last step) of less than 1 x $10^{-3}$ eV per formula unit.

## 3. Results and discussion

### 3.1. Studied reaction paths

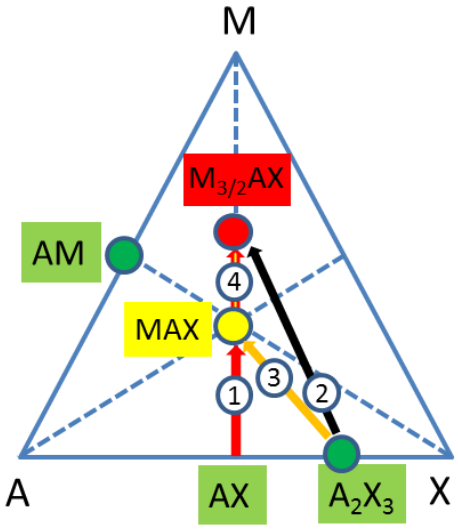


**Figure 39:** Ternary phase diagram of the *M-A-X* system with different reaction paths.

The studied compositional and structural transformations are rationalized from the phase diagram (Figure 39). Along the line $AX + M$ cubic PbS and orthorhombic SnS can be transformed as solid powders with Ni at elevated temperatures (T > 400 °C, path 1) to trigonal layered *shandite*-type $Ni_3Pb_2S_2$ and isotypic $Ni_3Sn_2S_2$. This path is also used under mild conditions (T = 166 – 197 °C) from SnS and PbS nanoparticles in a reductive solution of $Ni^{2+}$[29, 57]. A diffusion driven mechanism was proven for the formation of the ternaries, whereas core-shell particles Ni@SnS are formed by a more rapid reduction. A similar mechanism for the conversion of the orthorhombic low gap semi-conductors $Bi_2S_3$ and $Bi_2Se_3$ to the layered monoclinic superconductor $Ni_3Bi_2X_2$ ($X$ = S, Se) however requires a change in the Bi:$X$ ratio. For the reaction of $Bi_2Se_3$ with $Ni^{2+}$, even 2 products compete with the known *parkerite* ($Ni_3Bi_2Se_2$) and *pyrite* (NiBiSe, Figure 39, paths 2 and 3). Upon a possible transformation of NiBiSe to $Ni_3Bi_2Se_2$ (= $Ni_{3/2}BiSe$) the Ni content is increased (Figure 39, path 4).

All compounds under consideration are summarized in Figure 40 to point out the structural differences of educts and products. Contrary to the 2-dimensional Bi-$X$ ($X$ = S, Se) structures in $Bi_2S_3$ and $Bi_2Se_3$, Bi and Se form Bi-Se dumbbells in *pyrite* related NiSbS type NiBiSe[9, 223, 267]. The $Ni_3Bi_2X_2$ compounds exhibit CsCl like Bi$X$ substructures with Ni atoms in half of available tetragonal bipyramides $X_2Bi_4$. Because of structural relations to O-deficite *perovskites* the monoclinic *parkerites* ($C2/m$) and trigonal *shandites* ($R\bar{3}m$) were classified as *half antiperovskites*[33, 211, 278]. They differ in Ni site occupation and contain low dimensional [$Ni_3X_2$] substructures related to P and As[279] with the rare situation of Ni(0) in linear $X$-Ni-$X$ coordination.

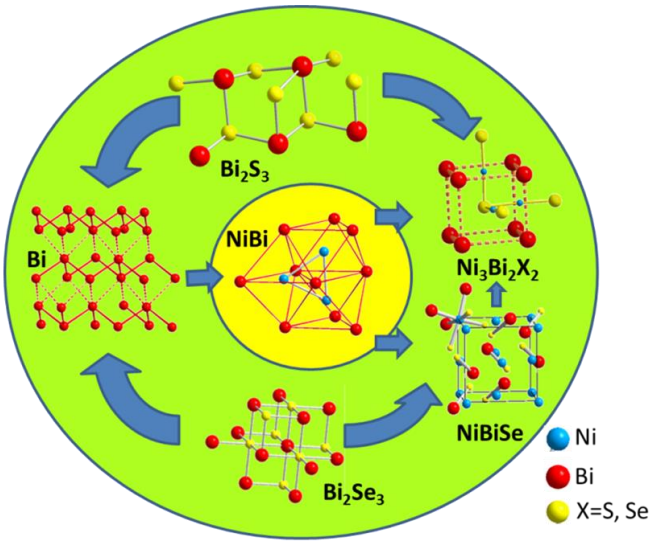


**Figure 40:** Schematic representation of the found reaction pathways from $Bi_2X_3$ ($X$ = S, Se) to Bi, NiBi, NiBiSe, and $Ni_3Bi_2X_2$.

### 3.2. Conversion chemistry in the $Bi_2S_3$-Bi-NiBi-$Ni_3Bi_2S_2$ system

The unknown mechanism for path 2 with $X$ = S is studied first and compared to the results of Shao and co-workers who proposed a simple diffusion driven reaction of nickel into $Bi_2S_3$[30]. However, the formation of $Ni_3Bi_2S_2$ thereby seems strange as not only an element (here Ni) is added but also one must be lost (expected: S). A different mechanism is indicated by the occurrence of elementary Bi as a side product that is observed in the diffraction pattern, but not commented. Based on this ambiguity our first aim was to clarify a more probable mechanism of the reaction.

The reported (one-pot) low-temperature self-template route to $Ni_3Bi_2S_2$ starts with $Bi_2S_3$, $NiCl_2$*6 $H_2O$ (molar ratio 1:3) in an ethylene glycol (eg)/ethylenediamine (en) mixture and additional NaOH to increase the reduction potential of the solution[30]. By a reproduction of the one-pot approach under slightly modified conditions, the starting material $Bi_2S_3$ is already entirely converted to $Ni_3Bi_2S_2$ and Bi as side phase after 30 min at 166 °C (Figure 41 a). This shows that the reaction already starts at even lower temperatures than thought before. After extending the reaction time to 10.5 h at 197 °C, Bi cannot be detected anymore in the XRD. It seems that the excess Bi was dissolved and washed out. In principle one could conclude on a self-template mechanism as proposed by Shao and co-workers[30]. The ribbon-shape structure of the reactant $Bi_2S_3$ and the obtained product $Ni_3Bi_2S_2$ can be seen in Figure 41 b) and c).

However, after sintering the product in an evacuated ampoule at 300 – 500 °C, $Bi_2S_3$ and Bi are still found as side phases, which were not crystalline enough to be detected before. One must conclude that the reaction is not just nickel diffusion into $Bi_2S_3$, but proceeds over multiple, different steps[109]. Therefore $Bi_2S_3$ might not act as the template during the reaction.

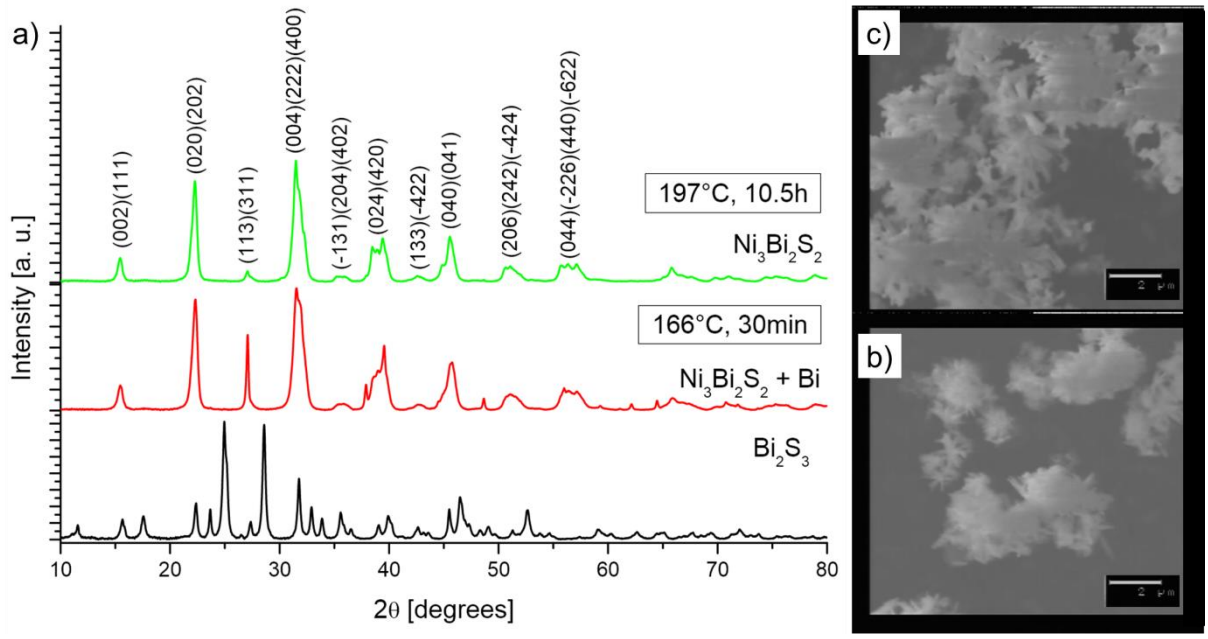


**Figure 41: a)** Reproduction of the one-pot reaction of $Ni_3Bi_2S_2$ with $Bi_2S_3$ and $NiCl_2*6H_2O$ in an eg/en/NaOH mixture. bottom) Starting material $Bi_2S_3$. middle) Reaction products after 166 °C for 30 min. top) Reaction products after 197 °C for 10.5 h. b) SEM picture of the reactant $Bi_2S_3$. c) SEM picture of the product $Ni_3Bi_2S_2$.

To elucidate the questioned mechanism of formation, the reevaluated one-pot synthesis was split into three parts (Figure 42). The exact amount of solvents and reagents which deviate from the standard one-pot synthesis, described in the experimental part, are summarized in the appendix (AR1-AR8). They are referenced with $AR_n$ with *n* as the number of the reaction in the appendix. In a first step $Bi_2S_3$ was reacted at 197 °C without the addition of $NiCl_2*6H_2O$, which led to elementary Bi as the only product after short time (AR1, Figure 42a). This is due to the temperature-dependent reduction potential of basic ethylene glycol. It is known that $Bi_2S_3$ can be reduced in ethylene glycol at temperatures above 150 °C and $S^{2-}$ ions are evolved[18, 280]. Surprisingly, intermetallic NiBi is obtained when reacting the obtained Bi particles with $NiCl_2*6H_2O$ at 197 °C in an eg/en/NaOH mixture for more than 10 h (AR2, Figure 42b). This step is very sensitive to the synthesis conditions, as NiBi is often contaminated with $NiBi_3$, possibly due to agglomerated Bi particles derived from the first reductive step. Reaction of the collected NiBi with $Na_2S$ or S (molar ratio 1:1 or 3:2) in an

eg/en/NaOH solution leads to $Ni_3Bi_2S_2$ and the obligatory Bi (AR3, Figure 42c and Scheme 2a). During the whole process no other possible binary or ternary compounds like $Ni_3S_2$ or NiBiS occurred. Trials to convert $NiBi_3$ into ternaries were not successful. We suggest that the mechanism of the one-pot synthesis most probably takes the same way over NiBi as intermediate and reactive template, as the occurring Bi side phase can be explained hereby. This is underlined as NiBi and $NiBi_3$ compounds also occur in the one-pot synthesis under large Ni excess (AR4). The morphologies of the Bi-NiBi-$Ni_3Bi_2S_2$ particles are also shown in Figure 42 on the right side. No rod-like structure, as observed during the one-pot synthesis can be seen. The particles seem to be more roundish and agglomerated. This can most likely be attributed to the fact that the elemental Bi had to be ground after the first reaction step as it clumped together to one big glob. During the one-pot reaction the transformations seem to be fast enough, so that no pronounced agglomeration occurs and the rod-like morphology is not destroyed. However, there is considerable morphology retention between NiBi and $Ni_3Bi_2S_2$. This proves that intermetallic NiBi can possibly not only act as reactive, but also as morphological template in the production of ternary chalcogenides. This will be the work of future studies.

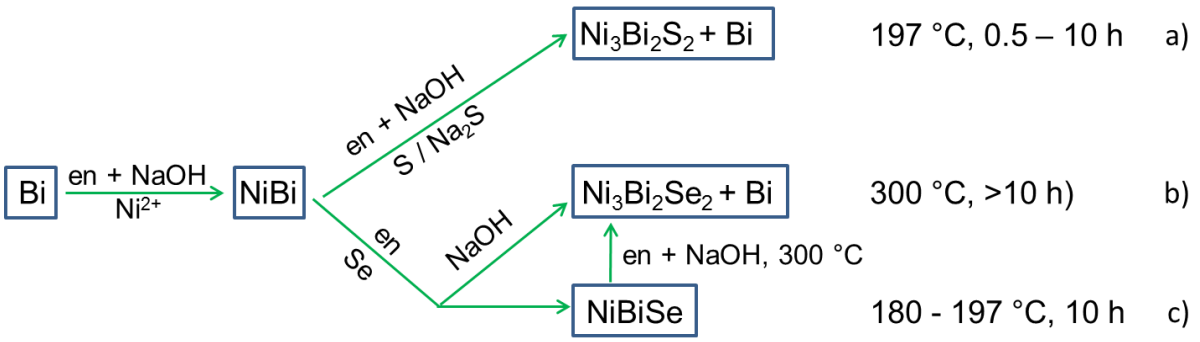


**Scheme 2:** Multi-step mechanisms to different ternaries in the evaluated Ni-Bi- S/Se system.

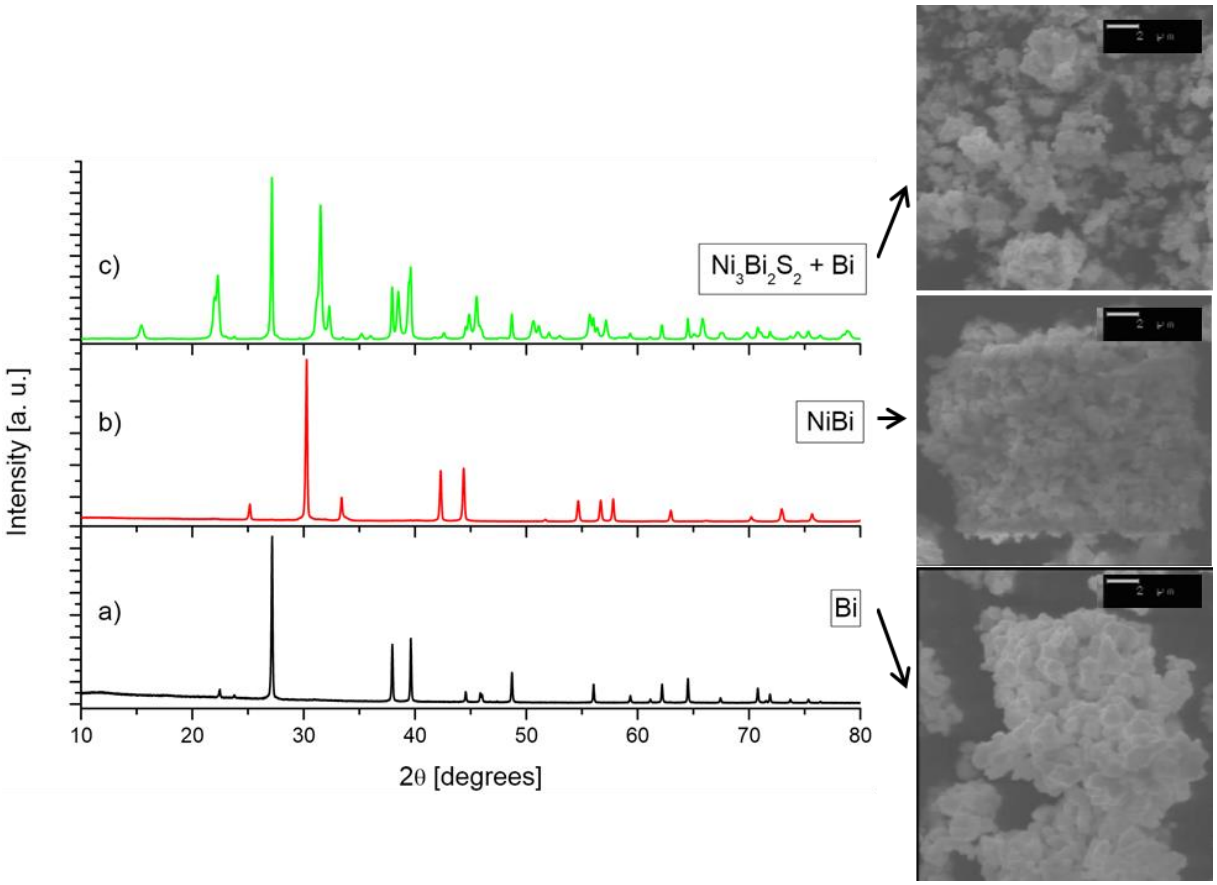


**Figure 42:** XRD patterns and corresponding SEM pictures of the decoupled one-pot reaction a) AR1: Collected Bi after reduction of $Bi_2S_3$ in an eg/en/NaOH mixture b) AR2: NiBi after reaction of Bi with $Ni^{2+}$ in an eg/en/NaOH mixture c) AR3: $Ni_3Bi_2S_2$ + Bi after reaction of NiBi with S or $Na_2S$ at 197 °C in an eg/en/NaOH mixture (molar ratio 1:1 or 3:2).

From the obtained results one must conclude the reactions, summarized in eq. (26)-(30). $Bi_2S_3$ decomposes in the eg/en/NaOH mixture, $Bi^{3+}$ is reduced by the polyol and $S^{2-}$ is complexed by en, leading to formal $[S(en)_x]$. In a second step $Ni^{2+}$ is reduced to Ni[173, 281] to form NiBi with the previously emerged Bi. Finally, NiBi reacts with $[S(en)_x]$ to $Ni_3Bi_2S_2$ and Bi is evolved. Excess $[S(en)_x]$ can just be washed out. Elemental sulfur can also be applied, as the reductive power of the polyol solution is reported to be strong enough to reduce it to $S^{2-}$[162]. Consequently, the observed reaction from $Bi_2S_3$ to $Ni_3Bi_2S_2$ is also related to a multi-step-process involving the formation of Bi and NiBi.

$Bi_2S_3 + 3\ x\ en \rightarrow 2\ Bi + 3\ [S(en)_x]$ **(26)**

$HOCH_2CH_2OH \rightarrow CH_3CHO + H_2O$ **(27)**

$2\ Ni^{2+} + 2\ CH_3CHO \rightarrow 2\ Ni_{in\ situ} + CH_3COCOCH_3 + 2\ H^+$ **(28)**

$Ni_{in\ situ} + Bi \rightarrow NiBi$ **(29)**

$3\ NiBi + 3\ [S(en)_n] \rightarrow Ni_3Bi_2S_2 + Bi + [S(en)_n]$ **(30)**

### 3.3. Conversion chemistry in the $Bi_2Se_3$-Bi-NiBi-NiBiSe-$Ni_3Bi_2Se_2$ system

One-pot attempts to synthesize the related $Ni_3Bi_2Se_2$ compound starting from $Bi_2Se_3$ and $NiCl_2*6H_2O$ in an eg/en/NaOH mixture resulted in a blend of NiSe, BiSe, NiBiSe and $Ni_3Bi_2Se_2$ (AR5). This joint appearance speaks for a close stability of binaries and ternaries with 1:1, 1:1:1 and 3:2:2 stoichiometries. The binary phases cannot be eliminated by a change in temperature and reaction time, which indicates an equilibrium situation that is not easily shifted completely towards one of the ternary products under these conditions.

After a successful application and identification of NiBi as reactive template for the synthesis of ternary $Ni_3Bi_2S_2$, it was now used for directed synthesis of its selenium homologues. Starting the reaction from NiBi, the controlled synthesis of ternary compounds is possible and no binary nickel or bismuth selenides occur in the end products. Interestingly, the 1:1:1 and 3:2:2 phases still occur as competing phases. At temperatures around 197 °C and moderate alkalinity both phases are detected (AR6). Our attempts to obtain phase pure NiBiSe remained difficult, as for all evaluated conditions (no matter if 3:2 or 1:1 stoichiometry) a small amount of $Ni_3Bi_2Se_2$ and Bi was present. Nevertheless, by working without NaOH and lower temperatures of 190 °C, NiBiSe is nearly the solely product (AR7, Figure 43a, Scheme 1c). Increasing the pH, temperature and reaction time (AR8, Figure 43b, Scheme 2b) to 300 °C for 14.5 h completely suppressed the formation of the 1:1:1 phase. In general, shorter reaction times, lower temperatures and/or less NaOH led to an increase of the NiBiSe phase. Additionally, the once formed 1:1:1 phase can be completely transformed to $Ni_3Bi_2Se_2$ under

the mentioned harsh conditions which suppress the 1:1:1 phase (AR9). We suppose that there is a narrow stability range for NiBiSe.

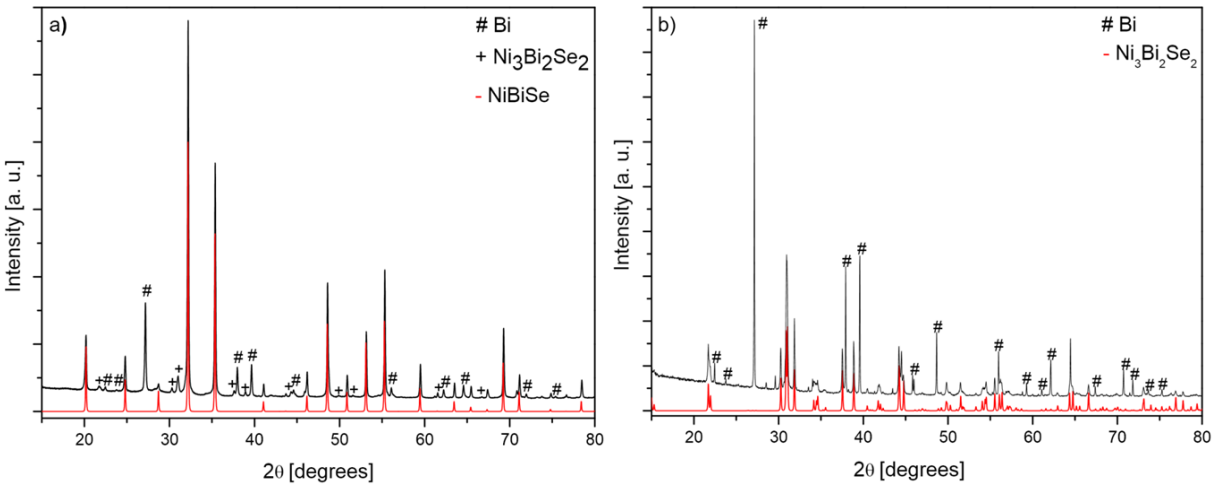


**Figure 43:** a) XRD results of AR7; Synthesis of NiBiSe, starting from NiBi at 190 °C without NaOH (Small side phase of $Ni_3Bi_2Se_2$ marked with + and Bi marked with #) b) XRD results of AR8; Synthesis of $Ni_3Bi_2Se_2$ and Bi, starting from NiBi at 300 °C in tetraethylene glycol (TEG), (Bi is marked with #).

Again one must conclude on a series of reactions (eq. (31)-(36)). During the one-pot reaction $Bi_2Se_3$ decomposes, $Bi^{3+}$ is reduced and $Se^{2-}$ is complexed to $[Se(en)_x]$. As a consequence, the binary NiSe and BiSe side phases are formed due to a strong affinity of $Se^{2-}$ to the metal ions. One part of the available $Bi^{3+}$ is reduced to $Bi^{2+}$ which reacts further to BiSe; the other part is reduced to the elemental state, which is able to form NiBi in a second step. NiBi can afterwards either form NiBiSe or $Ni_3Bi_2Se_2$, depending on the harshness of the reaction conditions. The key to the reaction is found in intact NiBi. By this means no $Ni^{2+}$ and $Bi^{3+}$ is available in the reaction medium and binaries can be avoided. The exact mechanism of the activation of the elemental selenium during the reaction could not be determined in this work. It is known that elemental selenium in ethylenediamine is able to react with elemental or ionic metals at room temperature or at least under solvothermal conditions, but no intermediate reaction products are known[162, 173]. Xie and co-workers propose a nucleophilic reaction between en and selenium and show that selenium is dissolved in ethylenediamine under solvothermal conditions[282]. This brown solution is shown to be a suitable selenium feed stock. Furthermore, en probably also activates the metal surface of Bi and NiBi[269]. In our case, the proposed activation of selenium with en is additionally supported by the reductive power of the polyol solution (eq. (27)-(28)).

$Bi_2Se_3 + 3\ n\ en \rightarrow 2Bi + 3[Se(en)_n]$ **(31)**

$Ni^{2+} + n\ en \rightleftharpoons [Ni(en)_n]^{2+}$ $Ni^{2+} + [Se(en)_n] \rightarrow NiSe + n\ en$ **(32)**

$Bi^{2+} + [Se(en)_n] \rightarrow BiSe + n\ en$ **(33)**

$Ni_{in\ situ} + Bi \rightarrow NiBi$ **(34)**

$3\ NiBi + 3[Se(en)_n] \rightarrow NiBiSe + n\ en$ **(35)**

$NiBiSe + n\ en \rightarrow Ni_3Bi_2Se_2 + Bi + [Se(en)_n]$ **(36)**

### 3.4. Quantum chemical calculations

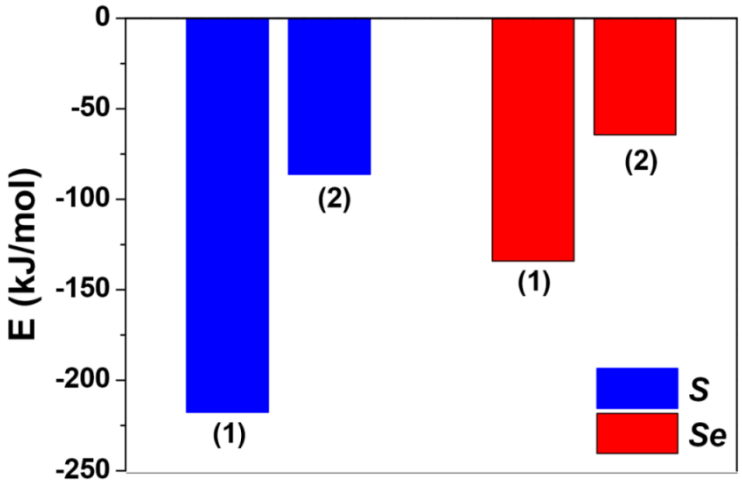


**Figure 44:** Energetic classification of educts and products for path (1): 3 NiBi +2 *X* → $Ni_3Bi_2X_2$ + Bi and path (2): NiBi + *X* → NiBi*X*.

For an interpretation of the experimental results, the conducted reactions were simulated in terms of energetic classifications of the educts and the products by quantum chemical calculations. As only elemental and metallic reactants have been used with NiBi as starting material, the idea of our recently developed scheme to systematically evaluate phase stabilities of competing systems with different compositions[9, 223, 224, 279, 283] is applied. Therein, the total electronic energy for educts and possible products is calculated under stoichiometric conditions, i.e. the number of atoms is maintained according to paths (1) and (2). For the present calculations are however restricted to the formation of the 1:1:1 and 3:2:2

phases from NiBi. A full approach that will take into account all possible side products will be published elsewhere. It is noteworthy, that although our approach does not require any experimental pre-information, the calculations reflect the experimental results, which will be shown hereinafter. The zero value in Figure 44 represents the energy of educts, i.e. a combination of the values for NiBi and the respective chalcogenide *X* that equals the utilized stoichiometry. The gain in energy with respect to the products is depicted for *X* = S, Se by bars according to the following scheme.

3 NiBi + 2 *X* → $Ni_3Bi_2X_2$ + Bi path (1)

NiBi + *X* → NiBi*X* path (2)

In case of *X* = S reaction path (1) to $Ni_3Bi_2S_2$ is preferred to path (2) to a still unknown NiBiS by more than 120 kJ/mole. For *X* = Se, the formation of $Ni_3Bi_2Se_2$ is also favored over NiBiSe. However, the difference in energy for the 3:2:2 phase is less than 70 kJ/mole. From a thermodynamic point of view the calculations give a hint that the difference in energy is related to the observation that both phases can be obtained experimentally for *X* = Se, but not for *X* = S and that NiBiSe can be converted to $Ni_3Bi_2Se_2$ under more harsh conditions. In case of *X* = S, only the more stable product is directly obtained ($Ni_3Bi_2S_2$) by the present approach. However, a final answer on the question if NiBiS can be obtained or not will be given from subsequent detailed calculations on the entire energy landscape with all possible side products[9, 223, 224, 279, 283, 284] and/or novel experiments.

## 4. Further characterizations on selected samples

### 4.1. Effect of sintering on cell parameters and size and strain of $Ni_3Bi_2S_2$ nanorods

To study the changes in microstructure during the early stage of sintering of $Ni_3Bi_2S_2$ nanorods, the powder was annealed at 200 – 700 °C for 3 h (heating and cooling rate of 5 °C/min) in an evacuated ampoule. The monoclinic symmetry (*C2*/m) of the *parkerite*-type compound can be verified to every time (Figure 45 a). Some small side phases of $Bi_2S_3$ and Bi become apparent at temperatures >200 °C. Figure 45 b) shows an enlarged section of the XRD powder diffraction patterns between 30 and 33.5 °C. As already observed for the

*shandite*-type compounds, higher temperatures cause a systematically narrowing of the Bragg reflections. This can be attributed to an increase of crystallite size and also to an increase of the degree of crystallization. Almost no shift of the 2θ values due to deviations in the crystal lattice after the annealing procedure can be seen. Nevertheless, the cell parameters obtained by Rietveld refinement with the program Fullprof[133] are seen to clearly expand after annealing at higher temperatures and come closer to the literature single crystal value (Figure 46 a, red line). These results are in concert with the literature, as the unit cell parameters of nanoparticles are usually lower than that of the bulk and the particle shape can have a big effect on total lattice variation[231, 232].

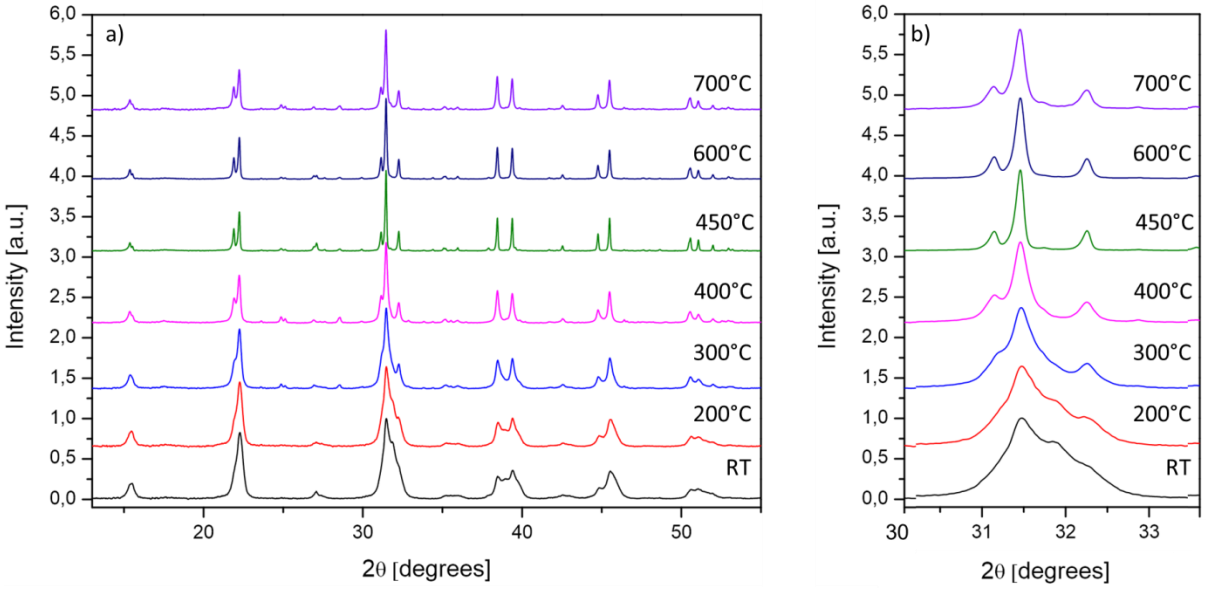


**Figure 45:** a) XRD of $Ni_3Bi_2S_{2,nanorod}$ after annealing at 200 – 700 °C for 3 h b) Enlarged section of the XRD between 30 and 33.5°.

An estimation of the crystallite sizes and strains was performed with the algorithm of Scherrer[172] and Wilson[136] and with the Williamson-Hall plot[137], implemented in the software package WinXPOW[131] (Figure 46 b). As expected, the crystallite size was found to increase with sintering temperature according to both methods. The opposite effect is observed for the strain. This contrary trend of size and strain parameters is well known for nanoparticles[233] and was already observed for dendritic $Ni_3Pb_2S_2$ nanoparticles in chapter III.5.3.1. Sinter processes generally decrease lattice defects and strain, but usually cause the coalescence of smaller grains, resulting in an increased average grain size for the nanoparticles[234]. The significant differing results in particle size between the Scherrer and Williamson-Hall method are due to the presence of strain, which also contributes to the

broadening of the peaks[235]. This is not considered in the Scherrer method. Therefore, the Scherrer equation leads to an underestimation of the size of the crystallite.

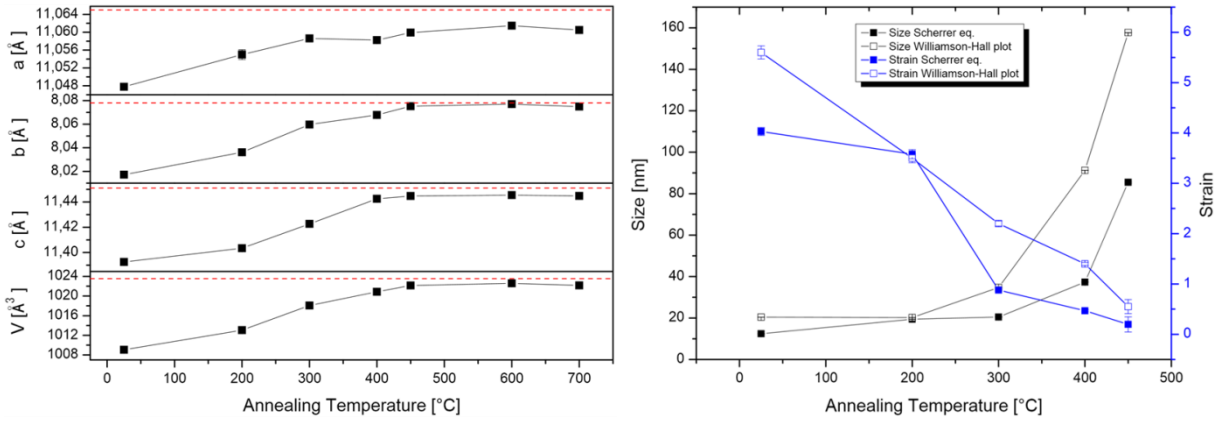


**Figure 46:** a) Cell parameter vs. annealing temperature of $Ni_3Bi_2S_2$ nanoparticles at 25 – 700 °C. The red dotted line marks the literature values for the cell parameter, obtained from single crystals[258]. b) Size and strain vs. annealing temperature of $Ni_3Bi_2S_2$ nanoparticles, calculated with the Scherrer and Wilson equation or Williamson-Hall plot for 25 – 450 °C. Temperatures above 450 °C are not included as the calculated values for size and strain exceeded the validity range of the Scherrer equation. All peaks were used for calculations.

## 4.2. Low-temperature structural properties of $Ni_3Bi_2S_2$ *parkerite*-type compounds with different morphology evaluated by in situ XRD

To determine the stability and temperature-dependent structural properties of $Ni_3Bi_2S_2$ bulk and nanords, LT-XRD spectra were recorded from RT to 12 K under high vacuum. Therefore the ground samples were enclosed in an alumina foil and transferred to the vacuum chamber of the XRD device. At each temperature, the samples were allowed to get into the steady-state for 30 min before the measurement was started. Both samples proved to be stable and the crystalline structure remained in monoclinic symmetry (*C2*/m) over the whole evaluated temperature range. Figure 47 shows the temperature dependence of the cell parameters, the unit cell volume, the *c*/*a* ratio and the *β*-angle of the examined samples.

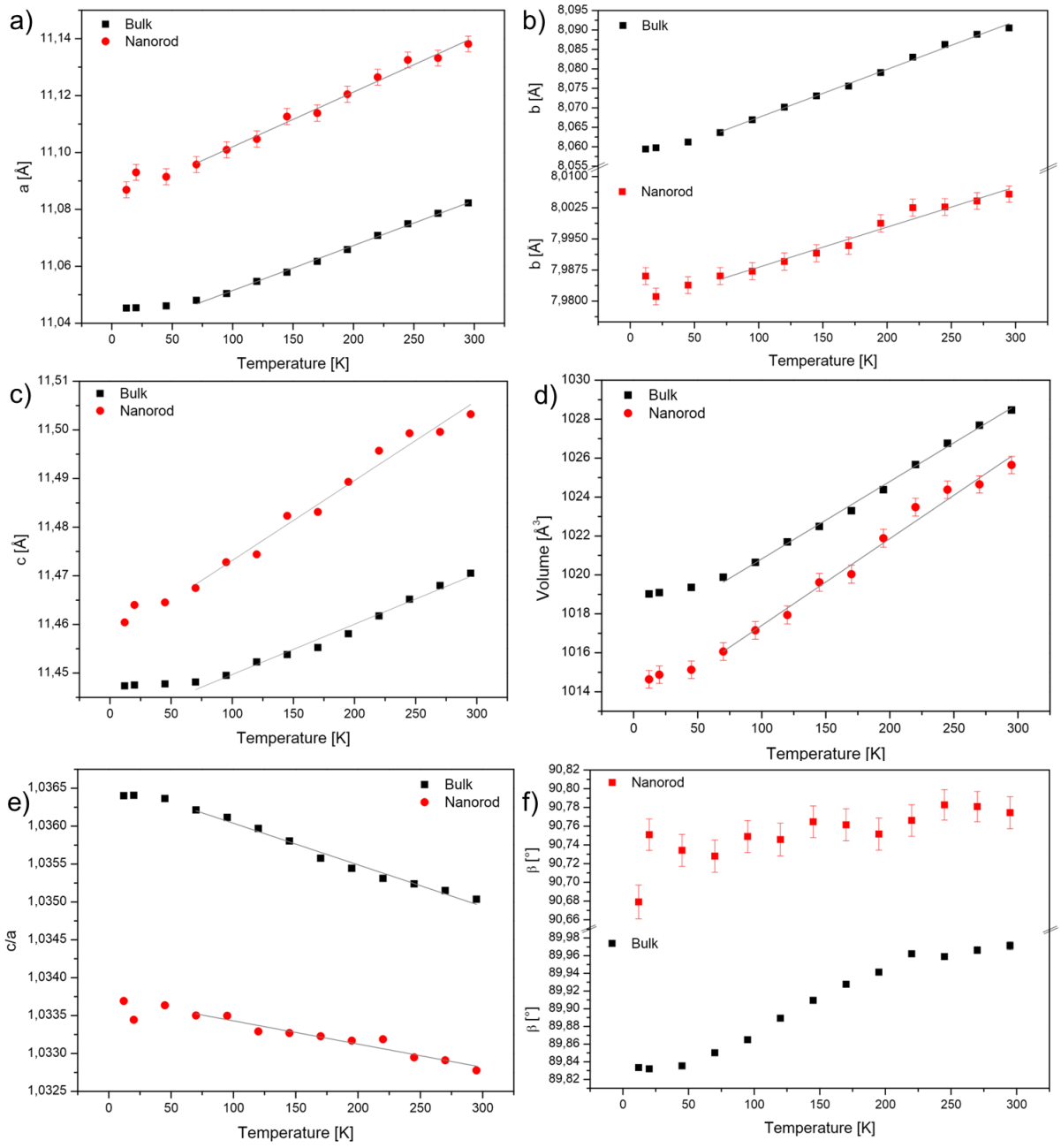


**Figure 47:** Temperature-dependence of a) the *a*-axis b) the *b*-axis c) the *c*-axis d) the unit cell volume e) the *c*/*a* ratio and f) the β angle of $Ni_3Bi_2S_2$ with bulk and nanorod like morphology.

For the *parkerite*-type $Ni_3Bi_2S_2$ compounds basically the same observations and conclusions can be made as for the *shandite*-type $Ni_3Pb_2S_2$ and $Ni_3Tl_2S_2$ samples examined in chapter III.5.3.2.

- An essential linear expansion of all evaluated parameters with the temperature is observed.

- A small levelling and bigger variance of the curves is seen between 12 – 50 K. This might hint on a maximum contraction which can be reached by "freezing" the atomic motion and has been observed for all evaluated samples of our work group so far.
- The refinement of the nanoscopic sample is much less accurate than that of the bulk one. This is indicated by the error bars and also in a bigger jog of the data points. For the ß-angle the results are so poor, that one can just assume a linear decrease of the angle, as observed for the bulk sample.
- The *c*/*a* ratio decreases linear with temperature.
- Besides the linear contraction, which is present in all samples, there are two main differences:
    - The slope of the linear fit of the cell parameters
    - The absolute value of the cell parameters of the samples at room temperature

Beginning with the latter one, it can be seen that the starting values at room temperature clearly differ between the two *parkerite* samples. The *a*- and *c*-axis of the nanorods are slightly higher but in return the *c*-axis is much smaller, so that in sum a smaller volume of the nanorods is preserved. This differs clearly to the results of the *shandite*-type $Ni_3Tl_2S_2$ nanorods where all cell parameters are bigger than that of the bulk sample and a bigger volume is the result.

As for the *shandite*-type compounds the ***thermal coefficient of expansions (TCE)*** were also evaluated for the $Ni_3Bi_2S_2$ samples (see Table 9). For its calculation the linear section between 70 and 295 K was used. $\alpha_{a,b,c}$ and $\beta$ (=volume expansivity) were calculated according to equation (22) and (24). For $\alpha'_{a,b,c}$ and $\beta'$ the slope $m$ from the origin fit was inserted into equation (23) and (25). The match between $\alpha_{a,b,c}$ and $\alpha'_{a,b,c}$ as well as between $\beta$ and $\beta'$ with an accordance on the second decimal place is quite ok, indicating an accurate linearity of the evaluated data points. A positive thermal expansion is obtained for both samples (Table 9) which can be explained by the increase of all cell axes and the cell volume with the temperature. The volume expansivity $\beta$ and $\beta'$ of the nanoparticular sample is significant larger than that of the bulk particles. This phenomenon was already presented for the *shandite* samples in chapter III.5.3.2 and was explained with the results of Lu and co-workers[245]. They observed larger displacements of the atoms from their ideal lattice locations and more defects in nc-Se samples with smaller grains. This obviously affects the TEC. The anisotropy of the *parkerite* phases can be seen in the large differences between the respective values of

the TECs. In other terms, this means that the unit cell contracts and expands in a different manner along the respective cell axes.

Compared to known TECs in literature it becomes clear that the *parkerite* and *shandite* phases behave more like alloys than pure metals, indicated by their high TEC values[285]. Interestingly, the values are even one tens higher than the one reported for anisotropic *Wurtzite*-type compounds[240].

**Table 9:** The lattice parameters of bulk and rod-like $Ni_3Bi_2S_2$ at 295 K. The mean thermal expansion values $\alpha_{a,b,c}$ between 290 – 70 K calculated, assuming a perfect linearity between the first and the last point. $\alpha'_{a,b,c}$ were calculated with the slope *m* of the origin-fits. The mean volume expansivity β calculated with dV/dT and β' calculated with the slope *m* of the origin-fits.

| | **$Ni_3Bi_2S_{2,bulk}$** | **$Ni_3Bi_2S_{2,nanorod}$** |
|---|---|---|
| $a_{\_295\ K}$ (Å) | 11.0823(2) | 11,138(3) |
| $b_{\_295\ K}$ (Å) | 8,0905(2) | 8,006(2) |
| $c_{\_295\ K}$ (Å) | 11,4705(3) | 11,503(3) |
| $\alpha_a$ ($K^{-1}$) | 1,3721*$10^{-5}$ | 1,6914*$10^{-5}$ |
| $\alpha_b$ ($K^{-1}$) | 1,4782*$10^{-5}$ | 1,0952*$10^{-5}$ |
| $\alpha_c$ ($K^{-1}$) | 8,6750*$10^{-6}$ | 1,3808*$10^{-5}$ |
| $\alpha'_a$ ($K^{-1}$) | 1,43*$10^{-5}$ | 1,73*$10^{-5}$ |
| $\alpha'_b$ ($K^{-1}$) | 1,53*$10^{-5}$ | 1,21*$10^{-5}$ |
| $\alpha'_c$ ($K^{-1}$) | 9,02*$10^{-6}$ | 1,43*$10^{-5}$ |
| β ($K^{-1}$) | 3,71*$10^{-5}$ | 4,15*$10^{-5}$ |
| β' ($K^{-1}$) | 3,86*$10^{-5}$ | 4,35*$10^{-5}$ |

## 5. Summary and discussion

In this chapter, we identified and tested a plausible multistep reaction pathway that results in the formation of ternary mixed metal chalcogenides in the Ni/Bi/*X* (*X* = S, Se) system. Our experiments identified three different pathways, which can take place:

(1) $AX \rightarrow M_{3/2}AX$

(2) $A_2X_3 \rightarrow M_{3/2}AX$

(3) $A_2X_3 \rightarrow MAX$.

According to the found results for *A* = Bi, Bi is formed first when the reaction is started from $Bi_2S_3$ or $Bi_2Se_3$. Bi is then converted to intermetallic NiBi that in turn can react to ternary compounds $Ni_zBiX$ with different *z*(Ni).

According to calculated high differences in the energy of formation the more stable of competing products is directly obtained ($Ni_3Bi_2S_2$, Scheme 2a). No binaries are formed independent from which reactant is applied ($Bi_2S_3$ or NiBi). In case of smaller differences between different binaries and ternaries, control of conversion to different stoichiometry is only possible by applying NiBi as intermetallic precursor, as seen for the selenium system. Intact NiBi avoids reactive $Ni^{2+}$ and $Bi^{3+}$ ions which otherwise are able to form different binaries. In the selenium system two different ternaries, $Ni_3Bi_2Se_2$ and NiBiSe appear in the phase diagram. Primarily, NiBiSe is formed when no NaOH is given to the reaction solution and lower temperatures of around 190 °C are applied (Scheme 2c). Under more harsh conditions of high pH and high temperatures $Ni_3Bi_2Se_2$ can be obtained (Scheme 2b). Furthermore, the present results also show that the conversion of one ternary compound into the other is possible along the *M*+*AX* line in the ternary phase diagram for NiBiSe to $Ni_3Bi_2Se_2$. Elucidation of these reaction pathways provides a look into the steps involved in the formation of solid-state compounds. The present conversion reaction opens ways to directed synthesis of various intermetallics and novel functional multinary compounds.

Annealing of $Ni_3Bi_2S_2$ nanorods between 200 - 700 °C leads to an increase of particle size and a corresponding decrease in strain. The evaluated in situ LT structural behaviour shows remarkable differences between bulk and $Ni_3Bi_2S_2$ nanorods. Worth special mention is that the volume expansivity $\beta$ and $\beta'$ of the nanoparticular sample is significant larger than that of the bulk particles.

# V. Synthesis, characterization and electrochemical performance of the *olivine*-type $LiNi_{1-y}Co_yPO_4$ solid solution and development of a cheap and easy system for the measurement of electrochemical cells

## 1. Introduction and objective[3]

One of the major challenges of today is to ensure a continuous supply of energy in response to the ever-growing demand. As society becomes more and more mobile and increasing proportions of energy are acquired by regenerative energy sources, which produce energy in a discontinuous manner[286], the demand for a reliable secondary (rechargeable) battery of high energy and power density has increased noticeably. Therefore new increasingly powerful mobile as well as stationary storage materials need to be explored. At the moment lithium-ion technology is one of the most promising to fulfill the upcoming needs of energy storage materials[126, 127]. The high potential in energy density compared to other techniques like lead acid, Ni-Cd and Ni-MH batteries are the main drivers for this technology. For example the energy density of lithium-ion is typically twice that of the standard nickel–cadmium[128].

### 1.1. Reasons for interest in nickel-containing *olivine* compounds

In search for high capacity and high security cathode materials for Li-ion batteries, *olivine*-type phosphates[50] became interesting in recent years. As a prototype compound, $LiFePO_4$ is a cheap material that is known as the mineral *triphylite* since 1834[287]. Main problems for applications like the synthesis of phase pure samples and the low electrical conductivity were solved within the last decade. $LiFePO_4$ is an example for novel materials for secondary Li-ion

[3] Parts of this chapter were already published in:
S. Rommel, N. Schall, C. Brünig, R. Weihrich, Challenges in the synthesis of high voltage electrode materials for lithium-ion batteries: a review on $LiNiPO_4$, *Monatsh. Chem.,* **2014**, *145*, 385-404.
S. M. Rommel, J. Rothballer, N. Schall, C. Brünig, R. Weihrich, Characterization of the carbon-coated $LiNi_{1-y}Co_yPO_4$ solid solution synthesized by a non-aqueous sol-gel route, *Ionics*, **2015**, 21, 325-333.

batteries that face a continuously rising demand of the world market. Due to its high cyclability and stability with respect to current pulses and temperature ranges, availability of raw materials, and lower costs compared to $LiCoO_2$, it is discussed as material for stationary applications in combination with lithium titanate anodes[288-290]. Its main disadvantage for mobile applications is the lower voltage (3.2 - 3.3 V against Li). However, a way to increase capacities and voltage of *olivines* is seen in cation substitution of Fe by Mn (4.1 V), Co, (4.8 V) and Ni (5.1 V) (Figure 48). Therein, $LiCoPO_4$ and $LiNiPO_4$ emerged as promising materials on the pathway to future high-voltage (5 V) batteries[288, 289]. $LiCoPO_4$ is currently under intensive investigation[291], whereas for $LiNiPO_4$ fundamental aspects are not yet understood.

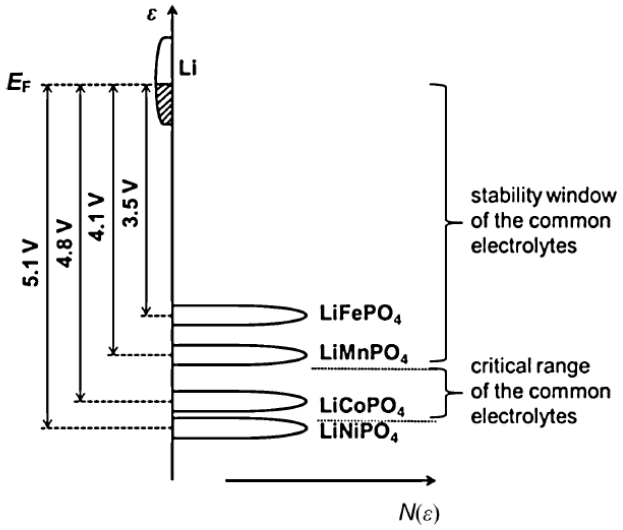


**Figure 48:** Relative energy levels of the $M^{3+}/M^{2+}$ redox couple vs. Li/ $Li^+$ in different $LiMPO_4$.

In our recent review we identified main problems in the synthesis and electrochemical properties of Ni- based *olivines* as electrode materials[55]. First, many published synthesis routes lead to impurities and side products[292-295]. Phase pure samples could be found by optimization of conditions in solid-state and hydrothermal reactions. The second problem could not be solved from these methods, i.e., reliable tuning of particle size in high-temperature reactions. Often, large particles are an obstacle for short paths of Li-ion diffusion[296]. This leads to the third problem, the electrochemical activity of $LiNiPO_4$ which is wedded with the low electric conductivity of the bulk material. $LiNiPO_4$ exhibits a several orders of magnitudes lower conductivity than $LiFePO_4$ and $LiCoPO_4$[297, 298]. To date, only heavily C-coated electrodes of $LiNiPO_4$ have ever shown a debatable kind of

activity[125, 294, 299, 300]. The not yet solved cyclability problems are however strongly related to the decomposition of state-of-the-art electrolytes at 5 V.

General synthesis procedures to circumvent these disadvantages are nanoparticle synthesis[301], coating with a conductive medium[125, 295, 302, 303], doping[296, 304] and also the application of solid solutions.

## 1.2. Preliminary remarks and objection of this section

This chapter is divided into two parts.

1. ) The synthesis, characterization and electrochemical performance of the *olivine*-type $LiNi_{1-y}Co_yPO_4$ solid solution
2. ) The development of a cheap, safe and easy system for the measurement of electrochemical cells

In the first part some of the mentioned problems of Ni containing olivine cathode materials are addressed from the formation of phase pure solid solutions of $LiNi_{1-y}Co_yPO_4$ ($y$ = 0, 0.25, 0.33, 0.66, 1) with a modified non-aqueous sol-gel route. This approach combines several positive properties, like small particles, an in situ carbon coating, a conducting nanophosphide network, as well as the production of essentially phase pure compounds. It opens the possibility to systematically tune and investigate material properties including particle size and electrochemical activity of the metal ions[297]. It is expected that the conductivity of the low-end member can be increased by the introduction of higher conductive ions and the overall electrochemical performance can be enhanced[305-308]. Combination of these procedures and improvements in electrolytes have already led to promising results for related *olivines*[294, 309-312] and other compounds[106, 313-315]. The substitution effects of Ni by Co are discussed from SEM, X-ray powder diffraction (XRD), and IR spectroscopy with respect to particle shape, lattice parameters, and bonding. For $LiNiPO_4$, the mechanism of its formation and conditions for the formation of phosphide by-products $Ni_3P$[316, 317] and $Ni_{12}P_5$[318] are carefully investigated. Finally, the electrochemical performance is shown and compared to values obtained for a solid-state synthesis of the same solid solution[308, 311].This is of particular interest, as to date, no publication has reported the nano synthesis and structural

properties of the $LiCoPO_4$ - $LiNiPO_4$ solid solution in combination with extensively electrochemical performance tests in a $LiPF_6$ containing electrolyte.

In the second part of this chapter a cheap and easy system for the electrochemical characterization of electrode materials is developed. As no glove box was available next to the potentiostat, the cell had to be designed so that it can operate in air. Therefore, a three-electrode cell was chosen as the principal construction motive. A closable system was built up which has the advantage that in principle also operating at higher temperatures or under different gases is possible.

The steps of procedure involved all parts:

- The mixing of the electrolyte ($LiClO_4$ in EC+DMC)
- The construction of the cell (Three-electrode cell)
- The synthesis of the evaluated materials ($LiFePO_4$, $LiCoPO_4$, $LiNiPO_4$, $LiCoO_2$, $Ni_3Pb_2S_2$…)
- The formation and optimization of the electrodes (current collectors, electrode device, preparation of the electrode slurry, preparation of the lithium counter and reference electrodes…)

The whole system was tested and optimized for cyclovoltammetric measurements during this thesis. Nevertheless, in principle galvanostatic charging and decharging is also possible in such a type of cell as proven by Memm and co-workers[319].

All steps were optimized with the aid of a self-synthesized reference material ($LiCoO_2$). Later on $LiFePO_4$ and also a first representative of the *shandite* family ($Ni_3Pb_2S_2$) was tested in the electrochemical cell. Nevertheless only very few measurements were possible due to the lack of measurement time.

### 1.3. The structure of *olivine*-type $LiNiPO_4$ and intrinsic advantages

Lithium nickel phosphate crystallizes in an ordered *olivine* structure with the space group *Pnma* (no. 62)[293, 297, 320-322]. The *olivine* structure can be considered as a hexagonal analogue of the *spinel* structure and is normally described as a slightly distorted hexagonal close

packing (HCP) of oxygen atoms[50]. $Li^+$ and $Ni^{2+}$ cations are located in half of the octahedral and $P^{5+}$ cations in 1/8 of the tetrahedral sites (Figure 49). The $NiO_6$ octahedra share four corners in the *bc* plane being cross-linked along the *a*-axis by the $PO_4$ groups. Li ions are located in rows, running along *b,* of edge shared $LiO_6$ octahedra. The *olivine* structure builds up a 3D network of perpendicular tunnels along the [010] and [001] direction, occupied by $Li^+$-ions[323]. This network is of great importance for lithium ion mobility and qualifies the *olivine* as a potential cathode material. Recent computational models and first principle calculations on Li*M*$PO_4$ have shown that in the orthorhombic *olivine* structure, the lowest $Li^+$ migration energy is found for the pathway along the [010] channel, following a curved trajectory[304]. This indicates 1D lithium-ion mobility along the *b*-axis during the charge-discharge process[304, 324]. Therefore, research primarily tries to design crystals with a *b*-axis which is as short as possible[325, 326].

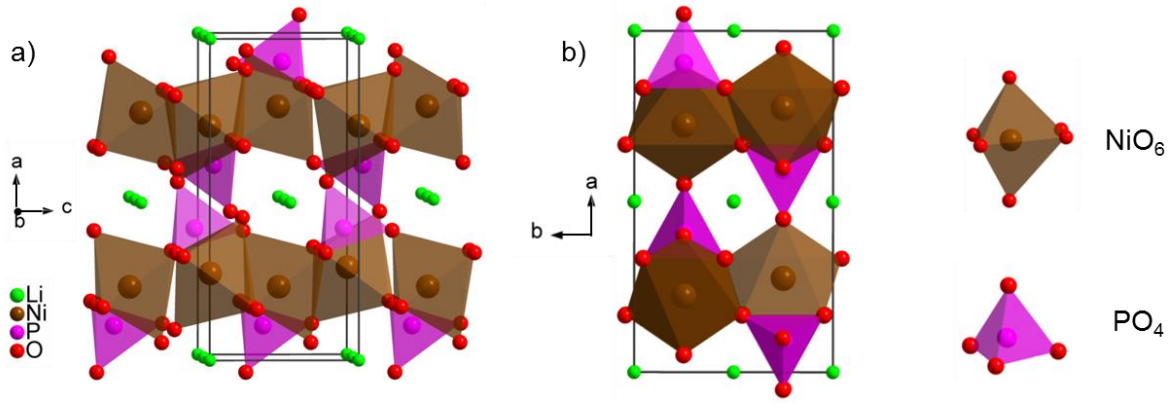


**Figure 49:** Crystal structure of $LiNiPO_4$; a) and b) Projections of the unit cell along *b* and *c* with interlinked $MO_6$ and $PO_4$ polyhedra.

A big advantage of this compound is that the strong P-O covalent bonds in the ($PO_4^{3-}$) polyanion stabilize the oxygen when fully charged and avoid $O_2$ release at high states of charge, making $LiNiPO_4$ an excellent, stable and safe material[327, 328]. The stronger the covalent bonding within the polyanion, the lower the $M^{2+/3+}$ redox energy and the higher the $V_{oc}$ vs. lithium for that couple (inductive effect)[50, 329, 330]. Despite that it should be noted that Hautier et al.[331, 332] calculated the critical oxygen chemical potential at which the charged (delithiated) cathode begins to evolve oxygen gas. This shows that $LiNiPO_4$ and $LiCoPO_4$ are thermodynamically less stable than $LiFePO_4$ and even $LiMnPO_4$. But still, in most situations phosphates can provide cathode materials with higher voltages than oxides by a similar thermal stability[332].

The tenor properties of $LiNiPO_4$, like conductivity, problems with the synthesis (phase purity, cation antisite defect), stability window of the electrolytes and electrochemical activation were already summarized in our review[55] and are not listed in detail here.

## 2. Characterization of the carbon-coated $LiNi_{1-y}Co_yPO_4$ solid solution synthesized by a non-aqueous sol-gel route

### 2.1. Experimental

*Synthesis*

Carbon-coated samples of the solid solution of $LiNi_{1-y}Co_yPO_4$ ($y = 0$, 0.25, 0.33, 0.66, 1.0) were prepared as powders by a modified non-aqueous sol-gel route described in reference [124]. Lithium acetate dihydrate (Janssen Chimica, 98%), nickel acetate tetrahydrate (Chempur, 99%)/cobalt acetyl acetonat (Merck, 98%) and phosphoric acid (Aldrich, 85%) were reacted in ethylene glycol (Merck, 99.5%) with a molar ratio of 1:1:1. Treating with ultrasound, low intensity heating, and rigorous stirring led to a homogeneous distribution of the precursors. The gels were prepared with a precursor concentration of 0.75 M. After aging for 2 days in sealed beakers with parafilm, the gel samples were agitated with a spatula and transferred into a quartz glass boat. The gel was heat treated at 700 °C under flowing argon gas for 12 h (heating ramp 1 °C/min, cooling ramp 0.5 °C/min) in a tube furnace.

*Analysis/Structural and electrochemical characterization*

X-ray powder diffraction of the crushed and ground powders was performed with a Huber G670 diffractometer equipped with an imaging plate and a tube for monochromatic Cu-Kα1-radiation (λ = 1.54060 Å, Ge-monochromator). Diffraction data were collected in a 2Θ-range from 4.0° to 100°. Morphologies of the as-prepared $LiNi_{1-y}Co_yPO_4$ samples were investigated with scanning electron microscopy using a Zeiss Digital Scanning Microscope DSM 950. The carbon content of the samples was determined by a combustion method performed at Clariant GmbH Laboratories. In this method, the material is combusted and the amount of carbon is determined by the amount of the carbon dioxide released. To evaluate the bonding nature of the coated carbon, Raman spectra were recorded with an Oriel MS260i Spectrometer with a

He-Ne laser ($\lambda = 632.78$ nm), equipped with a CCD camera (Andor DB401-UV). FIR and MIR measurements were performed on a FT-IR Spectrometer (Varian 670 FT-IR). UV-Vis measurements were operated on a NIR-UV/VIS Spectrometer (Omega 20, Bruins Instruments).

For electrochemical tests, the synthesized powder was first mixed intimately with carbon black powder (Timcal, Super P) and a polyvinylidene fluoride binder (Solvay Speciality Polymers, Solef 1530) in a 90:5:5 weight ratio. The same was treated with N-methylpyrrolidinone (solvent) to form a slurry. The mixture was coated uniformly on a carbon-coated aluminum foil and then vacuum dried at 150 °C for 3 h. The circular electrodes were punched out from the coated foil (area: 1.33 $cm^2$), pressed (under 2-ton pressure) and vacuum dried at 160 °C for about 20 h. Cells, consisting of a lithium anode, synthesized $LiNi_{1-y}Co_yPO_4$ cathode and a non-aqueous electrolyte containing 1 M $LiPF_6$ dissolved in 1:1 v/v EC:DMC (Merck, LP30 R48) with a cell guard separator were assembled in an argon-filled glove box and sealed prior to electrochemical studies. A BaSyTec battery cycler was used for testing. Cells were cycled at 27 °C at a discharge rate of 2 C and cut of voltages of 2.5 and 5.5 V. Charge and discharge rate was calculated for a reduced theoretical capacity of 150 $mAhg^{-1}$. No carbon correction was applied.

## 2.2. Results and discussion

*Synthesis and Characterization of the $LiNi_{1-y}Co_yPO_4$ phases*

Figure 50 (on top) shows the homogeneous gels formed after subsequent settling of the precursor solutions. A green over blue to grey-purple color was obtained for the respective $y = 0$, 0.25, 0.33, 0.66, and 1 samples. The arrow indicates that the gelation time increased with the amount of the corresponding cobalt precursor, i.e., with rising cobalt acetylacetonate content, a longer duration of the gelation was observed. The carbon content of the samples was evaluated via a combustion method. Results are listed in Table 10. The average values of 8-13 % carbon content are much higher than those reported by Yang and Xu[124] for a related approach. As $LiNiPO_4$ results in the lowest carbon coating, a big amount of the carbon might arise from the cobalt acetylacetonate. The fact that the argon flow was just controlled by a

bubble counter and that no pressure valve was used might lead to the unexplainable fluctuations in the carbon content, especially for $LiNi_{0.33}Co_{0.66}PO_4$.

In order to assure reliable results of the bonding structure of the coated carbon, exemplarily a Raman measurement was performed for $LiCoPO_4$ (see Figure 76 in the appendix). The relative intensity ratio of the D- and the G-band illustrates that highly disordered graphite structure is obtained by the present method.

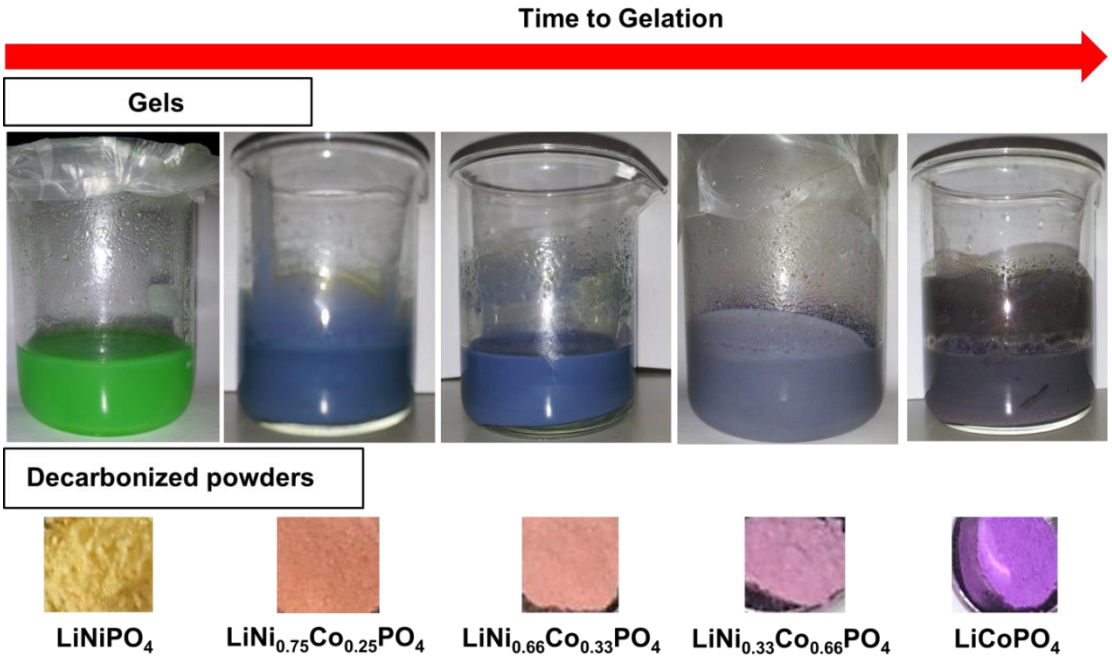


**Figure 50:** Formed gels of the precursor solutions after aging for 2 days (top); decarbonized powders (bottom). The concentration of $Co^{2+}$ rises from left to right. With higher cobalt content, a longer duration for the hardening of the gels is observed.

**Table 10:** Carbon content of the $LiNi_{1-y}Co_yPO_4$ samples.

| Sample | Carbon content [% wt] |
|---|---|
| $LiNiPO_4$ | 7,7 |
| $LiNi_{0.75}Co_{0.25}PO_4$ | 12,2 |
| $LiNi_{0.66}Co_{0.33}PO_4$ | 13,9 |
| $LiNi_{0.33}Co_{0.66}PO_4$ | 8,4 |
| $LiCoPO_4$ | 13,7 |

To be able to visually confirm the successful formation of the solid solution, the samples have been decarbonized. After decarbonizing the samples at 700 °C for 3 h, a color range from yellow over orange to purple is clearly related to increasing *y* in $LiNi_{1-y}Co_yPO_4$ (see Figure 50 bottom). Due to the respective UV-Vis spectra (Figure 77 in the appendix), the change in color is related to a shift of the absorption band from 420 to 600 nm.

The crystallite sizes have been calculated by using Scherrer's equation applying the 101, 111, and 311 reflex[172]. For the prepared $LiNi_{1-y}Co_yPO_4$ samples a crystallite size of 145±80 nm was obtained. The fine crystallite size compared to the larger crystals derived from conventional solid-state synthesis can be ascribed to the sol-gel method applied in this work. This effect is mainly due to the carbon nanopainting generated from ethylene glycol in which the precursors were dispersed to form the gel. In Figure 51, the morphologies of selected samples of the solid solution are presented. Loosely aggregated, spherical particles are obtained for samples with low Ni content. For a higher Ni content, morphology changes to unregularly shaped and heavy agglomerated particles. This indicates a relation to the time for gel formation.

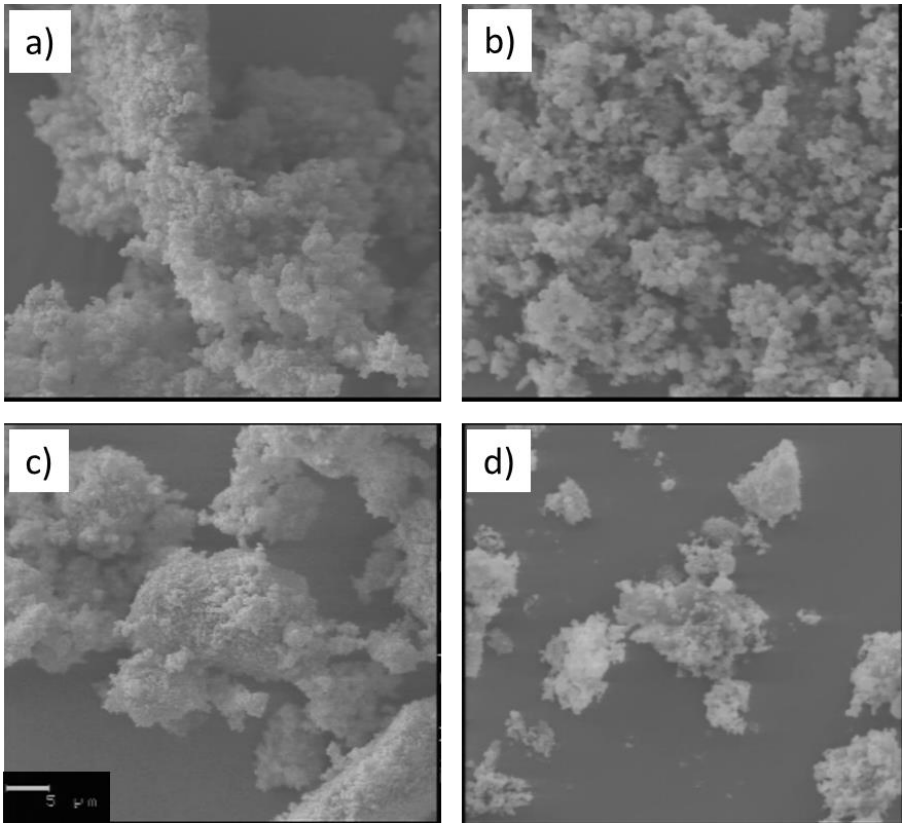


**Figure 51:** SEM picture for selected compositions of a) $LiCoPO_4$, b) $LiNi_{0.33}Co_{0.66}PO_4$, c) $LiNi_{0.66}Co_{0.33}PO_4$, and d) $LiNiPO_4$ with a resolution of 5 µm.

X-ray powder diffraction patterns of $LiNi_{1-y}Co_yPO_4$ ($y = 0$, 0.25, 0.33, 0.66, 1) are shown in Figure 52. Among all these XRD patterns, no evidence of additional diffraction peaks for crystalline carbon (graphite) appeared. One can conclude that the carbon generated from ethylene glycol and other organic species is amorphous. Further, the coating does not have any detectable influence on the crystal structure of $LiNi_{1-y}Co_yPO_4$. The diffraction patterns can be indexed to *olivine*-type structures that are isotypic to $LiFePO_4$. Here Li is found on the crystallographic *4a* site and Ni and Co share the *4c* site[320].

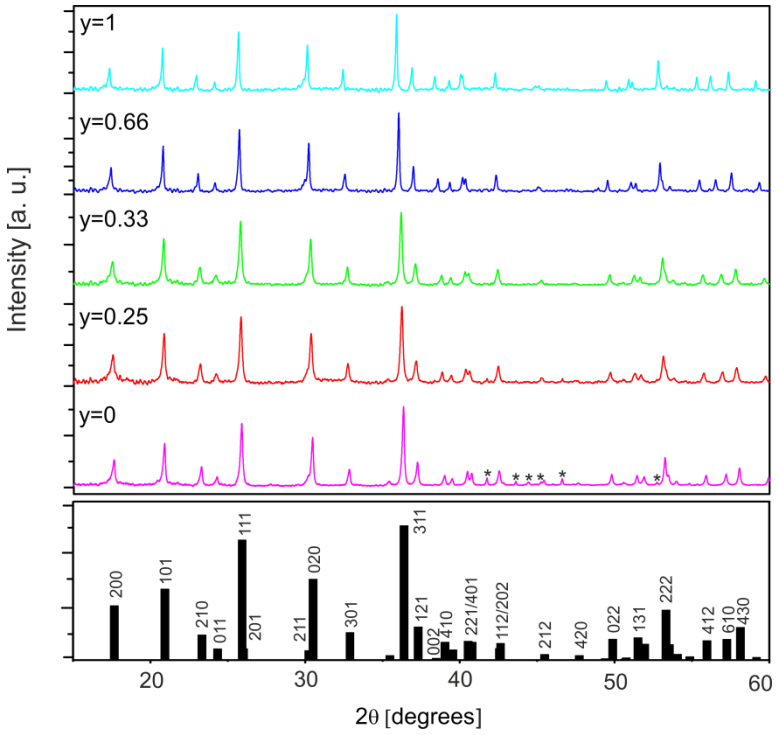


**Figure 52:** XRD patterns of the solid solution of $LiNi_{1-y}Co_yPO_4$. The side phase $Ni_3P$ is marked with an asterisk (*).

Whereas the Co containing compounds are single phase, $Ni_3P$ can be clearly indexed as side phase of the $LiNiPO_4$ sample. This indicates that extensive carbothermal reduction (CTR) of the phosphate has taken place. The side phase disappears with rising cobalt content (see also Figure 78 in the appendix). This is assumed to be related to the more facile reduction of Ni(II) in $LiNiPO_4$ versus Co(II) in $LiCoPO_4$. According to Nazar et al.[295, 303], nanophase phosphide network ($Ni_3P$) in olivine phases forms an efficient electrical conduit, and the insulating $LiMPO_4$ nanocrystallites can be rendered electrically conductive through this approach. This makes it worth to have an extended look at the mechanism of formation of $LiNiPO_4$ and its phosphide side phases which appear in this sol-gel synthesis.

In principle, any of the carbon-coated Li*M*$PO_4$ compounds have the propensity to undergo carbothermal reduction at higher temperatures. Figure 53 shows the results of the calcined $LiNiPO_4$ gel bodies at 500, 600, 700, 800, and 900 °C. At 500 and 600 °C, the phase pure $LiNiPO_4$ olivine is apparent. Rising the temperature to 700 °C, $LiNiPO_4$ is present together with $Ni_3P$ and a minor phase of Ni. We conclude that at this temperature, the carbon of the nickel oxalate precursor and ethylene glycol reduces a certain percentage of the nickel to the elemental state, and this is directly consumed in the production of $Ni_3P$. At 800 °C, the amount of $LiNiPO_4$ begins to diminish and $Ni_{12}P_5$ is formed. Carbon is oxidized to CO and $CO_2$. At temperatures higher than 800 °C and thus a more powerful reducing atmosphere, $LiNiPO_4$ is almost completely reduced to $Ni_{12}P_5$.

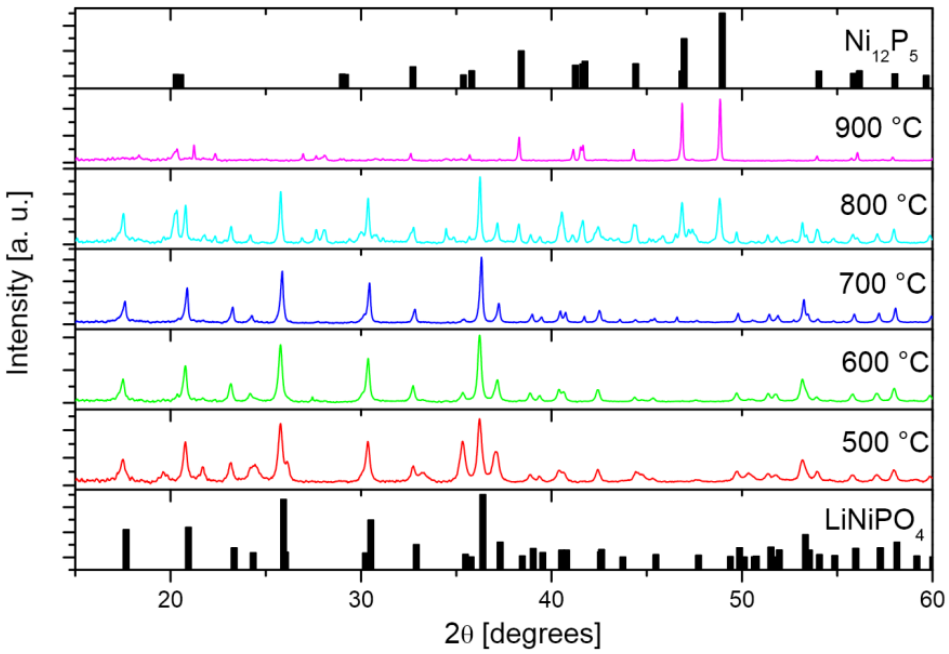


**Figure 53:** XRD of the $LiNiPO_4$ precursor heated to 500, 600, 700, 800, and 900 °C for 12 h. $Ni_3P$ is marked with an asterisk (*).

Rietveld refinement of all samples of the solid solution was performed using the program package Jana2006[132]. Variations of the lattice parameters of the different olivine phases are shown in Figure 54. The values are normalized relative to the value of $LiNiPO_4$ ($y = 0$). Absolute values of the cell parameters are listed in the appendix (Table 11). A linear correlation between lattice parameters and the content ratio of nickel was found (Vegard's law, Figure 54), suggesting the existence of a solid solution in the whole substitution range ($0 \leq y \leq 1$)[333]. All lattice parameters of the unit cell linearly grow with increasing cobalt content from $a$=10.0374(6) Å, $b$=5.8587(3) Å, c=4.6802(3) Å to a=10.2052(10) Å, b=5.9226(6) Å,

c=4.7003(5) Å. The values are in good agreement with previously reported data. The lower cell volume of $LiNiPO_4$ (275 $Å^3$) compared to $LiCoPO_4$ (284 $Å^3$) is often discussed to have an effect on the ionic conductivity. A first reason for the expansion is found in Shannon radii of $Co^{2+}$ ion ($r$ = 88.5 pm) and $Ni^{2+}$ ion ($r$ = 83 pm) in octahedral coordination[334]. However, different effects are observed for the *a*-, *b*-, and *c*-axes; the lowest incline is found for the *c*-axis. Similar behavior was reported for $LiFe_{1-y}Mn_yPO_4$, $LiMn_{1-y}Co_yPO_4$[313] and $LiFe_{1-y}Ni_yPO_4$[106, 335, 336] that must be related to the crystal structure and the interconnection of the $NiO_6$, $CoO_6$, and $PO_4$ polyhedra (Figure 49). Therein, layers of $CoO_6$ and $NiO_6$ polyhedra share corners beaded along the *b*-axis. This causes a stiff arrangement along *b* but flexibility due to simple tilting of the octahedral along *c*. The large substitution effects on the *a*-axis are due to the stiff $PO_4$ tetrahedra that interlink the $CoO_6$ and $NiO_6$ octahedra between the layers (see also [336]). Relatively strong substitution effects are thus found on the unit cell parameter *a* due to the radii of the 3*d* metal cations (Ni, Co). As a result, the sizes for $Li^+$ ion diffusion channels are remarkably reduced for the $LiNiPO_4$ compared to $LiCoPO_4$.

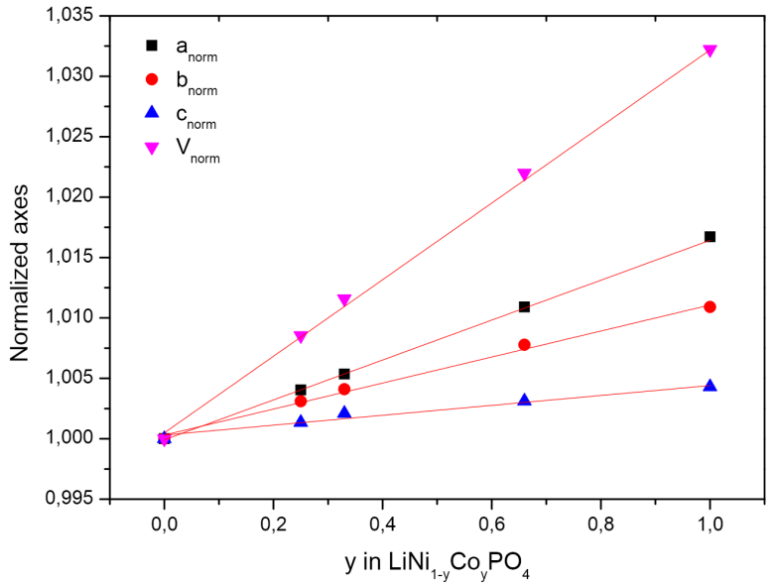


**Figure 54:** Evolution of the cell parameters with rising cobalt content, *y*, for the $LiNi_{1-y}Co_yPO_4$ ($y$ = 0, 0.25, 0.33, 0.66, 1) phase. The values have been normalized to the value at $y$ = 0.

These obtained results match with the IR spectra presented in Figure 55. By a comparison with literature data[293, 305, 311, 337, 338], the bands could be assigned to the different modes of the absorbance spectra of $LiNiPO_4$ (Figure 55 a). This spectrum can be clearly divided into two subregions, which correspond to the external and internal $PO_4$ vibrations (below and above 400 $cm^{-1}$, respectively). The broad nature of the stretching bands in the region from 700 to

1,200 $cm^{-1}$ is due to the asymmetrical bonding of the distorted $PO_4^{3-}$ tetrahedron. Dominant bands are marked by a solid line in Figure 55 b for the substitution of Ni by Co in $LiNiPO_4$. Accordingly, mainly the shoulder at 520 $cm^{-1}$ related to *M*-O stretching is shifted to lower values signalling stronger bonds for *M* = Ni than for *M* = Co. Only tiny effects are found for the P-O mode at 550 $cm^{-1}$. Corresponding vibrations are illustrated by arrows in Figure 55 c. Considering also the shift of the δ(Li-O) vibration to values below 300 $cm^{-1}$, the mentioned effects underline the relation to rising Li-ion conductivity with a higher Co content as proven in [311].

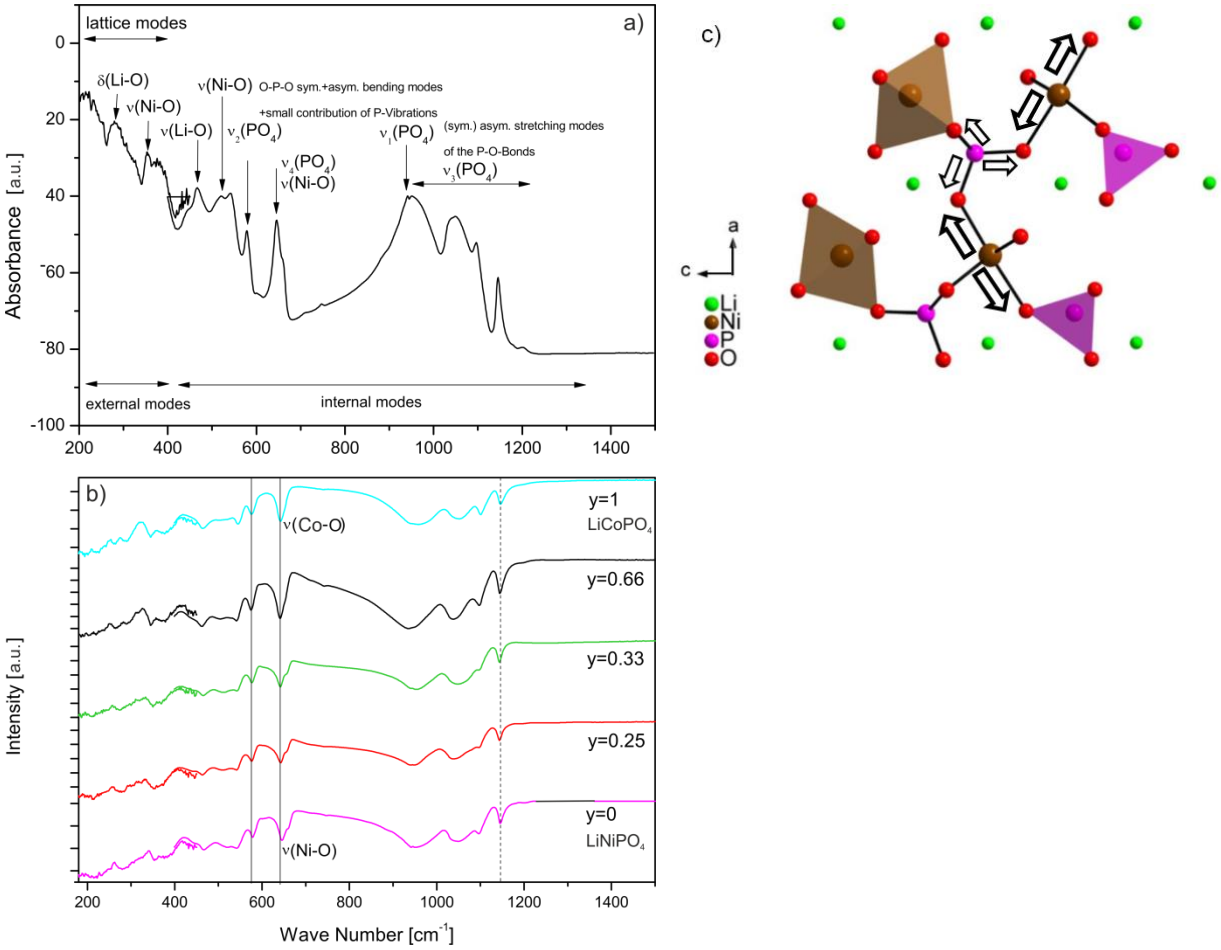


**Figure 55:** a) Absorbance-spectra of $LiNiPO_4$ with assignments to the corresponding modes. b) FTIR and MIR spectra of the solid solution $LiNi_{1-y}Co_yPO_4$. The solid lines illustrate some bands which are shifted with substitution. The dotted line shows a band where no shift can be observed. c) Illustration of the *olivine* structure in the *ac* plane. The arrows show the influence of substitution of Ni against Co in $LiNiPO_4$. With rising cobalt content, the Ni/Co-O and P-O bond length increases. There is a bigger effect on the Ni/Co-O bond, which is shown by enlarged arrows.

*Electrochemical performance*

The electrochemical performance of selected $LiNi_{1-y}Co_yPO_4$ samples was evaluated via constant current charge/discharge testing, as illustrated in Figure 56 a). A high current rate of 2 C was applied to decrease possible electrolyte decomposition. The $LiCoPO_4$ cell offered a first discharge capacity of 114 $mAhg^{-1}$ and a long distinct discharge plateau around 4.7 V which is a typical electrochemical behavior of the $Li/LiCoPO_4$ cell[299, 310]. For $LiNi_{0.33}Co_{0.66}PO_4$, a sloping voltage profile is observed and a slightly lower discharge capacity. To better reveal the performance of the $LiNi_{0.33}Co_{0.66}PO_4$ cathode, charge and discharge curves are outlined in Figure 79 in the appendix. In general, capacity of all samples decreases almost linear with lower cobalt content. No plateaus above 5.0 V are observed for the whole solid solution, where the $Ni^{3+/}Ni^{2+}$redox couple would be expected (≈5.2 - 5.4 V[125]).

Figure 56 b) shows the specific capacity vs. cycle number of the selected samples. These cyclability tests reveal a gradual capacity fading for all samples. The samples exhibit a significant irreversible capacity loss in the first cycles which is likely due to the passivation process of the aluminum current collector as proposed by Sharabi et al[339]. The relative irreversible capacity loss of $LiNi_{0.33}Co_{0.66}PO_4$ is smaller compared to the pure $LiCoPO_4$. After 15 cycles, $LiCoPO_4$ and $LiNi_{0.33}Co_{0.66}PO_4$ obtain the same capacity of around 57 $mAhg^{-1}$. One can conclude that the Ni content might have a positive impact on kinetics of the Li insertion/deinsertion process and consequently account for a slight stabilization effect on capacity retention. Regarding the low capacity which is obtained for the high nickel containing samples ($y$ = 0, 0.25, 0.33) one is left with the suspicion, that the redox reaction of Ni in the structure does not occur, as also proposed by others[306].

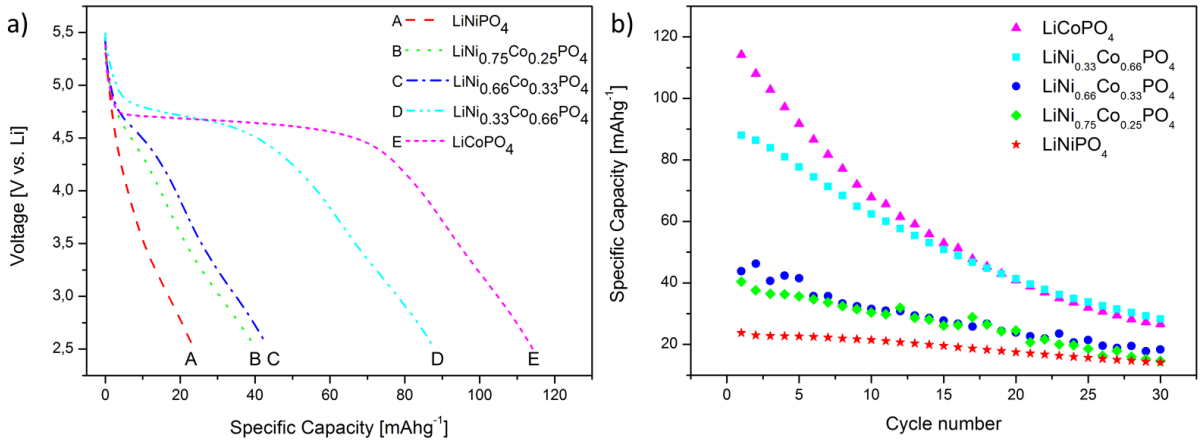


**Figure 56:** a) First discharge curves for A) $LiNiPO_4$, B) $LiNi_{0.75}Co_{0.25}PO_4$, C) $LiNi_{0.66}Co_{0.33}PO_4$, D) $LiNi_{0.33}Co_{0.66}PO_4$, and E) $LiCoPO_4$. b) Specific capacity vs. cycle number for $LiNi_{1-y}Co_yPO_4$ sample electrodes. Current rate 2 C; voltage range 2.5 – 5.5 V.

In order to better reveal features of the electrochemical behavior, dQ/dV (differential capacity) vs. voltage curves were evaluated. A plateau in the voltage profile appears as a peak in the differential curve. Figure 57 a) shows the differential capacity curve for the pure $LiCoPO_4$ electrode. The two peaks in the oxidation process (charge) at 4.84-4.87 and 4.93-4.98 V indicate the two-step redox-reaction which is typical for $LiCoPO_4$[291, 309]. For the reduction process (discharge) it is not obvious if there are one or possibly two badly resolved peaks around 4.66-4.70 V. Furthermore, the voltage difference between corresponding oxidation-reduction peaks in the dQ/dV diagram is higher in the initial charge-discharge cycle than in the following cycles. This behavior indicates the slow kinetic of the initial delithiation and a higher polarization of $LiCoPO_4$ in the first cycle. All peaks show a decrease in height with cycling, suggesting an overall loss in active material or cyclable lithium.

The respective first charge and discharge curves for $LiCoPO_4$ can be seen in Figure 57 b). As expected, two plateaus which are separated by a transition region are indicated in the charge curve. The discharge curve exhibits only one plateau, characteristic for a one-step mechanism. This is in accordance with CV experiments which also show only one reduction peak[340]. In general, the different character of the charge and discharge curves for $LiCoPO_4$ and the mixed *olivines* points to the irreversible structural transformation of the cathode compound during cycling.

The incremental capacity analysis for $LiNiPO_4$ looks totally different (Figure 57 c). There is only one big segregated peak at 4.46-4.62 V in the first charge curve (one runaway in the

charge curve around [4.455 V, -11049.360 $mAhg^{-1}$ $V^{-1}$] has been eliminated). In the higher voltage region, where decomposition of the carbonate-based electrolyte is expected, irregular deflections can be observed and possibly eclipse a further oxidation peak. Moreover, no reduction peaks can be observed. The peak at 4.46 - 4.62 V is by far too low for the expected $Ni^{3+'}/Ni^{2+}$redox couple. Possibly, $LiNiPO_4$ undergoes an irreversible structure deformation or a passivating SEI is built. Furthermore, the current transient could be due to a contribution of a parasitic reaction. In fact, it seems not to be possible to reinsert $Li^+$ in the charged structure. In comparison, the $LiNi_{0.66}Co_{0.33}PO_4$ sample shows reversible Lithium intercalation and deintercalation (Figure 57 d). No such peak around 4.62 V which is apparent in the $LiNiPO_4$ sample is observed. Shrinking peak intensities and a growing voltage difference between oxidation and reduction peak explain the results of declining reversibility.

A completely different picture is observed for the $LiNi_{0.33}Co_{0.66}PO_4$ (Figure 57 e) sample in the dQ/dV plot. Here, the oxidation peak around 4.6 V rises again. Additionally, a double peak around 4.87-5.0 V can be seen. There is evidence to suggest that the first peak is driven by the same phenomenon as in the $LiNiPO_4$ sample. Although the shapes have changed, it is quite certain that the $LiCoPO_4$ part is responsible for the second double peak. In the following cycle, the first peak disappears completely and the second peak takes almost the shape of the pure $LiCoPO_4$ sample. In the discharge cycle, one big peak can be observed at 4.67 – 4.73 V. This peak is slightly shifted in the higher voltage region, which can be a hint on a certain activity of the Ni portion (Figure 57f). At higher magnification (see Figure 57 f, inset), around 5 V an additional reduction peak for the $LiNi_{0.33}Co_{0.66}PO_4$ sample is indicated. This peak is present in all cycles. So to conclude, there might be a certain kind of activity of the $Ni^{3+}/^{2+}$ redox couple at this special Ni:Co ratio.

To summarize, with increasing Ni content, the electrochemical activity is drastically reduced. No activity is observed in the voltage region which is expected for the $Ni^{2+}/Ni^{3+}$ redox couple. From that, one can draw the conclusion that the nickel part is not electrochemically active in samples with high nickel content synthesized by this sol-gel process. A possible explanation is that the intercalation process is inhibited because of the mentioned crystal structure changes. Additionally, one could also think about particle surface reactions of $LiNiPO_4$ with C. From the present result, one must conclude that this question is not yet answered, especially as Ni seems active in $LiNi_{0.33}Co_{0.66}PO_4$. Remembering the SEM results, which show an increasing agglomeration towards higher nickel content, morphology of the samples might also play a

role. In general, the capacity fading of all selected samples can most likely be ascribed to the applied electrolyte. Aurbach et al.[341] show that the $LiPF_6$ salt used in the electrolyte can partly react with $LiCoPO_4$ upon cycling. Furthermore, the oxidative electrolyte decomposition at the high operation voltage which is already known for $LiCoPO_4$ and other high-voltage materials has to be mentioned[342]. It is obvious that the problem of the anodic stability of the electrolyte should be even more serious for $LiNi_{1-y}Co_yPO_4$ cathode materials[308, 311] with its higher oxidation potential of $Ni^{3+}/^{2+}$. Changing the electrolyte and additional usage of HF scavenger separators seem to be a promising approach to improve electrochemical performance of this solid solution[339, 343].

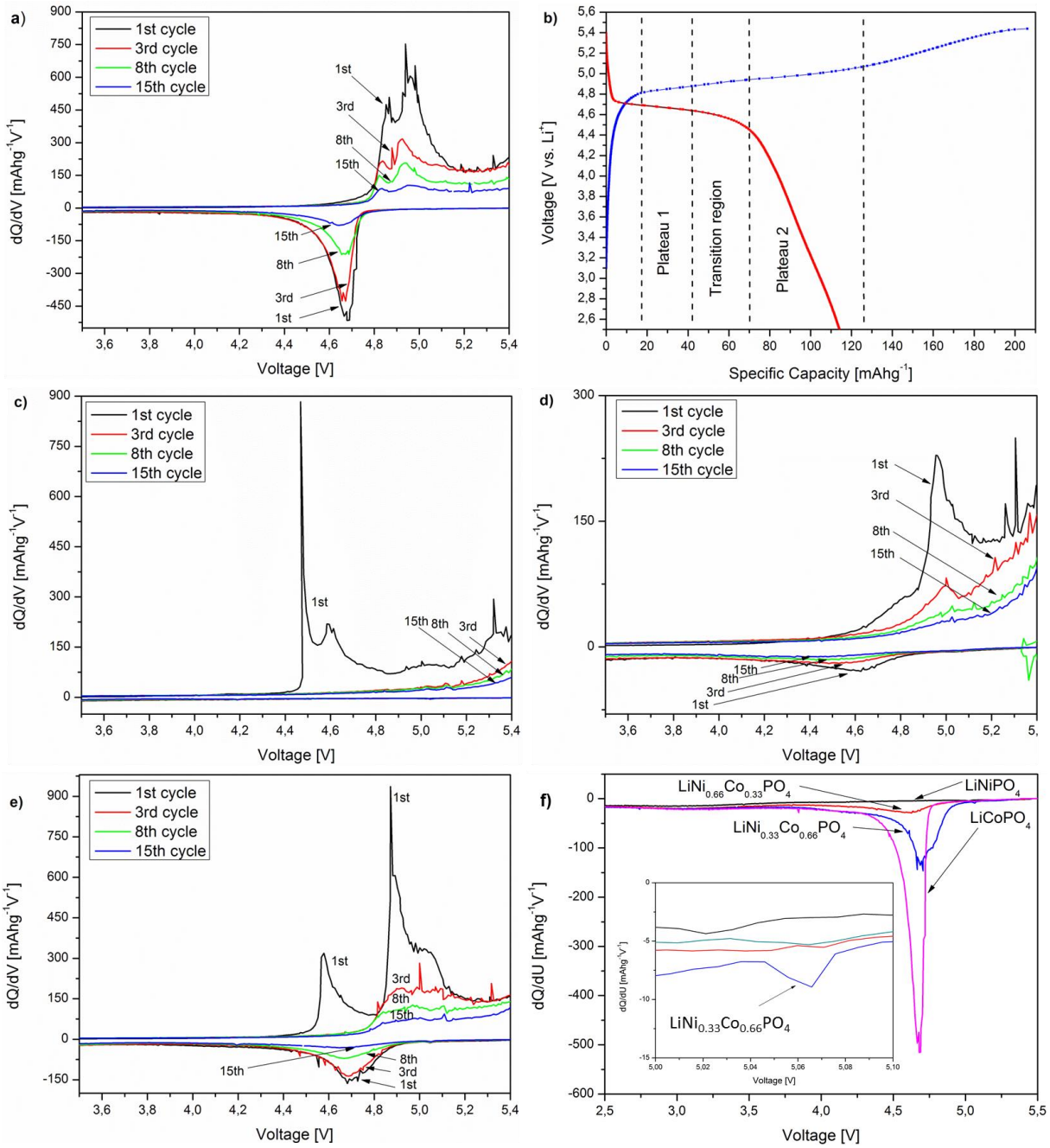


**Figure 57:** a) Differential capacity curve, dQ/dV vs. V of $LiCoPO_4$. b) First charge and discharge curve of $LiCoPO_4$, c) dQ/dV vs. V of $LiNiPO_4$, d) dQ/dV vs. V of $LiNi_{0.66}Co_{0.33}PO_4$, and e) dQ/dV vs. V of $LiNi_{0.33}Co_{0.66}PO_4$. f) dQ/dV vs. V of the first discharge curve for the whole solid solution. Inset dQ/dV vs. V of the first discharge curve for the whole solid solution at a higher resolution.

# 3. The development of a cheap, safe and easy system for the measurement of electrochemical cells

## 3.1. Experimental

For the establishment of a first electrochemical characterization method for electrode materials, a processing chain was developed of which all steps can be done in our working group. The steps are cheap, easy and optimized for minimal expenses. Exclusively cheap elements (glassware, electronics, aluminium sample holder) were used and $LiPF_6$ was replaced by $LiClO_4$ to bypass the risk of HF-formation.

*Design of the three-electrode cell*

As "reaction vessel" a screw lid glass of around 40 ml was taken. Three copper-wires were surrounded by shrink tubes and put through drilled holes in the cap. The cap was sealed by hot-melt adhesive on both sides to ensure internal cohesion of the system. A Teflon spacer was included between the copper wires to fix them in the right position. At the bottom of the copper wires, gold-coated clips were welded and banana plugs at the other end. The banana plugs serve as connection to the potentiostat (Figure 58), whereas the clips are used to mount the electrodes. The space from the clips to the bottom was kept short to minimize the required amount of electrolyte for each measurement. Operating outside of the glove box is possible with this system after the reaction vessel is screw down under protective environment.

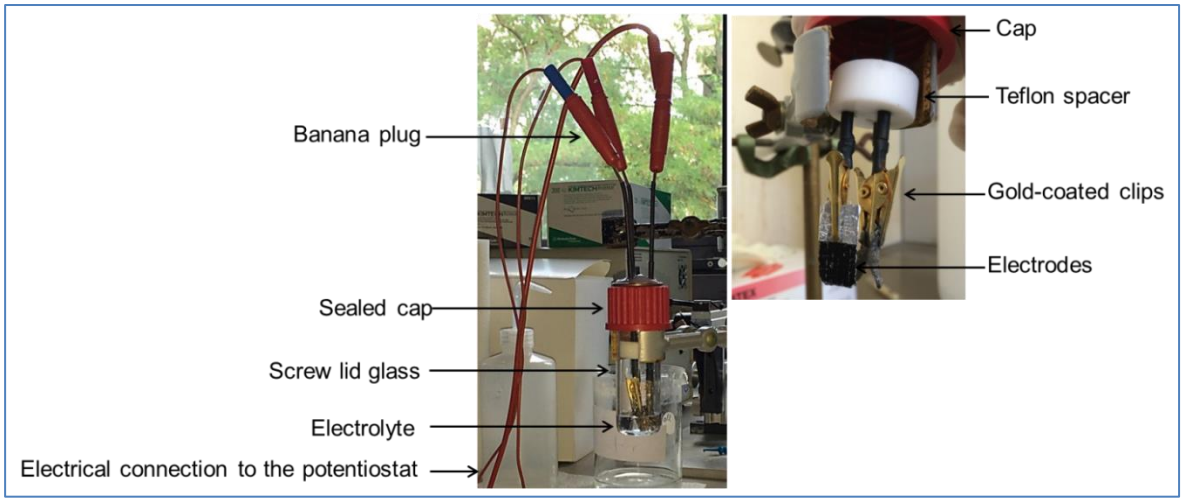


**Figure 58:** The applied three-electrode cell.

*Mixing of the electrolyte*

For the electrolyte a 1 M solution of $LiClO_4$ in a mixture of ethylene carbonate and dimethylene carbonate (v:v = 50:50) was prepared. Therefore a specified volume of dimethylene carbonate was put into a two-necked flask under protective atmosphere. Afterwards, ethylene carbonate was melt at 100 °C and the same volume was given into the flask under stirring. $LiClO_4$, the conducting salt, was inserted as last compound. For a good mixing, the solution was stirred for 1 h at 90 °C and stored under argon.

*Preparation of the working-electrode*

*Preparation of the electrode slurry*

The electrode slurry was prepared with the composition of 70 wt% active material (e.g. $LiNiPO_4$), 15 wt% conductive carbon black (acetylene black) and 15 wt% binder (Polyvinylpyrrolidone, PVDV). First, the active material and conductive carbon black were finely ground together in an agate mortar to ensure a good blending. Then the binder was also ground together with the other parts. The electrode slurry was prepared by adding an adequate amount of N-Metyhlpyrrolidone (NMP) and mixing it with the ground material (Figure 59 a-b). Hereby NMP acts as the solvent of PVDV. Different amounts of NMP were tried out. It became apparent that very fluid slurry is not appropriate for the electrode “holders” as it does not adhere sufficiently on the respective electrode holders.

*Preparation of the electrode*

Two different electrode holders were tested. When a simple aluminium foil was used, some serious problems encountered. First, without a doctor blade attachment it proved to be almost impossible to wangle a homogeneous layer onto the aluminium foil. Second, the dried layer did not adhere sufficiently enough on the foil so that parts detached as powder, especially when the foil was bent or dipped into the electrolyte solution. Third, as the electrodes are surrounded by the electrolyte, in principle both sides should be coated with the slurry.

To bypass the problems which occurred with the aluminium foil, finely woven aluminium net was chosen as the preferred choice. The slurry was spread onto the net and waited overnight

(Figure 59 c-d). On the next day, the electrode was dried on air at 160 °C for a few hours (heating ramp 5 °C/min). The arid electrode was wrapped with aluminium and pressed at 2 t for 5 min. Afterwards it was contacted with aluminium at the uncoated end and stored in argon (Figure 59 e-f). Before the electrode was used it was dried again at 150 °C under vacuum and directly transferred to the glove box under protective atmosphere (Figure 59 g-h).

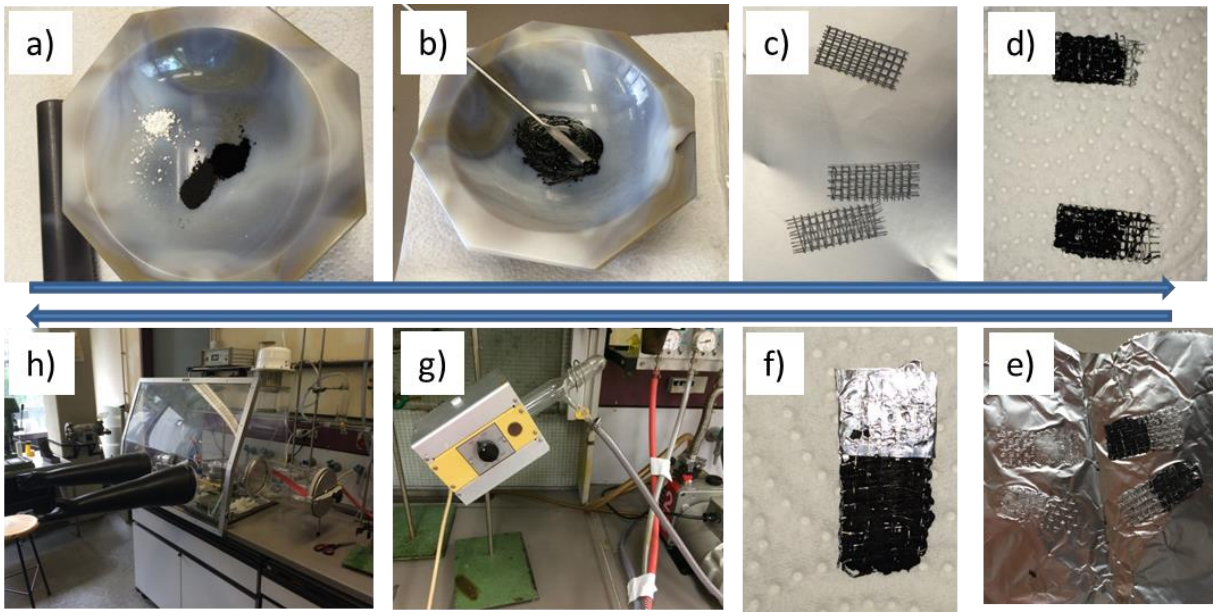


**Figure 59:** Preparation of the electrode slurry and completing of the electrode.

*Preparation of the reference and counter electrode*

Elemental lithium was used as reference and counter electrode. Therefore a small, flat stripe was cut from a lithium rod which was stored in paraffin oil. The lithium stripe was freed of the paraffin oil and sandpapered with the aid of a stamp and a rough plastic cutting board.

*Assembling of the three-electrode cell*

The final assembling of the three-electrode cell was done in a self-made glove box under argon. The electrolyte was filled into the screw lid glass up to a defined height, so that the clips were not touched. After that, the working electrode (contained the active material) and

the reference and counter electrode (contained lithium) were mounted on the clips. As the screw lid glass was carefully screwed down, it could be transported to the potentiostat.

*Measuring of a CV experiment*

The CV experiments were performed in the laboratories of the Institute for Analytical Chemistry (University of Regensburg). The three-electrode cell was connected with the potentiostat by the banana plugs and fixed on a place where no vibration was possible. Sometimes also a Faraday cage was used. In a typical experiment the voltage was altered with a specific scan rate (e.g. 0.02 $mVs^{-1}$) and the corresponding modifications of the current were detected and evaluated. Electrochemical interactions of the active electrode with the working electrode could be seen on variations of the current.

*Synthesis of the active materials*

The sol-gel synthesis of $LiNiPO_4$, $LiNi_{0.33}Co_{0.66}PO_4$ and $LiCoPO_4$ was already described in chapter V.2.1. For $LiFePO_4$ the same synthesis protocol was applied. $LiCoO_2$ was prepared according to Tao and co-workers[344]. $LiNO_3$ and Co(II) acetylacetonate with molar ratio 1:1 was mixed and dissolved in 7 ml ethyleneglycol and 3 ml distilled water to form a sol. The sol was then kept at 120 °C for 24 h. The obtained gel was pre-fired at 250 °C and calcined at 500 °C overnight to form the $LiCoO_2$ phase.

## 3.2. Results

### 3.2.1. Proof of principle

Main challenges which had to be overcome were the application of a suitable electrode holder, the work out and application of the appropriate viscosity of the electrode slurry and the contacting of the electrode holder. The electrolyte and the three-electrode cell were prepared/built up once and used without further amendments.

The proof of principle of the applied setup was done with the help of the well-known and good characterized $LiCoO_2$[345]. Its usability as electrode material was already discovered in 1980 by John B. Goodenough and co-workers[346]. The first Li-ion battery which was commercialized by Sony in 1991 used $LiCoO_2$ as the positive electrode and graphite as the negative electrode. This vast interest led also to the discovery of a high- and low-temperature phase of $LiCoO_2$ (HT- or LT-$LiCoO_2$). HT layered $LiCoO_2$ is usually produced by high temperatures above 500 °C and is of the trigonal space group $R\bar{3}m$ with oxygen anions occupying the *6c* sites and lithium and cobalt cations occupying *3a* and *3b* octahedral sites respectively, with c/a=4.99[347]. This gives a structure of lithium layers alternating with cobalt layers between layers of oxygen. The *spinel* LT-phase with c/a=4.90 gives an ideal cubic-close-packed oxygen-ion lattice (space group *Fd3m*).

The XRD pattern of the applied $LiCoO_2$ sample which was prepared by a sol-gel synthesis can be seen in Figure 60 a. Aside the diffraction peaks of the $LiCoO_2$ phase a small side phase of $Co_3O_4$ is observed. The lattice parameters calculated, assuming a hexagonal setting, show excellent agreement with those reported in the literature ($a$ = 2.810(2) Å, $c$ = 14.059(4) Å)[348]). The c/a ratio of ~5 indicates that the system is predominantely the HT-phase of $LiCoO_2$, although the compound was prepared at relatively low temperatures. This can be attributed to the sol-gel process which is known to reduce the required temperature[349]. However, it is very difficult to identify the presence of minimal quantities of the *spinel* LT-$LiCoO_2$ phase co-existing with the HT-$LiCoO_2$ phase using X-ray diffraction methods[350].

The cyclic voltammogram with multiple cycles for $LiCoO_2$ is shown in Figure 60 b. A scan rate of 0.2 mV $s^{-1}$ in the potential window range of 3.0 – 4.4 V was applied. An electrochemical reaction depicted by one big peak at 4.29 V in the anodic region (oxidation) and two peaks around 4.09 V and 3.68 V in the cathodic region (reduction) is observed. This is roughly in accordance with Rossen and co-workers who report that a standard HT-$LiCoO_2$ has most of its capacity in the region of 3.8 V to 4.3 V[347]. The big broad peaks at 4.29 V and 3.68 V refer to the oxidation and reduction of the layered HT-$LiCoO_2$ with $Li^+$ deinsertion/insertion, respectively. This is linked to the first order metal-insulator transition between two hexagonal phases[351] at a redox potential around 3.99 V. The expected order/disorder phase transitions, coupled to a lattice distortion from the hexagonal to the monoclinic structure at higher voltage (and therefore a higher state of charge) are not visible in the anodic region, but are indicated in the cathodic region around 4.09 V[352, 353]. In general

the electron transfer of the reaction is very slow as the main peaks are very broad and the separation between the mid-peak potentials is very large (610 mV)[354]. Nevertheless, the shape of the individual cycles only slightly changes, with a greater deviation from the first to the second one. During the subsequent cycles, the CV curves exhibit moderately good reproducibility and similar shapes, reflecting reversibility of lithium storage[355]. The cathode materials even seem to be activated after the first cycle as the peaks are getting narrower and the separation are getting smaller in the second cycle.

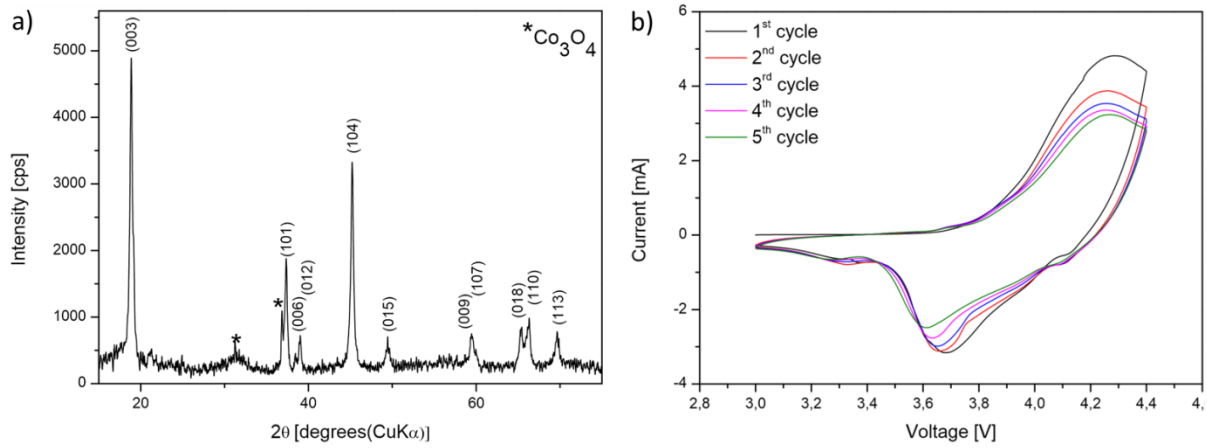


**Figure 60:** XRD pattern of HT-$LiCoO_2$ and corresponding cyclic voltammogram curves in the potential window range of 3.0 – 4.4 V at a scan rate of 0.2 mV $s^{-1}$.

Some CV experiments were also performed for the sol-gel synthesized *olivine*-type $LiFePO_4$ and $LiCoPO_4$ (Figure 61). $LiFePO_4$ exhibits oxidation peaks at 3.93 - 4.05 V and distinct reduction peaks at 2.77 - 2.86 V, consistent with a two-phase redox reaction at about 3.40 V. Thereby, the value of the redox reaction is in absolute accordance with the literature[356, 357]. For $LiCoPO_4$ an oxidation peak is indicated around 5.28 V and a corresponding reduction peak around 4.49 V. This results in the expected redox potential of ~4.89 V[310]. Unfortunately, the experiment is not able to resolve the reported two-step oxidation reaction (see also chapter V.2). Higher potentials >5 V cannot be used as the electrolyte would suffer from such a high potential. The kinetics of the electron transfers of both samples are very slow, indicated by the broad peaks and the big potential difference of 1.07 V and 0.79 V for $LiFePO_4$ and $LiCoPO_4$, respectively.

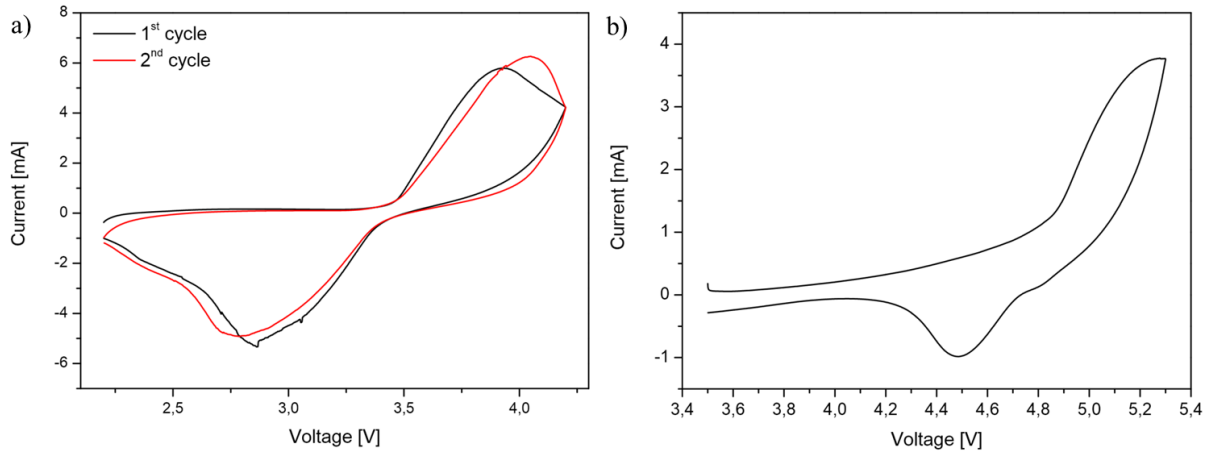


**Figure 61:** a) Cyclic voltammogram curves of $LiFePO_4$ in the potential window range of 2.2 - 4.2 V at a scan rate of 0.2 mV $s^{-1}$. b) Cyclic voltammogram curve of $LiCoPO_4$ in the potential window range of 3.5 - 5.3 V at a scan rate of 0.2 mV $s^{-1}$.

These results prove that the setup is in principle able to detect and depict electrochemical processes, even for multiple cycles. The redox potential of "easy" reactions can be determined in an adequate manner. Nevertheless, the kinetics of the electron transfers seem to be very slow which leads to very broad peaks. Therefore, the setup is not suitable for complex processes, where small peaks directly adjacent to one another. Furthermore, very broad potential windows have to be scanned to depict the whole electrochemical process. Therefore, the system is more suitable for electrochemical processes in the low-voltage region where broad potential ranges can be applied.

### 3.2.2. The electrochemical reaction of $Ni_3Pb_2S_2$

The *shandite*-type compounds with its hexagonal symmetry (space group $R\bar{3}m$) can be considered as a layered structure. Therefore, two different useful reactions with lithium are conceivable. On the one hand, lithium ions could be (reversibly) intercalated/deintercalated between the layers as seen for $TiS_2$ where Li can be inserted over a large range of concentrations leading to compositions $Li_xTiS_2$, $x = 0 - 1$[358]. On the other hand, as already mentioned in the introduction, a so-called "conversion reaction" may be present. Hereby, the reversible electrochemical reaction mechanism of Li with transition-metal oxides or other chalcogenides general proceeds like a displacive redox reaction[45, 46, 359, 360]. At the end of the conversion reaction nanosized metal particles are embedded in a $Li_2Q$ matrix (eq. (37)).

$TM_xQ_y + 2\,y\,e^- + 2\,y\,Li^+ \rightarrow x\,[TM]^0 + y\,Li_2Q$ **(37)**

*TM* = transition metal, *Q* = O, Se, Te

In subsequent charge-discharge cycles reversible redox processes involve metals and their oxides (eq. (38)).

$X\,[TM]^0 + y\,Li_2Q \rightarrow x\,TMO + (y*2)\,Li$ **(38)**

For the evaluation of the electrochemical reaction of $Ni_3Pb_2S_2$, a $Ni_3Pb_2S_2$ bulk sample was prepared as electrode material in the same manner as already mentioned in chapter V.3.1. As $Ni_3Pb_2S_2$ does not contain any lithium, the electrode was applied as the potential anode in the system. The material was first discharged from 2.5 V to 0 V and afterwards charged to 2.5 V again. An interesting electrochemical reaction with lithium is observed. Remarkably, the first CV sweep is substantially different from the subsequent one. The small peak, which is centred at around 1.5 V is only present in the first discharge curve and disappears upon the subsequent cycling. It can be most likely be ascribed to the decomposition reactions of the electrolyte solution and the formation of a SEI layer[361, 362]. The cycling shows a strong fading during progressive cycling at a slow rate of 0.15 mV $s^{-1}$, as already the second cycle looks completely different. One cathodic around 1 V and two anodic peaks around 0.5 and 1.7 V are indicated in the second cycle. If one compares the reaction of $Ni_3Pb_2S_2$ with that of $MnFe_2O_4$[45], which reacts in a conversion reaction, a big similarity of the cyclic voltammogram curves is seen.

Assuming, that $Ni_3Pb_2S_2$ reacts in a typical conversion reaction with lithium, the big capacity fading can be explained accordingly. The formation of a new metallic and/or sulfidic phase and also the insertion/extraction of lithium itself may lead to large volume changes. Mechanical stresses and aggregation of the particles which can lead to a loss of contact to the current collector[363, 364] are also conceivable. Even if the formulation of reaction equations with the little information would be too unscientific, some theoretical interpretations should be allowed. In the structure of the ternary *shandite* phase, the transition metal Ni in the oxidation number 0 and the main group metal Pb in the oxidation number +II are present. Therefore, $Pb^{2+}$ is the only species which can be reduced in the system. It might be possible that in a first reaction Ni, Pb and $Li_2S$ are formed, which would explain the violent reaction in the first cycle. Furthermore it seems reasonable that PbS and different nickel sulfides, together

with elemental lithium are formed in a second step. The stability of PbS would then prevent a further reaction.

Nevertheless, no statement about the exact Li-storage mechanism of the $Ni_3Pb_2S_2$ anode can be made, without the help of ex-situ XRD data and other analytical methods (e.g. Mössbauer spectroscopy) on the $Ni_3Pb_2S_2$ anode material. Therefore, $Ni_3Pb_2S_2$ has to be discharged/charged to different potentials to obtain different Li contents. Furthermore, various voltage windows and sweep rates should be evaluated, as this e.g. drastically improved the reversibility for $MnFe_2O_4$[45]. Especially, nanoscale dendritic $Ni_3Pb_2S_2$ should also be evaluated as potential anode material, as nanomaterials proved to be able to enhance the electrochemical reactions many times over.

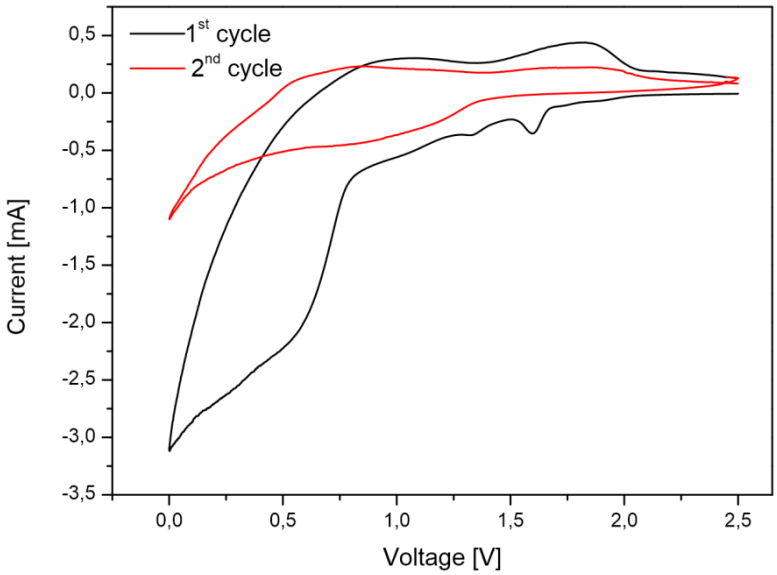


**Figure 62:** Cyclic voltammogram curves of $Ni_3Pb_2S_{2,bulk}$ in the potential window range of 0 - 2.5 V at a scan rate of 0.15 mV $s^{-1}$.

## 3.3. Potential possibilities for the improvement of the applied electrochemical measurement setup

The cyclovoltammetric measurements revealed some weaknesses of the applied setup, e.g. slow electron transfer and poor capacity retention. Not much effort could be put into the troubleshooting so far as only sparse measurement time was available. It can be assumed that one has to deal with error propagation as the whole "system" was established from scratch.

The problematic already starts with the mixing of the electrolyte, which had to be done in a simple perspex box. It is debatable if the integrity of the electrolyte can be guaranteed. The usage of a simple copper grid as "electrode holder" and gold-coated clamps might also be problematic as already small impurities affect the electrochemical results. Furthermore, the preparation of the electrode slurry is not optimal by just grinding and mixing all ingredients in an agate mortar.

In general it should be considered to downsize the whole cell as too much expensive electrolyte is wasted for each measurement. Moreover, working under big electrolyte excess falsifies the battery character and slows down the kinetics. A first improvement suggestion without the need to change the whole setup is to use a slower sweep rate to allow the observation of defined voltammetric fingerprints. Furthermore, ball-milling of the electrode material can homogenize and downsize the particles, which improves the kinetics of the electrochemical reaction. A further simple improvement strategy is to work with bigger batch sizes. Especially during the preparation of the electrode slurry a magnetic stirrer could then be used to ensure a better mixing of the electrode slurry.

## 4. Summary and discussion

Co-/Ni substitution effects were studied on phase pure compounds of the solid solution $LiNi_{1-y}Co_yPO_4$ ($y = 0$, 0.25, 0.33, 0.66, 1) as prepared via a non-aqueous sol-gel method that includes carbon coating. Crystallite size for the as-prepared samples was found to be below 30 nm due to XRD and SEM analyses. For $LiNiPO_4$, the formation and the conditions for the formation of the phosphide by-products $Ni_3P$ and $Ni_{12}P_5$ were investigated that were recently related to the formation of conductive networks on *olivine* particles. The primary particles of the high nickel containing samples appear to be highly agglomerated and irregular in shape. Due to XRD analyses, *olivine*-type crystal structures are confirmed for the entire solid solution. The lattice parameters change linearly with $y$. Different effects for $a$ and $b$ lattice parameters are related to stiff and flexible interlinking of $MO_6$ ($M$=Co, Ni) and $PO_4$ polyhedrons for the different directions. The increasing cell volumes from $M$ = Ni to $M$ = Co are accompanied by weakened $M$-O bonds as shown by FTIR spectroscopy. The results underline discussed size effects on the channels for lowered $Li^+$-ion conductivity in $LiNiPO_4$.

The electrochemical reactivity and cycle life degrade with increasing Ni content in $LiNi_{1-y}Co_yPO_4$ samples. At a Ni content of 33%, a stabilization effect of cycle life is observed and dQ/dV plots show a shift of the reduction peak to higher voltage regions. Ni seems to show small electrochemical reversibility at this Ni/Co ratio. The fast capacity fading is likely related to the oxidation of the electrolyte and the poor stability of the charged $CoPO_4$ and $NiPO_4$ phases. Thus, selection of an electrolyte with better anodic stability or some coating to protect the surface would be necessary to maintain the stability of the electrodes.

In the second part of this chapter an own setup for the electrochemical testing of electrode materials was established. Despite some deficiencies, the correct redox potential of some known compounds could be determined and the continuous measurement of multiple cyclovoltammetric cycles proved to be feasible. Nevertheless, the kinetics of the electron transfer is very slow which results in very broad peaks. More complex reactions with peaks that are close to proximity will therefore lead to problems, as some peaks might not be resolved or overlap. Already now, and especially after some minor improvements galvanostatic charging tests can also be performed with this approach. A first test of $Ni_3Pb_2S_2$ as potential anode material revealed a violent reaction with lithium, which seems to justify further research.

# VI. Conclusions and further work

In this thesis different nano- and microscale multinary nickel compounds with varying compositions and structures were evaluated. It was focussed on compositions of the ternary *shandite*- and *parkerite*-type ($Ni_3A_2X_2$, $A$ = In, Tl, Pb, Sn, Bi; $X$ = S, Se) compounds, as well as on the *olivine*-type compounds ($LiMPO_4$, $M$ = Fe, Ni, Co). Thereby, the evaluation of the effect of the synthesis conditions on the composition, structure, morphology and properties of the samples put out the main part. Furthermore, big attention was given to the respective mechanisms of formation of the compounds, in solution and solid-state based synthesis routes. The polyol and sol-gel technique were chosen as they support small and well crystalline particles and offer the possibility to change various parameters independently. To characterize the electrochemical behaviour of some selected samples, galvanostatic cycling tests and cyclovoltammetric measurements were applied. The morphology and structure of the

compounds was evaluated by scanning electron microscopy and HT-/LT-powder diffraction, respectively.

In the main part of this thesis a generalized synthesis protocol for the morphological controlled low-temperature synthesis of $Ni_3A_2X_2$ materials was developed. The concept involves the conversion reaction of binary chalcogenides to multimetal ternaries in an alkaline polyol medium. Most often, a unidirectional diffusion of the in situ produced nickel into the binary chalcogenide takes place. By carefully adjusting the parameters, all sulfur containing *shandite*-type compounds could be prepared from solution. It should be highlighted, that it was possible to synthesize spherical $Ni_3Sn_2S_2$, dendritic $Ni_3Pb_2S_2$ and star-like $Ni_3Tl_2S_2$ by this approach. The selenium containing compounds proved to be more difficult, although they proceed by the same mechanism. Only incomplete conversions of the binary selenium compounds could be observed. By carefully adjusting the redox and equilibrium conditions it was furthermore learned how to selectively direct the reaction to conversion reactions (binary chalcogenide→ternary or different binaries) or "deposition reactions" (binary→core-shell/hybrid particle). The knowledge of such fundamentally processes might contribute to the continuous development of the synthesis methods for inorganic materials. After the successful synthesis, selected samples were further characterized in terms of specific surface area, thermomechanical and electrochemical properties. Especially concerning the thermomechanical properties, big differences were observed for nano and bulk particles.

The second part describes the synthetic approach of converting intermetallics to multimetal chalcogenides of the *parkerite*- and *pyrite-type* series. The reported pathway over $Bi_2S_3$ as morphological template could have been disproved by a disassembly of the reaction into a three-step mechanism with the reaction intermediates Bi-NiBi-$Ni_3Bi_2S_2$. Instead of $Bi_2S_3$, Bi and NiBi are identified as reactive and morphological template. Based on these results the generality of the approach of converting intermetallics (here NiBi) to multinary chalcogenides could be shown for the selenium containing homologues. Starting from NiBi it was possible to selectively direct the reaction to NiBiSe or $Ni_3Bi_2Se_2$ by a change in reaction conditions. This is the first report of the application of intermetallics for the conversion reaction to ternaries, where even the metal content (in that case nickel) can be set, selectively. It is concluded that intermetallics can be used on a broad base for the synthesis of multimetal chalcogenides.

The third part of this work was devoted to the systematic structural and electrochemical characterization of the *olivine*-type compounds $LiNiPO_4$, $LiCoPO_4$ and its solid solution, $LiNi_{1-y}Co_yPO_4$. Based on a non-aqueous sol-gel synthesis, single phase particles with particle sizes below 300 nm were obtained. Rising electronic conductivity by cobalt substitution could be related to larger cell volumes, longer atomic distances, and weaker P-O and *M*-O bonds. The formation of the conducting side phase $Ni_3P$ by carbothermal reduction was detected in $LiNiPO_4$ at temperatures, higher than 650 °C and could be suppressed by Co substitution. It is assumed to be related to the more facile reduction of Ni(II) in $LiNiPO_4$ versus Co(II) in $LiCoPO_4$. Galvanostatic cycling revealed drastically reduced electrochemical activity with rising nickel content. Surprisingly, at a Ni content of 33%, a stabilization effect of cycle life was observed and dQ/dV plots showed a shift of the reduction peak to higher voltage regions. Ni seems to show small electrochemical reversibility at this Ni/Co ratio.

Simultaneously, a home-made cyclovoltammetric cell was built for the electrochemical testing of electrode materials which can also operate outside a glove box. All steps, from the electrolyte, over the electrodes (cathode, anode, reference electrode) and the cell were established from scratch. The operational functionality was shown for first examples and quite accurate results were obtained. The application of $Ni_3Pb_2S_2$ as anode material showed first interesting electrochemical reactions with lithium, which should be evaluated further.

# VII. Bibliography

[1] S. Chung, J. T. Bloking, Y. Chiang *Nat. Mater.* **2002**, *1*, 123-128.

[2] T. Wu, H. Zhang *Angew. Chem. Int. Ed.* **2015**, *54*, 4432-4434.

[3] M. Herlitschke, A. Tchougréeff, A. Soudackov, B. Klobes, L. Stork, R. Dronskowski, R. Hermann *New J. Chem.* **2014**, *38*, 4670-4677.

[4] J. Koenig, M. Winkler, T. Dankwort, A. Hansen, H. Pernau, V. Duppel, M. Jaegle, K. Bartholomé, L. Kienle, W. Bensch *Dalton Trans.* **2015**, *44*, 2835-2843.

[5] T. M. Tritt *Science* **1999**, *283*, 804-805.

[6] P. Pust, V. Weiler, C. Hecht, A. Tücks, A. S. Wochnik, A. Henß, D. Wiechert, C. Scheu, P. J. Schmidt, W. Schnick *Nat. Mater.* **2014**.

[7] S. J. Irvine, RSC Energy and Environment Series No. 12, *Materials challenges: inorganic photovoltaic solar energy*, Royal Society of Chemistry, Cambridge, UK, **2014**.

[8] E. Braun, S. MacDonald, *Revolution in miniature: The history and impact of semiconductor electronics*, Cambridge University Press, Cambride, UK, **1982**.

[9] F. Bachhuber, J. Rothballer, T. Söhnel, R. Weihrich *J. Chem. Phys.* **2013**, *139*, 214705.

[10] R. Weihrich, S. F. Matar, E. Betranhandy, V. Eyert *Solid State Sci.* **2003**, *5*, 701-703.

[11] G. Kuhn, S. Mankovsky, H. Ebert, M. Regus, W. Bensch *Phys. Rev. B* **2013**, *87*, 085113.

[12] F. Fievet, J. Lagier, M. Figlarz *MRS Bull* **1989**, *14*, 29-34.

[13] F. Fievet, J. Lagier, B. Blin, B. Beaudoin, M. Figlarz *Solid State Ionics* **1989**, *32*, 198-205.

[14] H. Jungk, C. Feldmann *J. Mater. Sci.* **2001**, *36*, 297-299.

[15] C. Feldmann *Adv. Funct. Mater.* **2003**, *13*, 101-107.

[16] R. E. Cable, R. E. Schaak *Chem. Mater.* **2005**, *17*, 6835-6841.

[17] R. Boldt, A. Grigas, M. Heise, T. Herrmannsdörfer, A. Isaeva, S. Kaskel, D. Köhler, M. Ruck, R. Skrotzki, J. Wosnitza *Z. anorg. allg. Chem.* **2012**, *638*, 2035-2043.

[18] M. Heise, J. H. Chang, R. Schönemann, T. Herrmannsdörfer, J. Wosnitza, M. Ruck, *Chem. Mater.* **2014**, 26, 5640-5646.

[19] A. M. Guloy, Z. Tang, R. Ramlau, B. Böhme, M. Baitinger, Y. Grin *Eur. J. Inorg. Chemi.* **2009**, *2009*, 2455-2458.

[20] D. Freudenmann, S. Wolf, M. Wolff, C. Feldmann *Angew. Chem. Int. Ed.* **2011**, *50*, 11050-11060.

[21] E. Ahmed, J. Breternitz, M. F. Groh, M. Ruck *CrystEngComm* **2012**, *14*, 4874-4885.

[22] Y. Lin, S. Dehnen *Inorg. Chem.* **2011**, *50*, 7913-7915.

[23] Y. Lin, W. Massa, S. Dehnen *Chem. Eur. J.* **2012**, *18*, 13427-13434.

[24] A. P. Alivisatos, S. Aloni, L. Amirav, P. K. Jain *J. Am. Chem. Soc.* **2010**, *132*, 9997-9999.

[25] Y. Vasquez, A. E. Henkes, C. J. Bauer, R. E. Schaak *J. Solid State Chem.* **2008**, *181*, 1509-1523.

[26] F. Dawood, B. M. Leonard, R. E. Schaak *Chem. Mater.* **2007**, *19*, 4545-4550.

[27] S. Penner, M. Armbrüster *Chem. Cat. Chem.* **2015**, *7*, 374-392.

[28] A. Ota, J. Kröhnert, G. Weinberg, I. Kasatkin, E. L. Kunkes, D. Ferri, F. Girgsdies, N. Hamilton, M. Armbrüster, R. Schlögl, M. Behrens *ACS Catal.* **2014**, *4*, 2048-2059.

[29] H. Wang, M. Shao, S. Wang, H. Gao, G. Shao *J. Cryst. Growth* **2008**, *310*, 3508-3511.

[30] G. Qian, M. Shao, Y. Tong, Y. Ni *J. Cryst. Growth* **2005**, *284*, 412-416.

[31] R. Weihrich, I. Anusca *Z. anorg. allg. Chem.* **2006**, *632*, 1531-1537.

[32] R. Weihrich, I. Anusca, M. Zabel *Z. anorg. allg. Chem.* **2005**, *631*, 1463-1470.

[33] R. Weihrich, S. F. Matar, V. Eyert, F. Rau, M. Zabel, M. Andratschke, I. Anusca, T. Bernert *Prog. Solid State Chem.* **2007**, *35*, 309-327.

[34] J. Rothballer, F. Bachhuber, F. Pielnhofer, S. M. Schappacher, R. Pöttgen, R. Weihrich *J. Europ. Inorg. Chem.* **2013**, *2*, 248-255.

[35] J. Rothballer, F. Bachhuber, S. M. Rommel, T. Söhnel, R. Weihrich *RSC Adv.* **2014**, *4*, 42183-42189.

[36] J. Corps, P. Vaqueiro, A. V. Powell *J. Mater. Chem. A* **2013**, *1*, 6553-6557.

[37] A. Umetani, E. Nagoshi, T. Kubodera, M. Matoba *Physica B* **2008**, *403*, 1356-1358.

[38] W. Schnelle, A. Leithe-Jasper, H. Rosner, F. M. Schappacher, R. Pöttgen, F. Pielnhofer, R. Weihrich *Phys. Rev. B* **2013**, *88*, 144404-1-144404-8.

[39] K. J. Range, F. Rau, M. Zabel, H. Paulus *Z. Kristallogr.* **1997**, *212*, 50.

[40] P. Gütlich, K. J. Range, C. Felser, C. Schultz-Münzenberg, W. Tremel, D. Walcher, M. Waldeck *Angew. Chem. Int. Ed.* **1999**, *38*, 2381-2384.

[41] C. N. Satterfield, Chapter 6 in *Heterogeneous catalysis in practice*, McGraw-Hill, Inc., **1980**

[42] F. Wang, R. Robert, N. A. Chernova, N. Pereira, F. Omenya, F. Badway, X. Hua, M. Ruotolo, R. Zhang, L. Wu *J. Am. Chem. Soc.* **2011**, *133*, 18828-18836.

[43] L. Li, F. Meng, S. Jin *Nano Lett.* **2012**, *12*, 6030-6037.

[44] F. Lin, D. Nordlund, T. Weng, Y. Zhu, C. Ban, R. M. Richards, H. L. Xin *Nature commun.* **2014**, *5*.

[45] S. Permien, H. Hain, M. Scheuermann, S. Mangold, V. Mereacre, A. K. Powell, S. Indris, U. Schürmann, L. Kienle, V. Duppel *RSC Adv.* **2013**, *3*, 23001-23014.

[46] W. Bensch, J. Ophey, H. Hain, H. Gesswein, D. Chen, R. Mönig, P. A. Gruber, S. Indris *Phys. Chem. Chem. Phys.* **2012**, *14*, 7509-7516.

[47] M. G. Kim, S. Lee, J. Cho *J. Electrochem. Soc.* **2009**, *156*, A89-A94.

[48] M. S. Whittingham *Science* **1976**, *192*, 1126-1127.

[49] T. Nagura, K. Tazawa *Prog. Batteries Sol. Cells.* **1990**, *9*, 20.

[50] A. K. Padhi, K. S. Nanjundaswamy, J. B. Goodenough *J. Electrochem. Soc* **1997**, *144*, 1188-1194.

[51] J.M. Tarascon, M. Armand *Nature* **2001**, *414*, 359-367.

[52] J. W. Fergus *J. Power Sources* **2010**, *195*, 939-954.

[53] B. L. Ellis, W. R. M. Mahnouk, Y. Makimura, K. Toghill, L. F. Nazar *Nat. Mater.* **2007**, *6*, 749-753.

[54] C. Delmas, M. Maccario, L. Croguennec, F. Le Cras, F. Weill *Nat. Mater.* **2008**, *7*, 665-671.

[55] S. M. Rommel, N. Schall, C. Brünig, R. Weihrich *Monatsh. Chem.* **2014**, *145*, 385-404.

[56] S. M. Rommel, J. Rothballer, N. Schall, C. Brünig, R. Weihrich *Ionics* **2015**, *21*, 325-333.

[57] S. M. Rommel, R. Weihrich *Chem. Eur. J.* **2015**, *21*, 9863-9867.

[58] S. M. Rommel, A. Krach, P. Peter, R. Weihrich *Chem. Eur. J.* **2016**, *accepted.*

[59] D. Bundesregierung, *Deutsches Ressourceneffizienzprogramm (ProgRess). Programm zur nachhaltigen Nutzung und zum Schutz der natürlichen Ressourcen. Beschluss des Bundeskabinetts vom 29.2. 2012*, Bundesministerium für Umwelt Naturschutz und Reaktorsicherheit **2012**.

[60] K. Kristof, P. Hennicke, *Endbericht des Projekts "Materialeffizienz und Ressourcenschonung "(MaRess)*, Wuppertal, Germany **2010**.

[61] C. Rao, G. Kulkarni, P. J. Thomas, P. P. Edwards *Chem. Eur. J.* **2002**, *8*, 28-35.

[62] L. Hunt *Gold Bulletin* **1976**, *9*, 134-139.

[63] O. M. Wilson, M. R. Knecht, J. C. Garcia-Martinez, R. M. Crooks *J. Am. Chem. Soc.* **2006**, *128*, 4510-4511.

[64] J. He, I. Ichinose, T. Kunitake, A. Nakao, Y. Shiraishi, N. Toshima *J. Am. Chem. Soc.* **2003**, *125*, 11034-11040.

[65] M. Brust, D. Bethell, C. J. Kiely, D. J. Schiffrin *Langmuir* **1998**, *14*, 5425-5429.

[66] S. Sohila, M. Rajalakshmi, C. Ghosh, A. Arora, C. Muthamizhchelvan *J. Alloys Compounds* **2011**, *509*, 5843-5847.

[67] A. Lu, E. e. Salabas, F. Schüth *Angew. Chem. Int. Ed.* **2007**, *46*, 1222-1244.

[68] A. M. Morales, C. M. Lieber *Science* **1998**, *279*, 208-211.

[69] Y. Pithawalla, M. El-Shall, S. Deevi *Scr. Mater.* **2003**, *48*, 671-676.

[70] H. Wei, W. Guo, Y. Sun, Z. Yang, Y. Zhang *Mater Lett* **2010**, *64*, 1424-1426.

[71] M. P. Boneschanscher, W. H. Evers, J. J. Geuchies, T. Altantzis, B. Goris, F. T. Rabouw, S. A. van Rossum, H. S. van der Zant, L. D. Siebbeles, G. Van Tendeloo, I. Swart, J. Hilhorst, A. V. Petukhov, S. Bals, D. Vanmaekelbergh *Science* **2014**, *344*, 1377-1380.

[72] M. Ambrosi, E. Fratini, P. Canton, S. Dankesreiter, P. Baglioni *J. Mater. Chem.* **2012**, *22*, 23497-23505.

[73] N. Phromviyo, E. Swatsitang, A. Chompoosor *Vacuum* **2014**, *107*, 208-212.

[74] I. Pastoriza-Santos, J. Pérez-Juste, L. M. Liz-Marzán *Chem. Mater.* **2006**, *18*, 2465-2467.

[75] R. Missen, W. Smith *Chem. Engi. Ed.* **2000, Fall**, *34*, 320-324.

[76] A. E. Henkes, Y. Vasquez, R. E. Schaak *J. Am. Chem. Soc.* **2007**, *129*, 1896-1897.

[77] B. D. Anderson, J. B. Tracy *Nanoscale* **2014**, *6*, 12195-12216.

[78] J. Svoboda, F. Fischer, P. Fratzl, A. Kroupa *Acta mater.* **2002**, *50*, 1369-1381.

[79] K. Matsukawa, K. Shirai, H. Yamaguchi, H. Katayama-Yoshida *Physica B: Condensed Matter* **2007**, *401*, 151-154.

[80] A. Höglund, C. Castleton, S. Mirbt *Phys Rev. B* **2008**, *77*, 113201.

[81] W. S. Seo, J. H. Shim, S. J. Oh, E. K. Lee, N. H. Hur, J. T. Park *J. Am. Chem. Soc.* **2005**, *127*, 6188-6189.

[82] T. Hyeon, S. S. Lee, J. Park, Y. Chung, H. B. Na *J. Am. Chem. Soc.* **2001**, *123*, 12798-12801.

[83] M. F. Casula, Y. Jun, D. J. Zaziski, E. M. Chan, A. Corrias, A. P. Alivisatos *J. Am. Chem. Soc.* **2006**, *128*, 1675-1682.

[84] Y. Yin, R. M. Rioux, C. K. Erdonmez, S. Hughes, G. A. Somorjai, A. P. Alivisatos *Science* **2004**, *304*, 711-714.

[85] E. Gonzalez, J. Arbiol, V. F. Puntes *Science* **2011**, *334*, 1377-1380.

[86] B. D. Anderson, J. B. Tracy *Nanoscale* **2014**, *6*, 12195-12216.

[87] S. Wang, Q. Huang, X. Wen, X. Li, S. Yang *Phys. Chem. Chem. Phys.* **2002**, *4*, 3425-3429.

[88] M. Kim, V. Ngoc Phan, K. Lee *CrystEngComm.* **2012**, *14*, 7535-7548.

[89] I. R. Franchini, G. Bertoni, A. Falqui, C. Giannini, L. W. Wang, L. Manna *J. Mater. Chem.* **2010**, *20*, 1357-1366.

[90] J. Yang, L. Levina, E. H. Sargent, S. O. Kelley *J. Mater. Chem.* **2006**, *16*, 4025-4028.

[91] W. Hu, H. Liu, F. Ye, Y. Ding, J. Yang *CrystEngComm* **2012**, *14*, 7049-7054.

[92] J. Yang, L. Levina, E. H. Sargent, S. O. Kelley *J. Mater. Chem.* **2006**, *16*, 4025-4028.

[93] J. Yang, J. Y. Ying *J. Am. Chem. Soc.* **2010**, *132*, 2114-2115.

[94] T. Mokari, A. Aharoni, I. Popov, U. Banin *Angew. Chem. Int. Ed.* **2006**, *45*, 8001-8005.

[95] J. Park, J. Cheon *J. Am. Chem. Soc.* **2001**, *123*, 5743-5746.

[96] W. Lee, M. G. Kim, J. Choi, J. Park, S. J. Ko, S. J. Oh, J. Cheon *J. Am. Chem. Soc.* **2005**, *127*, 16090-16097.

[97] J. Park, M. G. Kim, Y. Jun, J. S. Lee, W. Lee, J. Cheon *J. Am. Chem. Soc.* **2004**, *126*, 9072-9078.

[98] E. L. Crane, Y. You, R. G. Nuzzo, G. S. Girolami *J. Am. Chem. Soc.* **2000**, *122*, 3422-3435.

[99] M. G. Kim, S. Sim, J. Cho *Adv. Mater.* **2010**, *22*, 5154-5158.

[100] J. Yang, J. Y. Ying *Chem. Commun.* **2009**, 3187-3189.

[101] A. E. Saunders, I. Popov, U. Banin *J. Phys. Chem. B* **2006**, *110*, 25421-25429.

[102] J. Yang, H. I. Elim, Q. Zhang, J. Y. Lee, W. Ji *J. Am. Chem. Soc.* **2006**, *128*, 11921-11926.

[103] J. Yang, E. Sargent, S. Kelley, J. Y. Ying *Nat. Mater.* **2009**, *8*, 683-689.

[104] K. Zhu, B. Yue, W. Zhou, H. He *Chem. Commun.* **2003**, 98-99.

[105] K. Lee, S. Lee, J. Cheon *Adv. Mater.* **2001**, *13*, 517-520.

[106] R. Qing, M. -. Yang, S. Meng, W. Sigmund *Electrochim. Acta* **2013**, *108*, 827-832.

[107] Y. Zhang, L. Zhou, D. Li, N. Xue, X. Xu, J. Li *Chem. Phys Lett.* **2003**, *376*, 493-497.

[108] Z. Shi, L. Xu, Y. Feng *J. Non Cryst. Solids* **2006**, *352*, 4003-4007.

[109] F. Dawood *Template directed synthesis and characterization of nanocrystalline metal oxides and chalcogenides*, Dissertation, Pennsylvania State University, **2010**.

[110] Y. Liu, J. Goebl, Y. Yin *Chem. Soc. Rev.* **2013**, *42*, 2610-2653.

[111] H. Dai, E. W. Wong, Y. Z. Lu, S. Fan, C. M. Lieber *Nature* **1995**, *375*, 769-772.

[112] X. Jiang, B. Mayers, T. Herricks, Y. Xia *Adv. Mater.* **2003**, *15*, 1740-1743.

[113] M. P. Brady, S. K. Wrobel, T. A. Lograsso, E. A. Payzant, D. T. Hoelzer, J. A. Horton, L. R. Walker *Chem. Mater.* **2004**, *16*, 1984-1990.

[114] D. H. Son, S. M. Hughes, Y. Yin, A. Paul Alivisatos *Science* **2004**, *306*, 1009-1012.

[115] F. Dawood, R. E. Schaak *J. Am. Chem. Soc.* **2008**, *131*, 424-425.

[116] H. Dong, Y. Chen, C. Feldmann *Green Chem.* **2015**, *17*, 4107-4132.

[117] D. R. Lide, *CRC handbook of chemistry and physics*, CRC press, Boca Raton, US, **2004**.

[118] F. Fievet, J. P. Lagier, M. Figlarz *MRS Bull.* **1989**, *December*, 29-34.

[119] S. E. Skrabalak, B. J. Wiley, M. Kim, E. V. Formo, Y. Xia *Nano Lett.* **2008**, *8*, 2077-2081.

[120] G. W. Scherer *J. Non Cryst. Solids* **1988**, *100*, 77-92.

[121] R. J. Corriu, D. Leclercq *Angew. Chem. Int. Ed.* **1996**, *35*, 1420-1436.

[122] L. C. Klein, *Sol-gel optics: processing and applications*, Springer Science & Business Media, New York, US, **2013**.

[123] B. D. Gangulibabu, N. Kalaiselvi, N. Jayaprakash, P. Periasamy *J. Sol-Gel Sci. Technol.* **2009**, *49*, 137-144.

[124] J. Yang, J. J. Xu *J. Electrochem. Soc.* **2006**, *153*, A716-A723.

[125] J. Wolfenstine, J. Allen *J. Power Sources* **2005**, *142*, 389-390.

[126] A. Kraytsberg, Y. Ein-Eli *Adv. Energy Mater.* **2012**, *2*, 922-939.

[127] M. K. Devaraju, I. Honma *Adv. Energy Mater.* **2012**, *2*, 284-297.

[128] The Green & Energy Consulting Group, *What is your battery size?* www.nexergy.com/media/BatteryGraph.JPG, **07.03.2011**.

[129] J. B. Goodenough *Ionics* **1994**, *69*, 184-198.

[130] J. B. Goodenough, Y. Kim *Chem. Mater.* **2010**, *22*, 587-603.

[131] WinXPow Stoe & Cie GmbH, Darmstadt, Germany, Powder Diffraction Software, Version 1.08.

[132] V. Petricek, M. Dusek, L. Palatinus, Institute of Physics, Praha, Czech Republic, *Jana2006. The crystallographic computing system*, Academy of Sciences of the Czech Republic, **2006** 162, 53.

[133] J. Rodriguez-Carvajal *Physica B.* **1993**, *192*, 55-69.

[134] J. F. Rusling, S. L. Suib *Adv. Mater.* **1994**, *6*, 922-930.

[135] J. J. Van Benschoten, J. Y. Lewis, W. R. Heineman, D. A. Roston, P. T. Kissinger *J. Chem. Educ.* **1983**, *60*, 772.

[136] G. M. Wilson *J. Am. Chem. Soc.* **1964**, *86*, 127-130.

[137] Y. T. Prabhu, K. V. Rao, V. S. S. Kumar, B. S. Kumari *World Journal of Nano Science and Engineering* **2014**, *4*, 21.

[138] T. Hughbanks *J. Alloys Compounds* **1995**, *229*, 40-53.

[139] J. Neuhausen, E. W. Finckh, W. Tremel *Chem. Ber.* **1995**, *128*, 569-573.

[140] L. Chen, J. D. Corbett *Inorg. Chem.* **2002**, *41*, 2146-2150.

[141] B. Harbrecht, H. Franzen *J. Less Common Metals* **1985**, *113*, 349-360.

[142] F. Meng, T. Hughbanks *Inorg. Chem.* **2001**, *40*, 2482-2483.

[143] T. Sakamoto, M. Wakeshima, Y. Hinatsu *J. Phys. Condens. Matter.* **2006**, *3*, 4417-4426.

[144] U. Kaluarachchi, W. Xie, Q. Lin, V. Taufour, S. Bud'Ko, G. Miller, P. Canfield, *Search for superconductivity in ternary chalcogenides $Bi_2Rh_3S_2$,* APS Meeting Abstracts **2015**, 25003.

[145] U. S. Kaluarachchi, W. Xie, Q. Lin, V. Taufour, S. L. Bud'ko, G. J. Miller, P. C. Canfield, *Phys. Rev. B.* **2015**, 174513.

[146] R. Weihrich, I. Anusca *Z. anorg. allg. Chem.* **2006**, *632*, 335-342.

[147] F. Pielnhofer, J. Rothballer, P. Peter, W. Yan, F. M. Schappacher, R. Pöttgen, R. Weihrich *Z. anorg. allg. Chem.* **2014**, *640*, 286-294.

[148] I. Anusca, A. Schmid, P. Peter, J. Rothballer, F. Pielnhofer, R. Weihrich *Z. anorg. allg. Chem.* **2009**, *635*, 2410-2428.

[149] R. Weihrich, A. Stückl, M. Zabel, W. Schnelle *Z. anorg. allg. Chem.* **2004**, *630*, 1767-1767.

[150] L. Bai, J. Fan, Y. Cao, F. Yuan, A. Zuo, Q. Tang *J. Cryst. Growth* **2009**, *311*, 2474-2479.

[151] S. Wu, D. Chen *J. Colloid Interface Sci.* **2003**, *259*, 282-286.

[152] C. Chinnasamy, B. Jeyadevan, K. Shinoda, K. Tohji, A. Narayanasamy, K. Sato, S. Hisano *J. Appl. Phys.* **2005**, *97*, 10J309.

[153] R. Eluri, B. Paul *J. Nanopart. Res.* **2012**, *14*, 1-14.

[154] K. Morinaga *Bull. Chem. Soc. Jpn.* **1956**, *29*, 793-799.

[155] T. D. George, W. W. Wendlandt *J. Inorg. Nucl. Chem.* **1963**, *25*, 395-405.

[156] H. Su, Y. Xie, S. Wan, B. Li, Y. Qian *Solid State Ionics* **1999**, *123*, 319-324.

[157] S. Gorai, D. Ganguli, S. Chaudhuri *Mater. Sci. Eng. B* **2005**, *116*, 221-225.

[158] N. G. Tsierkezos, D. Schröder, H. Schwarz *Int. J. Mass. spectrom.* **2004**, *235*, 33-42.

[159] J. Park, M. G. Kim, Y. Jun, J. S. Lee, W. Lee, J. Cheon *J. Am. Chem. Soc.* **2004**, *126*, 9072-9078.

[160] S. K. Panda, S. Gorai, S. Chaudhuri *Mater. Sci. Eng. B* **2006**, *129*, 265-269.

[161] D. Wang, D. Yu, M. Shao, X. Liu, W. Yu, Y. Qian *J. Cryst. Growth* **2003**, *257*, 384-389.

[162] Z. Quan, C. Li, X. Zhang, J. Yang, P. Yang, C. Zhang, J. Lin *Cryst. Growth Des.* **2008**, *8*, 2384-2392.

[163] A. Ferancova, S. Rengaraj, Y. Kim, S. Vijayalakshmi, J. Labuda, J. Bobacka, M. Sillanpää *Electrochim. Acta* **2013**, *92*, 124-131.

[164] W. Lv, X. Wang, Q. Qiu, F. Wang, Z. Luo, W. Weng *J. Alloy. Compd.* **2010**, *493*, 358-361.

[165] S. Yu, J. Yang, Y. Wu, Z. Han, J. Lu, Y. Xie, Y. Qian *J. Mater. Chem.* **1998**, *8*, 1949-1951.

[166] S. Gao, D. Liu, D. Xu, D. Li, Y. Hong, H. Chen, Q. Dai, S. Kan, H. Li, G. Zou *Smart Mater. Struct.* **2007**, *16*, 2350.

[167] A. I. Baranov, A. A. Isaeva, L. Kloo, B. A. Popovkin *Inorg. Chem.* **2003**, *42*, 6667-6672.

[168] A. Clauss, M. Warasteh, K. Weber *Neues JB Miner. Monat.* **1978**, 256-268.

[169] M. Zabel, S. Wandinger, K. J. Range *Z. Naturforsch.* **1979**, *34b*, 238-241.

[170] H. P. Bortner, Darstellung und Eigenschaften ternärer Sulfide $M_3M'_2X_2$ mit Shandit-Struktur, Diplomarbeit, Universität Regensburg **1982**.

[171] M. Zabel, *Darstellung und Struktur ternärer Chalkogenide $M_3M'_2X_2$ (M = Co, Ni,; M' = In, Tl, Sn, Pb; X = S, Se) und $M_xTl_2X_4$ (M = Fe, Co, Ni; X = S, Se)*, Dissertation, Universität Regensburg, **1979**.

[172] P. Scherrer *Göttinger Nachrichten Gesell.* **1918**, *2*, 98-100.

[173] Y. Gao, H. Niu, C. Zeng, Q. Chen *Chem. Phys. Lett.* **2003**, *367*, 141-144.

[174] W. S. Sheldrick, M. Wachhold *Angew. Chem. Int. Ed.* **1997**, *36*, 206-224.

[175] R. S. Ningthoujam, N. S. Ajbhiye, S. Sharma *Pramana-J. Phys.* **2009**, *72*, 577-586.

[176] M. S. Hegde, D. Larcher, L. Dupont, B. Beaudoin, K. Tekaia-Elhsissen, J. M. Tarascon *Solid State Ion.* **1996**, *93*, 33-50.

[177] J. D. Grice, R. B. Ferguson *Can. Mineral.* **1974**, *12*, 248-252.

[178] M. E. Fleet *Am. Mineral.* **1977**, *62*, 341-345.

[179] A. Leineweber, O. Oeckler, U. Zachwieja *J. Solid State Chem.* **2004**, *177*, 936-945.

[180] F. Bachhuber, A. Krach, A. Furtner, T. Söhnel, P. Peter, J. Rothballer, R. Weihrich *J. Solid State Chem.* **2015**, *226*, 29-35.

[181] A. Götze, P. Urban, O. Oeckler, H. Kohlmann *Z. Naturforsch. B: Chem. Sci.* **2014**, *69*, 417-422.

[182] J. McAndrew, M. Peacock *Amer. Mineral* **1950**, *35*, 425-439.

[183] A. Baranov, A. Isaeva, B. Popovkin, R. Shpanchenko *Russ. Chem. B+* **2002**, *51*, 2139-2144.

[184] E. Gonzalez, J. Arbiol, V. F. Puntes *Science* **2011**, *334*, 1377-1380.

[185] G. Guisbiers, L. Buchaillot *Nanotechnology* **2008**, *19*, 435701.

[186] R. Bitti, J. Dixmier, A. Guinier *Comptes. Rendus. B* **1968**, *266*, 565.

[187] K. Range, M. Zabel *Mater. Res. Bull.* **1968**, *3*, 519.

[188] S. Natarajan, G. S. Rao, R. Baskaran, T. Radhakrishnan *J. Less Common Metals* **1988**, *138*, 215-224.

[189] A. Michelet, G. Collin, O. Gorochov *J. Less Common Metals* **1984**, *97*, 73-78.

[190] G. Steigmann, H. Sutherland, J. Goodyear *Acta Crystallogr.* **1965**, *19*, 967-971.

[191] H. Hahn, W. Klingler *Z. anorg. allg. Chem.* **1949**, *260*, 97-109.

[192] R. Diehl, R. Nitsche *J. Cryst. Growth* **1975**, *28*, 306-310.

[193] R. Diehl, C. Carpentier, R. Nitsche *Acta Crystall. B-Stru* **1976**, *32*, 1257-1260.

[194] K. Schubert, E. Dörre, E. Günzel *Naturwissenschaften* **1954**, *41*, 448-448.

[195] L. Liu, H. Liu, H. Kou, Y. Wang, Z. Zhou, M. Ren, M. Ge, X. He *Crys. Growth Des.* **2008**, *9*, 113-117.

[196] J. Ketelaar, E. Gorter *Z. Kristallogr.* **1939**, *101*, 367-375.

[197] B. Leclerc, M. Bailly *Acta Crystall. B-Stru* **1973**, *29*, 2334-2336.

[198] H. Hahn, W. Klingler *Z. anorg. allg. Chem.* **1949**, *260*, 110-119.

[199] K. Nakamura, S. Kashida *J. Phys. Soc. Jpn.* **1993**, *62*, 3135-3141.

[200] B. Leclerc, T. Kabre *Acta Crystall. B-Stru* **1975**, *31*, 1675-1677.

[201] I. Bružaitė, V. Janickis *Central Eur. J. Chem.* **2013**, *11*, 629-635.

[202] S. Youssef *Physica A* **1995**, *215*, 176-180.

[203] R. Mane, C. Lokhande *Mater. Chem. Phys.* **2000**, *65*, 1-31.

[204] K. A. Yee, T. A. Albright *J. Am. Chem. Soc.* **1991**, *113*, 6474-6478.

[205] M. Hanias, A. Anagnostopoulos, K. Kambas, J. Spyridelis *Mater. Res. Bull.* **1992**, *27*, 25-38.

[206] J. Kalomiros, N. Kalkan, M. Hanias, A. Anagnostopoulos, K. Kambas *Solid State Commun.* **1995**, *96*, 601-607.

[207] V. Estrella, R. Mejía, M. Nair, P. Nair *Mod. Phys Lett. B* **2001**, *15*, 737-740.

[208] Y. Ni, M. Shao, Z. Wu, F. Gao, X. Wei *Solid State Commun.* **2004**, *130*, 297-300.

[209] N. Kalkan, M. Hanias, A. Anagnostopoulos *Mater. Res. Bull.* **1992**, *27*, 1329-1337.

[210] R. Weikl, T. Merz, R. Weihrich *Z. anorg. allg. Chem.* **2008**, *634*, 2088-2088.

[211] F. Bachhuber, I. Anusca, J. Rothballer, F. Pielnhofer, P. Peter, R. Weihrich *Solid State Sci* **2011**, *13*, 337-343.

[212] K. Klepp, H. Boller *Monatsh. Chem.* **1978**, *109*, 1049-1057.

[213] N. N. Greenwood, A. Earnshow, *Chemistry of the Elements,* Pergamon Press, Frankfurt, **1978**.

[214] A. G. Lee, *Coord. Chem. Rev.1972, 8, 289-349.*.

[215] K. Range, H. Paulus, F. Rau, M. Zabel *Z. Kristallogr.* **1997**, *212*, 136-136.

[216] J. Hiller, *Neues JB Miner. Monat.* **1951**, 265.

[217] A. Clauss, M. Waraste, K. Weber *Neues Jahrb. Mineral. Monatsh.* **1978**, 268.

[218] R. G. Pearson *J. Am. Chem. Soc.* **1963**, *85*, 3533-3539.

[219] S. Haumann *Internal communication*.

[220] M. Zabel, S. Wandinger, K. Range *Z.Naturforsch.34b* **1979**, 238-241.

[221] I. Anusca *Neue Shandite und Parkerite.Darstellung und röntgenographische Charakterisierung*, Dissertation, Universität Regensburg, **2009**.

[222] K. Klepp, H. Boller *Monatsh. Chem.* **1978**, *109*, 1049-1057.

[223] F. Bachhuber, J. Rothballer, T. Söhnel, R. Weihrich *J. Comput. Chem.* **2014**, *89*, 114-121.

[224] F. Bachhuber, A. Krach, A. Furtner, T. Söhnel, J. Rothballer, R. Weihrich *J. Solid State Chem.* **2015**.

[225] A. Höglund, C. Castleton, S. Mirbt *Phys. Rev. B* **2008**, *77*, 113201.

[226] B. K. Patra, A. K. Guria, A. Dutta, A. Shit, N. Pradhan *Chem. Mater.* **2014**, *26*, 7194-7200.

[227] S. Lowell, J. E. Shields, M. A. Thomas, M. Thommes, *Characterization of porous solids and powders: surface area, pore size and density*, Springer Science & Business Media, Luxemburg, **2012**.

[228] T. Pecoraro, R. Chianelli *J. Catal.* **1981**, *67*, 430-445.

[229] M. S. Dhlamini, J. J. Terblans, R. E. Kroon, O. M. Ntwaeaborwa, J. M. Ngaruiya, J. R. Botha, H. C. Swart *S. Afr. J. Sci.* **2008**, *104*, 398-400.

[230] L. Qian, S. Wang, Y. Zhao, K. Lu *Acta mater.* **2002**, *50*, 3425-3434.

[231] I. Leontyev, A. Kuriganova, N. Leontyev, L. Hennet, A. Rakhmatullin, N. Smirnova, V. Dmitriev *RSC Adv.* **2014**, *4*, 35959-35965.

[232] W. Qi, M. Wang *J. Nanopart. Res.* **2005**, *7*, 51-57.

[233] G. Caruntu, R. Rarig Jr, I. Dumitru, C. J. O'Connor *J. Mater. Chem.* **2006**, *16*, 752-758.

[234] T. Raming, A. Winnubst, 1. M. van Kats, A. Philipse *J. Colloid Interface Sci.* **2002**, *249*, 346-350.

[235] M. Distaso, D. Segets, R. Wernet, R. K. Taylor, W. Peukert *Nanoscale* **2012**, *4*, 864-873.

[236] L. Marks *Rep. Prog. Phys.* **1994**, *57*, 603.

[237] H. Purdum, P. Montano, G. Shenoy, T. Morrison *Phys. Rev. B* **1982**, *25*, 4412.

[238] M. Leszczynski, T. Suski, H. Teisseyre, P. Perlin, I. Grzegory, J. Jun, S. Porowski, T. Moustakas *J. Appl. Phys.* **1994**, *76*, 4909-4911.

[239] K. J. Malloy, J. A. Van Vechten *J. Vac. Sci. Technol. B* **1991**, *9*, 2212-2218.

[240] H. Iwanaga, A. Kunishige, S. Takeuchi *J. Mater. Sci.* **2000**, *35*, 2451-2454.

[241] C. Huang, D. Agrawal, H. McKinstry *J. Mater. Sci.* **1995**, *30*, 3509-3514.

[242] J. James, J. Spittle, S. Brown, R. Evans *Meas. Sci. Technol.* **2001**, *12*, R1-R15.

[243] Y. Zhao, H. Sheng, K. Lu *Acta Mater.* **2001**, *49*, 365-375.

[244] K. Lu, M. Sui *Acta Metal. Mater.* **1995**, *43*, 3325-3332.

[245] Y. Zhao, K. Lu *Phys. Rev. B* **1997**, *56*, 14330.

[246] W. M. Skinner, G. Qian, A. N. Buckley *J. Solid State Chem.* **2013**, *206*, 32-37.

[247] D. G. Kerfoot, *Nickel* in Ullmann's Encyclopedia of Industrial Chemistry**, 2002**.

[248] M. Hrovat, K. Hackstein, H. Huschka, H. Pirk, T. Schmidt-Hansberg *Nucl. Technol.* **1983**, *61*, 460-464.

[249] X. Zhu, Z. Wen, Z. Gu, S. Huang *J. Electrochem. Soc.* **2006**, *153*, A504-A507.

[250] J. Du Preez, *A thermal investigation of the parkerite series, Nasionale Pers.* **1945**, *22A*, 94-104.

[251] M. I. Zargarova, K. S. Kakhramanov, R. M. Roshal, G. G. Guseinov *Inorg. Mater. (USSR)* **1976**, *12*, 1557-1559.

[252] K. Mariolacos *Chem. Erde-Geochem.* **1986**, *45*, 338-344.

[253] M. Bhargava, K. Schubert *J. Less Common Met.* **1973**, *33*, 181-189.

[254] P. Brand *Z. anorg. allg. Chem.* **1967**, *353*, 270-280.

[255] C. E. Michener, M. A. Peacock *Am. Mineral.* **1943**, *28*, 343-355.

[256] D. L. Scholtz *Trans. Geol. Soc. S. Africa* **1937**, *39*, 81-210.

[257] M. E. Fleet *Am. Mineral.* **1973**, *58*, 435-439.

[258] A. I. Baranov, A. V. Olenev, B. A. Popovkin *Russ. Chem. Bull. Int. Ed.* **2001**, *50*, 353-358.

[259] A. Clauss *Naturwissenschaften* **1977**, *64*, 145-145.

[260] R. Schenck, P. v. d. Forst *Z. anorg. allg. Chem.* **1939**, 145-304.

[261] F. Hulliger *Nature* **1963**, *198*, 382-383.

[262] A. Clauss, K. Weber *Neues JB Miner. Monat.* **1975**, 385-395.

[263] T. Sakamoto, M. Wakeshima, Y. Hinatsu, K. Matsuhira *Phys. Rev. B* **2008**, *78*, 024509.

[264] T. Sakamoto, M. Wakeshima, Y. Hinatsu, K. Matsuhira *Phys. Rev. B* **2007**, *75*, 060503.

[265] N. T. N. Truong, T. P. N. Nguyen, V. T. H. Pham, K. T. Trinh, S. Lee, C. Park *JPN J. Appl. Phys.* **2015**, *54*, 045001.

[266] Z. Hu, Z. Zhu, F. Cheng, K. Zhang, J. Wang, C. Chen, J. Chen *Energ. Environ. Sci.* **2015**, *8*, 1309-1316.

[267] R. Weihrich, D. Kurowski, A. C. Stückl, S. F. Matar, F. Rau, T. Bernert *J. Solid State Chem.* **2004**, *177*, 2591-2599.

[268] Z. Liu, S. Peng, Q. Xie, Z. Hu, Y. Yang, S. Zhang, Y. Qian *Adv. Mater.* **2003**, *15*, 936-940.

[269] Y. Li, Z. Wang, Y. Ding *Inorg. Chem.* **1999**, *38*, 4737-4740.

[270] J. P. Perdew, B. K., M. Ernzerhof *Phys. Rev. Lett.* **1996**, *77*, 3865-3868.

[271] J. P. Perdew, K. Burke, M. Ernzerhof *Phys. Rev Lett.* **1997**, *78*, 1396-1396.

[272] G. Kresse, J. Hafner *Phys. Rev. B* **1994**, *49*, 14251-14269.

[273] G. Kresse, J. Furthmüller *Phys. Rev. B* **1996**, *54*, 11169-11186.

[274] G. Kresse *J. Non Cryst. Solids* **1995**, *192–193*, 222-229.

[275] G. Kresse, J. Furthmüller, *Comput. Mater. Sci.*, **1996**, 15-50.

[276] P. E. Blöchl *Phys. Rev. B* **1994**, *50*, 17953-17979.

[277] G. Kresse, D. Joubert *Phys. Rev. B* **1999**, *59*, 1758-1775.

[278] R. Weihrich, W. Yan, J. Rothballer, P. Peter, S. M. Rommel, S. Haumann, F. Winter, C. Schwickert, R. Pöttgen *Dalton Trans.* **2015**, *44*, 15855-15864.

[279] F. Bachhuber, J. von Appen, R. Dronskowski, P. Schmidt, T. Nilges, A. Pfitzner, R. Weihrich *Angew. Chem.* **2014**, *126*, 11813-11817.

[280] G. Valiulienė, A. Žielienė, B. Šimkūnaitė, L. Naruškevičius, L. T. Tamašiūnaitė, V. Pakštas, A. Selskis *J. Solid State Electrochem.* **2010**, *14*, 203-212.

[281] A. Kumar, P. Vaishali AND Ramamurthy *Int. J. Chem. Kinet.* **2000**, *32*, 286-293.

[282] J. Lu, Y. Xie, F. Xu, L. Zhu *J. Mater. Chem.* **2002**, *12*, 2755-2761.

[283] F. Bachhuber, J. von Appen, R. Dronskowski, P. Schmidt, T. Nilges, A. Pfitzner, R. Weihrich *Angew. Chem. Int. Ed.* **2014**, *53*, 11629-11633.

[284] M. Jansen, I. V. Pentin, J. C. Schön *Angew. Chem. Int. Ed.* **2012**, *51*, 132-135.

[285] R. S. Krishnan, R. Srinivasan, S. Devanarayanan, *Thermal Expansion of Crystals: International Series in The Science of The Solid State*, Pergamon Press, Frankfurt, **2013**.

[286] H. Ibrahim, A. Ilinca, J. Perron *Renew. Sust. Energ. Rev.* **2008**, *12*, 1221-1250.

[287] J. N. Fuchs *J. Prakt. Chem.* **1834**, *3*, 98-104.

[288] C. M. Julien, A. Mauger *Ionics* **2013**, *19*, 951-988.

[289] K. Zaghib, A. Mauger, H. Groult, J. B. Goodenough, C. M. Julien *Materials* **2013**, *6*, 1028-1049.

[290] C. Sun, S. Rajasekhara, Goodenough J. B., F. Zhou *J. Am. Chem. Soc.* **2011**, *133*, 2132-2135.

[291] N. N. Bramnik, K. G. Bramnik, T. Buhrmester, C. Baehtz, H. Ehrenberg, H. Fuess *J. Solid State Electrochem.* **2004**, *8*, 558-564.

[292] M. Piana, M. Arrabito, S. Bodoardo, A. D'Epifanio, D. Satolli, F. Croce, B. Scrosati *Ionics* **2002**, *8*, 17-26.

[293] C. M. Julien, A. Mauger, K. Zaghib, R. Veillette, H. Groult *Ionics* **2012**, *18*, 625-633.

[294] L. Dimesso, D. Becker, C. Spanheimer, W. Jaegermann *J. Solid State Electrochem.* **2012**, *16*, 3791-3798.

[295] B. Ellis, S. P. Herle, Y. -. Rho, L. F. Nazar, R. Dunlap, L. K. Perry, D. H. Ryan **2007**, *Faraday Discuss.*, 119-141.

[296] D. Wang, J. Xiao, W. Xu, J. G. Zhang *The 15th International Meeting on Lithium Batteries*, Investigation of $LiNiPO_4$ as a Cathode Material for Lithium Ion Battery **2010**, *Abstract #372*.

[297] K. Rissouli, K. Benkhouja, J. R. Ramos-Barrado, C. Julien *Mater. Sci. Eng. B* **2003**, *98*, 185-189.

[298] O. Garcia-Moreno, M. Alvarez-Vega, F. Garcia-Alvarado, J. Garcia-Jaca, J. M. Gallardo, M. L. Sanján, U. Amador *Chem. Mater.* **2001**, *13*, 1570-1576.

[299] S. Okada, S. Sawa, M. Egashira, J. Yamaki, M. Tabuchi, H. Kageyama, T. Konishi, A. Yoshino *J. Power Sources* **2001**, *97*, 430-432.

[300] A. Örnek, E. Bulut, M. Can *Mater. Charact.* **2015**.

[301] C. Delacourt, P. Poizot, S. Levasseur, C. Masquelier *Electrochem. Solid-State Lett.* **2006**, *9*, A352-A355.

[302] S. Kandhasamy, A. Pandey, M. Minakshi *Electrochim. Acta* **2012**, *60*, 170-176.

[303] S. P. Herle, B. Ellis, N. Coombs, L. F. Nazar *Nat. Mater.* **2004**, *3*, 147-152.

[304] C. A. J. Fisher, V. M. H. Prieto, M. S. Islam *Chem. Mater.* **2008**, *20*, 5907-5915.

[305] M. Minakshi, P. Singh, D. Appadoo, D. E. Martin *Electrochim. Acta* **2011**, *56*, 4356-4360.

[306] N. N. Bramnik, D. M. Trots, H. J. Hofmann, H. Ehrenberg *Phys. Chem. Chem. Phys.* **2009**, *11*, 3271-3277.

[307] M. Minakshi, P. Singh, D. Ralph, D. Appadoo, M. Blackford, M. Ionescu *Ionics* **2012**, *18*, 583-590.

[308] J. Wolfenstine, J. Allen *J. Power Sources* **2004**, *136*, 150-153.

[309] N. N. Bramnik, K. Nikolowski, C. Baehtz, K. G. Bramnik, H. Ehrenberg *Chem. Mater.* **2007**, *19*, 908-915.

[310] K. Amine, H. Yasuda, M. Yamachi *Electrochem. Solid-State Lett.* **2000**, *3*, 178-179.

[311] D. Shanmukaraj, R. Murugan *Ionics* **2004**, *10*, 88-92.

[312] L. Dimesso, C. Spanheimer, W. Jaegermann *Mater. Res. Bull.* **2013**, *48*, 559-565.

[313] T. Muraliganth, A. Manthiram *J. Phys. Chem. C* **2010**, *114*, 15330-15540.

[314] D. Bhuvaneswari, Gangulibabu, C. Doh, N. Kalaiselvi *Int. J. Electrochem. Sci.* **2011**, *6*, 3714 - 3728.

[315] W. Wang, Y. Yang, Y. Liang, L. Cui, H. S. Casalongue, Y. Li, G. Hong, Y. Cui, H. Dai *Angew. Chem.* **2011**, *50*, 7364-7368.

[316] S. Rundquist, N. Ersson *Ark. Kemi* **1968**, *30*, 103.

[317] W. Jeitschko, A. J. Foecker, D. Paschke, M. V. Dewalsky, C. B. Evers, B. Kuennen, A. Lang, G. Kotzyba, U. C. Rodewald, M. H. Möller *Z. anorg. allg. Chem.* **2000**, *626*, 1112-1120.

[318] S. Rundqvist, E. Larsson *Acta Chem. Scand.* **1959**, *13*, 551-560.

[319] M. Memm, *Präparation und Charakterisierung von Hochvolt-Kathodenmaterialien für Lithium-Ionen-Akkumulatoren auf Basis von Lithium-Übergangsmetall-Phosphoolivinen*, Dissertation, Universität Ulm **2011**.

[320] I. Abrahams *Acta Cryst.* **1985**, *C41*, 1-4.

[321] C. V. Ramana, A. Ait-Salah, S. Utsunomiya, U. Becker, A. Mauger, F. Gendron, C. M. Julien *Chem. Mater.* **2006**, *18*, 3788-3794.

[322] R. E. Newnham, M. J. Redman *J. Am. Chem. Soc.* **1965**, *48*, 547.

[323] S. Geller, J. L. Durand *Acta Cryst.* **1960**, *13*, 325-331.

[324] M. S. Islam, D. J. Driscoll, C. A. J. Fisher, P. R. Slater *Chem. Mater.* **2005**, *17*, 5085-5092.

[325] A. V. Murugan, T. Muraliganth, P. J. Ferreira, A. Manthiram *Inorg. Chem.* **2009**, *48*, 946-952.

[326] L. Jinsub, K. Donghan, M. Vinod, K. Jaekook *Phys. Scr.* **2010**, *T139*, 014060-014065.

[327] S. L. Shang, Y. Wang, Z. G. Mei, X. D. Hui, Z. K. Liu *J. Mater. Chem.* **2012**, *22*, 1142-1149.

[328] A. Yamada, S. C. Chung, K. Hinokuma *J. Electrochem. Soc.* **2001**, *148*, A224-A229.

[329] M. C. Tucker, M. M. Doeff, T. J. Richardson, R. Fiñones, J. A. Reimer, E. J. Cairns *Electrochem. Solid State Lett.* **2002**, *5*, A95-A98.

[330] K. S. Nanjundaswamy, A. K. Padhi, J. B. Goodenough, S. Okada, H. Ohtsuka, H. Arai, J. Yamaki *Solid State Ionics* **1996**, *1-2*, 1-10.

[331] S. P. Ong, A. Jain, G. Hautier, B. Kang, G. Ceder *Electrochem. Commun.* **2010**, *12*, 427-430.

[332] G. Hautier, A. Jain, S. P. Ong, B. Kang, C. Moore, R. Doe, G. Ceder *Chem. Mater.* **2011**, *23*, 3495-3508.

[333] L. Vegard *Z. Physi. A* **1921**, *1*, 17-26.

[334] R. D. Shannon *Acta Cryst.* **1976**, *A32*, 751-767.

[335] I. K. Lee, C. M. Kim, S. J. Kim, C. S. Kim *J. Appl. Phys.* **2012**, *111*, 07D722-1-07D722-3.

[336] J. Molenda, A. Kulka, A. Milewska, W. Zając, K. Świerczek *Materials* **2013**, *6*, 1656-1687.

[337] A. Goni, L. Lezama, M. I. Arriortua, G. E. Barberisa, T. Rojo *J. Mater. Chem.* **2000**, *10*, 423-428.

[338] M. T. Paques-Ledent, P. Tarte *Spectrochim. Acta A, Mol. Spectrosc.* **1973**, *29*, 1007-1016.

[339] R. Sharabi, E. Markevich, V. Borgel, G. Salitra, D. Aurbach, G. Semrau, M. A. Schmidt, N. Schall *Electrochem. Commun.* **2011**, *13*, 800-802.

[340] S. M. G. Yang, V. Aravindan, W. I. Cho, D. R. Chang, H. S. Kim, Y. S. Lee *J. Electrochem. Soc.* **2012**, *159*, A1013-A1018.

[341] E. Markevich, R. Sharabi, H. Gottlieb, V. Borgel, K. Fridman, G. Salitra, D. Aurbach, G. Semrau, M. A. Schmidt, N. Schall, C. Bruenig *Electrochem. Commun* **2012**, *15*, 22-25.

[342] N. Penazzi, M. Arrabito, M. Piana, S. Bodoardo, S. Panero, I. Amadei *J. Eur. Ceram. Soc.* **2004**, *24*, 1381-1384.

[343] R. Sharabi, E. Markevich, K. Fridman, G. Gershinsky, G. Salitra, D. Aurbach, G. Semrau, M. A. Schmidt, N. Schall, C. Bruenig *Electrochem. Commun* **2013**, *28*, 20-23.

[344] S. Tao, Q. Wu, Z. Zhan, G. Meng *Solid State Ionics* **1999**, *124*, 53-59.

[345] W. Johnston, R. Heikes, D. Sestrich *J. Phys. Chem. Solids* **1958**, *7*, 1-13.

[346] K. Mizushima, P. Jones, P. Wiseman, J. B. Goodenough *Mater. Res. Bull.* **1980**, *15*, 783-789.

[347] E. Rossen, J. N. Reimers, J. R. Dahn *Solid State Ionics* **1993**, *62*, 53-60.

[348] J. Akimoto, Y. Gotoh, Y. Oosawa *J. Solid State Chem.* **1998**, *141*, 298-302.

[349] I. Oh, S. Hong, Y. Sun *J. Mater. Sci.* **1997**, *32*, 3177-3182.

[350] S. Kang, S. Kang, K. Ryu, S. Chang *Solid State Ionics* **1999**, *120*, 155-161.

[351] C. A. Marianetti, G. Kotliar, G. Ceder *Nat. Mater.* **2004**, *3*, 627-631.

[352] M. Antaya, K. Cearns, J. Preston, J. Reimers, J. Dahn *J. Appl. Phys.* **1994**, *76*, 2799-2806.

[353] J. N. Reimers, J. Dahn *J. Electrochem. Soc.* **1992**, *139*, 2091-2097.

[354] B. Garcia, J. Farcy, J. Pereira-Ramos, J. Perichon, N. Baffier *J. Power Sources* **1995**, *54*, 373-377.

[355] P. Nie, L. Shen, H. Luo, H. Li, G. Xu, X. Zhang *Nanoscale* **2013**, *5*, 11087-11093.

[356] M. Takahashi, S. Tobishima, K. Takei, Y. Sakurai *Solid State Ionics* **2002**, *148*, 283-289.

[357] Y. Hu, M. M. Doeff, R. Kostecki, R. Finones *J. Electrochem. Soc.* **2004**, *151*, A1279-A1285.

[358] M. S. Whittingham *Prog. Solid State Chem.* **1978**, *12*, 41-99.

[359] P. Poizot, S. Laruelle, S. Grugeon, L. Dupont, J.M. Tarascon *Nature* **2000**, *407*, 496-499.

[360] J. Cabana, L. Monconduit, D. Larcher, M. R. Palacin *Adv. Mater.* **2010**, *22*, E170-E192.

[361] D. Aurbach, A. Zaban, A. Schechter, Y. Ein-Eli, E. Zinigrad, B. Markovsky *J. Electrochem. Soc.* **1995**, *142*, 2873-2882.

[362] J. Xie, X. Zhao, G. Cao, M. Zhao, S. Su *J. Alloy Compd.* **2005**, *393*, 283-286.

[363] J. Wang, C. Feng, Z. Sun, S. Chou, H. Liu, J. Wang *Sci. rep.* **2014**, *4*.

[364] G. Binotto, D. Larcher, A. Prakash, R. Herrera Urbina, M. Hegde, J.M. Tarascon *Chem. Mater.* **2007**, *19*, 3032-3040.

[365] C. M. Julien, K. Zaghib, A. Mauger, M. Massot, A. Ait-Salah, M. Selmane, F. Gendron *J. Appl. Phys.* **2006**, *100*, 063511-1-7.

[366] D. Mattia, M. P. Rossi, B. M. Kim, G. Korneva, H. H. Bau, Y. Gogotsi *J. Phys. Chem. B* **2006**, *110*, 9850-9855.

[367] S. Polarz, B. Smarsly, J. H. Schattka *Chem. Mater.* **2002**, *14*, 2940-2945.

[368] W. Low *Phys. Rev.* **1958**, *109*, 247-255.

[369] A. D. Liehr, C. J. Ballhausen *Ann. Phys* **1959**, *6*, 134-155.

[370] G. R. Rossman *J. Solid State Chem.* **1981**, *39*, 277-287.

# APPENDIX

# Appendix Chapter III

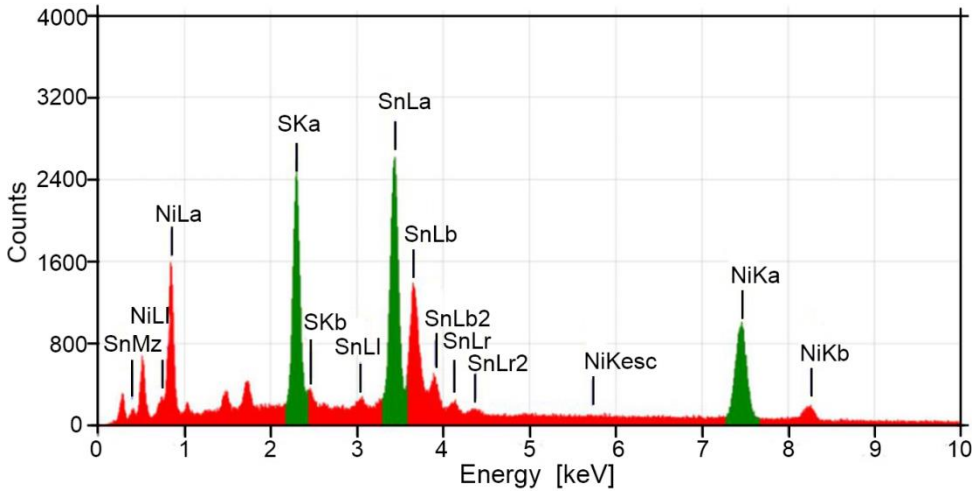


**Figure 63:** Energy dispersive X-ray spectrum of the optimized $Ni_3Sn_2S_2$ sample.

### Cell constants of the optimized $Ni_3Sn_2S_2$ sample

Wavelength : 1.540598

Number of accepted peaks : 29

2Theta window : 0.150

2Theta zeropoint : -0.1324 ( fixed )

Symmetry : Trigonal_H R

Spacegroup : R -3 m ( No. 166 )

Initial cell parameters :

Cell_A : 5.4550

Cell_C : 13.1880

Refined cell parameters :

Cell_A : 5.455(3)

Cell_C : 13.188(3)

Cell_Volume: 339.81(23)

Number of single indexed lines : 20

Number of unindexed lines : 6

Final 2Theta window : 0.1300

| | | | | | | | | | |
|---|---|---|---|---|---|---|---|---|---|
| 1 | 19.960 | | 1 | 0 | 1 | 19.949 | 0.0104 | 8.9 | 4.4449 | 4.4472 |
| 2 | 20.206 | | 0 | 0 | 3 | 20.184 | 0.0219 | 33.7 | 4.3911 | 4.3959 |
| 3 | 23.178 | | 0 | 1 | 2 | 23.143 | 0.0351 | 68.0 | 3.8344 | 3.8401 |
| 4 | 24.972 | | --- not indexed --- | | | | | 3.0 | 3.5629 | |
| 5 | 32.560 | | --- not indexed --- | | | | | 9.7 | 2.7478 | |
| 6 | 32.845 | | 1 | 1 | 0 | 32.811 | 0.0340 | 100.0 | 2.7246 | 2.7273 |
| 7 | 33.144 | | 1 | 0 | 4 | 33.108 | 0.0361 | 96.1 | 2.7007 | 2.7036 |
| 8 | 38.720 | | 0 | 2 | 1 | 38.698 | 0.0220 | 33.6 | 2.3237 | 2.3249 |
| | | ? | 1 | 1 | 3 | 38.827 | -0.1069 | | | 2.3175 |
| 9 | 38.957 | ? | 1 | 1 | 3 | 38.827 | 0.1301 | 10.3 | 2.3101 | 2.3175 |
| | | | 0 | 1 | 5 | 39.084 | -0.1267 | | | 2.3029 |
| 10 | 40.360 | | --- not indexed --- | | | | | 15.4 | 2.2330 | |
| 11 | 40.589 | | 2 | 0 | 2 | 40.537 | 0.0521 | 77.8 | 2.2208 | 2.2236 |
| 12 | 41.062 | | 0 | 0 | 6 | 41.032 | 0.0302 | 47.1 | 2.1964 | 2.1979 |
| 13 | 47.345 | | 0 | 2 | 4 | 47.305 | 0.0401 | 93.2 | 1.9185 | 1.9201 |
| 14 | 51.876 | | 2 | 0 | 5 | 51.925 | -0.0492 | 10.1 | 1.7611 | 1.7595 |
| 15 | 52.204 | | 1 | 0 | 7 | 52.232 | -0.0285 | 8.1 | 1.7508 | 1.7499 |
| 16 | 53.086 | | 1 | 2 | 2 | 53.098 | -0.0128 | 9.2 | 1.7238 | 1.7234 |
| 17 | 53.533 | | 1 | 1 | 6 | 53.501 | 0.0319 | 15.9 | 1.7104 | 1.7114 |
| 18 | 58.675 | | 3 | 0 | 0 | 58.575 | 0.1001 | 27.5 | 1.5722 | 1.5746 |
| | | | 2 | 1 | 4 | 58.764 | -0.0889 | | | 1.5700 |
| 19 | 59.305 | | 0 | 1 | 8 | 59.329 | -0.0242 | 9.8 | 1.5570 | 1.5564 |
| 20 | 62.624 | | 3 | 0 | 3 | 62.615 | 0.0084 | 2.0 | 1.4822 | 1.4824 |
| 21 | 63.400 | | 0 | 0 | 9 | 63.431 | -0.0304 | 2.9 | 1.4659 | 1.4653 |
| 22 | 68.754 | | 2 | 2 | 0 | 68.787 | -0.0335 | 16.8 | 1.3642 | 1.3637 |
| 23 | 69.459 | | 2 | 0 | 8 | 69.478 | -0.0191 | 15.3 | 1.3521 | 1.3518 |
| 24 | 72.712 | | --- not indexed --- | | | | | 3.0 | 1.2994 | |
| 25 | 73.821 | | --- not indexed --- | | | | | 5.3 | 1.2826 | |
| 26 | 74.602 | | 1 | 0 | 10 | 74.666 | -0.0639 | 3.8 | 1.2711 | 1.2702 |
| 27 | 78.671 | | --- not indexed --- | | | | | 8.5 | 1.2153 | |
| 28 | 83.168 | | 0 | 1 | 11 | 83.041 | 0.1267 | 14.6 | 1.1606 | 1.1620 |
| 29 | 83.919 | | 0 | 2 | 10 | 83.978 | -0.0589 | 9.7 | 1.1521 | 1.1514 |

Average delta(2Theta) = 0.043

Maximum delta(2Theta) = 0.127 ( peak 9 ) = 3.0 * average

Figure of Merit F(23) = 13.4 ( 0.043, 40 )

Durbin-Watson serial correlation = 2.609 ( not significant )

Sqrt[ sum( w * delta(q)^2 ) / ( Nobs - Nvar ) ] = 0.00035931

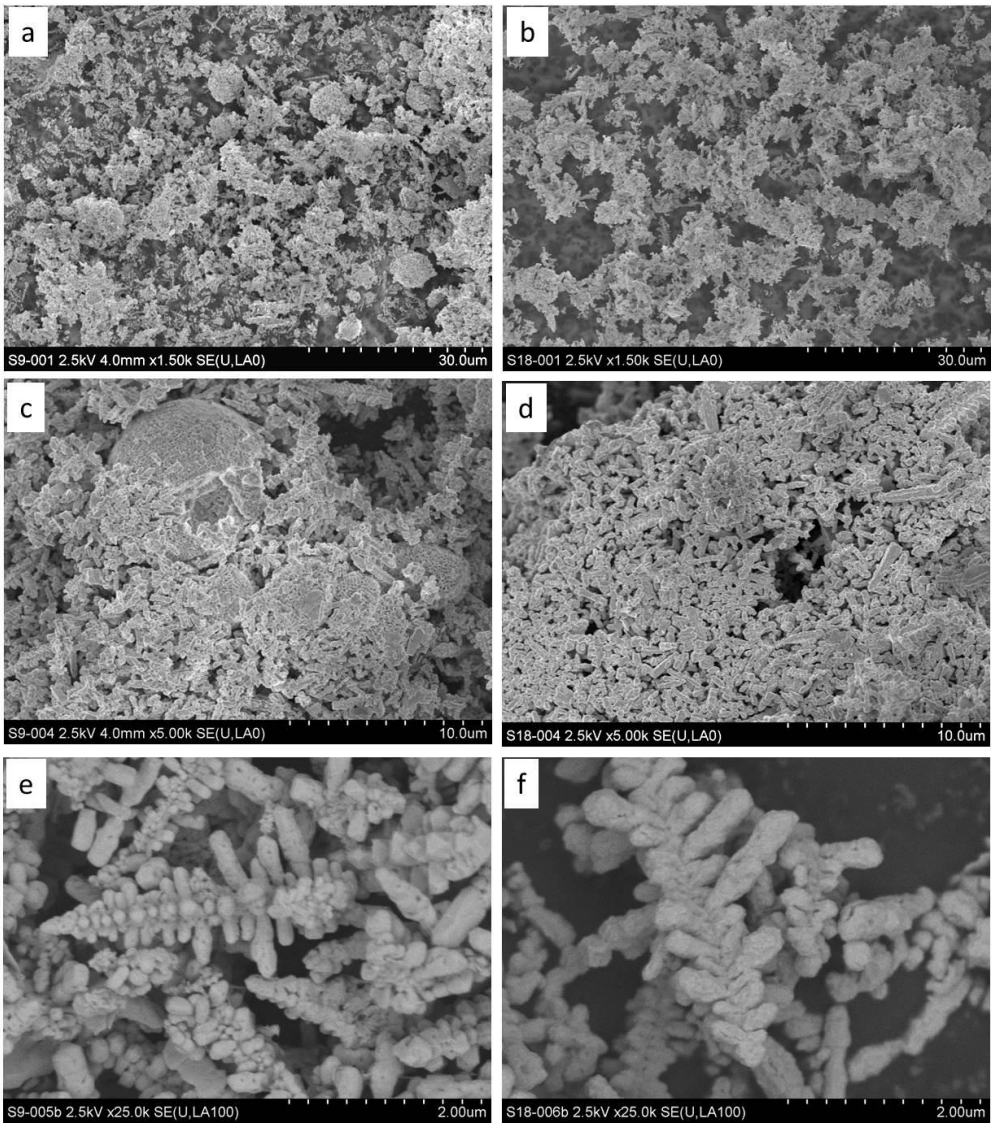


**Figure 64:** SEM pictures of the synthesis of $Ni_3Pb_2S_{2,dendrites}$ from $PbS_{dendrites}$ with the changed detector.

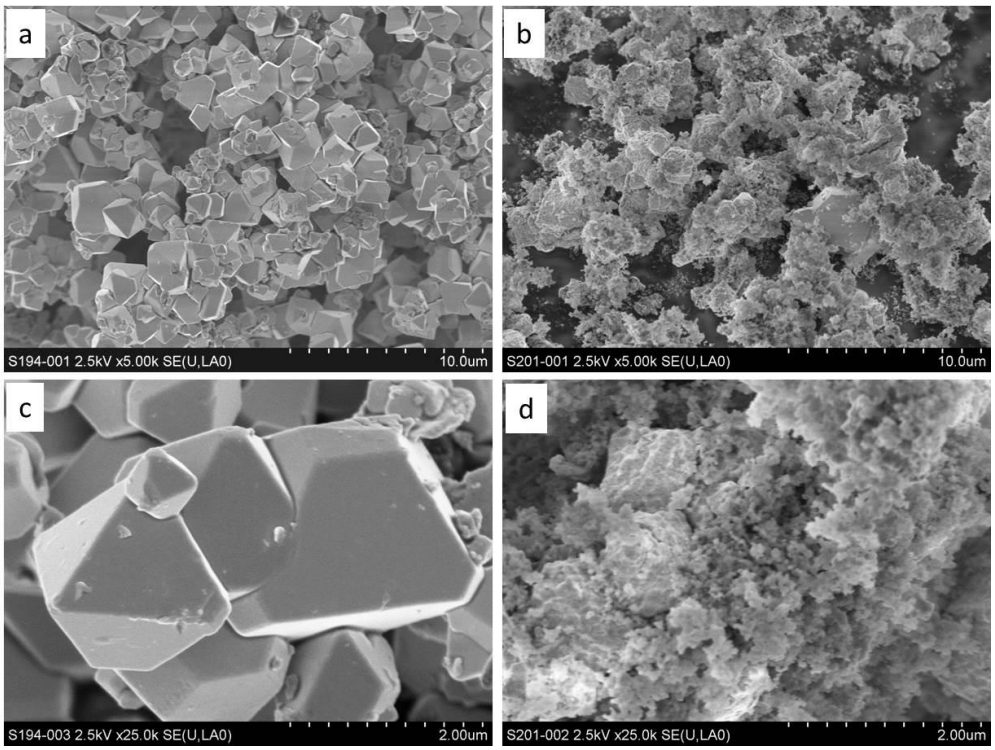


**Figure 65:** SEM pictures of the synthesis of $Ni_3Pb_2S_{2,Octahedron}$ from $PbS_{Octahedron}$ with the other detector.

## Cell constants of $Ni_3Pb_2S_{2,dendrite}$

Wavelength : 1.540598

Number of accepted peaks : 20

2Theta window : 0.060

2Theta zeropoint : 0.1490 ( fixed )

Symmetry : Trigonal_H R

Spacegroup : R -3 m ( No. 166 )

Initial cell parameters :

Cell_A : 5.5731

Cell_C : 13.6080

Refined cell parameters :

Cell_A : 5.5731(19)

Cell_C : 13.608(5)

Cell_Volume: 366.03(15)

Number of single indexed lines : 10

Number of unindexed lines : 4

Final 2Theta window : 0.0600

| N | 2Th[obs] | H | K | L | 2Th[calc] | obs-calc | Int. | d[obs] | d[calc] |
|---|---|---|---|---|---|---|---|---|---|
| 1 | 19.559 | 1 | 0 | 1 | 19.499 | 0.0599 | 11.9 | 4.5350 | 4.5488 |
| | | 0 | 0 | 3 | 19.555 | 0.0039 | | | 4.5359 |
| 2 | 22.575 | 0 | 1 | 2 | 22.568 | 0.0067 | 65.8 | 3.9354 | 3.9366 |
| 3 | 32.138 | 1 | 1 | 0 | 32.095 | 0.0431 | 100.0 | 2.7829 | 2.7866 |
| | | 1 | 0 | 4 | 32.165 | -0.0273 | | | 2.7806 |
| 4 | 37.859 | 0 | 2 | 1 | 37.831 | 0.0279 | 8.8 | 2.3745 | 2.3762 |
| | | 1 | 1 | 3 | 37.862 | -0.0026 | | | 2.3743 |
| 5 | 39.566 | 2 | 0 | 2 | 39.593 | -0.0268 | 29.9 | 2.2759 | 2.2744 |
| 6 | 39.731 | 0 | 0 | 6 | 39.710 | 0.0208 | 24.2 | 2.2668 | 2.2680 |
| 7 | 46.080 | 0 | 2 | 4 | 46.077 | 0.0025 | 36.2 | 1.9682 | 1.9683 |
| 8 | 50.540 | 2 | 0 | 5 | 50.505 | 0.0345 | 4.1 | 1.8045 | 1.8056 |
| | | 1 | 0 | 7 | 50.578 | -0.0383 | | | 1.8032 |
| 9 | 51.636 | --- not indexed --- | | | | | 2.7 | 1.7687 | |
| 10 | 51.927 | 1 | 1 | 6 | 51.942 | -0.0153 | 19.5 | 1.7595 | 1.7590 |
| 11 | 56.867 | --- not indexed --- | | | | | 1.7 | 1.6178 | |
| 12 | 57.213 | 3 | 0 | 0 | 57.213 | -0.0005 | 17.6 | 1.6088 | 1.6088 |
| | | 2 | 1 | 4 | 57.258 | -0.0451 | | | 1.6077 |
| 13 | 57.431 | 0 | 1 | 8 | 57.392 | 0.0399 | 7.3 | 1.6032 | 1.6043 |
| 14 | 66.981 | --- not indexed --- | | | | | 4.0 | 1.3960 | |
| 15 | 67.236 | 2 | 0 | 8 | 67.290 | -0.0537 | 9.6 | 1.3913 | 1.3903 |
| 16 | 71.857 | 3 | 1 | 2 | 71.814 | 0.0429 | 5.7 | 1.3128 | 1.3134 |
| | | 3 | 0 | 6 | 71.893 | -0.0359 | | | 1.3122 |
| 17 | 72.487 | --- not indexed --- | | | | | 0.9 | 1.3029 | |
| 18 | 76.405 | 1 | 3 | 4 | 76.397 | 0.0079 | 5.2 | 1.2456 | 1.2457 |
| 19 | 80.906 | 2 | 2 | 6 | 80.911 | -0.0055 | 8.0 | 1.1872 | 1.1872 |
| 20 | 85.297 | 4 | 0 | 4 | 85.275 | 0.0213 | 1.2 | 1.1370 | 1.1372 |

Average delta(2Theta) = 0.019

Maximum delta(2Theta) = 0.054 ( peak 15 ) = 2.8 * average

Figure of Merit F(16) = 20.0 ( 0.019, 42 )

Durbin-Watson serial correlation = 2.186 ( not significant )

Sqrt[ sum( w * delta(q)^2 ) / ( Nobs - Nvar ) ] = 0.00022328

## Cell constants of $Ni_3Pb_2S_{2,bulk}$

Wavelength : 1.540598

Number of accepted peaks : 29

2Theta window : 0.040

2Theta zeropoint : 0.1900 ( fixed )

Symmetry : Trigonal_H R

Spacegroup : R -3 m ( No. 166 )

Initial cell parameters :

Cell_A : 5.5871

Cell_C : 13.5969

Refined cell parameters :

Cell_A : 5.5871(4)

Cell_C : 13.5969(10)

Cell_Volume: 367.58(4)

Number of single indexed lines : 28

Number of unindexed lines : 0

Final 2Theta window : 0.0400

| N | 2Th[obs] | H | K | L | 2Th[calc] | obs-calc | Int. | d[obs] | d[calc] |
|---|---|---|---|---|---|---|---|---|---|
| 1 | 19.444 | 1 | 0 | 1 | 19.457 | -0.0132 | 4.8 | 4.5616 | 4.5586 |
| 2 | 19.557 | 0 | 0 | 3 | 19.571 | -0.0140 | 10.7 | 4.5355 | 4.5323 |
| 3 | 22.529 | 0 | 1 | 2 | 22.537 | -0.0074 | 100.0 | 3.9434 | 3.9421 |
| 4 | 32.004 | 1 | 1 | 0 | 32.012 | -0.0080 | 66.8 | 2.7942 | 2.7936 |
| 5 | 32.146 | 1 | 0 | 4 | 32.155 | -0.0100 | 63.7 | 2.7823 | 2.7815 |
| 6 | 37.760 | 0 | 2 | 1 | 37.737 | 0.0230 | 17.3 | 2.3805 | 2.3819 |
| | | 1 | 1 | 3 | 37.799 | -0.0391 | | | 2.3781 |
| 7 | 39.521 | 2 | 0 | 2 | 39.505 | 0.0163 | 74.2 | 2.2784 | 2.2793 |
| 8 | 39.745 | 0 | 0 | 6 | 39.743 | 0.0015 | 18.2 | 2.2661 | 2.2662 |
| 9 | 46.021 | 0 | 2 | 4 | 46.009 | 0.0122 | 52.5 | 1.9706 | 1.9711 |
| 10 | 50.457 | 2 | 0 | 5 | 50.449 | 0.0084 | 4.5 | 1.8072 | 1.8075 |
| 11 | 50.586 | 1 | 0 | 7 | 50.596 | -0.0101 | 2.1 | 1.8029 | 1.8026 |
| 12 | 51.737 | 1 | 2 | 2 | 51.720 | 0.0172 | 30.4 | 1.7655 | 1.7660 |
| 13 | 51.925 | 1 | 1 | 6 | 51.914 | 0.0110 | 21.8 | 1.7596 | 1.7599 |
| 14 | 57.064 | 3 | 0 | 0 | 57.057 | 0.0070 | 15.7 | 1.6127 | 1.6129 |
| 15 | 57.155 | 2 | 1 | 4 | 57.148 | 0.0072 | 17.7 | 1.6103 | 1.6105 |
| 16 | 57.420 | 0 | 1 | 8 | 57.419 | 0.0015 | 14.0 | 1.6035 | 1.6036 |
| 17 | 60.937 | 3 | 0 | 3 | 60.920 | 0.0168 | 1.2 | 1.5191 | 1.5195 |
| 18 | 66.928 | 2 | 2 | 0 | 66.937 | -0.0098 | 14.6 | 1.3970 | 1.3968 |
| 19 | 67.262 | 2 | 0 | 8 | 67.268 | -0.0051 | 8.8 | 1.3908 | 1.3907 |
| 20 | 70.498 | 2 | 2 | 3 | 70.490 | 0.0081 | 2.0 | 1.3347 | 1.3348 |
| 21 | 71.630 | 3 | 1 | 2 | 71.617 | 0.0136 | 9.5 | 1.3164 | 1.3166 |
| 22 | 71.768 | 3 | 0 | 6 | 71.777 | -0.0091 | 5.3 | 1.3142 | 1.3140 |
| 23 | 72.101 | 1 | 0 | 10 | 72.097 | 0.0045 | 4.6 | 1.3089 | 1.3090 |
| 24 | 76.197 | 1 | 3 | 4 | 76.211 | -0.0142 | 6.7 | 1.2484 | 1.2482 |
| 25 | 76.444 | 1 | 2 | 8 | 76.446 | -0.0020 | 7.4 | 1.2450 | 1.2450 |
| 26 | 80.602 | 0 | 4 | 2 | 80.601 | 0.0010 | 9.6 | 1.1909 | 1.1909 |
| 27 | 80.757 | 2 | 2 | 6 | 80.755 | 0.0018 | 8.1 | 1.1890 | 1.1891 |
| 28 | 81.069 | 0 | 2 | 10 | 81.063 | 0.0057 | 6.0 | 1.1852 | 1.1853 |
| 29 | 85.020 | 4 | 0 | 4 | 85.051 | -0.0309 | 2.6 | 1.1400 | 1.1396 |

Average delta(2Theta) = 0.010

Maximum delta(2Theta) = 0.031 ( peak 29 ) = 3.1 * average

Figure of Merit F(29) = 68.8 ( 0.010, 42 )

Durbin-Watson serial correlation = 1.706 ( not significant )

Sqrt[ sum( w * delta(q)^2 ) / ( Nobs - Nvar ) ] = 8.8982e-005

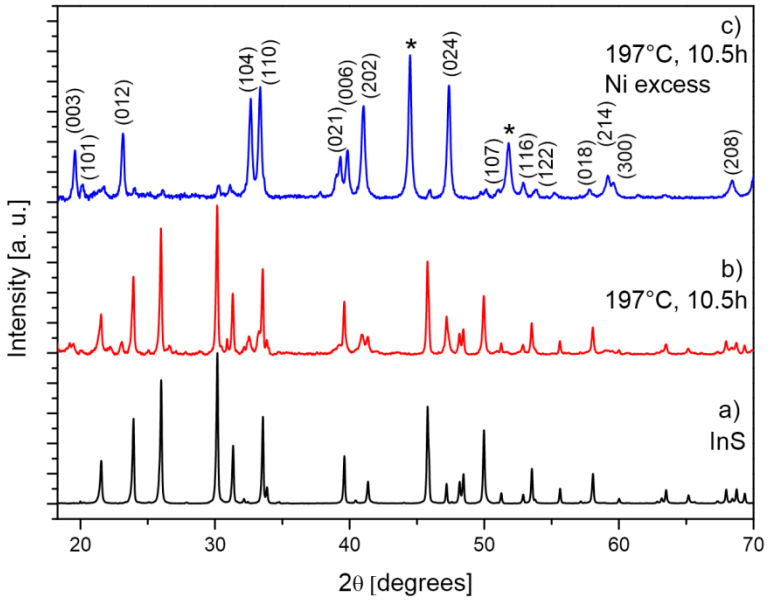


**Figure 66:** a) Starting material $InS_{,bulk}$, b) Result after reacting at 197 °C for 10.5 h c) Result after reacting at 197 °C for 10.5 h with fourfold nickel excess.

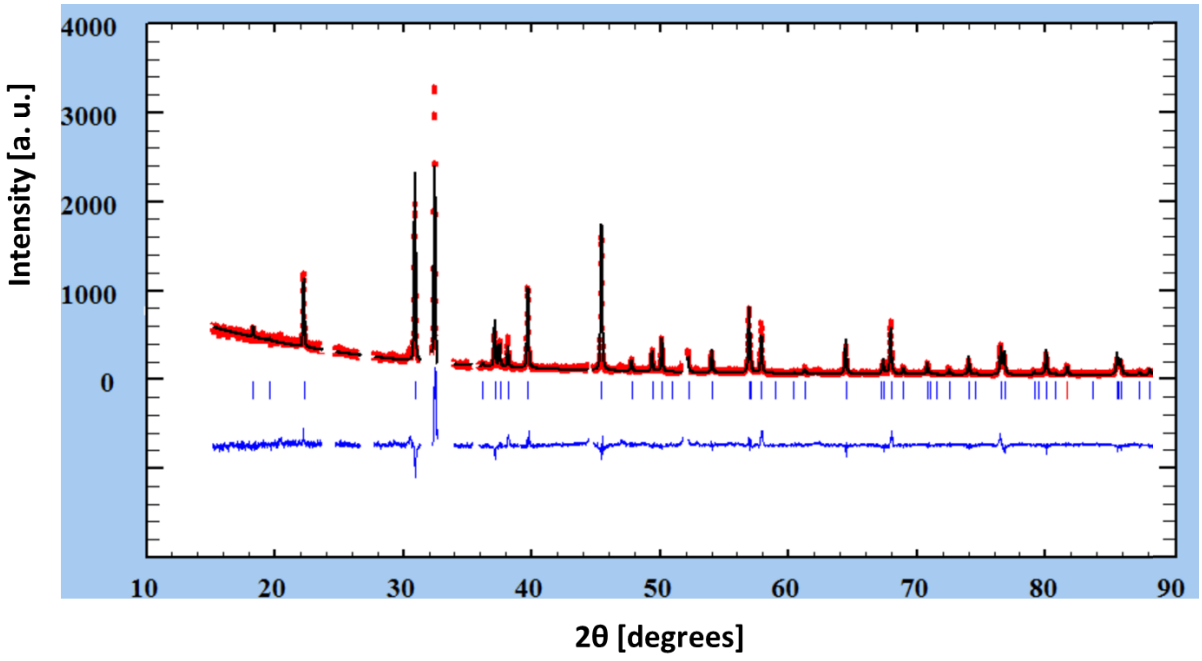


**Figure 67:** Rietveld refinement of a solid-state sample, mainly consisting of *shandite*-type $Ni_3Tl_2Se_2$. For the refinement a hexagonal model with $R\bar{3}m$ symmetry was chosen in analogy to the known *shandite*-family.

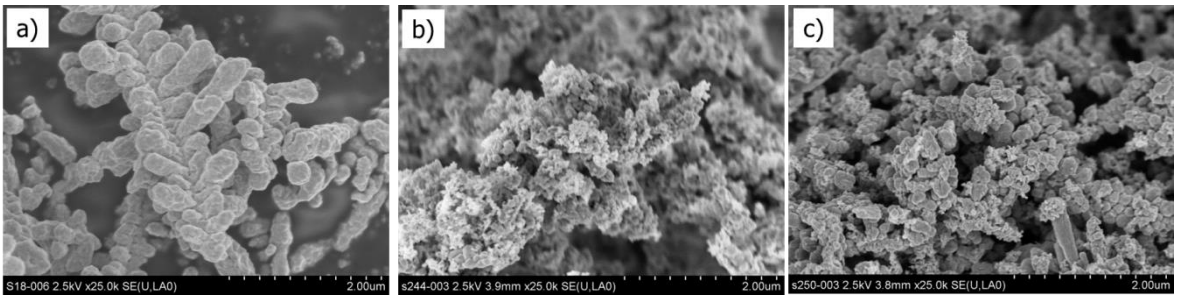


**Figure 68:** a) $PbS_{dendrite}$ b) $Ni@PbS_{dendrite}$ c) $Ni_3Pb_2S_2$ after annealing of $Ni@PbS_{cube}$ at 500 °C for 7 d.

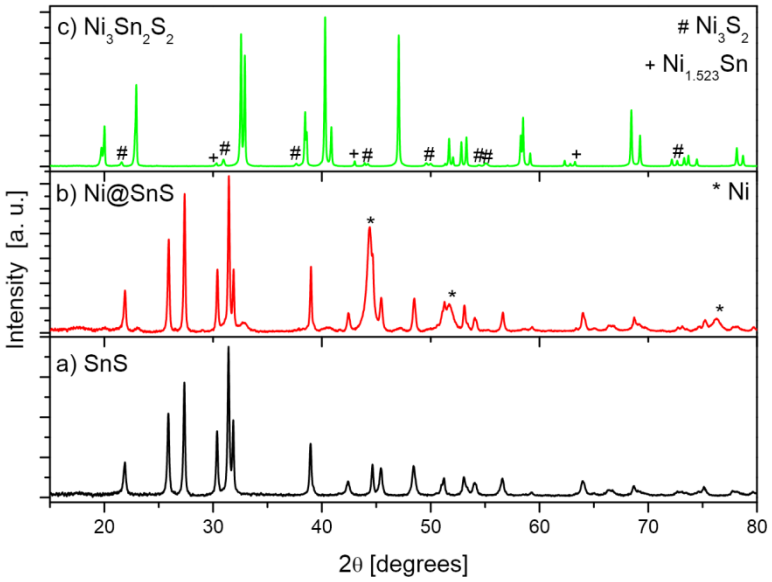


Figure 69: a) Pristine SnS (b) Product after reaction with hydrazine to Ni@SnS core-shell particles (c) Reaction of Ni@SnS to $Ni_3Sn_2S_2$ in a solid state reaction at 700 °C (7 days).

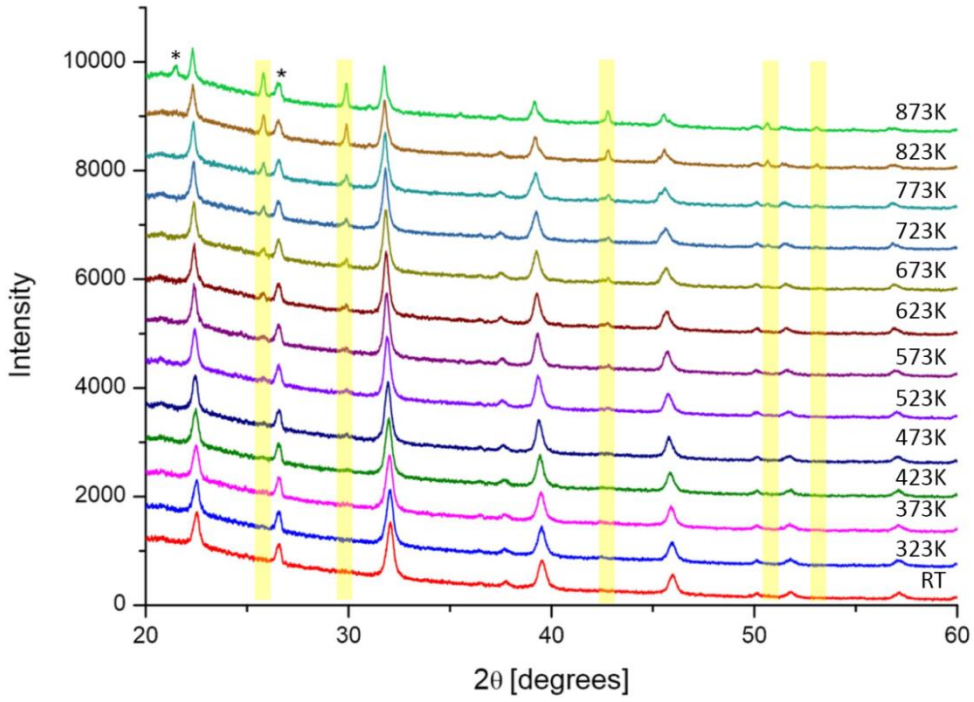


**Figure 70:** In situ HT-XRD of dendritic $Ni_3Pb_2S_2$ in the temperature range between RT and 873 K.

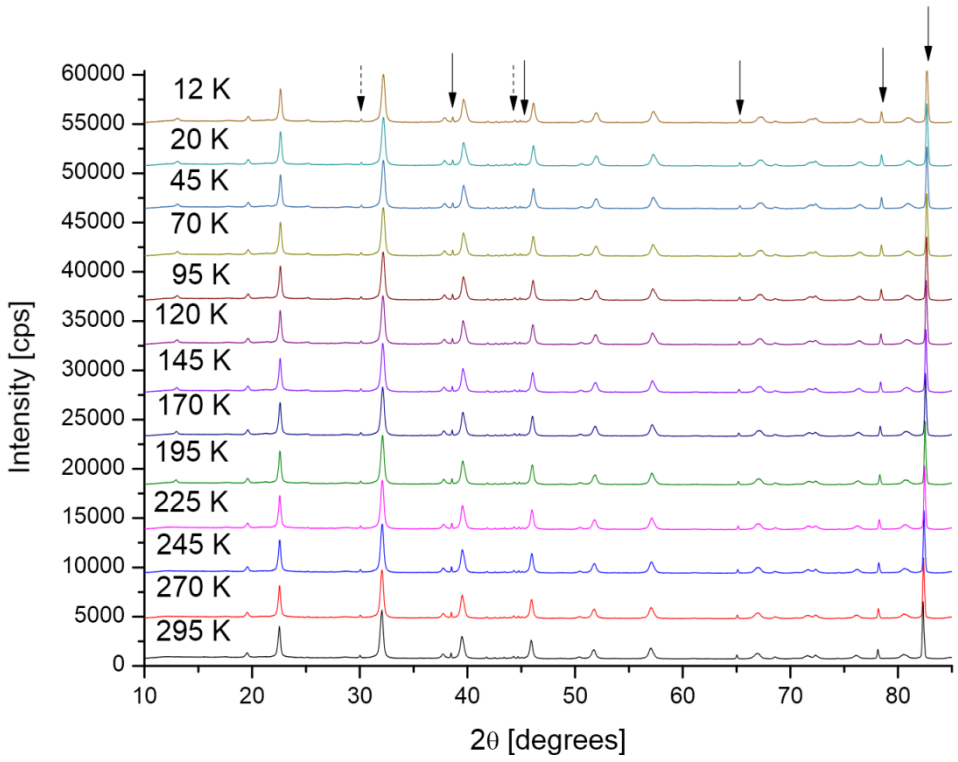


**Figure 71:** LT-XRD of octahedral $Ni_3Pb_2S_2$ in the temperature range between 291 and 12 K. The arrows mark the Al foil, which was used as sample holder during the measurements. The dotted arrows mark a small side phase of NiPb.

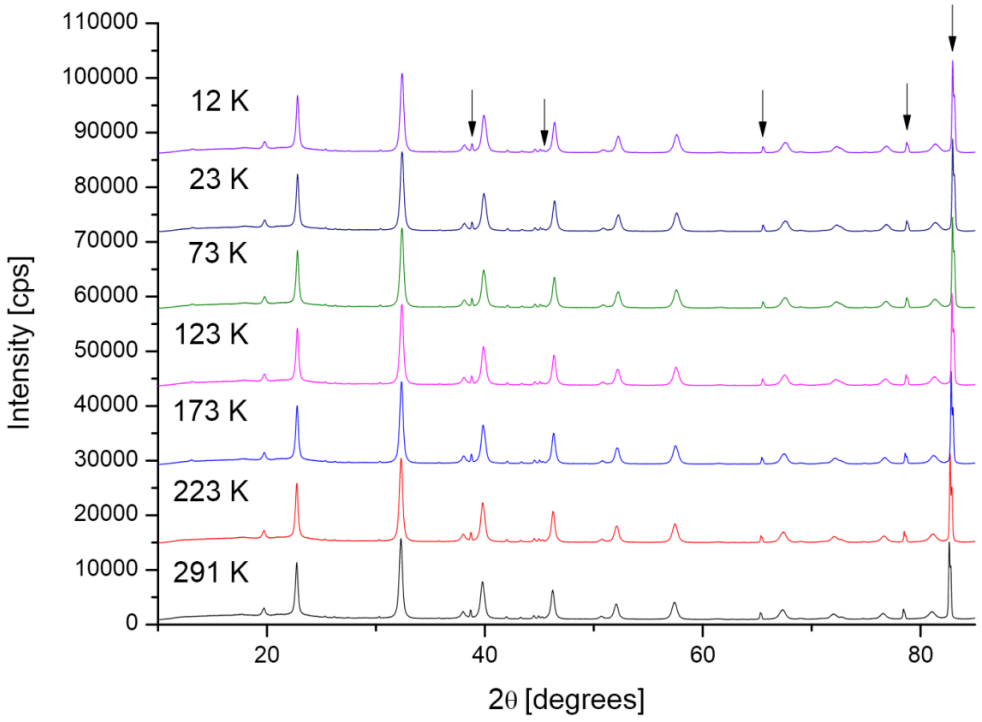


**Figure 72:** LT-XRD of dendritic $Ni_3Pb_2S_2$ in the temperature range between 291 and 12 K. The arrows mark the Al foil which was used as sample holder during the measurements.

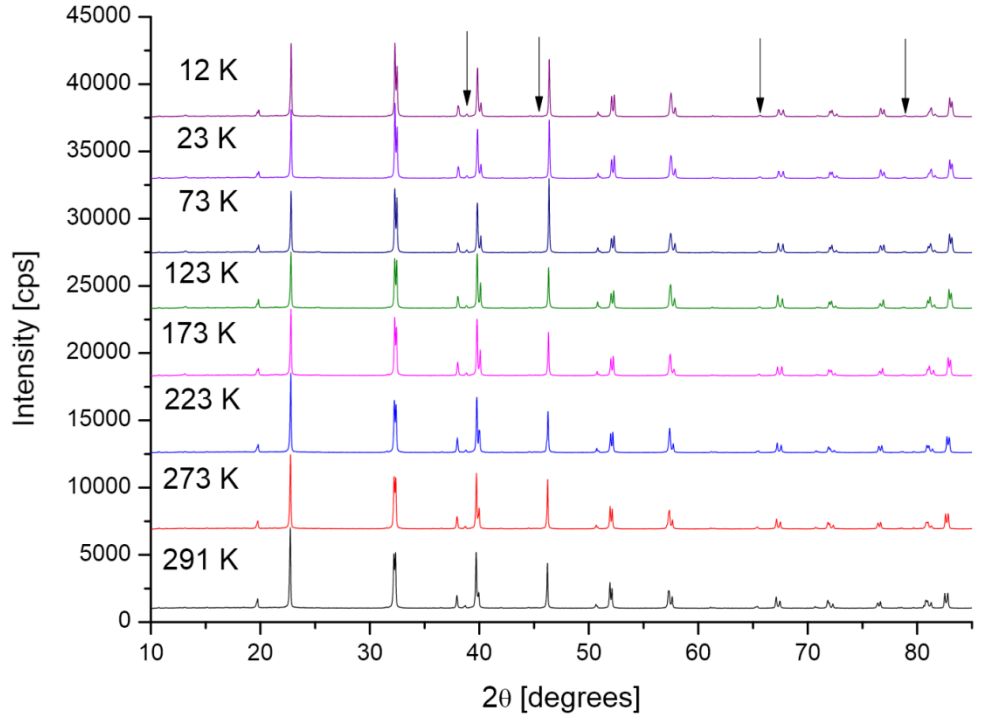


**Figure 73:** LT-XRD of bulk $Ni_3Pb_2S_2$ in the temperature range between 291 and 12 K. The arrows mark the Al foil which was used as sample holder during the measurements.

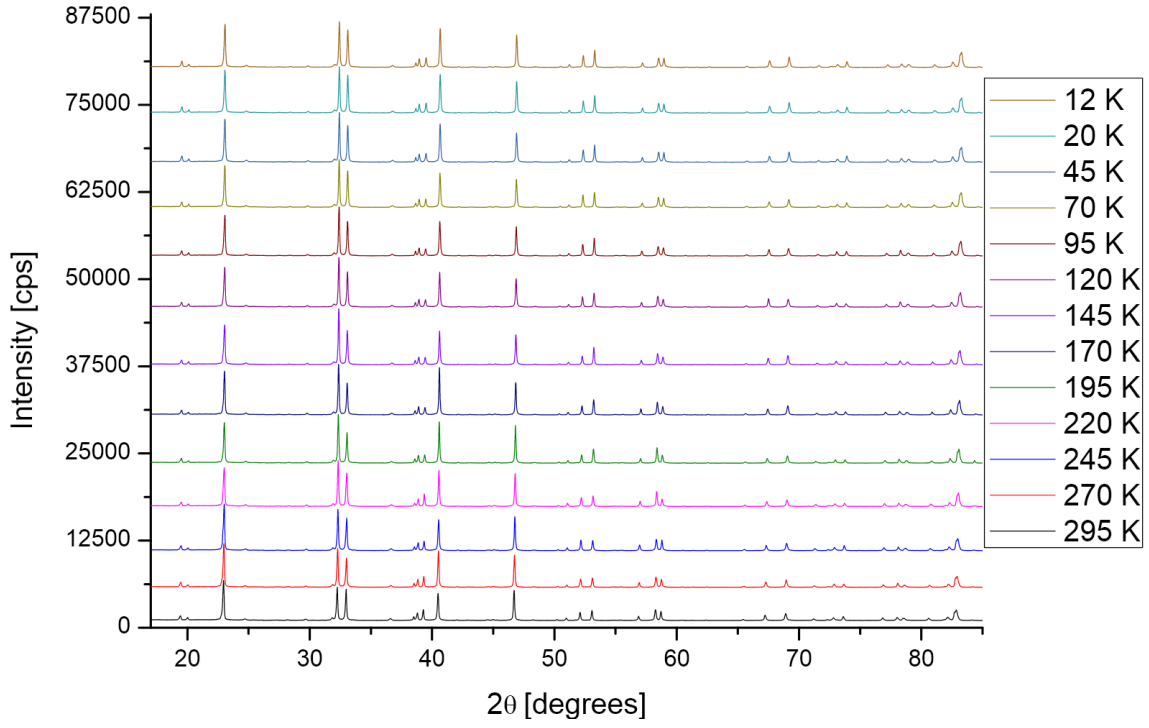


**Figure 74:** LT-XRD of bulk $Ni_3Tl_2S_2$ in the temperature range between 295 and 12 K.

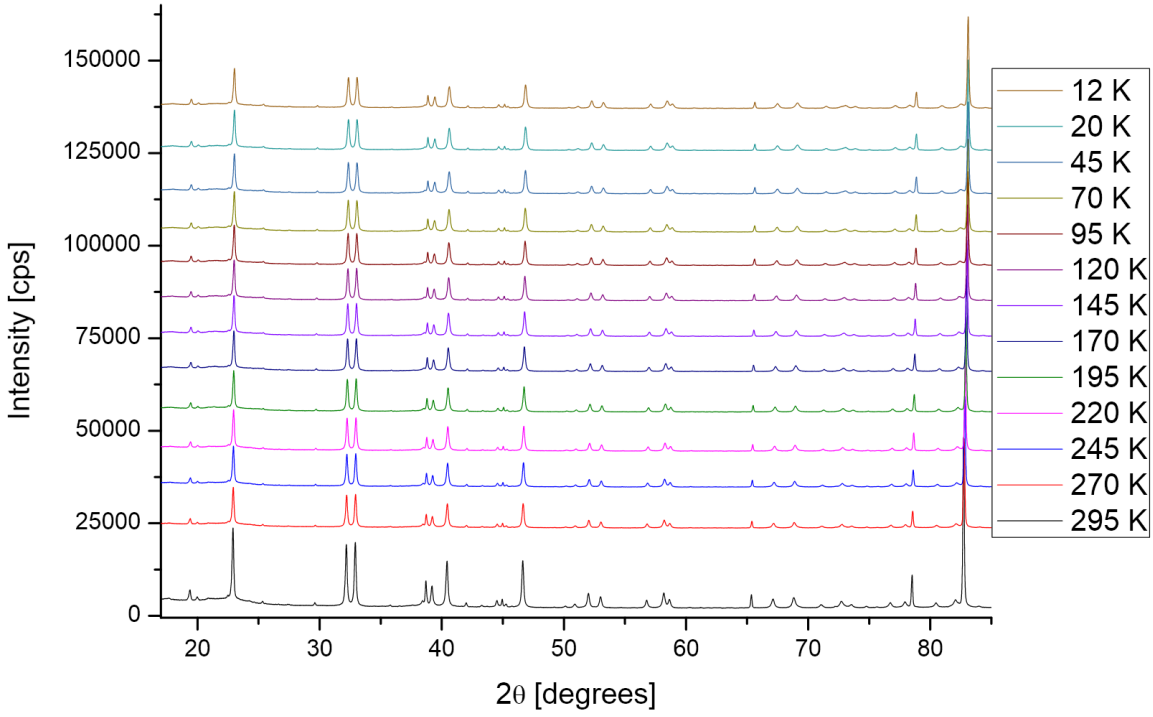


**Figure 75:** LT-XRD of nano $Ni_3Tl_2S_2$ in the temperature range between 295 and 12 K.

# Appendix Chapter IV

## General information about the reactions

All reactions were performed in air without the application of any protective gas.

Stirring $NiCl_2*6H_2O$ in ethylene glycol or tetraethylene glycol led to a green solution. After the addition of ethylenediamine the colour changed to purple. Under reductive conditions (reflux in an alkaline polyol solution) the colour gradually changed to grey-black, as the $Ni^{2+}$ was reduced to elemental Ni.

When NiBi and elemental selenium were applied, the solution exhibited no special colour before the heating process. After the reaction, the solution showed an orange to brown opaque colour.

When NiBi and elemental sulfur were applied, the solution exhibited no special colour before the heating process. After the reaction, the solution was almost transparent without a definitely colouring.

The colour of all resulting Bi, NiBi, $Ni_3Bi_2X_2$ ($X$=S, Se) and NiBiSe samples was grey to black. Hereby the resulting Bi (AR1) clumped together to one big glob as no surfactant was used. All other samples resulted in fine powders which adhered in the centrifuge tubes and had to be scraped off.

A determination of the yield was therefore difficult. An almost entire turnover of the reactants is expected.

## More precise synthesis conditions

***AR1: Synthesis of Bi:*** In a first step, the $Bi_2S_3$ nanorods were converted to elemental Bi. Therefore $Bi_2S_3$ (1.17 g) was refluxed in basic ethylene glycol (eg: 70 mL; NaOH: 0.545 g) and ethylenediamine (46 mL) at 197 °C for 5 hours. The amount of en was increased because of the high amount of $Bi_2S_3$.

***AR2: Synthesis of NiBi:*** The resulting Bi clump was crushed and ground and washed with $H_2O$ and EtOH. NiBi was synthesised by refluxing the obtained bismuth powder (0.764 g) with $NiCl_2$*$6H_2O$ (0.868 g) in basic ethylene glycol (eg: 50 mL; NaOH: 2.60 g) and ethylenediamine (24 mL) at 197 °C overnight. The obtained powder was washed with $H_2O$ and EtOH.

***AR3: Synthesis of $Ni_3Bi_2S_2$ (+Bi) starting from NiBi:*** A mixture of NiBi (0.79 g) and $Na_2S$ (0.261 g)/S(0.063 g) in 70 mL ethylene glycol was added to a 100 mL round-bottom flask, magnetically stirred and treated with ultrasound. Then NaOH (2.15 g) and ethylenediamine (19.95 mL) were added. After the NaOH dissolved completely the flask was heated and the mixture was refluxed at 197 °C for 14.5 h. After cooling to room temperature, the products were centrifuged and washed several times with water and ethanol and dried at 60 °C.

***AR4: One-pot synthesis of $Ni_3Bi_2S_2$ under large Ni-excess:*** A mixture of $Bi_2S_3$ (0.098 g) and $NiCl_2$ *$6H_2O$ (0.357 g) in 70 ml ethylene glycol was added to a 100 ml round-bottom flask, magnetically stirred and treated with ultrasound. Then NaOH (0.545 g) and ethylenediamine (5.05 mL) were added. After the NaOH dissolved completely the flask was heated and the mixture was refluxed at 197 °C for 2.5 h under air. After cooling to room temperature, the products were centrifuged and washed several times with water and ethanol and dried at 60 °C.

***AR5: One-pot synthesis of $Ni_3Bi_2Se_2$ starting from $Bi_2Se_3$:*** A mixture of $Bi_2Se_3$ (0.163 g) and $NiCl_2$*$6H_2O$ (0.178, molar ratio 1:3) in 70 ml ethylene glycol was added to a 100 ml round-bottom flask, magnetically stirred and treated with ultrasound. Then NaOH (0.545 g) and ethylenediamine (5.05 mL) were added. After the NaOH dissolved completely the flask was heated and the mixture was refluxed at 197 °C for 10.5 h. After cooling to room temperature, the products were centrifuged and washed several times with water and ethanol and dried at 60 °C.

***AR6: Reaction of NiBi with Se to a mixture of NiBiSe and $Ni_3Bi_2Se_2$:*** A mixture of NiBi (0.063 g) and Se (0.014 g, ratio 3:2) in 70 mL ethylene glycol was added to a 100 mL round-bottom flask, magnetically stirred and treated with ultrasound. Then NaOH (0.30 g) and ethylenediamine (20 mL) were added. After the NaOH dissolved completely the flask was heated and the mixture was refluxed at 197 °C for 10 h. After cooling to room temperature,

the products were centrifuged and washed several times with water and ethanol and dried at 60 °C.

***AR7: Synthesis of NiBiSe starting from NiBi and Se:*** The reaction was performed according to reaction SR6.A mixture of NiBi (0.063 g) and Se (0.019 g, ratio 1:1) in 70 mL ethylene glycol was added to a 100 mL round-bottom flask, magnetically stirred and treated with ultrasound. Then ethylenediamine (20 mL) was added (no NaOH was given to the reaction mixture). The flask was heated and the mixture was maintained at 190 °C for 10 h under continuous stirring. After cooling to room temperature, the products were centrifuged and washed several times with water and ethanol and dried at 60 °C.

***AR8: Synthesis of $Ni_3Bi_2Se_2$ (+Bi) starting from NiBi:*** The reaction was performed according to reaction SR6, except that tetraethylene glycol (TEG) instead of eg was used. A mixture of NiBi (0.070 g) and Se (0.014 g, ratio 3:2) in 70 mL tetraethylene glycol was added to a 100 mL round-bottom flask, magnetically stirred and treated with ultrasound. Then ethylenediamine (20 mL) and NaOH (0.545 g) were added. After the NaOH dissolved completely the flask was refluxed at 300 °C for 14.5 h under continuous stirring. After cooling to room temperature, the products were centrifuged and washed several times with water and ethanol and dried at 60 °C.

***AR9: Reaction of NiBiSe to $Ni_3Bi_2Se_2$:*** 0.1 g of the almost single phase NiBiSe sample from SR7 and tetraethylene glycol (70 mL) were added to a 100 mL round-bottom flask, magnetically stirred and treated with ultrasound. Then ethylenediamine (20 mL) and NaOH (0.545 g) were added. After the NaOH dissolved completely the flask was refluxed at 300 °C for 14.5 h. After cooling to room temperature, the products were centrifuged and washed several times with water and ethanol and dried at 60 °C.

# Appendix Chapter V

In order to assure reliable results of the bonding structure of the coated carbon, exemplarily a Raman measurement was performed for $LiCoPO_4$. The two peaks at 1280 $cm^{-1}$ and 1560 $cm^{-1}$ are assigned to the disordered band (D band) and graphitic band (G band) which indicates the existence of polycrystalline graphite[365]. The relative intensity ratio of the D band (normally

forbidden set of modes activated by the defects in the $sp^2$ network) and the G band (assigned to the $E_{2g}$ stretching vibration mode of $sp^2$ carbon) depends on the perfection of the graphite layer structure and illustrates that the graphite structure is highly disordered, which is typical for materials carbonized at temperatures between 600-850 °C[366, 367].

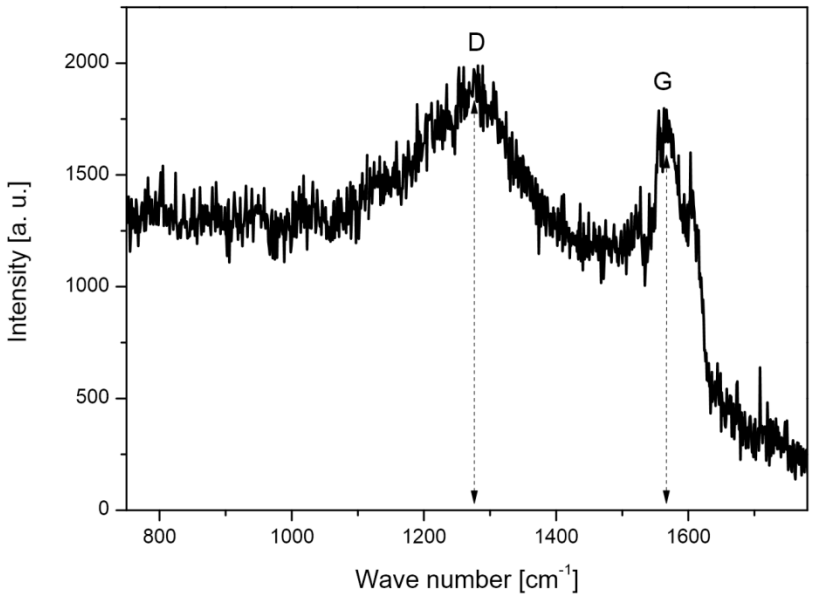


**Figure 76:** Raman spectrum of the $LiCoPO_4$ sample. The typical signals for polycrystalline graphite are present for the prepared sample.

For a complete structural characterization UV-Vis measurements were performed on all samples and results are shown in Figure 77. The bulk color of several of the $Ni^{2+}$ materials is determined primarily by the location of the transmission window defined by the wings of the absorption bands in the 800- and 400 nm regions. The ones around 400 nm are associated with metal ion absorption bands in proximity to an ultraviolet charge transfer tail[368, 369]. For the bright yellow $LiNiPO_4$ compound it is centered in the region 570-580 nm in step with the literature for nickel entering six coordinated sites significantly distorted from octahedral geometry[370]. The more cobalt is enriched in the structure, the more the first absorption band moves to higher wave lengths and the pronounced splitting of the absorption bands is getting smaller.

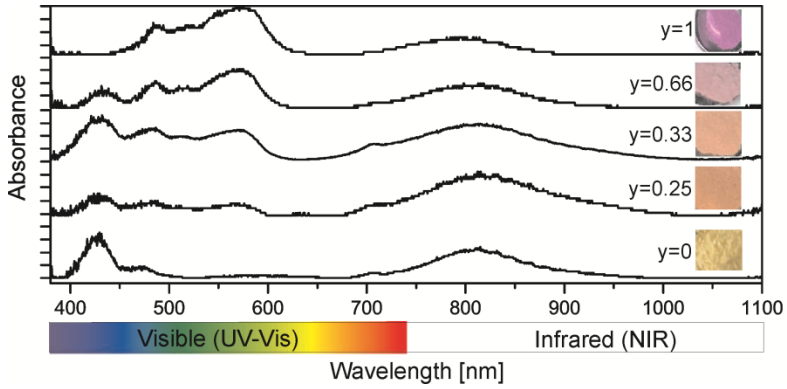


**Figure 77:** UV-Vis spectrum of $LiNi_{1-y}Co_yPO_4$ ($y$=0, 0.25, 0.33, 0.66, 1).

Figure 78 shows an enlarged view of the XRD patterns in the range between 40-47 2θ. Rising cobalt content leads to a left shift of the peaks. The side phases $Ni_3P$ and Ni which are most pronounced in $LiNiPO_4$ are also marked.

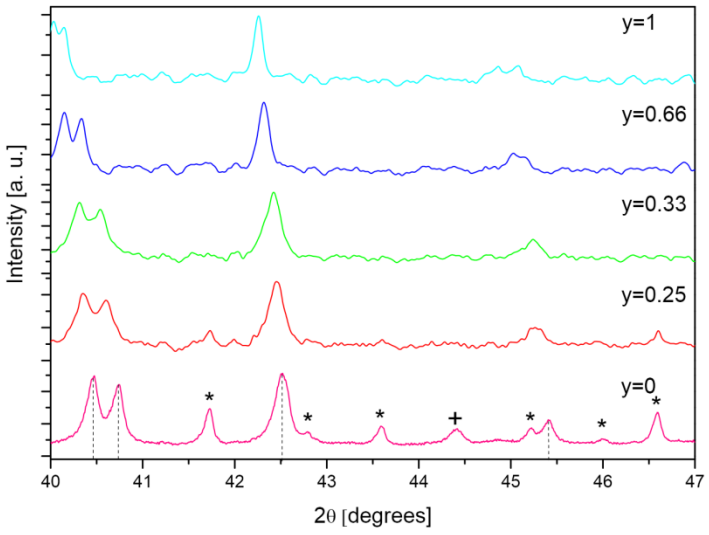


**Figure 78:** Enlarged view of the section between 40 and 47 degrees, with |$LiNiPO_4$, as well as $^{*}Ni_3P$ and $^{+}Ni$ as side phases.

Table 11 lists the refined cell constants of the examined solid-solution, which were used in Figure 54. The refinement was performed with the program Jana2006[132].

**Table 11:** Refined cell constants of the $LiNi_{1-y}Co_yPO_4$ solid-solution.

| Sample | *a*-axis [Å] | *b*-axis [Å] | *c*-axis [Å] | Volume [Å$^3$] | $R_p$ | $W_{rp}$ |
|---|---|---|---|---|---|---|
| $LiNiPO_4$ | 10.0374(6) | 5.8587(3) | 4.6802(3) | 275.22(3) | 4,44 | 6,34 |
| $LiNi_{0.75}Co_{0.25}PO_4$ | 10.0780(2) | 5.8769(13) | 4.6865(12) | 277.57(11) | 2,35 | 2,96 |
| $LiNi_{0.66}Co_{0.33}PO_4$ | 10.0912(9) | 5.8827(5) | 4.6900(5) | 278.41(5) | 2,93 | 3,75 |
| $LiNi_{0.33}Co_{0.66}PO_4$ | 10.1469(9) | 5.9043(5) | 4.6948(5) | 281.27(4) | 2,33 | 2,93 |
| $LiCoPO_4$ | 10.2052(10) | 5.9226(6) | 4.7003(5) | 284.09(5) | 2,41 | 3,01 |

In Figure 79 the charge and discharge curves for $LiNi_{0.33}Co_{0.66P}O_4$ are shown. The variations in the charge curve are most likely due to electrolyte decomposition. Moreover, the fading of the discharge capacity is severe. This is convenient with cyclability tests, which show the capacity retention of the electrodes versus the cycle number.

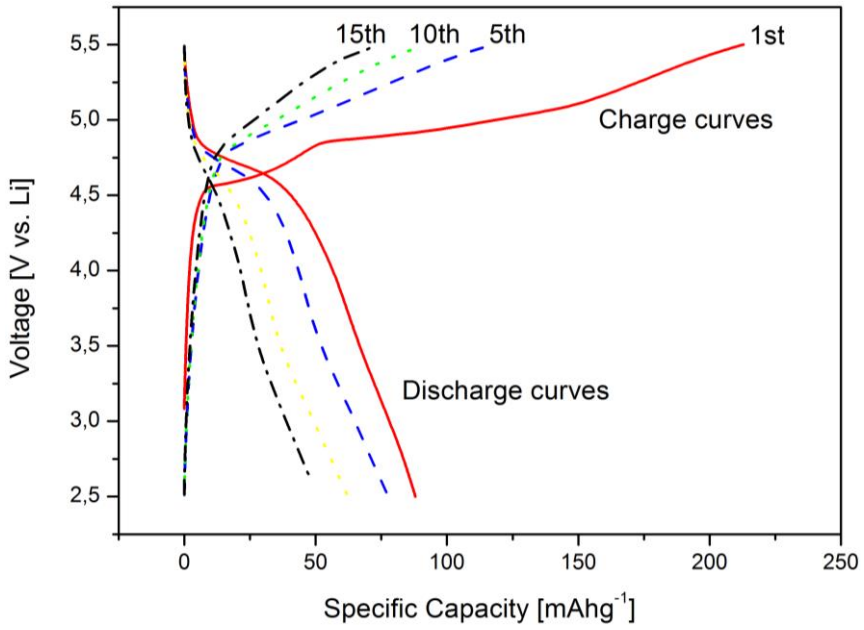


**Figure 79:** Charge and Discharge curves for $LiNi_{0.33}Co_{0.66}PO_4$ at a current rate of 2 C; Voltage range: 2.5 - 5.5 V